

ALLOY DEVELOPMENT OF A NEW PLATINUM-BASED BULK METALLIC GLASS

THÈSE N° 7517 (2017)

PRÉSENTÉE LE 3 MARS 2017

À LA FACULTÉ DES SCIENCES ET TECHNIQUES DE L'INGÉNIEUR
LABORATOIRE DE MÉTALLURGIE MÉCANIQUE
PROGRAMME DOCTORAL EN SCIENCE ET GÉNIE DES MATÉRIAUX

ÉCOLE POLYTECHNIQUE FÉDÉRALE DE LAUSANNE

POUR L'OBTENTION DU GRADE DE DOCTEUR ÈS SCIENCES

PAR

Hamed KAZEMI

acceptée sur proposition du jury:

Prof. D. Damjanovic, président du jury
Dr L. Weber, directeur de thèse
Prof. J. Schroers, rapporteur
Dr A. Blatter, rapporteur
Prof. R. Logé, rapporteur



ÉCOLE POLYTECHNIQUE
FÉDÉRALE DE LAUSANNE

Suisse
2017

For Ali & Esmat

*“Experiment is the only means of knowledge at our disposal.
Everything else is poetry, imagination.”*

Max Planck, Physicist

*“Work is the best of narcotics, providing the patient be
strong enough to take it.”*

Beatrice Webb, Sociologist & Economist

*“Keep the company of those who seek the truth,
run from those who have found it.”*

Vaclav Havel, Writer & Statesman

Remerciements

Je souhaite exprimer ma reconnaissance au personnel et la gestion de Hublot S.A. pour le soutien financier de ce projet. J'aimerais adresser mes remerciements les plus cordiaux à M. Jean-Claude Biver pour sa vision vis-à-vis l'importance de l'innovation sur les matériaux, celle-ci nous a permis de mettre en œuvre ce projet. Mes remerciements à l'équipe R&D de Hublot, en particulier M. Senad Hasanovic et son successeur, M. Luca Bianco. Ensuite je voudrais présenter mes remerciements aux membres du jury ; Prof. Roland Logé, Prof. Jan Schroers, Dr. Andreas Blatter ainsi que le président du jury Prof. Dragan Damjanovic pour le temps et l'attention qu'ils ont apportés à lire et commenter ma thèse.

Cette thèse est le récit du voyage d'une idée née peut-être un jour sur un bout de papier jusqu'à la production d'un premier prototype qui semble à quelque chose plutôt réelle. A l'origine, cette idée-là est celle de mon directeur de thèse Dr. Ludger Weber. Je tiens à lui présenter mes remerciements les plus chaleureux pour la confiance qu'il m'a accordée, sa supervision tout au long cette thèse et sa gentillesse inépuisable. Je lui suis reconnaissant pas seulement pour tout ce-que qu'il m'a enseigné de la métallurgie mais aussi pour tout ce-que j'ai appris de lui au niveau humain.

Bien évidemment, ce travail est le fruit d'un effort collectif fournit par un Troïka légendaire aussi appelé « Le Dream Team » dont Dr. Cyrill Cattin fait partie des fondateurs. Son humeur estivale, son énergie positive intarissable ainsi que sa rigueur à la Schwizerdütsch ont été les éléments clé pour le succès de ce projet et pour surmonter les challenges qui sont les compagnons de voyage de n'importe quelle thèse. Je dois un remerciement tout particulier à Prof. Andreas Mortensen le directeur du laboratoire de la métallurgie mécanique (LMM) à l'EPFL. Grâce à lui et l'ambiance solidaire et bienveillante de son laboratoire, ce dernier est devenu ma deuxième maison.

Ce travail aurait été impossible sans l'aide et le soutien indispensable de notre personnel technique Cyril Dénéreaz, Raphaël Charvet et Willy Dufour. Leurs expertises, leur profes-

sionnalisme ainsi que leur amabilité m'ont été essentiels et très précieux. Durant ce projet, j'ai eu la chance et le grand plaisir d'avoir les étudiantes et les étudiants qui m'ont beaucoup apporté. Ces personnes brillantes ont eu des contributions significatives à cette thèse ainsi qu'à mon séjour à l'EPFL. Mes remerciements à Anne-Juliette Dedisse, Gilles Hodel, Tatiana Pachova, Chloé Waeber, Aigoul Schreier, Mathilde Taconnet de Perrot, Maxime Garnier, Maïté Blank, Gionata Schneider, Félix Müller, Damien Chevret, Luca Bianco et finalement Eloïse Masquelier. Ceux qui ont fait leurs thèses au LMM pourraient témoigner que le succès de nos projets serait inatteignable sans le soutien de l'atelier MX avec son personnel aimable et professionnel. Leurs conseils, leur disponibilité et leur gentillesse sont exemplaires. Je garderai des souvenirs inoubliables de nos fameux dîners de Noël. Je tiens à remercier Pierre-André Despont, Werner Brönnimann, Adrien Grisendi, Jean-Marc Colomb, Eric Vassalli, Yves Ruschetta et Sévérino Tehrani.

J'aimerais aussi remercier mon ami Dr. Hossein Nadjafi à Bern, pour son aide avec le traitement de surface au laser, ainsi que nos discussions inspirantes. Mes remerciements aux collègues à Neuchâtel notamment Dr. Cyril Cayron pour sa gentillesse et sa disponibilité.

Je dois un très grand merci à mes très très très chers amis Maïté Blank, Gionata Schneider, Alex St-Amour et Visilia Ng ainsi que leurs familles tellement aimables et pleines de bonté. Je les remercie pour leur amitié qui ne m'a jamais quitté et leur soutien dans les moments difficiles, je leur dois beaucoup.

J'aimerais remercier ma chère amie Fabienne Ubezio pour son soutien, son écoute, son encouragement ainsi que ces conseils précieux. Son amitié m'est très cher. Un merci tout exclusive aussi à sa famille si charmante Sylvain, Louis, Inès et Jules. Merci à mes amis Gilles Nahon et Flora Trujillo pour leur amitié généreuse, merci en particulier pour les sympathiques soirées de «Cards Against Humanity».

Merci à mes amis scout Lionel et Mélina Michelet. J'ai passé des moments magnifiques dans leur compagnie et parmi les autres scouts valaisans, notamment l'inoubliable camp d'été à Venise! J'ai passé de très bons moments avec les anciens du labo, j'aimerais remercier Arda-Bey connu pour sa sagesse, Roberto (Roby le Dr. Boom!!!) avec qui j'ai passé les soirées « à l'espagnole!», Jérôme le chef pâtissier 3-étoiles, Alain très attaché à son Valais et finalement Gabriella et son Tiramisu mondialement connu. Je remercie aussi Madame Zanetta l'ancien secrétaire du laboratoire et Andreas Rossoll « Charpy » qui m'a offert mon premier petit-boulot quand je suis venu en Suisse. Mes remerciements à Homeira Sunderland qui m'a présenté à Ludger au début de mon master quand j'étais en

cherche d'un projet de semestre, qui savait à cette époque-là que j'allais faire plus de 6 ans au LMM !?

Un très grand merci à mon très cher ami Senad pour son appui pendant ce projet, son amitié généreuse ainsi que ses conseils. J'aimerais remercier aussi les autres collègues au LMM, Léa, Martin, Vaclav et Goran. Un grand merci à Marta et Ana mes voisins de bureau pour leur soutien et leur gentillesse. Un Merci tout spécial à Alexander, pour ses pronostiques astrologiques et son encouragement surtout pendant la rédaction de la thèse. Un grand merci à mon ami d'enfance Ali Eghtesadi avec qui j'ai beaucoup de souvenir et qui m'accueilli chaleureusement lors mes passages aux Etats-Unis d'Amérique.

აგრეთვე მინდა დიდი მადლობა გადავუხადო ჩემი ძვირფასი ძმაკაცი, კახა მულიანი, და სხვა საყვარელი მეგობრები საქართველოში.

Tout ce-que j'ai dans la vie est simplement et entièrement grâce à ma famille. Ma grande mère Fatima « Hajkhanoom », mon père Ali, ma mère Esmat, mes sœurs Hosna et Reyhané et mon beau-frère Hesam. Une pensée douce pareillement à mes grands-pères Ghorban-Ali « Agha-joon » et Abbas-Gholi ainsi que ma grande mère Sultane «Deda» qui me regardent les trois depuis les cieux.

Ma chère famille vous êtes ma richesse, mon abri, mes meilleurs amis, mes confidences et tout ce qu'il a de plus précieux sur cette terre. Je remercie le ciel pour m'avoir bénie avec un tel trésor et ensuite je vous remercie pour tout, je vous remercie infiniment et de tout mon cœur. ჩემო ძვირფასებო! თქვენ ხართ ჩემი სიხარული და ჩემი სიცოცხლე! გულით და სულით მადლობელი ვარ თქვენთან ყველაფერსთვის!

Lausanne le 11 February 2017

Abstract

The aim of the present thesis is the development of a new platinum-based bulk metallic glass based on the ternary system of Pt-B-Si that i) complies with the hallmarking standard Pt 850 (i.e. with at least 85 wt.-pct of platinum); ii) provides high hardness ($HV > 600$) and iii) has a critical casting diameter larger than 5 mm. To this end, the low melting point areas in the Pt-B-Si ternary system have first been established. Then, the partial substitution of platinum by various transition metals (TM) as well as partial substitution of silicon by germanium and its concomitant effect on the characteristic temperatures of the metallic glass, i.e. the temperature of glass transition, T_g , the temperature of crystallization, T_x , as well as the solidus, T_s , and liquidus temperature, T_l , have been assessed. Particular attention was given to the evolution of the temperature difference $\Delta T = T_x - T_g$ that characterizes the formability of the alloy in its supercooled liquid region.

A ternary eutectic valley has been located between the binary eutectics of $Pt_{71}B_{29}$ and $Pt_{73}Si_{27}$ with a ternary eutectic point at a composition of $Pt_{73}B_{15}Si_{12}$ with a T_s of about 700°C. Another region of low T_s was the composition line connecting this ternary eutectic to a second binary eutectic $Pt_{58}B_{42}$.

Among the TMs' studied, copper lowered the melting point of the alloy most efficiently in the region of 620°C and raised the T_g from around 250 to 280°C at substitution of one fourth.

Starting from the ternary eutectic point and advancing along the low melting point valley towards the second eutectic ($Pt_{58}B_{42}$), the most promising composition was found at $Pt_{50}Cu_{16.6}Si_{9.4}B_{24}$ with a melting range of 570-630°C and a T_g of roughly 300°C. For this composition, the partial substitution of silicon by germanium by up to one third had shifted the primary crystallization of α -Pt and B_4Si to the temperature of a secondary crystallization of a so far unknown compound. The optimized alloy exhibiting 5 mm critical casting diameter was found to be $Pt_{49.95}Si_{6.4}B_{24}Ge_3Cu_{16.65}$ with ΔT of 50 °C.

The unknown crystalline compound mentioned above was characterized by synchrotron X-ray diffraction and resulted in the identification of a new hexagonal phase with lattice parameters of $a = 8.973(1) \text{ \AA}$ and $c = 2.959(1) \text{ \AA}$. Despite exhibiting a clear glass transition and a supercooled liquid region in the DSC analysis, 5 mm as-cast samples typically contain ordered domains with the same hexagonal structure of 2-3 nm in size. By increasing the degree of crystallinity the unit cell volume of the hexagonal lattice decreased due to rejection of copper atoms into the glassy matrix while the size of the pre-crystalline domains in the remaining glassy matrix increased to 8 nm. The enrichment of the remaining glass matrix in copper was also identified as principal reason for the continuous change of glass transition temperature upon partial crystallization.

The hardness of the alloys developed here ranged between 450 and 600 HV in the amorphous state. It was observed that partial crystallization could increase the hardness close to 800 HV yet it results in fragilization of the alloy. In order to increase the superficial hardness of the alloy above 700 HV while keeping the bulk glassy and resilient, laser surface treatment was done.

Fluxing with B_2O_3 was investigated to further increase the critical casting diameter of the alloys. However, neither could the oxygen level be lowered nor the glass forming ability of the alloy be improved by extensive fluxing at 1100°C . On the other hand minor addition of scandium was effective in lowering the oxide level in the alloy below the quantitative detection limit of 5 ppm. Minor addition of rare earth (RE) and group 3A elements was further investigated in the series of alloys with the general formula $\text{Pt}_{49.95}\text{Cu}_{15.65}(\text{RE or 3A})_1\text{Si}_{6.4}\text{Ge}_3\text{B}_{24}$ (RE = Sm, Ho, Tb, Gd, and Dy; 3A = Sc, Y). All elements substituted by 1 at.-pct of copper increased the T_g , between 6 and 17°C with a similar yet somewhat larger effect on T_x .

Keywords

Platinum – Bulk Metallic Glass – Amorphous Metals

Résumé

L'objectif de cette thèse était de développer un nouveau verre métallique à base de platine à partir du système ternaire de Pt-B-Si. Cet alliage devait i) être conforme à la norme de poinçonnage Pt 850 (c.-à-d. contenir au moins 85 % pds de platine); ii) avoir une dureté supérieure à 600 HV et iii) avoir un diamètre critique de coulée supérieur à 5 mm. Afin de remplir ces critères, les zones à faible point de fusion du système Pt-Si-B ont d'abord été établies. L'influence d'une substitution partielle du platine par différents métaux de transition (MT), ainsi celle de la substitution partielle du silicium par le germanium ont ensuite été étudiées. Leurs effets sur les températures caractéristiques du verre métallique, c.-à-d., la température de transition vitreuse, T_g , de cristallisation, T_x , du solidus, T_s , et du liquidus, T_l , a été évalué. Une attention particulière a été accordée à l'évolution de la différence de température $\Delta T = T_x - T_g$ qui caractérise la formabilité de l'alliage dans la région où il forme un liquide en surfusion.

Une vallée eutectique ternaire a ainsi été localisée entre les eutectiques binaires $\text{Pt}_{71}\text{B}_{29}$ et $\text{Pt}_{73}\text{Si}_{27}$. Son point eutectique a été identifié à la composition $\text{Pt}_{73}\text{B}_{15}\text{Si}_{12}$ avec $T_s = 700^\circ\text{C}$. La ligne de composition reliant cet eutectique ternaire à l'eutectique binaire $\text{Pt}_{58}\text{B}_{42}$ a également été identifiée comme étant une zone à faible T_s .

La suite du travail a permis de montrer que, parmi les MTs étudiés, le cuivre était plus efficace pour abaisser T_s et augmenter T_g . Lorsqu'un quart du platine est remplacé, $T_s = 620^\circ\text{C}$ et $T_g = 280^\circ\text{C}$.

En partant du point eutectique ternaire et en passant le long de la vallée ayant un faible point de fusion en direction de l'eutectique $\text{Pt}_{58}\text{B}_{42}$, la composition la plus prometteuse a été trouvée pour $\text{Pt}_{50}\text{Cu}_{16.6}\text{Si}_{9.4}\text{B}_{24}$. La plage de fusion de cet alliage varie de $570\text{--}630^\circ\text{C}$ et sa T_g se situe à 300°C . Pour cette composition, l'influence d'une substitution partielle (0-33%) du silicium par du germanium a permis d'augmenter la température de cristallisation des phases primaires $\alpha\text{-Pt}$ et B_4Si jusqu'à atteindre celle d'un composé secondaire inconnu. Une diffraction de rayons X en synchrotron a toutefois permis d'identifier que sa structure est hexagonale et que ses paramètres de mailles sont $a = 8,973(1) \text{ \AA}$ et $c =$

2,959 (1) Å. L'alliage optimisé, permettant d'atteindre un diamètre critique de coulée de 5 mm est $\text{Pt}_{49.95}\text{Si}_{6.4}\text{B}_{24}\text{Ge}_3\text{Cu}_{16.65}$ avec ΔT de 50 °C. Si les analyses DSC effectuées sur alliage montrent clairement une transition vitreuse, ainsi qu'une région du liquid en surfusion prononcée, les mesures de diffraction de rayons-X par synchrotron ont permis de montrer que ce désordre apparent est en réalité formé de domaines ordonnés dont la taille varie de 2 à 3 nm et dont la structure est la même que celle de la nouvelle phase cristalline hexagonale. Une augmentation du degré de cristallinité permet la croissance des zones ordonnées jusqu'à 8 nm. Durant ce processus, la taille de la maille diminue car les atomes de cuivre sont rejetés dans la phase vitreuse. Cet enrichissement en cuivre de la matrice vitreuse restante a été identifié comme étant le principal facteur expliquant le changement continu de la T_g lors de la cristallisation partielle.

La dureté des alliages développés se situe entre 450 et 600 HV à l'état amorphe. Il a été observé que la cristallisation partielle pouvait augmenter la dureté jusqu'à 800 HV, mais elle induit une fragilisation de l'alliage. Afin d'augmenter la dureté superficielle de l'alliage au-dessus de 700 HV, tout en gardant le cœur amorphe et tenace, il est proposé d'effectuer un traitement de surface au laser.

Afin d'augmenter le diamètre critique de coulée des alliages, la possibilité d'effectuer un fluxage avec du B_2O_3 a d'abord été étudiée. Aucune diminution du niveau d'oxygène, ni aucune augmentation du diamètre critique de coulé n'a pas été observée. En revanche, il a été montré qu'une addition mineure de scandium abaisse le niveau d'oxygène dans l'alliage au-dessous de la limite de détection quantitative de 5 ppm. L'influence de quantités mineures de terre-rares (TR) et d'éléments du groupe 3A a également été étudiée pour une série d'alliages ayant la formule générale suivante : $\text{Pt}_{49.95}\text{Cu}_{15.65}$ (TR ou 3A) $_1\text{Si}_{6.4}\text{Ge}_3\text{B}_{24}$ (TR = Sm, Ho, Tb, Gd et Dy ; 3A = Sc, Y). Quelle que soit l'élément ajouté, la T_g , augmente de 6 à 17 °C avec un effet similaire mais un peu plus prononcé sur la T_x .

Mots-clés

Platine – verre métallique – matériaux amorphes

Contents

Remerciements	vii
Abstract.....	xi
Keywords.....	xii
Résumé	xiii
Mots-clés.....	xiv
Chapter 1 Introduction.....	1
1.1 Platinum, the noblest of metals.....	1
1.2 The potential of Pt-based metallic glasses	3
1.3 Developing and processing a new hard Pt-based BMG for watch application	4
1.4 Objectives of this thesis	6
Chapter 2 State of the art.....	7
2.1 Historical and phenomenological approach to glass forming	7
2.2 Glass vs. Crystal.....	9
2.3 Topological considerations in glass formation	13
2.4 Criteria for predicting the glass forming ability (GFA)	16
2.5 Guidelines for alloy development and optimization	20
2.6 Relaxation of glasses.....	23
2.7 Crystallization in BMG's	27
2.7.1 Crystallization in metallic glasses due to irradiation damage.....	27
2.7.2 Crystallization in metallic glasses due mechanical deformation	28
2.7.3 Crystallization in metallic glasses by dealloying	31
2.7.4 Crystallization in metallic glasses during annealing.....	32
2.8 Glass transition temperature (T_g) and mechanical properties	47
Chapter 3.....	53
Development of a new family of phosphorous-free Pt-based bulk metallic glasses	53
Abstract.....	54
1. Introduction	54
2. Experimental Procedure	57
2.1. Materials and processing	57
2.2. Characterization	58

3.	Results.....	59
3.1.	Pt-Si-B ternary eutectic.....	59
3.2.	Effect of platinum substitution by transition metals	61
3.3	Substitution of silicon by germanium	65
3.4	Mechanical properties.....	67
3.5	Critical casting thickness.....	67
4.	Discussion	68
4.1.	Pt-Si-B ternary eutectic.....	68
4.2.	Effect of substitution	69
4.3.	Crystallization	70
4.4.	Mechanical properties.....	70
4.5	Critical casting thickness.....	72
5.	Conclusions	72
	Acknowledgement.....	76
	References:.....	76
Chapter 4.....	Effects of partial crystallization in Pt-Si-B-based bulk metallic glasses on glass transition and crystallization of the remaining amorphous matrix	79
	Abstract	80
1.	Introduction	80
2.	Experimental methods	82
2.1.	Materials.....	82
2.2.	Annealing in stabilized salt bath	83
2.3.	Characterization techniques	83
2.3.1.	Thermal analysis	83
3.	Experimental results	84
3.1.	Partial crystallization during annealing	84
3.2.	Mechanical properties	85
3.3.	Physical and thermophysical properties	87
3.4.	Microstructural and compositional analysis	88
4.	Discussion	90
4.1.	Link between residual enthalpy of crystallization and degree of crystallinity	90
4.2.	Evolution of mechanical properties with increasing crystallinity	91
4.3.	Density change upon crystallization	92
4.4.	Local compositional variation upon crystallization	93
4.5.	Evolution of the characteristic temperatures, T_g and T_x	95
5.	Conclusion	97
	Acknowledgements.....	98
	References:.....	98

Chapter 5.....	101
Synchrotron radiation X-ray diffraction study of crystallization in Pt-Si-B-Ge-Cu bulk metallic glass	101
Abstract	102
1. Introduction	102
2. Experimental procedures	104
3. Results.....	105
3.1. Thermal analysis	105
3.2. XRD analysis of amorphous and partially crystallized samples	106
3.3. Determination of the structure of the crystalline phase	106
3.4. Evolution of the crystalline average domain size upon crystallization	110
4. Discussion	112
4.1. General XRD analysis of amorphous and partially crystallized samples	112
4.2. Evolution of the lattice parameter in the crystalline and the nano-domain phase	113
5. Conclusions	115
Acknowledgments.....	116
References:.....	116
Chapter 6.....	119
Influence of rare earth and group IIIA elements and fluxing on the thermophysical properties of a Pt-Si-B-Ge-Cu bulk metallic glass	119
Abstract.....	120
1. Introduction	120
2. Experimental procedures	122
2.1. Materials	122
2.2. Characterization techniques	123
2.3. Fluxing with B ₂ O ₃	124
2.4. Annealing in a stabilized salt bath	124
3. Results.....	125
4. Discussion	134
5. Conclusions	136
Acknowledgements.....	139
References:.....	139
Chapter 7 Processing of BMGs.....	141
a. Alloy Preparation	143
b. Melt spinning.....	145
c. Gravity casting	146
d. Arc-melting.....	147
e. Atomization	147
i. Formation of droplets.....	147
ii. Cooling and solidifying of droplets	150

f.	Forming in the supercooled liquid region	152
g.	Fabrication of a watch case by thermoplastic forming	155
h.	Laser surface treatment	163
Chapter 8	Miscellaneous	167
a.	Influence of Mn-addition on glass formation	167
b.	Formation of Boron-rich primary phases	171
Chapter 9	Conclusions and perspectives	177
a.	Achieved results	177
b.	Future development	179
References	181
Curriculum Vitae	189

Chapter 1 Introduction

Platinum is the rarest of the three classical precious metals—gold, silver, platinum—used in jewelry. Its primary production is either from elemental sources or as a by-product of nickel production. Platinum has a silver grey luster and is fairly inert against most chemicals. On the other hand, it has exceptional catalytic properties, which are put to service in the most important industrial application of platinum by mass: catalysts in cars. As the second largest application, roughly 30 percent of the world's platinum production is used for jewelry including high-end watches.

Pure platinum, as most face centered cubic (fcc) metals, is very soft and consequently suffers from inadequate scratch resistance. Therefore, for watch making and jewelry application, platinum is alloyed with other elements to improve its mechanical properties. Due to the high platinum content required by the current hall-marking standards for platinum, the increase in strength remains however typically limited. There is therefore a significant technological interest in finding techniques to improve the mechanical strength in platinum alloys. The technological goal of this thesis is the development and characterization of a new hard platinum alloy for watch making, and in particular as a structural component e.g. watchcases. The approach chosen for doing so has been the development of a new platinum-based bulk metallic glass. In the following chapter, a general overview is given on the conventional crystalline platinum alloys as well as a general introduction to metallic glasses and their exceptional mechanical and physical properties.

1.1 Platinum, the noblest of metals

Platinum has a substantial presence in both industrial and luxury applications. As of the end of 2015, the main industrial sectors responsible for platinum consumptions are namely autocatalysis, jewelry and other industrial applications e.g. electronics and glassmaking. The main suppliers of platinum are South Africa followed by Russia; Figure 1:1 shows the figures of supply and demand for platinum market as the end of 2015.

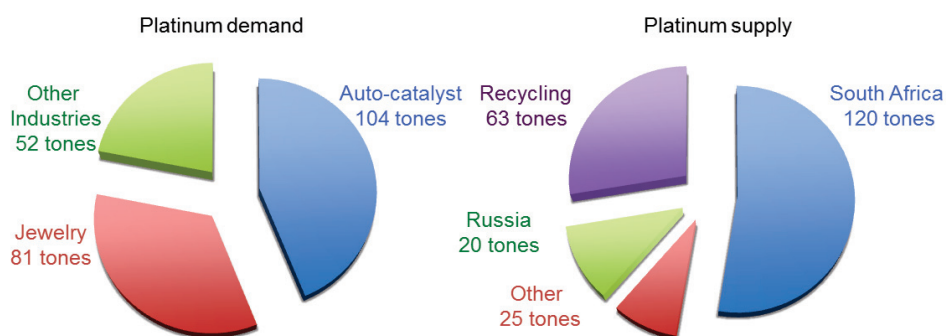


Figure 1:1 Global supply and demand of platinum as the end of 2015. [1]

Pure platinum suffers from inadequate scratch resistance due to its inherently low hardness (~ 60 HV). Thus for jewelry and watch-making applications, alloying platinum with other elements is necessary to provide adequate mechanical properties and in particular improve the hardness. Platinum alloys currently used in jewelry contain more than 85 wt.% of platinum. The most common purity level required for commercialized platinum alloys is Pt950 designating 95 wt.% of platinum. There are also hallmarking standards of Pt900 and Pt850 respectively containing 90 wt.% and 85 wt.% platinum. The general requirements for an alloy for jewelry application can be described as followings:

- Accordance with existing hallmarking standards. (e.g. Pt850 or higher)
- Scratch and wear resistance, quantified by hardness.
- Chemical inertness; resistance to corrosion, oxidation and tarnishing.
- The ease of processing, in terms of the ability to be cast, deformed and machined.

Common alloying elements for platinum alloys for jewelry and watch-making are namely copper, palladium, ruthenium, iridium, cobalt, chromium, gallium, and indium [2].

- Solution hardening (e.g. Co, Pd, Ru, Ir, Co, Cr [2–5])
- Precipitation hardening (e.g. Ti, Al, V [2,5–9])
- A combination of methods such as solution hardening and deformation (e.g. Pt-Ga-In [10])

It has further been reported that platinum can be case hardened by charging the surface region with boron [11].

All of the above-mentioned alloys are crystalline. A significant drawback of crystalline Pt-based alloys is their rather high melting temperature. Due to the limited amounts of alloying elements hardness of crystalline platinum alloys hardly goes beyond 300 HV. In recent years another promising possibility for developing new alloys fulfilling the criteria necessary for jewelry application has appeared: platinum-based bulk metallic glasses.

1.2 The potential of Pt-based metallic glasses

Metallic glasses form a new class of materials that have been studied since the sixties of the 20th century. At the beginning limited to very small volumes due to the high cooling rates required to prevent crystallization, metallic glasses can now be produced with a smallest dimension of several millimeters or even centimeters. Metallic glass forming compositions are often found near low lying eutectics, i.e. for compositions for which the liquid state is stabilized down to relatively low temperature with respect to the melting points of its components. Hence, the first class of platinum-based bulk metallic glasses has been developed based on the Pt-P eutectic composition with a melting point around 500 °C. In this system, bulk metallic glasses are developed by substituting a considerable portion of Pt with transition metals such as Cu, Co and Ni. Examples of alloys in this system capable of providing glassy structure while maintaining acceptable purity for jewelry applications are Pt_{57.5}Cu_{14.7}Ni_{5.3}P_{22.5} developed by Schroers et al. [12] corresponding to 85 wt.% of Platinum. An alloy with higher purity level in the same system is Pt_{74.7}Cu_{1.5}Ag_{0.3}P₁₈B₄Si_{1.5} developed by Demetriou et al. corresponding to 95 wt.% of platinum [13]. Glass formers of the Pt-Ni-Cu-P family have a rather low critical cooling rate of 10³K/s [14]. One of the most interesting features of Pt-based BMG is the possibility of being shaped in the super-cooled liquid region (SCLR), i.e. the temperature range between the glass transition and crystallization in which the material relaxes into a viscous liquid exhibiting viscosities in the range of 10¹⁰-10⁷ Pa.s. Forming in super-cooled liquid region provides the opportunity of producing parts with rather complex shapes, while maintaining an excellent surface quality [15]. Thermoplastic forming in the super-cooled liquid region can be of particular interest for watch-making industry reducing the costs and time of fabrication for parts with rather complex geometry. The hardest Pt-P-based bulk metallic glasses exhibit a hardness of 420 HV i.e. beyond the hardness values typically observed in conventional crystalline Pt-alloys [16]. Yet the phosphorous present in the system brings about undesirable features such as difficult processing due to reactivity of phosphorous.

It is worth noticing, phosphorous is not the only alloying element leading to a low-melting eutectic. Reviewing the phase diagram databases eight alloying elements can be identified leading to a eutectic temperature below 1000°C (in order of rising eutectic temperature): P, As, Sb, Bi, Ge, B, Si and Te. It is interesting to note that the four elements leading to the lowest temperature come all from the group VB of the periodic table. The melting point and the composition of the eutectic increases from each period to the next. The liquidus and eutectic lines around the platinum rich eutectic are indicated in Figure 1:2. It is clear that besides phosphorous essentially the eutectics of platinum with B, Si and As would be interesting to build upon.

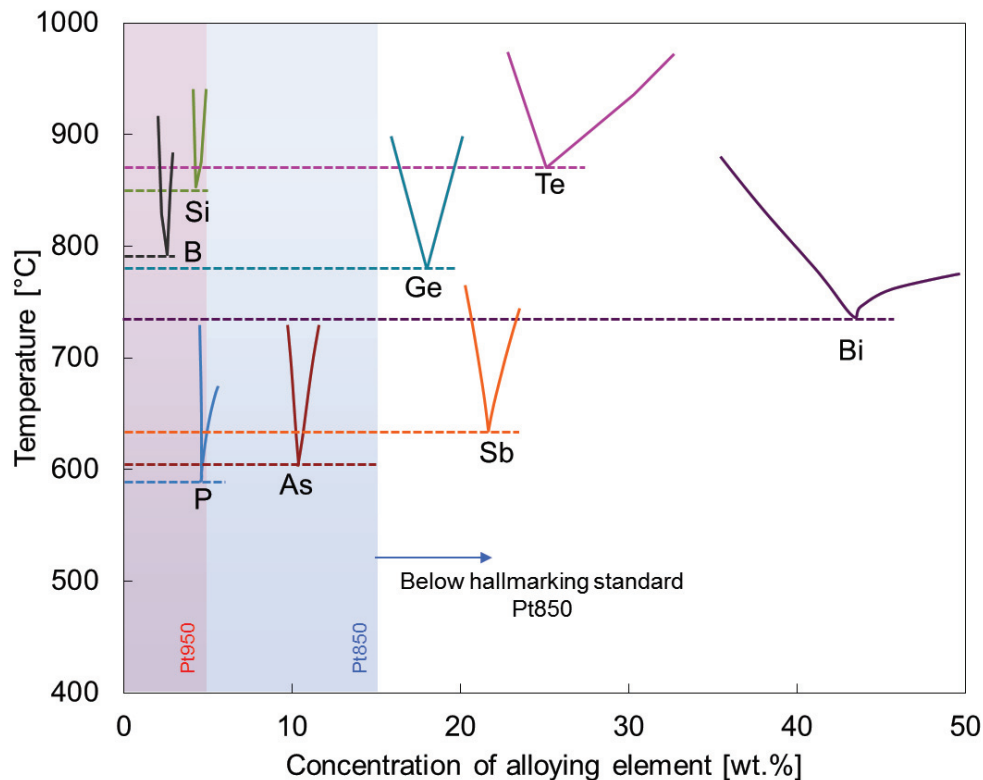


Figure 1:2 Positions of other low-lying Pt-X eutectics in the temperature composition space.

1.3 Developing and processing a new hard Pt-based BMG for watch application

It is clear that both Pt-Si and Pt-B are capable of producing relatively deep eutectics at 29 at.-pct of Boron and 23 at.-pct of Silicon [17],[18]. Compared to Pt-As based alloys, the Pt-Si and Pt-B systems leave still some room for further alloying elements that might facilitate the glass formation. On the other hand, the eutectic temperature of these binaries is significantly above that of the Pt-P and Pt-As system. A potential remedy to this shortcoming is

to investigate ternary eutectics. Comparing the Pt-Si-B system with similar ternary systems such as Ni-Si-B, Co-Si-B and Fe-Si-B hints towards the existence of an even deeper ternary eutectic [19,20]. Some of these Ni-Si-B and Fe-Si-B alloys have also been obtained in amorphous form [21–28]. The ternary eutectic reaction in the system Pt-Si-B could by analogy be estimated to happen between 700-750°C. The experimental observation of a ternary eutectic at roughly 700°C during preliminary research has built the starting point of the present thesis.

It was further also encouraging to see that the Pt-Si-B system was some sort of a model case on topological ground [29–32]: the atomic size ratio Pt:Si:B is near¹ 1:0.8:0.6 and the smallest atom is more abundant than the middle sized one. Last but not least, the choice of the Pt-Si-B system was comforted by the observation in the literature that both Si and B have been found to improve the hardness in Pt-based alloys [34,35].

There is considerable work in the literature evaluating different minor and major substitutions on characteristic temperatures such as T_g , T_x , T_s and T_l for improving the glass forming ability. Transposing these results to the system at hand [36,37] constitutes the main body of work to be done in the optimization process. The following activities are, hence, the steps taken for developing and processing a new hard Pt-based BMG with superior hardness destined for watch application:

- a) Thermodynamic exploration of the platinum-rich corner of Pt-Si-B ternary phase diagram for locating the whereabouts of possible ternary eutectic point using Differential Scanning Calorimetry (DSC) accompanied by the study of microstructure.
- b) Considering the analogies between Pt-Si-B and other existing glass formers, minor substitution of the base metal with other elements can be helpful for increasing the chance of glass formation.
- c) The possibility of forming metallic glass in this system is studied, while using high cooling rates induced by melt spinning.
- d) The effect of composition on characteristic temperatures such as glass transition, T_g , crystallization, T_x , end of solidification, T_s , and, onset of solidification, T_l is evaluated and their functionality according to the composition is investigated.

¹ The atomic radii depend on the compound and the nature of the bond, therefore it is not judicious to define a unique atomic size for each individual atom [33].

- e) Production of glassy alloys with larger dimensions by suction casting is done.
- f) The influence of crystallization and processing parameters on thermo-physical and mechanical properties are extensively studied.
- g) A set-up for producing prototype watch components from the glassy feedstock is designed and made.

1.4 Objectives of this thesis

The objectives of this thesis can be summarized as follows:

- Producing a Pt 850 alloy with critical casting diameter larger than 5 mm usable for watch applications.
- Development of a Pt 850 alloy with superior hardness ($HV > 600$).
- Investigation of the influence of processing parameters and crystallization on physical and mechanical properties of the newly developed Pt-based BMG.
- Establishing the dependence of the glass forming ability and thermophysical properties on composition.

Chapter 2 State of the art

2.1 Historical and phenomenological approach to glass forming

Interestingly enough, glass is defined by what it is not! Glass or an amorphous material is a non-crystalline solid [38]. Glassy or amorphous materials are characterized by the absence of crystalline periodicity in long-range order. By definition glass is a frozen liquid, which does not crystallize when cooled down from the liquid state below its glass transition temperature (T_g). The glass transition temperature is arbitrarily defined as the temperature at which viscosity becomes larger than 10^{13} Pa·s. Glassy materials are found in all major bonding classes: covalent, ionic, van der Waals, hydrogen bond, and metallic [39]. Among these, metallic glasses require the highest cooling rate for glass formation. This is due to the isotropic character of metallic binding [40].

Glass has been known to humanity for millennia. To the general public, glass is used as a term to describe brittle and transparent materials abundantly used in each aspect of our daily lives. Chemically, the material that we call glass is a mixture of metal or semimetal oxides. The most abundant kind of oxide glass is obtained from melting silica sand and can be easily formed, or turned into different colors or taints by addition of different impurities or “additives”. In physics, however, glass is more generally a solid state of matter lacking translational symmetry. Compared to crystalline material for which melting is typically a phase transformation of 1st order with a significant jump in viscosity at the melting point, a glass is a material exhibiting a so called “glass transition” and subsequent rapid decrease in viscosity as the temperature goes from the glass transition to the melting point. The glass transition temperature, T_g , is arbitrarily defined at a viscosity of 10^{13} Pa·s and is typically significantly below the melting point, T_m .

Glassy structures are, thermodynamically metastable and are formed because the kinetics of forming crystalline structures are slow compared to the time available upon cooling between T_m and T_g . In oxide glasses and polymers the time for crystallization can be from a

few seconds to several hours or days particularly due to steric hindering of side chains in polymers. In metals, however, crystallization is typically much faster due to the isotropic nature of the metallic bond. The first observation of the glassy state in metallic systems was done by Klement et al. [41] in 1960 in a $\text{Au}_{75}\text{Si}_{25}$ alloy. Amorphous structures in metals can be obtained if the metal is cooled from the liquid state to below the glass transition temperature in nano- to microseconds for pure metals or milliseconds to seconds for alloys.

Quite a number of techniques have been devised to attain amorphous states in metals and alloys. These methods commonly apply a very efficient cooling rate: e.g. melt spinning, splat cooling, atomization, radiative cooling of miniaturized structures, and copper mould casting of small volumes². With the advent of the highly stable bulk metallic glasses and concomitant advances in melt treatment technology by fluxing, amorphous metals can nowadays be obtained even by gently cooling the liquid in a quartz mould.

Structure-wise, glass is very close to a frozen-in liquid, which does not crystallize when cooled down from the liquid state below its glass transition temperature (T_g). While the physical understanding of the glass formation and the glass transition are still only partly solved problems, the phenomenological recipe to design alloys able to be solidified in the glassy state have been established over the years. According to Inoue [42] there are three golden rules making a composition capable of bulk glass formation [42]:

- A bulk metallic glass should be composed of at least three elements.
- There should be a significant difference in atomic sizes of the main 3 constituents of the system. (More than 12%).
- The heat of mixture of the main three elements should be quite negative.

The first rule is also known as the “confusion principle” i.e. putting together elements capable of producing different crystalline structures, which are energetically equally favourable thus upon quenching settling down for one individual crystalline structure is rendered difficult [43]. The second rule indicates the importance of atomic topology and close packing of atoms in the liquid state increasing the viscosity and inhibiting the necessary chemical fluctuations necessary for producing the nuclei. Furthermore, strong glass formers oc-

² We exclude here the processes of amorphous metal deposition from the gas phase upon cryogenic substrates as well as all forms of mechanical means to render a structure amorphous, i.e. high energy ball milling and the like.

cur at the vicinity of deep eutectics [44,45]. Research has brought significant detail and ramification to these golden rules. In what follows the literature on the major features of metal glass theory is reviewed.

2.2 Glass vs. Crystal

In his seminal paper, Turnbull [46] describes glass as a form of hardened cooled liquid. The quantitative indication of this hardness described in his statement is the shear viscosity being the proportionality factor between the rate of shear deformation and the applied shear stress in a Newtonian liquid. The viscosity value separating liquids from glass is arbitrarily set to 10^{12} poise (10^{13} Pa·s). The increase of the viscosity as a function of temperature is described by Fulcher's equation:

$$\eta = A \cdot \exp\left(\frac{a}{T-T_0}\right) \quad (2.1)$$

where A , a and T_0 are parameters depending on the specific materials. Looking at Eq.(2.1) the viscosity is relatively low above T_l (liquidus) and decreases slowly by temperature, yet by approaching T_0 the viscosity increases rapidly, hence the glass transition temperature is the temperature at which the viscosity is 10^{12} poise. The viscosity can be plotted against the inverse of temperature scaled by T_g resulting in what is known as Angell-plot shown in Figure 2:1.

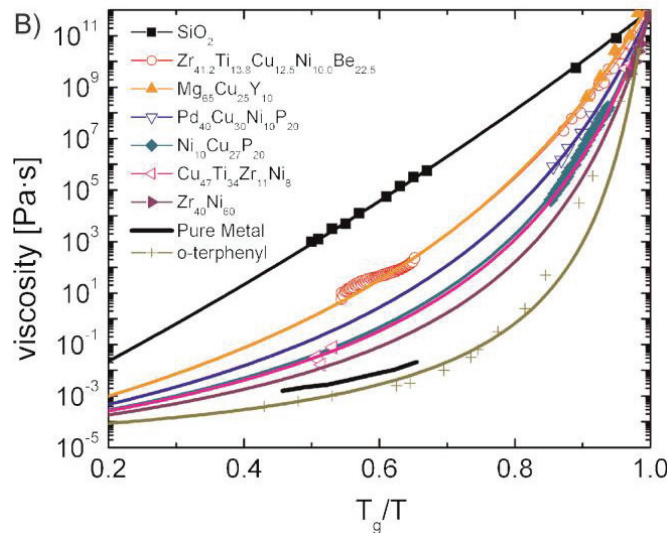


Figure 2:1 Angell plot, showing the temperature dependence of some metallic and non-metallic glass liquids (from [15]).

Commonly, liquids with strong directional bonding such as silica show a relatively weak dependency of viscosity to temperature maintaining a viscous state at the whole range of temperatures while fragile liquids exhibit a low viscosity at high temperature and by approaching the T_g the viscosity increases rapidly [47]. The quantification of the degree of the dependency of viscosity to temperature is described by the fragility index, m , given by:

$$m = \left. \frac{d \log(\eta)}{d(T_g/T)} \right|_{T=T_g} \quad (2.2)$$

A strong glass like silica has a fragility index of $m \approx 20$. A high value of m (i.e. $m > 100$) on the other hand characterizes a fragile liquid whose vitrification requires higher cooling rates. Most metallic glasses show intermediate liquid fragility below 60.

For a liquid to turn into glass or vitrify, crystallization must be avoided. Crystallization is induced through nucleation and growth. In order to form a nucleus an interface has to be created between the liquid and the crystal, which requires energy and acts as a barrier. The driving force is the change of Gibbs free energy between the crystal and the liquid. For a cluster to be stable enough to become a nucleus it should be of a critical size, thus random chemical fluctuation in liquid should bring a certain number of atoms corresponding to the composition of the nucleus together to attain a stable state. Commonly, there are quenched-in nuclei or heterogeneous sites present in solidifying liquids, thus usually crystallization upon solidification is triggered by heterogeneous nucleation. In absence of heterogeneous nucleation sites the nucleation is necessarily homogeneous. Homogeneous nucleation requires typically much larger undercooling than heterogeneous nucleation. This in turn may lead to significant increase in viscosity, particularly for strong solids, at the undercooling sufficient for homogeneous nucleation. This highlights the importance of avoiding impurities or oxides in particular when preparing the materials for glass formation. For avoiding crystallization, if the number of crystal nuclei appearing at a given temperature δn , in a given volume v_1 , appearing at a specific frequency, I ((nucleation frequency)/(time*volume)) one can write [46]:

$$\delta n = I v_1 \delta t. \quad (2.3)$$

For the first crystal embryo to form from the liquid the time $t_{min} = n^* \tau_i$, (n^* being the critical number of atoms and τ_i the mean time of each atomic fluctuation) is needed [46]. Now, for a liquid with larger viscosity, the chemical fluctuations necessary for bringing together the

needed composition of atoms are less frequent. Eq. (4) describes the frequency of nucleus formation [46]:

$$I = \frac{k_n}{\eta} \exp(-b\alpha^3\beta/T_r(\Delta T_r)^2) \quad (2.4)$$

k_n and b are constants while α and β are dimensionless parameters:

$$\alpha = \frac{(N\bar{V}^2)^{1/3}\sigma}{\Delta H_m}, \beta = \frac{\Delta H_m}{RT_m} = \frac{\Delta S_m}{R} \quad (N: \text{Avogadro's number}) \quad (2.5)$$

The main force against nucleation is described by α , which is proportional to the surface tension of liquid-crystal interface. β is the area of crystal melted at the melting temperature by the enthalpy of ΔH_m . The temperature-dependence of I and u (the speed of crystal-liquid interface) are depicted in Figure 2:2.

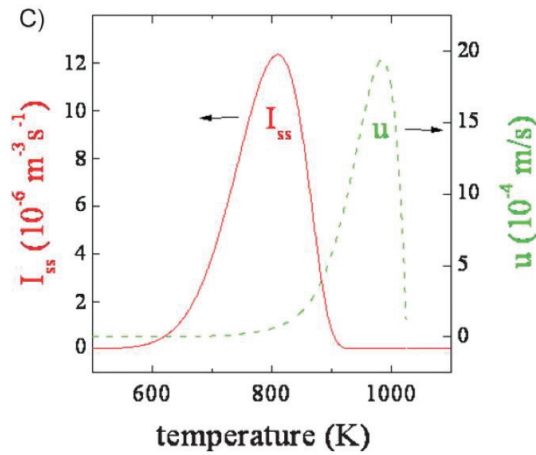


Figure 2:2 Temperature dependence of I and u (from [15]).

For example, at viscosities close to 10^{-2} poise and $\tau_i \sim 10^{-12} \text{ s}$, for a hypothetical cluster of 100 atoms, the time necessary for formation would be in the order of 10^{-10} s . Under these conditions this liquid would solidify or vitrify if it was cooled at a rate greater than 10^{12} K/s (provided the nucleation and not the growth is the critical step). In reality, such cooling rates are not practical for producing glass, e.g. melt-spinning applies a cooling rate in the order of only 10^6 K/s and the most efficient splat coolers go not beyond 10^9 K/s [48]. Now looking back at Fulcher's equation describing the dependence of viscosity to temperature, Eq. (1), *the increase in the driving force for crystallization upon cooling is accompanied by increasing inability to crystallize due to temperature dependent viscosity* [15]. In a system capable of glass formation, the temperature dependence of viscosity is more severe than the dependence of Gibbs free energy on temperature. The C-shape of the T-T-T diagrams

comes from the difficulty to attach fresh atoms to the growing crystal which becomes more difficult by increasing the viscosity. Figure 2:2 shows an example of an experimental determination of data points of such a T-T-T curve. It should be noted that obtaining the data points in the vicinity of the nose of the T-T-T diagram is not an easy task due to rapid kinetics of crystallization. It should be noted that measuring the data points at the vicinity of the nose of the diagram as depicted in Figure 2:3 is extremely difficult and only possible by electromagnetic levitation. The nose of a T-T-T diagram for a moderate glass former lies at 10^{-4} s, while that of a bulk metallic glass can be as low as 10 s [15].

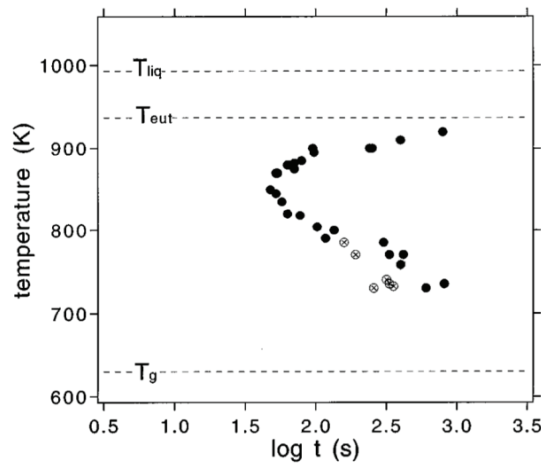


Figure 2:3 Time-Temperature-Transformation depicting the onset of crystallization in $\text{Zr}_{41.2}\text{Ti}_{13.8}\text{Cu}_{12.5}\text{Ni}_{10.0}\text{Be}_{22.5}$ glassy alloy (from [49]).

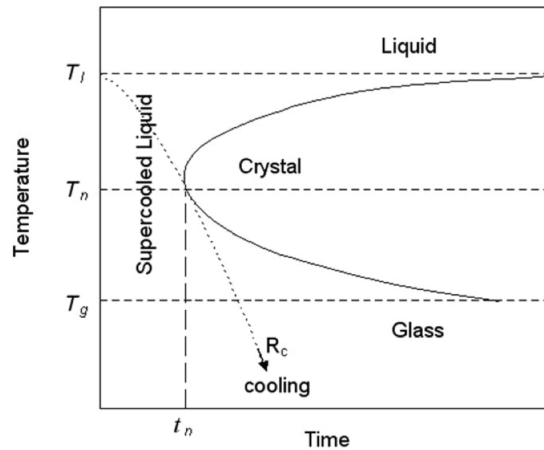


Figure 2:4 Time-temperature-transformation diagram for the onset of crystallization of glass forming liquid, and the critical cooling rate above which crystallization is avoided (from [50]).

Therefore, a cooling rate higher than the critical cooling rate represented by the tangent to the nose of the C-shaped curve would result in glass formation, cf. Figure 2:4.

The rate of crystallization can be described by the crystal nucleation rate, I , and the speed, u , of crystal-liquid interface. Both of these quantities are strongly dependent on reduced temperature, T_r , and undercooling, ΔT_r , given by:

$$T_r = \frac{T}{T_m}, \Delta T_r = \frac{T_m - T}{T_m} \quad (2.6)$$

T_m is the equilibrium crystallization temperature, i.e. the melting temperature, and T the actual temperature. The rate of the displacement, u , of the liquid-crystal interface is given by

$$u \cong \frac{k_u}{\eta} f(\Delta T_r) \quad (2.7)$$

where k_u is a system-dependent constant. Eq.(2.7) indicates that u is related to the undercooling (i.e. the driving force for crystallization) and inversely related to the viscosity, η .

As was mentioned previously, strong glass formers occur often in the vicinity of eutectic compositions. Sometimes, one or even two of the components formed in the eutectic decomposition are very close to the eutectic composition. In the event that the solids formed in the eutectic decomposition are far from the composition of the liquid significant chemical fluctuations are necessary for creating clusters corresponding to the desired chemical composition of stable embryos. Furthermore, the significant atomic size difference between the constituents of glass formers brings about formation of close packing in liquid further increasing the viscosity and hindering the chemical fluctuations necessary for nucleation.

2.3 Topological considerations in glass formation

One of the particularities of strong glass formers is the small difference between the density of liquid and the density of the solid in fully crystalline form. This difference is in the range of 0.3-0.54 % [33] and thus only a small fraction of the typical 4-6% of shrinkage for crystalline solid bcc and fcc metals at solidification. Such a small difference indicates the formation of locally highly close packed structures, so-called clusters, in the liquid state in bulk metallic glasses. The close packing and formation of dense structures in liquid reduces the diffusivity of atoms thus hinders nucleation and crystallization [33]. It further indicates that the enthalpy of crystallization is rather small, which, for a given loss of entropy

upon crystallization, leads to a low melting temperature and a low driving force for crystallization.

By considering atoms as hard spheres for a single sized particle size the highest random atomic packing density is 64%. As a principle of powder technology, by introducing significant atomic size distribution the packing density can be somewhat increased. The earliest work [51] on the structure of amorphous/liquid structure has presented atoms in the system as hard spheres and restriction is imposed by the inability of the atoms to get closer than their respective diameter. The shortcoming of considering atoms as hard spheres is the fact that atomic radii depend on each individual compound and have not a fixed value. The atomic radius is closely related to the neighbouring atoms and the nature of the atomic bonds as reflected by the concept of enthalpy of mixing. In case of a strong interaction, exchange energies are positive, i.e. the heat of mixing is negative, and atoms will typically get closer. Furthermore, the average coordination of the atoms will also affect the apparent or effective radius.

In short the two main parameters determining the topological conditions of the alloys are *atomic sizes* and their respective *atomic concentrations*. One of the most consequent works on evaluation of the topological aspects of glass forming compositions are done by Miracle and coworkers [44,52–57]. His statistical analysis elucidated that successful bulk metallic glasses have characteristic ratios of atom sizes and relative concentration [55]. Examples of such common trends are presented in Figure 2:5.

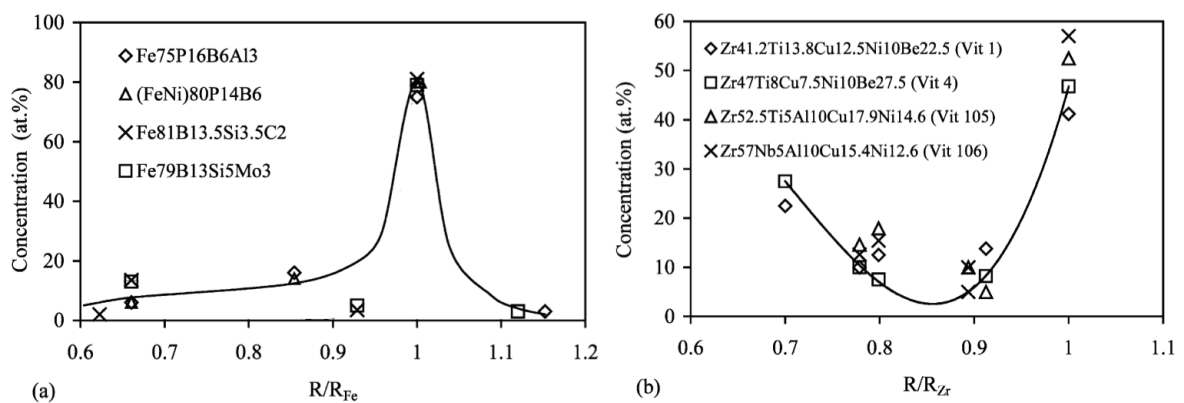


Figure 2:5 Normalized atomic radii vs. composition diagrams of (a) ordinary Fe-based and (b) bulk Zr-based amorphous alloys (from [44]).

As it can be seen in Figure 2:5, each data point corresponds to an atomic concentration and the corresponding size relative to the main element. The data point belonging to the

same alloys produce a single curve that can be concave or convex. Commonly, strong glass formers exhibit a convex curve in such diagrams. Naturally, all binary and some ternary alloys can only show selected regions of this type of atomic size distribution plot (e.g. Figure 2:5). Yet, the trend for most of intermediate glass formers is similar, meaning the larger the difference in the atomic radii of the base metal and solute, the smaller is the solute concentration. In the case of strong glass formers, i.e. Zr-, Rare earth metal- or Pd-based BMG's the atomic size distribution plot is characterized by a minimum at an intermediate atomic size as shown in Figure 2:4 (b). The base element in these glass formers has the largest atomic size and the smallest atom often has the next-highest concentration [44]. According to Egami and Waseda [58] vitrification is favoured by local atomic strains generated by size differences between base metal and the solute atoms reaching a critical level. This results in a topological instability of a given crystalline structure by changing the local atomic coordination number [58].

$$C_{Solute}^{min} \cong \frac{0.1 * r_{Base\ atom}^3}{|r_{Solute\ atom}^3 - K^3 r_{Base\ atom}^3|} \quad (2.8)$$

As can be seen in Eq. (2.8), the critical solute concentration for vitrification decreases with increasing difference in atomic size of the constituents. The majority of the convex shapes such as Figure 2:5 (b) cannot be described by the criterion presented in Eq. (2.8). Eq. (2.8) is true in the case of all the alloying elements occupying the substitutional positions. Yet for small atoms such as boron or carbon the hypothesis of a substitutional occupancy is no longer valid, thus interstitial solute atoms produce a different strain in the crystal lattice compared to the one calculated by Egami and Waseda [45].

Glass former with at least one element larger than the base metal and at least one element smaller, (e.g. Figure 2:5 (a)) are generally more stable than their binary amorphous counterparts.

In the case of substitutional atoms, the smaller atoms tend to produce compressive lattice strains while the larger atoms produce tensile strains in the matrix. The resulting strain fields with opposite signs attract one another, thus reducing the internal stresses and forming relatively more stable short-range ordered configurations (clusters). If these short-range configurations or clusters are based on the crystal symmetry, their formation will favour the crystal and make amorphization more difficult. Yet, if the short-range ordered

clusters are not compatible with the crystal symmetry of the solid solution, their formation should favour vitrification [44].

Considering the potential cluster formation in the liquid leading to dense packing can be used as a guideline for alloy development. According to the relative size of alloying elements and the base elements preferential clusters appear in BMG's. In the case of Pt-Si-B system, a common ratio of cluster can be seen in the $r_{Si}/r_{Pt}=0.8$, corresponding to a cluster in which 10 Pt atoms are surrounding one Si atom. The $r_B/r_{Pt}=0.63$ present a less common cluster yet it corresponds to an atom of boron surrounded by 8 atoms of platinum. A mixture of 8 and 10 clusters in liquid would increase the chance of glass formation upon solidification, as it has been the case in Ca-Mg-Cu bulk metallic glasses [59]. In Pt-Si-B system an alloy with a composition of $Pt_{60}Si_{10}B_{30}$ would correspond to such 8 and 10 cluster model. Such cluster packing models have also been used to rationalize the size distribution and concentration conditions in Al-RE-based BMGs [60].

2.4 Criteria for predicting the glass forming ability (GFA)

For any alloy development activity it is essential to have a yardstick for selecting the optimized composition while avoiding sample production at large scale. The most apparent indication of a strong glass or an alloy with a good glass forming ability (GFA) is the critical diameter (d_c) into which the material can be cast or processed while retaining the amorphous structure. The critical cast diameter is directly related to the critical cooling rate (CCR) for avoiding crystallization, the basic assumption being that the cooling rate is limited by thermal conductivity in the amorphous metal rather than the mould/sample heat transfer characteristic to a given cooling method. However, measuring the CCR for each individual composition is not practical. Thus, numerous models and criteria have been proposed to link the GFA to thermodynamic parameters of the alloy. The most common criteria based on which the GFA of a composition can be evaluated, are presented in the following.

The first yardstick, the reduced glass transition temperature (T_{rg}), was proposed by Turnbull based on homogeneous nucleation theory and is given by [46],:

$$T_{rg} = T_g / T_l \quad (2.9)$$

T_g is the glass transition temperature and T_l the liquidus temperature, both on the Kelvin scale. Turnbull [46] claimed that a good glass former should have a T_{rg} larger than $2/3$. The factors defining the glass transition temperature in an alloy being not well understood, it is commonly held that the most direct way to increase the reduced glass transition temperature is to reduce the liquidus temperature. This is in line with the experimental observations that strong glass-formers are often located in the compositional vicinity of deep eutectics. Albeit it has quite early on been observed that the glass transition temperature does also vary with composition in a non-negligible way the hunt for low melting points is still a good first shot. A first approach to find the composition of lowest melting point in a multicomponent alloy is by centrifugation of the melt during solidification: the changes in density between the solidifying solid and the remaining liquid will separate the solidified phases from the liquid [61,62].

Since solidification and, hence, liquidus temperature can easily be observed by a change in reflectivity of the surface, screening of liquidus temperatures in multicomponent alloys can be done by combinatorial methods. Schroers and coworkers [63–65] have devised a neat way of analyzing T_g and ΔT in a combinatorial approach. The basic idea is to deposit a range of multicomponent alloys on a wafer by gradient sputtering. Underneath the deposited glass the wafer is structured such that the deposited layer adheres only on a grid and does not stick over a circular area. The circular area has an access to a layer of thermally unstable material that decomposes at intermediate temperature, creating a gas pressure underneath the membrane. When the wafer is heated, the gas-producing compound decomposes and the metal glass membrane starts bulging up under the gas pressure once T_g is reached. The deformation stops either when the bubble bursts or when the crystallization temperature T_x is reached. By monitoring optically at which temperature the deformation starts and stops upon heating a T_g , T_x vs. composition map can be drawn.

The theoretical understanding of the glass transition and the effect of alloying elements on it, is not very advanced. According to Angell [66] Glass transition is “...*generally and correctly thought of as that phenomenon in which a viscous liquid passes continuously into the amorphous solid state during cooling*”. The relation between the atomic composition and the T_g is not established yet. Langer [67] states that “*It is remarkable that, after many decades of intense study, there is still no generally accepted, fundamental understanding of glassy states of matter or the processes by which they are formed*”.

Furthermore, glass transitions exhibit characteristic thermodynamic properties. Kauzmann showed in 1948 [68] that the entropy presumed for a specific heat measurement in a high-temperature glass-forming material appears to extrapolate down to a value comparable to the entropy of the corresponding crystalline state at a thermodynamic transition temperature T_K , roughly the same as the dynamic temperature T_0 in Eq (2.1). The specific heat C_p increases rapidly and irreversibly from lower to higher values with increasing temperature near the T_g . Langer [67] suggests that a considerable fraction of the degrees of freedom of a glassy material appears to be frozen. The quenched glass thus *“somehow is unable to explore a statistically significant fraction of its configuration space on experimental time scales”* [67]. Upon reheating, the frozen or deactivated degrees of freedom are reactivated and the specific heat suddenly rises again.

Chen [69] has proposed that the excess entropy of disorder associated with random mixing of hard spheres of different sizes lowers the glass transition temperature, while strong interactions between unlike atoms regardless of whether they are metals or metalloids respectively increases the T_g [69]. Chen further observed that by increasing x in $(\text{Pd}_{1-x}\text{M}_x)_{0.835}\text{-Si}_{0.165}$, T_g varies linearly with $M=\text{Rh}$, Ag and Au , whose atomic volumes are similar to Pd , while for $M=\text{Cu}$, Ni , Co and Fe with much smaller atomic volume, the increase is nonlinear [69]. The main shortcoming of T_{rg} is the absence of any information regarding the thermal stability once the glass is formed. Crystallization temperature, T_x , and the range of temperature, ΔT , separating it from the glass transition, called the super-cooled liquid region SCLR, is an important indication of the thermal stability that is particularly important in view of thermoplastic forming in the viscous state. Inoue [70] suggested that a strong glass former exhibits both a large value of T_{rg} as well as a wide super-cooled liquid region ΔT .

Therefore, an empirical criterion taking into account the thermal stability of the glass former has been proposed [71] as the parameter γ given by:

$$\gamma = \frac{T_x}{T_g + T_l} \quad (2.10)$$

Strong glass formers exhibit values larger than 0.4 [72]. There is a quite reasonable correlation between γ and maximum critical casting diameter d_c [72]. There is, however, no physical picture behind Eqn. (2.10) and it is without surprise that this criterion fails to pre-

dict the GFA in certain alloys such as $\text{Cu}_{47}\text{Ti}_{33}\text{Zr}_{11}\text{Ni}_8\text{Si}_1$ [73]. With some algebra one finds that

$$\gamma = \frac{1 + \frac{\Delta T}{T_g}}{1 + \frac{1}{T_{rg}}} \quad (2.11)$$

which means that the smaller T_{rg} the larger ΔT must be to reach the strong glass former limit of $\gamma=0.4$. On the other hand, if T_{rg} is equal to 0.6, the criterion is fulfilled if $\Delta T = 0.067 T_g$. For $T_{rg} = 2/3$ (the limiting value proposed by Turnbull) $\gamma \leq 0.4$ no matter what value of ΔT . As it was mentioned before another important criterion for evaluating the glass forming ability is the temperature dependence of viscosity in the vicinity of T_g . The fragility index, m , is described in Eq. (2). Senkov [74] claimed that the critical cooling rate is a function of both m and T_{rg} . Thus in order to predict the GFA both of those criteria should be taken into account. It has been found that the fragility index correlates well with the critical cooling rate R_c . An example of such correlation has been presented in Figure 2:5.

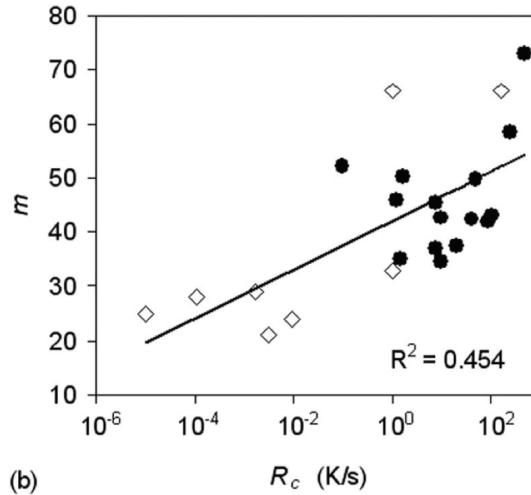


Figure 2:6 The evolution of fragility index in regard to the super cooled liquid region (from [75]).

From what has been presented above it becomes clear that it is difficult to produce a universal criterion for evaluating the GFA of all glass formers, yet all of the criteria presented in this section can be useful as a tool when applied judiciously to the process of alloy development. This reflects the fact that despite a 50 years history in metallic glass research, many questions regarding the glass formation and glass transition await still an answer.

2.5 Guidelines for alloy development and optimization

Despite decades of work and study for developing new guidelines and indicators for alloy development, a good amount of work is still based on trial and error while producing a large number of samples and alloys. This is done in the perspective of creating an image of the trends and functionalities of thermo-physical properties to the composition. An approach to present the strategies for substitution or addition of different alloying elements can be based on optimization of the topology of the system by taking into account the interaction between different species present in the composition [37].

Numerous observation have been made in individual systems e.g. Chen et al. [37] observed that replacing a small amount of Pt in Pt-P system with a transition metal of smaller atomic size such as Ni, Co, Fe or Cu strongly facilitates the glass formation. By doing so, T_g decreases with an increase in the misfit between the unlike atoms. At the same time, strong interatomic interaction has found to increase the T_g . Chen et al. [37] have attributed such behaviour to the entropy of disorder and short-range ordering near the glass transition temperature. This is also in line with the confusion principle put forward by Greer [43], in which by multiplying the possible crystalline structures the crystallization is frustrated due to energetically equality between probable configurations.

As a general guideline addition of elements of different atomic size and strong interaction, can potentially lower the melting point and raise the T_g hence enhancing the glass forming ability [36].

Another method for developing glass formers in new systems is to find analogies within similar systems. Interestingly enough, there are many similarities in the ternary systems of Fe-Si-B [76,77], Ni-Si-B [78–83] and Co-Si-B [24–26,84]. One of the interesting similarities is the range of temperature of the ternary eutectic in these systems. It turns out that the ternary eutectic temperature in these three systems is roughly 125 °C below the average of the binary eutectic temperatures. From the comparison of these with Pt-Si-B system a ternary eutectic temperature can be estimated to about 700°C. Many examples of minor substitution can be found in $\text{Fe}_{79}\text{Si}_5\text{B}_{16}$ [85]. Through substitution of Iron by vanadium, chromium, niobium, manganese, molybdenum, and tantalum, the crystallization temperature increases with increasing size of the substituting atom, i.e. in decreasing order: tantalum, niobium, molybdenum, vanadium, manganese and chromium.

Existence of strong metal-metalloid glass formers has been attributed to optimization of the dense random packed metal network into which the generally smaller metalloid atoms occupy the interstitial positions. This can be the explanation of glass forming ability of Fe, Ni, Co with Si-B metal-metalloid systems [86]. A topological theory based on different cluster types has been proposed by Miracle [29–32].

In general, one can categorize the different composition modifications into three functional classes [87]:

- Elimination of heterogeneities (e.g. yttrium as oxygen-scavenging in Zr-based alloys)
- Stabilization of the liquid region and thus reducing the liquidus temperature.
- Destabilization of the competing crystalline phases.

These three mechanisms result in improving the GFA and/or the thermal stability by influencing the crystallization process. Lu and Liu proposed the categorization of alloying elements according to their size [87]:

- Small metalloid elements such as C, B, Si, Ge.
- Intermediate transition metals: Fe, Ni, Co, Cu, Mo, Zn, Nb, Ta, Ti.
- Large elements: Zr, Sn, Sc, Sb, Y, La and Ca.

There are examples of minor element addition/substitution dramatically changing the GFA, for example Inoue et al. found that substituting 3 at.-pct of Si with B in $\text{Pd}_{76}\text{Si}_{18}$ improves the thermal stability by increasing the width of the super-cooled liquid region from 47 °C to 70 °C in $\text{Pd}_{76}\text{Si}_{15}\text{B}_3$, an indication of stronger glass forming ability [88]. Choi-Yim et al. reported the addition of 0.5-1 at.% of Si to Cu-Ti-Zr-Ni doubling the critical diameter d_c of the metallic glass [89]. Furthermore, addition of 0.5-2 at.% of B in Ni-Nb-Sn system improves the glass forming ability by increasing the critical casting diameter from 1 mm to 3 mm [90].

The influence of minor addition of small atoms on GFA can be explained firstly by the increasing the dense packing in the liquid and efficient formation of clusters as small atoms can fill the interstices. Miracle and Sanders [29] suggest that efficient atomic packing in amorphous alloys produce a relatively low system volume, which reduced the thermodynamic free volume and thus the free energy of the amorphous structure. Furthermore, effi-

ciently packed atoms produce more viscous liquids, which considerably reduced the kinetics of nucleation and growth of competing crystalline phases [29]. According to Miracle and Sanders [29], the existence of local atomic configurations (i.e. clusters) with high local atomic packing efficiencies increases the chance of vitrification thanks to the general rule that the mixture of spheres of different sizes produces a more efficiently packed structure compared to individual constituents. The packing efficiency increases by increasing the atomic size difference between the constituents. Metallic glasses typically have a radius ratio R (the solute atom radius normalized by the solvent atom radius) between 0.6 and 1.4 and solute atom fraction ranging from 5 to 30% [91]. Miracle suggests specific atomic radius ratio R^* brings about efficient atomic packing over a length scale defined by these atomic cluster. Miracle and Sanders [91] present expressions for well-known clusters such as tetrahedral ($R^*=0.225$, coordination number : $N^T=4$), octahedral ($R^*=0.414$: $N^T=6$), icosahedral ($R^*=0.0.902$, $N^T=12$). Analysis of various metallic glasses as well as a number of silicate glasses show a strong preference for these specific radius ratios [91]. This methodology has been applied for a number of topologically distinct glasses, including systems where the solutes are smaller than the solvent (Fe–B, Ni–B, Co–P and Nb–Ni) and systems where solutes are larger than the solvent (Ni–Nb, Al–Y and Al–Y–Ni) [31]. Miracle [31] suggests that packing is generally efficient not only around solute atoms, but also around solvent atoms.

The influence of minor element addition can also be evaluated with respect to the different solubility of small atoms in competing crystalline phases [87]. The necessary redistribution of these small solute atoms for the growth of crystalline phase can be a factor for frustration of crystal growth and reducing the kinetics of crystallization in general [87]. The risk in addition of significant amounts of small elements in particular boron, carbon, and silicon is the formation of highly stable compounds i.e. borides, carbides, and silicides. Hence, such additions are rather common in late transition metals of the VIIIA and IB group, but are not used in glasses of early transition metals.

The addition of intermediate transition metals can be justified both by the confusion principle as well as by the creation of local strain in lattice destabilizing the lattice [58]. Addition of these elements with high interaction with the base metals atoms can often influence the T_g and T_i resulting in stronger glass formers.

Similar to small atoms, the differential solubility of large atoms in competing crystals forming from the liquid phase and the redistribution of them necessary for crystal growth may result in frustration and slowing down of the crystallization. Often, the composition of glass formers are slightly off the exact composition of the eutectic reaction, thus the suppression of primary phases due to limited solubility of large atoms can be beneficial for delaying the crystallization. Additionally, the presence of large atoms may favor the formation of efficient clusters to formation of long range crystalline order [87],[92]. Interestingly, a minor addition of as little as 0.3 at.% of the somewhat larger Ag-atoms to $\text{Pt}_{74.7}\text{Cu}_{1.5}\text{P}_{18}\text{B}_4\text{Si}_{1.5}$ alloy dramatically improves glass forming ability, by increasing the critical diameter by a factor of two albeit starting at a rather low level [13].

As it was mentioned before, minor additions are often introduced to eliminate or passivize the heterogeneities such as oxides thus suppressing or substantially reducing heterogeneous crystallization. Removal of these oxides and purification can be done either through melt treating such as fluxing with B_2O_3 (introduced in [93] and now widely used e.g. [94–106]) or addition of atoms with high affinity towards oxygen under a mechanism known as “oxygen scavenging” [107–112]. The fluxing with B_2O_3 is limited to alloys containing elements with low oxygen affinity relative to boron and hence not suited for Al-, Zr- and Ti-based glasses. For those, the scavenging approach is more appropriate, e.g. addition of Yttrium drastically improves the glass forming ability [113].

As has been reported by Granata et al. [96] fluxing led to boron take up in Pd-Si-Cu BMGs, which leaves wondering whether the positive effect of fluxing in Pd-Si binaries is not also in part due to boron pick-up.

2.6 Relaxation of glasses

Given the metastable nature of glass, the kinetics of crystallization from the glassy state is analogous to crystallization from the liquid phase with the difference that the rate of transformation is much slower in the latter [114]. The thermal stability of glass as well as the relaxation kinetics are both governed by the atomic transport in the glassy material, in the temperature range of the glass transition. The structural relaxation and, at higher temperature, the crystallization from the amorphous phase that follows it change the physical and mechanical properties of glass. Figure 2:7 schematically shows different states of glass and crystal and their respective energy levels.

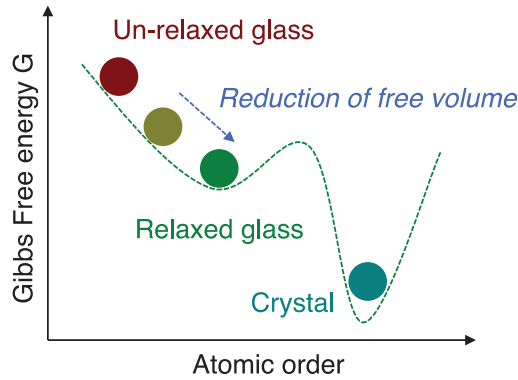


Figure 2:7 Free energy levels of different states if glass and its crystalline counterpart.

The glass transition is commonly determined by a differential scanning calorimeter at moderate heating rates of 10-20 K/min and often taken as the inflection point in specific heat C_p against temperature. The dependence of T_g to alloying elements can be different from one individual atom to another. Figure 2:8 shows the different dependence of T_g to alloying elements in binary systems [114].

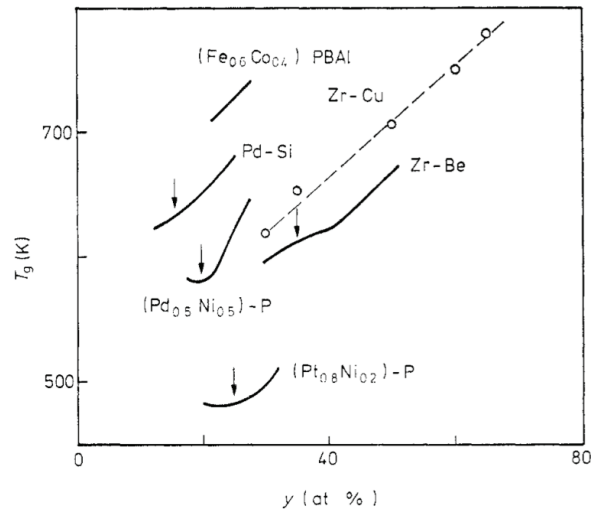


Figure 2:8 dependency of T_g to composition in the different alloys systems with the general formula of $A_{100-y}B_y$. The arrows indicate the eutectic composition (from [114]).

Chen [114] claims that the increase of T_g in these systems is due to the composition approaching stable intermetallics and is attributed to structural and compositional ordering which in turn decreases the configurational states of the systems. Inversely in the case of alloys such as Fe-Si, Co-Si as well as Pd-Si and $(Pd,Ni)_{80}P_{20}$, the T_g is lowered by the increase of metalloid contents. This is counter-intuitive since including more metalloids up to a certain point will increase the packing density and T_g . Chen claims that this is due to formation of short range ordering in melt during the cooling process. From basic reasoning

T_g could be believed to be related to the cohesive energy. However, often the thermodynamic data, i.e. heat of mixing among all constituents, are not available and estimation of the overall cohesive energy contains large uncertainties, leading to significant scatter in correlations between cohesive energy and glass transition temperature [114]. The true nature of the dependence of glass transition to composition remains difficult to identify.

Part of the increased Gibbs free energy level in un-relaxed glasses, cf. Fig. 2:7, comes from the presence of free volume and hence not fully saturated atomic bonds in the frozen-in liquid that is the glass. The generation of free volume is analogous to, yet theoretically somewhat more complicated than, the formation of vacancies in a crystal. Figure 2:9 schematically shows the process of the loss of free volume or what is known as structural relaxation that affect the mechanical and physical properties of glasses.

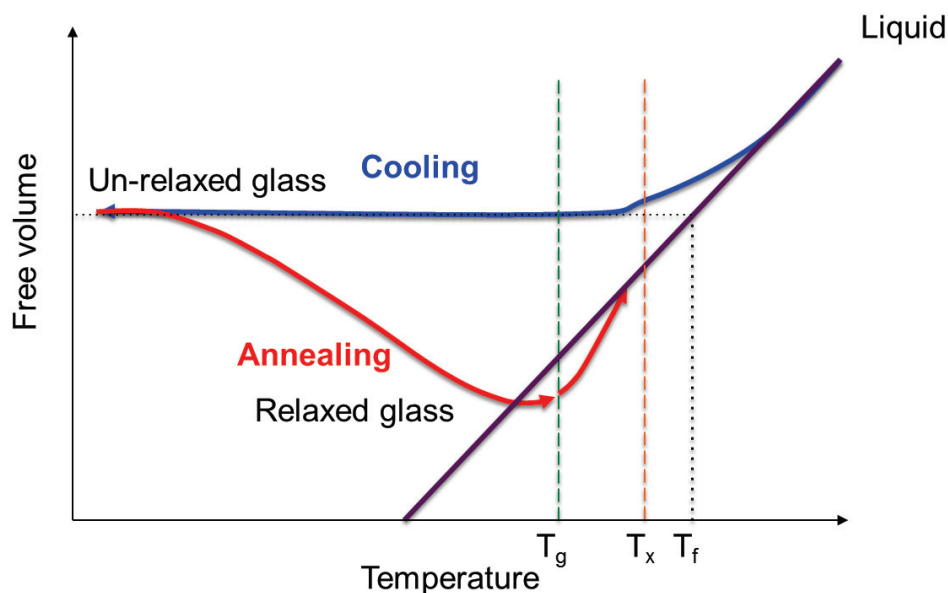


Figure 2:9 The relaxation process and loss of free volume in glasses. Reproduced from [115].

As it can be seen Figure 2:9, upon cooling, there is a certain volume trapped in the glass that is equally distributed. By annealing at temperatures below the T_g this volume slowly disappears bringing about in certain alloys a relaxation induced embrittlement as well as the change in other physical properties such as density or electrical resistance [114,116–119]. It is possible to directly measure the loss of free volume or the excess volume trapped in the structure of glasses upon cooling by high precision density measurement using $[\text{CH}_3(\text{CH}_2)_{11}\text{CH}_3]$ as working fluid thanks to its low vapor pressure (3.4 Pa) and small

surface tension (2.77×10^{-2} N/m) [120]. Figure 2:9 shows an example of such precise measurement showing the increase of density in $\text{Pd}_{40}\text{Ni}_{40}\text{P}_{20}$. Annihilation of the free volume in metallic glasses is accompanied by variation of the enthalpy. Thus it is also possible to measure the changes in the free volume during relaxation using differential scanning calorimetry (DSC) [121].

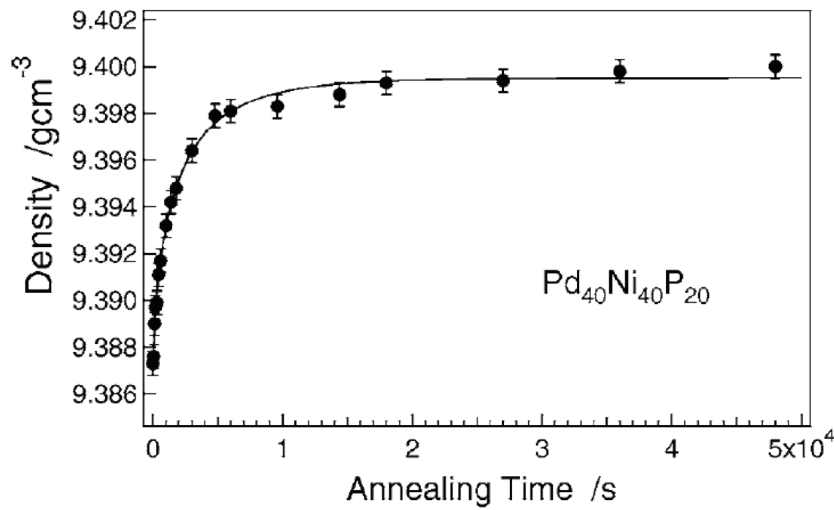


Figure 2:10 Loss of free volume due to structural relaxation in $\text{Pd}_{40}\text{Ni}_{40}\text{P}_{20}$ (from [120]).

The structural relaxation i.e. loss of the free volume as shown in Figure 2:9 can be responsible for loss of ductility and fragilization of the alloys [117–119,122,123]. For example the elastic modulus and hardness of alloy $\text{Zr}_{52.5}\text{Cu}_{17.9}\text{Ni}_{14.6}\text{Al}_{10}\text{Ti}_5$ increase upon loss of free volume while its ductility is considerably reduced [124]. Interestingly enough not only the loss of the free volume but diffusion of certain alloying elements at temperatures quite far from the glass transition temperature might bring about the change in the properties [125]. The example is $(\text{Co}, \text{Ni}, \text{Fe})_{75}\text{P}_{16}\text{B}_6\text{Al}_5$ alloys series where migration of Boron at temperatures much below T_g will bring about the change in the mechanical properties and, most importantly, the embrittlement of the alloy. When phosphorous was completely replaced by boron such embrittlement was no more observed [125].

Various physical and mechanical properties are affected by the degree of relaxation or the amount of free volume trapped in the structure of glasses upon quenching: properties such as density[126], hardness [127], fracture toughness [128] strain at fracture [129–131]. The relaxation time, i.e. the time necessary for annihilation of the free volume, is not only func-

tion of the temperature but also a function of the overall amount of free volume and configurational entropy which itself is directly related to the cooling rate [114].

The variation of a given property upon relaxation may be strongly different from one system to the next. Hence, for each system a specific indicator for the degree of relaxation must first be identified, and the change must be easily quantifiable. Along these lines Fe-based BMG's embrittle to a much larger extent than Pd or Zr based glasses [119]. Producing samples allowing the quantification of brittleness, however, might be quite cumbersome

2.7 Crystallization in BMG's

As it was shown in Figure 2:7, the metallic glasses are undercooled liquids, which are metastable by nature [132]. Annealing of the alloy above its glass transition is the easiest way to start what is called crystallization from the amorphous phase, which reduced the energy of the system through formation of more energetically stable crystalline phases. Crystallization from the amorphous phase can also happen due to irradiation [133–135], mechanical deformation [136–141] and dealloying [142]. In the following sections each one of these causes of crystallization will be shortly discussed.

2.7.1 Crystallization in metallic glasses due to irradiation damage

Irradiation by high-energy particles (ions or neutrons) is known to change the microstructure as well as the properties of materials. Figure 2:11 indicates schematically the effect of irradiation on metallic materials: fast particles create atomic displacements leading to vacancies and interstitials, the pair of the two being called a "Frenkel pair". By this process, disorder is increased and the Gibbs free energy is raised. At sufficiently high levels of disorder the long range periodicity is destroyed leading to solid state amorphization similar to the one obtained in some alloys by high-energy ball-milling [143].

The smaller the Gibbs energy difference between the crystalline compound and its amorphous counterpart more likely is the occurrence of the solid-state vitrification. This is the case for liquids and solids with very similar enthalpies, which is one of the scenarios leading to very deep eutectics.

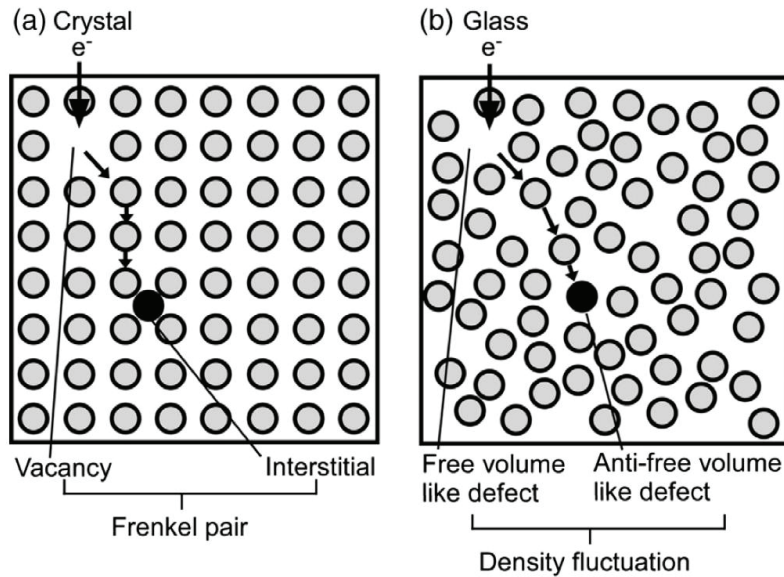


Figure 2:11 Schematic illustration of the defect created by single atom displacement in a metallic crystal and a metallic glass under MeV electron irradiation. (a) A vacancy–interstitial pair is formed by displacement of an atom, resulting in Frenkel pair formation in metallic crystal. (b) An anti-free volume is formed by displacement of an atom, resulting in density fluctuations in metallic glass (from [143]).

Inversely, in the case of metallic glasses the variation of density or in other words the uneven distribution of the free volume under MeV electron irradiation can cause crystallization. As it can be seen in Figure 2:11 (b), upon arrival of the incident beam a pair of a free volume like defect and its counterpart (anti free volume like defect) is formed. The density fluctuation as mentioned above is the trigger for crystallization in metallic glasses [143]. As suggested by Nagase et al. [143] the stability of an amorphous phase against irradiation increases by the crystallization temperature. Commonly, the crystallization upon irradiation in metallic glasses is facilitated through the following three phenomena: i) an increase in free energy of the amorphous phase; ii) the formation of crystalline clusters through modification of the atomic configuration near radiation induced defects; and iii) enhanced diffusion [143].

2.7.2 Crystallization in metallic glasses due mechanical deformation

The main plastic deformation mechanism in metallic glasses is formation of shear bands. The plastic deformation remains limited and highly localized in shear bands. Recently it has been observed that crystallization happen around shear bands [137]. The crystallization supposedly occurs through either localized increase in temperature during the for-

mation of shear bands or shear induced viscous flow. Interestingly, Yavari et al. [144] observed that the nano-crystallization only happened on the compressive side of a bent $\text{Pd}_{40}\text{Cu}_{30}\text{Ni}_{10}\text{P}_{20}$ metallic glass, thus rise in temperature alone cannot explain this phenomenon. Furthermore, it is difficult to quantify the temperature rise during the formation of shear bands in the experimentally viable time window. Flores and Dauskardt [145] using infrared imaging technique captured the detailed temperature distribution and heat dissipation around the crack tip in the alloy Zr-Ti-Ni-Cu-Be. They estimated the temperature rise of 52.2 K, 20 ms after the arrest of the crack tip upon an advance of 0.9 mm. In another study done by nano-indentation of Zr-Cu-Ni-Al-Ti, the temperature rise was estimated to be only 0.05 K yet there is still nanocrystallisation [139,146]. In his seminal paper, Argon [147] proposed that the plastic deformation in metallic glasses is accommodated by localized irreversible rearrangement of atomic regions, involving tens of atoms i.e. so-called Shear Transformation Zones (STZs) [147]. Figure 2:11 shows schematically a 2D projection of a STZ before and after transformation.

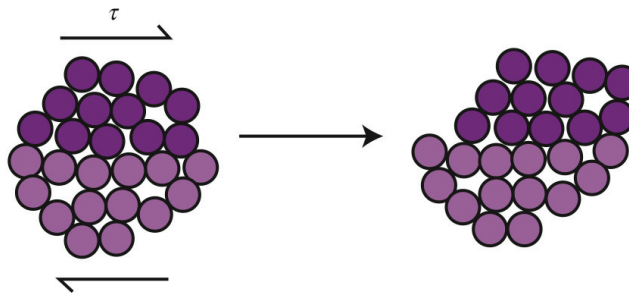


Figure 2:12 Shear transformation zones in metallic glasses. A two-dimensional schematic of a shear transformation zone in an amorphous metal. A shear displacement occurs to accommodate an applied shear stress τ , with the darker upper atoms moving with respect to the lower atoms (from [148]).

A STZ can also be regarded as a basic shear transformation unit in metallic glasses, containing a higher degree of free volume or locally lower density. In other words, a STZ is a region more susceptible to irreversible rearrangement of atoms compared to its surroundings. Yan et al. [149] presented results obtained by High Resolution Transmission Electron Microscopy (HRTEM) that during cold-rolling and formation of shear bands in $\text{Zr}_{60}\text{Al}_{15}\text{Ni}_{25}$, a phase decomposition occurred in the vicinity of the shear band. The shearing in the shear bands results in a drop in shear modulus in nano-sized regions in the shear bands accompanied by a significant decrease of viscosity. Such low values of viscosity are comparable to the viscosity values measured in the supercooled liquid region. At

lower viscosities the diffusion of atoms as atomic transport is facilitated, thus redistribution of atoms results in formation of phase separation or nanocrystallisation. Figure 2:13 shows schematically, the formation of softened regions during shearing [149].

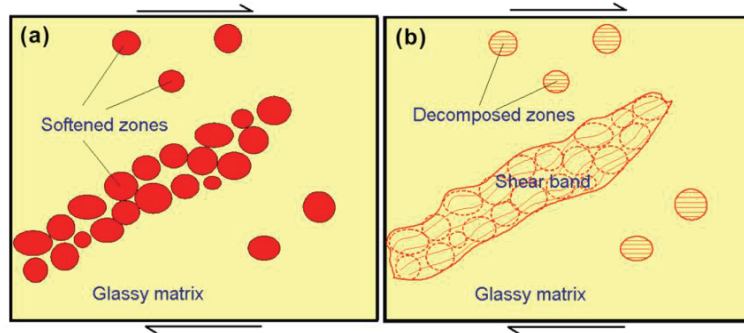


Figure 2:13 (a) Schematic illustration of the formation of localized shear zones in the glassy matrix due to shearing, and (b) occurrence of decomposition/nanocrystallisation within the isolated shear zones and the formation of a shear band resulting from a chain-like coalescence of neighboring shear zones (from [149]).

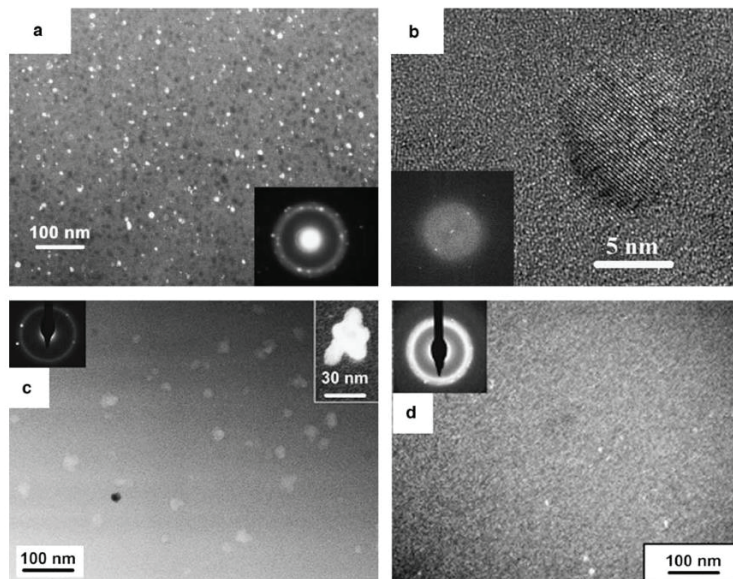


Figure 2:14 TEM images of an $\text{Al}_{88}\text{Y}_7\text{Fe}_5$ disc prepared by HPT. (a) Dark-field image and the corresponding SAED pattern. A high number density of Al-nanocrystals with a size of about 12 nm develops within the amorphous matrix. (b) HRTEM micrograph of a nanocrystal showing $\{1\ 1\ 1\}$ Al lattice fringes surrounded by the amorphous phase. The corresponding Fourier transform is given as inset. (c) Bright-field TEM image after annealing the as-quenched alloy at 245 °C for 30 min. (d) Dark-field TEM image after cold-rolling to an equivalent strain of $\epsilon = -11.5$. The few white structures correspond to the nanocrystals that have formed during the rolling deformation (from [150]).

Applying severe plastic deformation such as High Pressure Torsion (HPT) has been found to strongly favour the development of nanocrystals in the $\text{Al}_{88}\text{Y}_7\text{Fe}_5$ [150]. Upon applying

severe plastic deformation through HPT fcc-Al crystallites are formed from the glassy matrix in the $\text{Al}_{88}\text{Y}_7\text{Fe}_5$. Figure 2:14 shows the High Resolution Transmission Electron Microscopy images of the $\text{Al}_{88}\text{Y}_7\text{Fe}_5$ discs after having been subjected to severe deformation by HPT. Boucharat et al. [150] observed that nanocrystals of fcc-Al are primarily formed in the shear bands and in their vicinity. A possible mechanism of crystallization upon severe plastic deformation is enhanced mobility of different atomic species within the shear bands. This is also supported by the homogenous dispersion of nanocrystals at a relatively high number density after HPT. Interestingly, the size distribution of nanocrystals formed upon severe deformation remains smaller compared to the fcc-Al crystallites formed during thermal annealing [150].

2.7.3 Crystallization in metallic glasses by dealloying

Nano-porous surfaces from precious metals such as gold are prepared by electrochemical dealloying of an amorphous metallic precursor. This is done to increase the surface area for applications such as catalysis where the surface per volume is of significant importance [151]. During dealloying, electrochemically less noble alloying elements are dissolved into the electrolyte while the noble atoms of the base metals rearrange themselves into fine ligaments creating a nonporous surface. If the precursor metal is crystalline, the ligaments retain the crystallographic orientation of the base metal. Inversely for amorphous base metals the formation of ligaments happens due to deviation of the composition from the glass forming composition leading to formation of ligaments by nucleation and growth of crystals from the amorphous matrix resulting in a finer structure [151]. Figure 2:15 shows the formation of crystalline ligaments from the glassy alloy $\text{Au}_{40}\text{Cu}_{28}\text{Ag}_7\text{Pd}_5\text{Si}_{20}$ during chemical treatment by different acids.

As a general rule, deviation of the composition from the glass forming composition due to corrosion [152], oxidation or electrochemical etching results in formation of crystals from the otherwise homogenous glassy matrix.

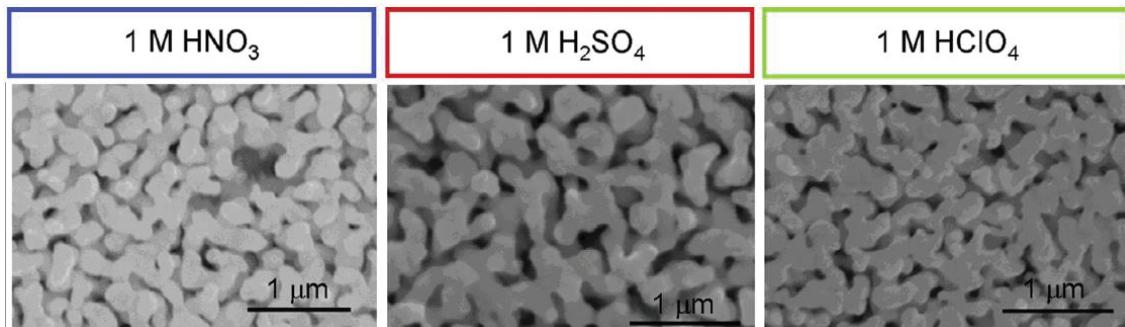


Figure 2:15 Secondary electron SEM images of samples of dealloyed $\text{Au}_{40}\text{Cu}_{28}\text{Ag}_7\text{Pd}_5\text{Si}_{20}$ in 1 molar HNO_3 , 1 molar H_2SO_4 , and 1 molar HClO_4 and aqueous solution (left to right, from [151]).

2.7.4 Crystallization in metallic glasses during annealing

Annealing amorphous metals above their T_g is a rather straightforward method for producing nanostructured materials. This can also be done through decreasing the cooling rate from the liquid state and allowing the formation of a fraction of crystalline phases. The sizes of these nano-crystals forming from the glassy matrix is in the range of 5 to 50 nm and a volume fraction of 30-80% giving a mean particle density of 10^{22} - 10^{28} m^{-3} [153]. The most apparent measure of the thermal stability of metallic glasses is the onset of crystallization. The kinetics of nucleation and growth of different phases define the final morphology of the microstructure.

The key thermodynamic quantity determining the transformation in far-from-equilibrium conditions is the change in volumetric Gibbs free energy associated with the transition from the amorphous to a crystalline state, i.e. the driving force for nucleation and growth. On a very general level, crystallization in metallic glasses can be categorized under three main categories, i.e. polymorphic, eutectic and primary crystallization. In polymorphic and eutectic transformation the rate of the crystal growth is independent of time and the crystallites grow until they impinge onto other crystals. In contrast, primary crystallization is often diffusion-controlled due to difference in the chemical composition between the parent phase and the crystallites [153]. This inhibits the unlimited grain growth; hence crystals are smaller compared to systems, which crystallize through eutectic or polymorphic crystallization. In the following sub-sections each of these categories will be elaborated.

An example of *polymorphic crystallization* is the glassy $\text{Fe}_{66}\text{Ni}_{10}\text{B}_{24}$, which crystallizes into Tetragonal $(\text{Fe,Ni})_3\text{B}$ [154]. At temperatures below the T_g the crystallization is controlled by

the diffusivity of different atomic species and growth of quenched-in nuclei. At temperatures above the T_g the crystallization is homogenous through nucleation and growth [154]. Crystallization in the alloys $Zr_{50}Co_{50}$ and $Zr_{67}Co_{33}$ also occurs through a polymorphic transformation. $Zr_{50}Co_{50}$, $Zr_{67}Co_{33}$, and $Fe_{66}Ni_{10}B_{24}$ transform directly into stable phases of ZrCo phase ($a=0.3919$ nm), metastable fcc $CoZr_2$ phase ($a=1.22$ nm), and tetragonal $(Fe,Ni)_3B$ [155].

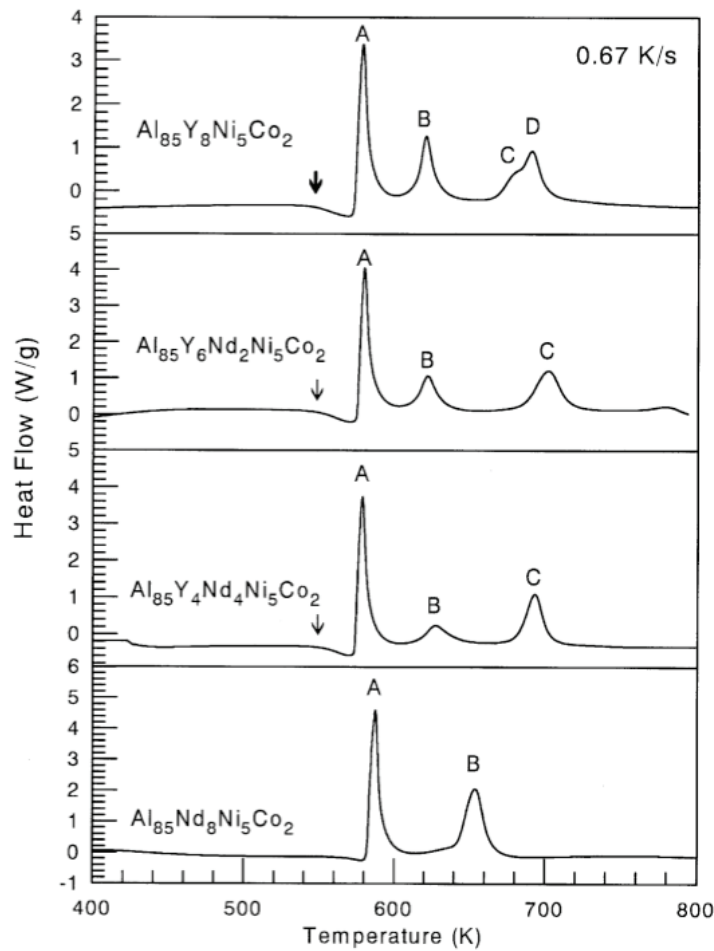


Figure 2:16 DSC traces of the alloys $Al_{85}Y_{8-x}Nd_xNi_5Co_2$ (from [157]). The glass transition temperature is indicated by an arrow.

Most prominent examples of *primary crystallization* are observed in the Al-based metallic glasses. Examples of Al-based metallic glasses are found in Al-RE (RE-Rare Earth) binary systems, and Al-RE-TM (TM-Transition Metal) ternary and higher systems produced by melt-spinning technique [156]. A good example of a combined adequate mechanical properties and GFA is found in the $Al_{85}Y_8Ni_5Co_2$. Interestingly, partial crystallization by annealing results in formation of α -Al which increases the tensile strength without reducing the

ductility. Louzguine and Inoue [157] found that by increasing substitution of Y with Nd in the alloys with the general formula of $\text{Al}_{85}\text{Y}_{8-x}\text{Nd}_x\text{Ni}_5\text{Co}_2$ the first crystallization corresponding to formation of α -Al is shifted towards higher temperature while the T_g is almost unchanged (Figure 2:16) [157]. This allowed widening the range between T_g and T_x and, hence, the appearance of a super cooled liquid region. The second and third crystallization peaks in the DSC patterns shown in Figure 2:16 correspond to formation of metastable intermetallic compounds.

In general, the formation of uniformly dispersed nano-size crystalline phases in a glassy homogenous matrix is a method for producing in-situ nanocomposites [158]. When a glassy metal is annealed, upon partial crystallization the hardness usually increases. At first glance, the increase of hardness may be attributed to the dispersion of particles. However, this is not the same as precipitation hardening as in alloys since there are no dislocations in amorphous metals. Kim et al. [159] suggest that the increase of the hardness of Al-Ni-Y can be explained by considering the rule of mixtures involving an amorphous matrix reinforced by nanophase α -Al. The nanophase α -Al is free of defects and can be considered as a “perfect crystal” possessing theoretical shear strength, while the matrix has the same strength as the completely amorphous materials. Kim et al. [159] do not take into account the enrichment of the remaining amorphous phase in solute atoms rejected upon formation of α -Al nanophase.

Hardness has also been found to be related to the morphology and the length-scale of crystalline phases. In order to obtain such a fine dispersion of nano-phases the crystallization must be primary or in other words, the composition of the crystalline phases must be different from the amorphous matrix, thus the growth of the primary phase will be limited by the diffusion halo. Furthermore, during partial crystallization the remaining amorphous phase undergoes structural relaxation but the contribution of the latter to the increase of the overall hardness is small. Thus, the increase in hardness is mainly influenced by the two mechanism, of phase-mixture i.e. composite effect and the changing composition of the remaining amorphous phase [158].

It is generally known in nanocomposites that the variation of the mechanical properties becomes significant once the percolation threshold is reached [160]. Greer [161] suggests that for in-situ nanocomposites consisting of nano-phase crystallites in a glassy matrix, it is still important to study the evolution of the properties of each phase during crystallization.

As it was suggested previously by Kim et al. [159], that crystallites only a few nanometres in diameter are dislocation-free thus supposedly crystallites should therefore exhibit the ideal shear strength, superior to that of bulk samples with the same composition. For the glassy matrix, the operation of the shear bands might be affected by the presence of crystallites. Csontos and Shiflet [162] observed nanocrystallization within the shear bands during deformation in the alloy $\text{Al}_{90}\text{Fe}_5\text{Gd}_5$. Thus the nanophase crystallites may be perceived to be too small to have any influence on formation or advance of shear bands. It seems reasonable, therefore, to assume that the glassy matrix has its usual hardness, and that the crystallites are much harder. In the case of Al-based nanocomposites produced by in-situ crystallization, the maximum volume fraction of crystalline phases is around 30%, i.e. far from the percolation threshold if we assume spherical or equiaxed nano-crystals. Commonly the nano-sized crystallites forming from the amorphous matrix are considered dislocation-free, and should show larger values of shear strength compared to their bulk counterparts. Furthermore the formation and growth of the shear bands has been shown to be affected by the presence of nano-sized crystallites [163].

Alloys in the Al-RE-TM system such as Al-Ni-Y and Al-Gd-Fe can be significantly hardened by partial crystallization. Commonly, such increase in the hardness is in the order of 50% [158]. Figure 2:17 shows the evolution of different mechanical properties as a function of crystallinity. It can be seen in Figure 2:17, the evolution of fracture strength; young's modulus and the fracture elongation follow the same trend. Interestingly enough the optimum combination of mechanical properties is found with 10% to 33% of the volume fraction of crystallites, while the hardness steadily increases and the lattice parameter of the α -Al steadily decreases. The α -Al lattice parameter is initially significantly larger compared to pure Al (0.4047 nm). It can be deduced that the fcc-Al phase is a supersaturated solid solution containing Y, Ni and Fe atoms [164]. Kim et al. [164] suggested that the presence of finely dispersed fcc-phase acts as a resistance to shear deformation and improves the degree of adiabatic heating leading to more importance viscous flow of the glassy matrix.

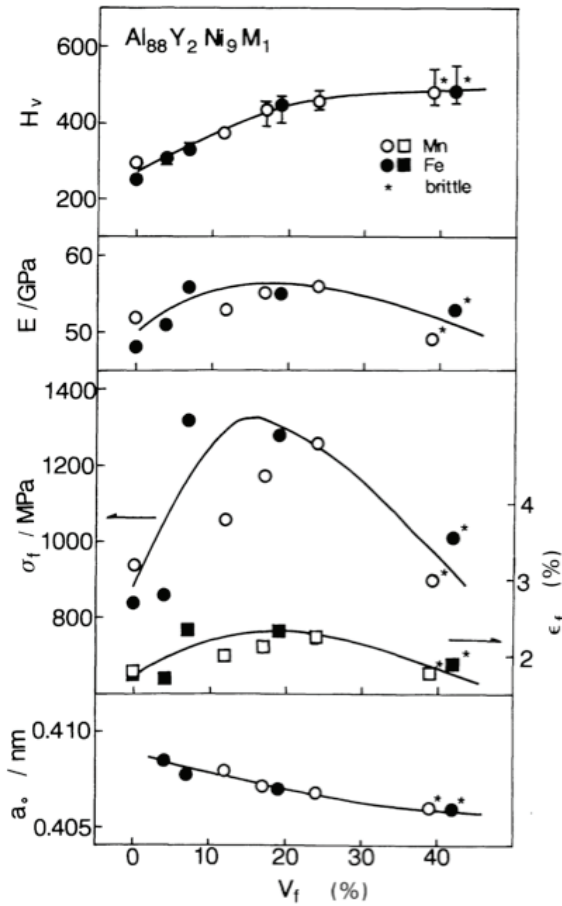


Figure 2:17 Hardness (H_v), Young's modulus (E), tensile fracture strength (σ_f), fracture elongation (ϵ_f), and the lattice parameter (a_0) of the α -Al crystallites of the melt spun ribbons of the alloy $Al_{88}Y_2Ni_8M_1$ ($M=Ni$ or Mn) as the function of the volume fraction of crystalline phase (from [164]).

Figure 2:18 shows the hardening effect of partial crystallization of the Al-based metallic glasses in the Al-Ni-Y system. Unlike Kim et al. [164], Zhong et al. [165] suggested that the main mechanism of hardening is the solute enrichment of the remaining amorphous phase. This was confirmed by the comparison between the hardness of the partially crystallized glass and the fully amorphous glassy alloys with higher solute contents. Figure 2:19 shows the hardness of the melt-spun ribbons of glassy Al-Ni-Y alloy as the function of total solute content. As it can be seen the increase in hardness as the function of the solute content is almost linear.

Looking back at figure 2:16 and the decrease of the lattice parameter of the α -Al crystallites during partial crystallization of $Al_{88}Y_2Ni_8M_1$ ($M=Ni$ or Mn), it seems that the solute content in the crystallized phases i.e. fcc-Al is reduced and these solute atoms are rejected

into the glassy matrix. These observations along with the observations made by Zhong [165] seem to suggest that the main contribution to the increase of the overall hardness is due to solute enrichment in the remaining glassy phase during partial crystallizations.

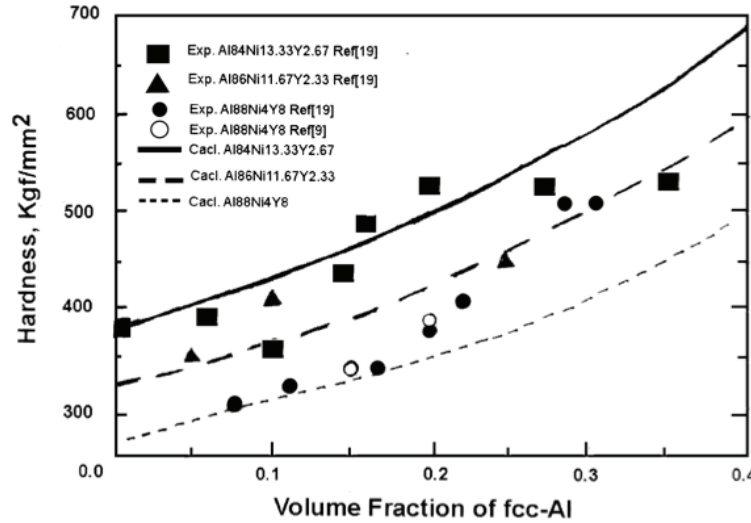


Figure 2:18 the hardening upon partial crystallization in the Al-Ni-Y systems as a function of the volume fraction of the α -Al crystallites, the solid lines show the hardness of the glassy matrix from the estimated solute enrichment during partial crystallization. The dashed lines is the calculated hardness of the nano-phase composite with the hypothesis of the rule of mixtures (from [158]).

As it was mentioned before during primary crystallization there is significant composition difference between the parent phase i.e. the glassy matrix and the crystallites. In the case of Al-Ni-Y alloys, solute diffusion is important for limiting the crystal diffusion and at a later stage of growth the solute concentration in the glassy matrix decreases. Finally the volume fraction of the crystallized phases is limited by the metastable equilibrium between the crystallites and the remainders of the parent phase. By analogy, Greer [158] suggested that by assuming that the main hardening mechanism is due to the compositional changes in the matrix it is possible to imagine systems where such variation of solute concentration in the matrix upon crystallization may bring about crystallization softening [158]. Boswell has observed the example of softening during crystallization in the alloy $\text{Pd}_{78} \text{Cu}_{5.5} \text{Si}_{16.5}$ [166].

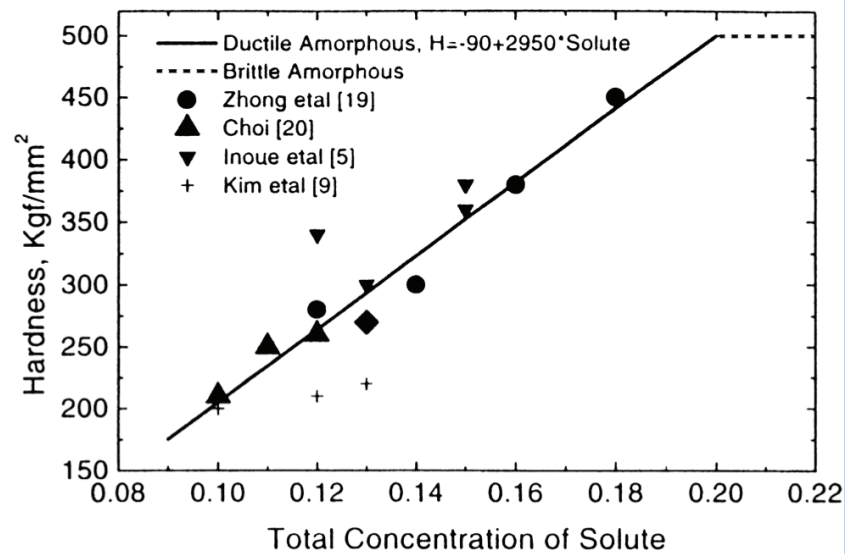


Figure 2:19 The hardness of fully amorphous ribbons of the alloys Al-Ni-Y as the function of total solute content from different studies [158].

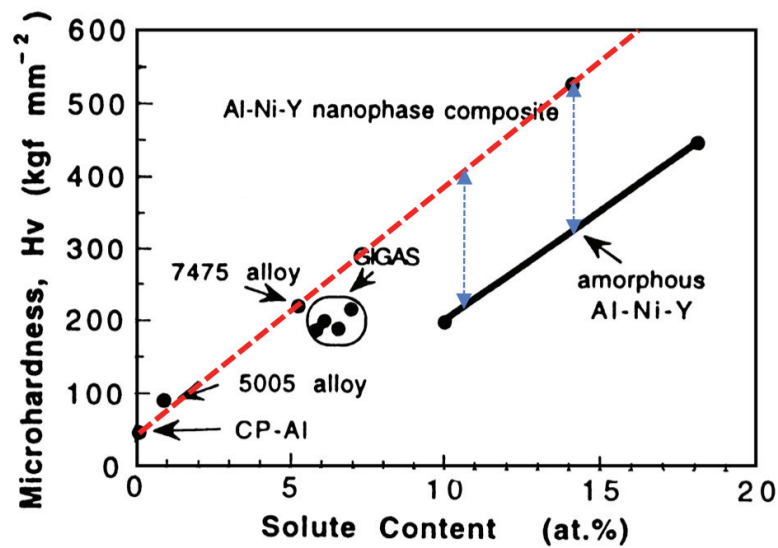


Figure 2:20 Hardness as a function of overall solute content for Al alloys, including commercial-purity Al, solution-strengthened 5005, age-hardened 7475 and consolidated GI-GAS alloys (with slight modifications after [158])

Greer [158] also compared the results of the partially crystallized Al-Ni-Y alloys with the micro hardness values of the conventional Al-based alloys the results are shown in Figure 2:20. As it can be seen despite the fundamentally different mechanisms of hardening in conventional solution hardened or age hardened Al-based alloys there is an apparent correlation between the total solute concentration and the hardness values.

As can be seen in Figure 2:20 the hardness of the amorphous Al-Ni-Y alloys stays below the main correlation relating the hardness to the solute content, while the nano-phase composite of Al-Ni-Y falls more or less on the extrapolation of the properties of the conventional Al-based alloys. It is possible to hypothesize that the main contribution of the partially crystallized Al-based alloys is to allow a higher content of solute in a microstructurally homogenous matrix without forming undesirable coarsely segregated or highly brittle microstructures [158].

Wu et al. [167] observed different morphologies of α -Al crystallites in the alloy $\text{Al}_{88}\text{Y}_7\text{Fe}_5$ according to different stages of crystallization upon thermal annealing. As it was mentioned before the kinetics of primary crystallization is controlled by the diffusivity of different species in the glassy matrix. During initial stages of isothermal annealing when α -Al crystallites are small and the diffusion fields do not overlap, the crystallites are almost spherical (Figure 2:21 a) and the growth is controlled by the diffusion expressed by the parabolic function such as Eq. (2.12).

$$R \approx \sqrt{D * t} \quad (2.12)$$

where R is the radius of the crystallite, D , the diffusivity of the matrix and t is the growth time. By advancement of the particle growth, the spacing between the crystallites stays in a first stage put and the development of a solute build-up around the nanocrystals eventually results in the overlap of the diffusion fields of individual crystallites and impedes further growth of nanocrystals [167]. In a later stage these overlapping diffusion fields will lead to coarsening of the precipitates. Figure 2:21 shows the different morphologies of fcc-Al crystallites at different stages of annealing. At advanced stages of crystallization, the interface between the crystallites and the glassy matrix becomes irregular or dendritic as perturbation develops in the amorphous parent phase. Such dendritic morphology for fcc-Al crystallites are shown in Figure 2:21 (b). The solute enrichment in the remaining amorphous phase further decreases the diffusivity of the solute atoms and leads to higher crystallization temperature i.e. improved thermal stability [167].

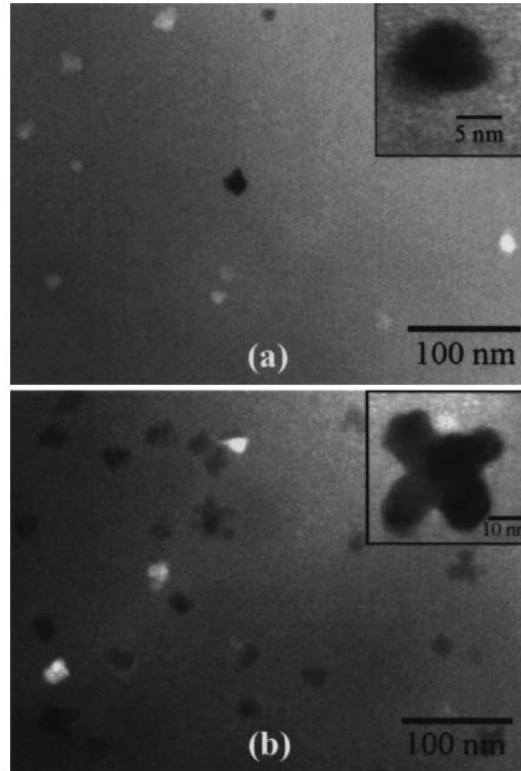


Figure 2:21 TEM bright-field images of an $\text{Al}_{88}\text{Y}_7\text{Fe}_5$ melt-spun sample after isothermal annealing at 518 K for 10 min (a) showing a high density ($3 \times 10^{21} \text{ m}^{-3}$) of Al nanocrystals with nearly spherical shape; and 30 min (b) showing higher particle density ($4.8 \times 10^{21} \text{ m}^{-3}$) of Al nanocrystals and the development of a dendritic morphology (from [167]).

Primary crystallization has also been observed in the $\text{Zr}_{58}\text{Nb}_5\text{Cu}_{25}\text{Al}_{12}$ [168]. Partial crystallization in the Zr-Nb-Cu-Al system has also been found to improve the tensile strength as well as the hardness while retaining adequate ductility. Figure 2:22 shows the XRD pattern of the partially crystallized $\text{Zr}_{58}\text{Nb}_5\text{Cu}_{25}\text{Al}_{12}$.

Fan et al. [168] measured the size of the crystallites in annealed $\text{Zr}_{58}\text{Nb}_5\text{Cu}_{25}\text{Al}_{12}$ using HRTEM to be from 5 to 12 nm. The crystallites of ZrAl and Zr_2Cu were both spherical or ellipsoidal in shape and almost defect-free. Figure 2:23 shows the evolution of the hardness and tensile fracture strength for the alloy $\text{Zr}_{58}\text{Nb}_5\text{Cu}_{25}\text{Al}_{12}$ as the function of the volume fraction of the crystallites.

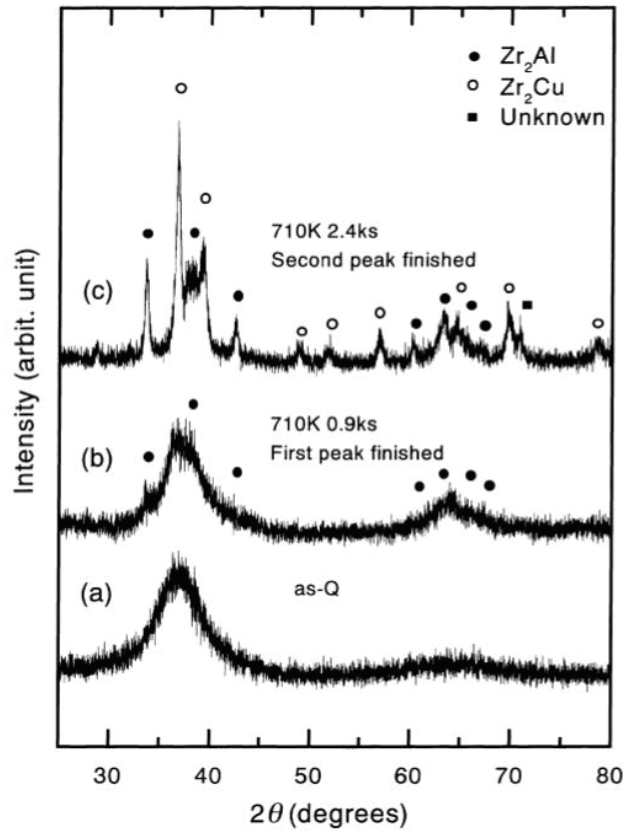


Figure 2:22 XRD pattern of the alloy $Zr_{58}Nb_5Cu_{25}Al_{12}$ annealed for different durations. Crystalline peaks indicate the formation of $ZrAl$ and Zr_2Cu crystallites (from [168]).

As it can be seen in Figure 2:23, both the hardness and the tensile fracture strength increase significantly upon crystallization. This improvement can be explained by the homogeneously dispersed crystals with sizes smaller than 15 nm in the amorphous matrix. Fan et al. [168] suggests that the strong interaction between the Zr and Al (mixing enthalpy, $\Delta H_m = -44$ kJ/mol [168]) leads to short range order domains in the liquid state. As the liquid is rapidly quenched below the solidus and the nucleation is suppressed, the liquid remains in a metastable state below the T_g and the atoms are frozen in their liquid configuration. Thus the short range ordered domains in the liquid remain intact in the amorphous phase and acts as the embryos for nucleation, thus contributing to the overall nanocrystallization.

Legg et al. [169] extensively studied the kinetics of crystallization in Pt-Cu-Ni-P bulk metallic glass. In their work, the crystallization kinetics were determined isothermally using a differential scanning calorimeter, by integrating the heat released during the crystallization, the total enthalpy and the timescales for 5, 50 and 95% crystallinity. The data points

shown in Figure 2:24, are divided into two groups, for the points above the “nose”, the measurement is done upon quenching the liquid, while the data below the nose are obtained by heating the amorphous phase. At low temperatures, i.e. below the nose, the crystallization time is decreased by increasing the temperature due to enhanced atomic mobility.

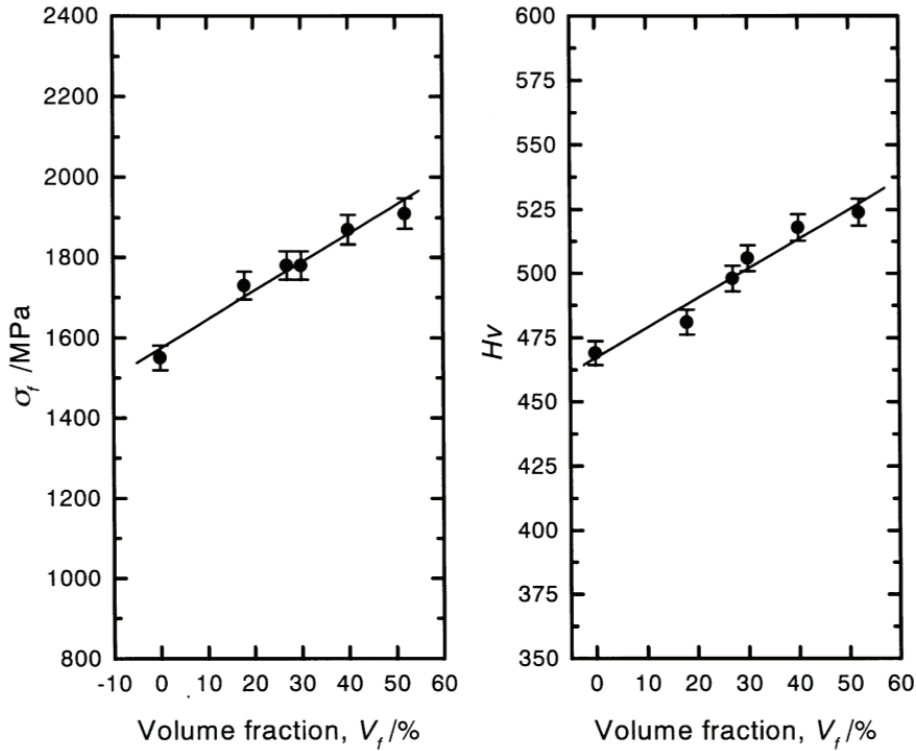


Figure 2:23 Variation of the tensile fracture strength and hardness (Hv) as the function of the volume fraction of the crystallites for the $Zr_{58}Nb_5Cu_{25}Al_{12}$ amorphous alloy (from [168]).

According to Legg et al. [169] the slower rate of crystallization from the amorphous phase at lower temperatures is less influenced by the presence of heterogeneous sites, while for crystallization at temperatures above the nose crystal formation seems to be initiated from heterogeneous sites showing the importance of the heterogeneous crystallization. This shows the importance of melt treatment processes such as fluxing with B_2O_3 capable of reducing or even eliminating certain heterogeneities, especially oxides.

Another strong glass former whose GFA can be significantly improved by fluxing with B_2O_3 is Pd-Ni-Cu-P [170–173]. Löffler et al. [174] determined the crystallization kinetics of $Pd_{40}Ni_{30}Cu_{10}P_{20}$ for temperatures between the T_g and the liquidus. They also examined the microstructure formed upon crystallization. The morphology of crystalline phases formed

from the amorphous parent phase is shown in Figure 2:25. Backscattered electron images show the clear segregation and compositional variations between the different crystalline phases formed from the amorphous phase. Based on the line scans shown in Figure 2:25, Löffler et al. divide the different regions in the micrograph to Cu(rich)/P(poor) and Cu(poor)/P(rich). As shown in Figure 2:25, there is also a distinctive dark phase (lighter atomic composition) present in the alloys with partial crystallization.

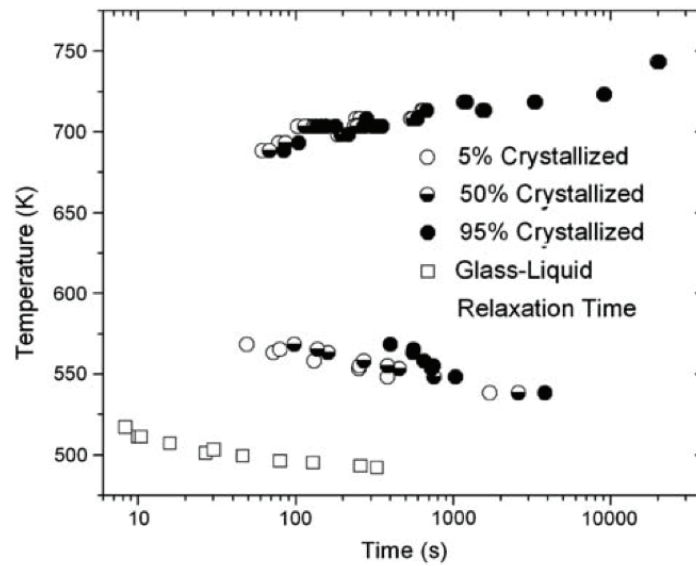


Figure 2:24 Partial TTT diagram for crystallization and relaxation of $\text{Pt}_{57.3}\text{Cu}_{14.6}\text{Ni}_{5.3}\text{P}_{22.8}$ from [169].

According to WDX results this relatively lighter phase contains approximately three times as much Cu as Pd, with only little Ni and P. Löffler et al. [174] concluded that this phase is tetragonal Cu_3Pd , which was confirmed by x-ray diffraction. The vicinity around these dark dendritic regions appearing as bright phase around the dendrite center are enriched in Pd and poor in Cu, as confirmed by WDX. The modulation of Cu and P was observed for all stages of isothermal annealing in $\text{Pd}_{40}\text{Ni}_{30}\text{Cu}_{10}\text{P}_{20}$ after 171 s at 700 K and after 58 s at 677 K.

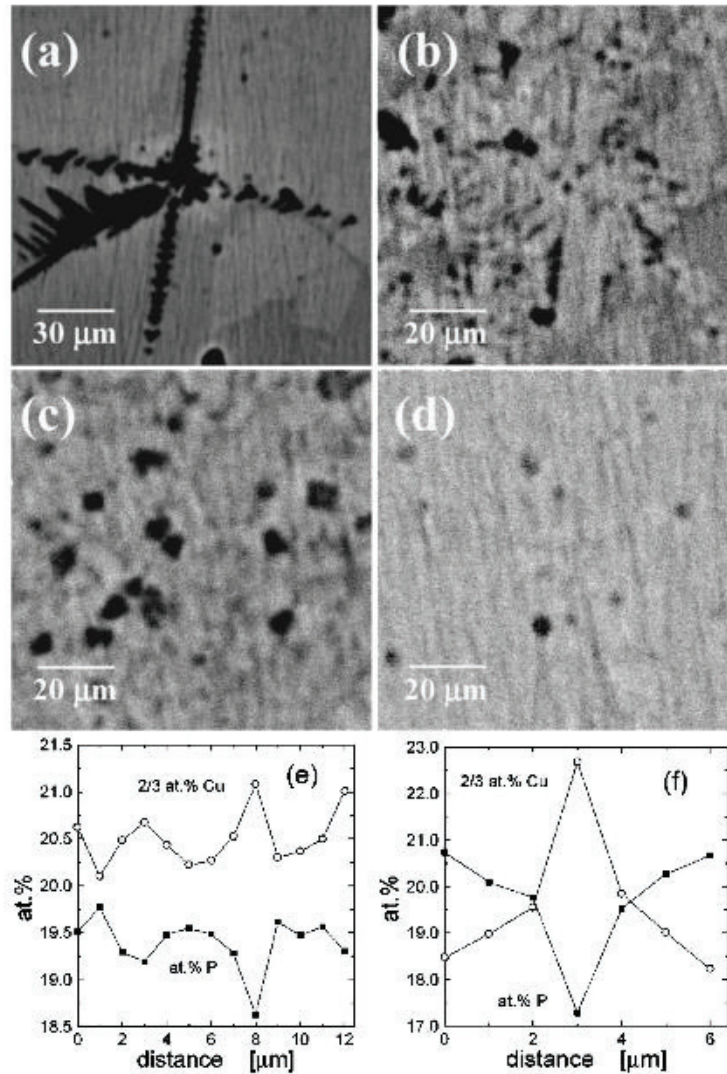


Figure 2:25 Electron backscattering images of $\text{Pd}_{40}\text{Ni}_{30}\text{Cu}_{10}\text{P}_{20}$ processed under different conditions; (a) quenched after 171 s at 700 K, (b) after 58 s at 677 K, (c) after 56 s at 677 K, and (d) after 129 s at 646 K. At all temperatures, a modulated structure in dark and light areas is observed; (e) and (f) illustrate the modulation for the samples shown respectively in (a) and (b) by means of line scans in which the local compositions were investigated by WDX in steps of 1 micron. For a better illustration, the P at.% is compared with two-thirds of the Cu composition (from [174]).

Ma et al. [175] have carried out a complete characterization of the crystallization process in the Pd-Cu-Ni-P system. They have found 4 different phases as shown in Figure 2:26, A = Cu_3Pd , B = $\text{Ni}_2\text{Pd}_2\text{P}$, C = $\text{Cu}_5\text{Pd}_3\text{P}_2$ and D = an unknown quaternary phase. Addition of Cu to the ternary Pd-Ni-P increases the number of the crystalline species forming from the amorphous phase and the degree of complexity of their crystal structures. This makes it difficult for multicomponent compounds to form, resulting in the improvement of the ther-

mal stability of the quaternary Pd-Cu-Ni-P alloys. The formation of at least four complex phosphides (ordered Cu_3Pd , $\text{Ni}_2\text{Pd}_2\text{P}$, $\text{Cu}_5\text{Pd}_3\text{P}_2$, and a Pd-P phosphide) in the Pd-Cu-Ni-P alloys, explains the exceptional high thermal stability and glass forming ability.

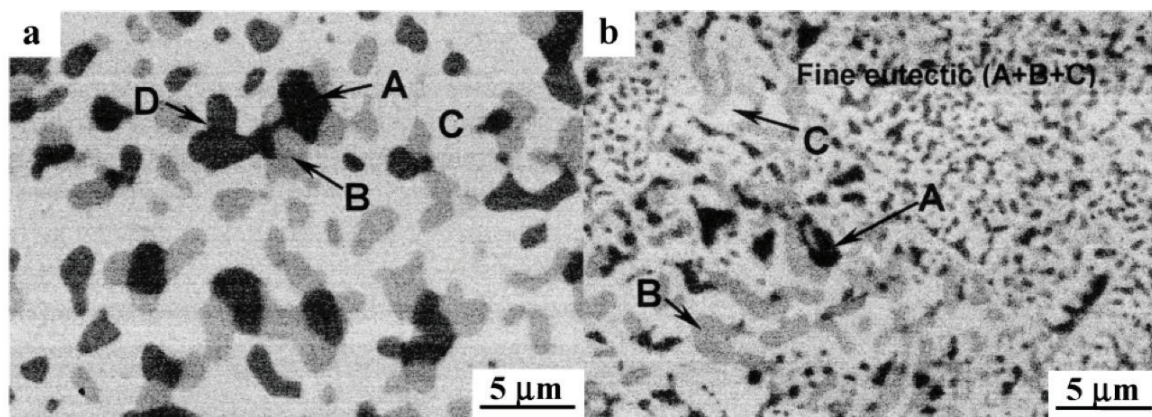


Figure 2:26 Back-scattered electron microcopy images of the alloy $\text{Pd}_{40}\text{Cu}_{30}\text{Ni}_{10}\text{P}_{20}$, (a) annealed at 770 K for 1 h and at 770 K for 200 h ($T_x = 650$ K) (from [175]).

As shown in Figure 2:26, Ma et al. [175] identified Cu_3Pd , $\text{Ni}_2\text{Pd}_2\text{P}$, $\text{Cu}_5\text{Pd}_3\text{P}_2$, and unidentified quaternary phosphide as the major equilibrium phases at 770K in the alloys $\text{Pd}_{40}\text{Cu}_{30}\text{Ni}_{10}\text{P}_{20}$. They claim that these equilibrium phases are different from those identified at the early stage of crystallization. Some of the phases shown in Figure 2:26 (a) in the alloy annealed for 1 h, completely decompose after 50 h annealing. Many of the crystallized phases formed in an early stage of crystallization are metastable phases that transform to stable phases after prolonged annealing[175].

Nishiyama and Inoue [176] found that the time to crystallization in the alloy $\text{Pd}_{40}\text{Cu}_{30}\text{Ni}_{10}\text{P}_{20}$ at a certain temperature above T_g depends on the volume of the sample [176]. They rationalized this finding by that the homogenous nucleation is dominated by the statistical probability, therefore, influenced by the volume of the sample. They carried out an in-situ HRTEM of the crystallization process to determine the time to crystallization on a nano-metric particle of $\text{Pd}_{40}\text{Cu}_{30}\text{Ni}_{10}\text{P}_{20}$, cf. Figure 2:27.

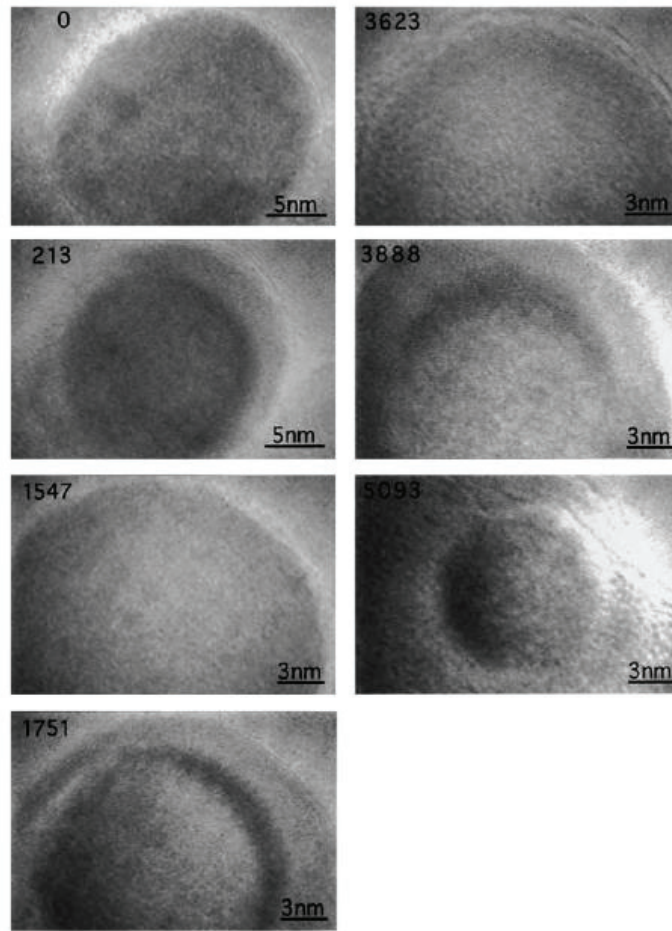


Figure 2:27: Continuous HREM images of the $\text{Pd}_{40}\text{Cu}_{30}\text{Ni}_{10}\text{P}_{20}$ particle sample with a diameter of about 25 nm during isothermal annealing at 683 K from 0 to 5093s (from [176]).

The sample volume dependence of the thermal stability and/or cooling rate should be distinguished from the Small-Droplet-Method developed by Turnbull and Cech [177], i.e., subdivided small particles have a lower probability for containing heterogeneous nucleation sites, therefore improving the undercoolability. The alloy used by Nishiyama and Inoue [176] was purified enough to eliminate any hetero-sites by a B_2O_3 flux treatment, and in a previous study Nishiyama et al. confirmed that the nucleation at 683 K is homogeneous [178]. Conversely, here it is assumed that it is difficult to form a nucleus if the diameter of sample becomes very close to r^* . This difficulty can be explained by the competition between the interfacial and volume free energies [176]. As can be seen in Figure 2:27, the formation of the fringes corresponding to the crystal of Pd_{15}P_2 appear at $t=213$ s. As the size of the samples is reduced, the latter becomes comparable to r^* , i.e. the critical nucleus radius, there is therefore a competition between the interfacial and volume free ener-

gies. As the size of the sample approaches r^* , the free energy becomes dominated by the interfacial energy rather than the volumetric term. Thus the driving force for nucleation is decreased and consequently the probability of nucleation is also reduced [176]. Therefore, for comparing the thermal stability of metallic glasses, samples of the same thermal/process history (e.g. fluxing) and the same size should be studied.

In a recent work done on the mechanical properties of precious-metal based BMGs, Cardinal et al. [179] studied the evolution of mechanical properties of Pt, Pd and Au-based BMGs as a function of the degree of crystallization. The result is shown in Figure 2:28.

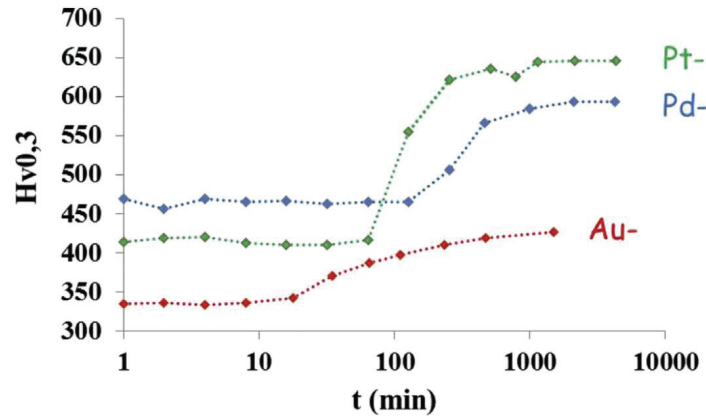


Figure 2:28: hardness as the function of the annealing time in $\text{Au}_{50}\text{Cu}_{25.5}\text{Ag}_{7.5}\text{Si}_{17}$ annealed at 393 K ($T_g=385$ K, $T_x=428$ K), $\text{Pt}_{60}\text{Cu}_{16}\text{P}_{22}\text{Co}_2$ annealed at 533 K ($T_g=546$ K, $T_x=568$ K) and $\text{Pd}_{35}\text{Pt}_{15}\text{Cu}_{30}\text{P}_{20}$ annealed at 578 K ($T_g=551$ K, $T_x=624$ K) (from [179]).

Despite the interesting increase of hardness in the case of the three mentioned BMGs, they all appear to suffer from severe fragilisation upon partial crystallization. The values of K_{Ic} for these three alloys in the partially crystallized state remain below $2 \text{ MPa}\cdot\text{m}^{0.5}$.

2.8 Glass transition temperature (T_g) and mechanical properties

Thanks to the lack of crystalline periodicity and the consequent absence of lattice defects such as dislocations, metallic glasses typically exhibit relatively high strengths [180],[181]. The mechanical response of metallic glasses is a strong function of the ratio of test temperature to the T_g [182]. Originally, Spaepen [183] presented the concept of deformation map describing the deformation mechanisms of metallic glasses as the function of temperature and strain rate. An example of such general maps is presented in Figure 2:29.

As it can be seen in Figure 2:29, at temperatures below T_g , metallic glasses plastically deform in an inhomogeneous manner commonly by formation of shear bands. Yet by in-

creasing the temperature and approaching the T_g , the deformation becomes homogenous. The homogenous flow in metallic glasses is Newtonian, i.e. the instantaneous strain rate is proportional to the applied stress, and their inverse ratio can be defined as the viscosity. Spaepen [183] states “*Plastic deformation, i.e., irreversible shear, of condensed matter occurs by the accumulation of local shear events. For these events to be irreversible upon the removal of the stress there must be a change of at least a few neighbours at their core, which corresponds to a local shear strain on the order of unity. The equivalent event in crystals is the bond exchange at the dislocation core.*” The equivalent of these so called defects or transformation sites in glassy materials are “shear transformation zones”, i.e. flow defects [183]. Eq. (2.13) describes the strain rate in a glass subject to an external stress σ , the flow defects of the volume v_0 undergo a strain of ϵ_0 at a rate depending on the stress level. In Eq. (2.13) k_f is a temperature-dependent rate constant, Ω , the atomic volume, k , the Boltzmann constant, c_f the concentration of defects and T the absolute temperature [183].

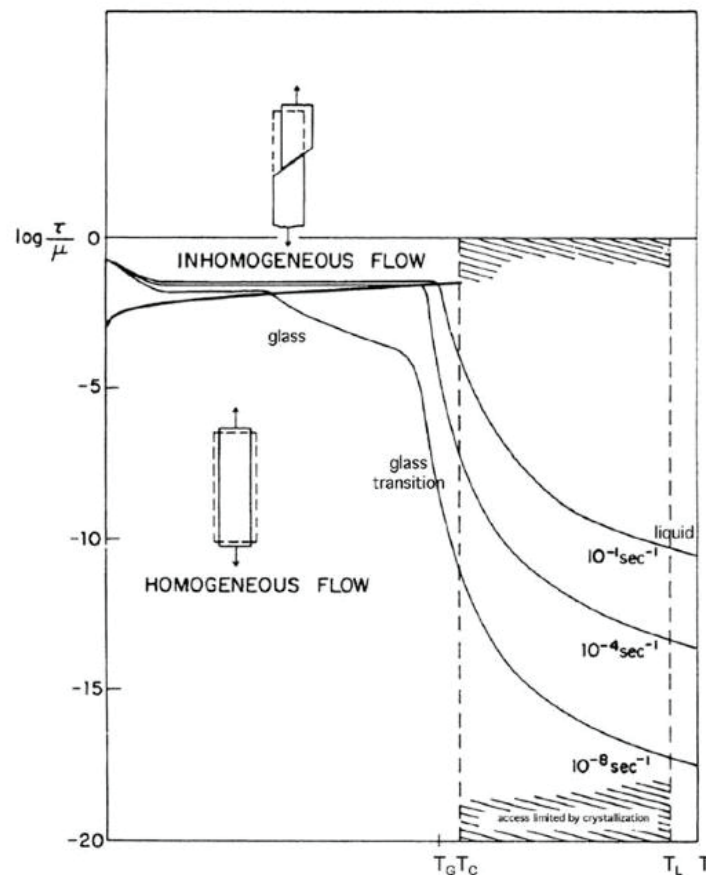


Figure 2:29 Example of a deformation map for a metallic glasses (from [183]).

$$\frac{d\varepsilon}{dt} = 2c_f k_f \frac{\varepsilon_0 v_0}{\Omega} \sinh\left(\frac{\varepsilon_0 v_0 \sigma}{2kT}\right) \quad (2.13)$$

Figure 2:30 shows the validity of the Eq. (2.13) fitted to the experimental data obtained on $\text{Pd}_{41}\text{Ni}_{10}\text{Cu}_{29}\text{P}_{20}$ sample annealed enough to eliminate any effect coming from structural relaxation. Therefore, the c_f is constant over the whole range of the test. The fitted curve shown in Figure 2:30 yields an activation volume of $\varepsilon_0 v_0 = 141 \text{ \AA}^3$.

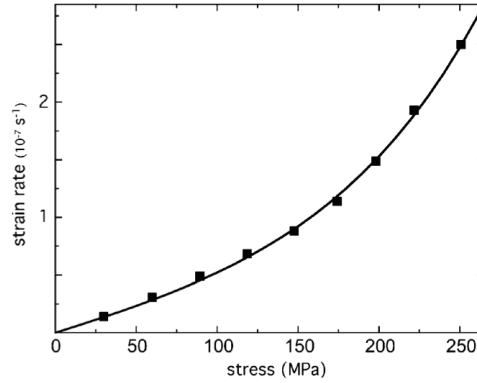


Figure 2:30 Stress-dependence of the strain rate of an annealed $\text{Pd}_{41}\text{Ni}_{10}\text{Cu}_{29}\text{P}_{20}$ glass at 550 K. The fit is a sinh, according to Eq. (10) (from [183]).

In liquid flow, where the stress is small enough Eq. (2.13) is reduced to Newtonian flow. Consequently the temperature-dependence of viscosity or the apparent resistance of the matter against shear, becomes dependent on the pre-factor $c_f k_f$. In the vicinity of T_g the apparent activation energy is too high compared to the cohesive energy for a single event, suggesting that there must be a cooperative process. The free volume model takes this into account and describes the flow defect as the “*Local density fluctuation that exceeds a critical value v^** ” [183] giving a concentration as described in Eq. (2.14).

$$c_f = \exp\left(\frac{-\gamma v^*}{v_f}\right) \quad (2.14)$$

In Eq. (2.14) γ is the geometrical overlap factor between 0.5 and 1, v_f is the average free volume per atom i.e. the difference in atomic volume and the actual fully closed packed state. The free-volume model describes v_f as the function of α , the coefficient of thermal expansion, temperature and the atomic volume Ω :

$$v_f = \alpha \Omega (T - T_0) \quad (2.15)$$

Spaepen [183] suggested that deformation at high stress levels creates defects, in the same time these defects can be annihilated and the “*stress-driven creation process is a*

reproducible one that is a function of the instantaneous stress, temperature and defect concentration". Formation of new flow defects requires creation of internal volume, as shear deformation of dense and randomly packed particles requires dilatation. The same is true for randomly close-packed atoms, shear and plastic deformation results in less perfect packing, and an increase in volume [183]. Spaepen claims that only a small fraction of such generated volume is retained as free volume. Additionally only a small fraction of the total energy applied to the sample is stored as new free volume and the rest is dissipated as heat, very similar to the case of formation of dislocations in crystals.

As shown in Figure 2:31, Yang et al. [184] described a correlation between the strength of BMGs and their respective glass transition temperature T_g . As it can be seen there is yet considerable scatter involved in this correlation. Interestingly enough there are similarities between the plastic deformation in BMGs and the glass transition in glasses. Yang et al. [184] suggested that both phenomena are facilitated by the collective atomic motion requiring sufficient energy to overcome the cohesive force between atoms, resulting in an increase of free volume. This energy can be in the form of mechanic work in the case of plastic deformation localized in the shear band or heat used to increase the temperature of the body. Both of these forms of energy will cause creation of free volume [147], [183]. There is a critical level of free volume beyond which both the glass transition and the shear localization are activated. Upon appearance of both these phenomena atomic mobility is rapidly extended macroscopically. The main difference between the glass transition and the plastic deformation is the distribution of energy in the body. In the case of glass transition the heat covers the whole body of glassy solid whereas upon plastic deformation, mechanical energy is closely confined within the shear band. In both cases the atomic bonding force to overcome is the same and the final status of the matter, i.e. reshuffled atoms, is similar [184]. Thus one can consider that the thermal energy needed to increase the temperature up to the T_g is equal to work during creation of shear strain of a basic shear unit (STZ) [184]:

$$\tau_y \gamma_0 \approx \int_{T_a}^{T_g} \rho C_p dT \quad (2.16)$$

where τ_y is the maximum shear stress upon yielding, the $\gamma_0 \approx 1$ is the shear strain of the basic shear unit (STZ), ρ is the density of the material, C_p is the heat capacity, T_g is the

glass transition temperature and T_a is the ambient test temperature. Based on Eq. (15) Yang et al. [184] demonstrate that the strength of the materials can be written as:

$$\sigma_y \approx 50 \frac{\Delta T_g}{V} \quad (2.17)$$

where ΔT_g is the temperature difference between the T_g and T_0 and V the molar volume. The heat released in the shear transformation zones (STZs) is high enough to increase the temperature near T_g [185]. This rapid rise in temperature close to T_g is enough to significantly decrease the viscosity and cause softening within the shear band, resulting ultimately in fracture of BMG.

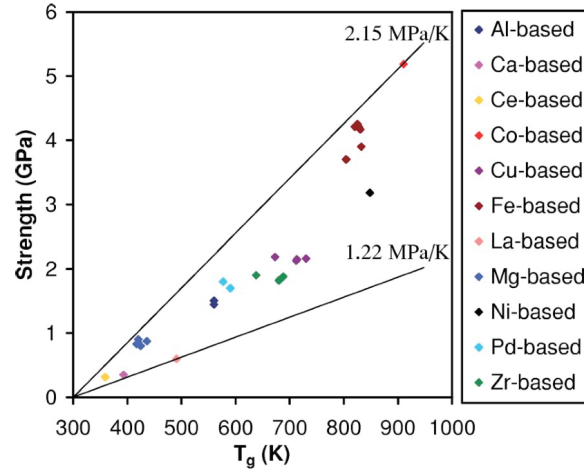


Figure 2:31 Strength of various BMGs as the function of their T_g (from [184]).

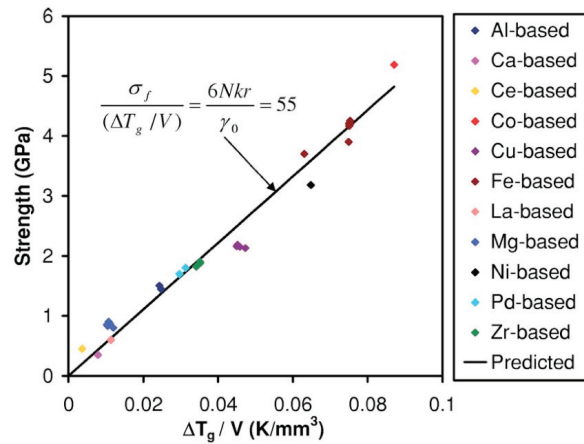


Figure 2:32 The correlation between the strength of various BMGs and the difference between the test temperature and T_g normalized by their respective molar volume (N : Avogadro number, k : Boltzmann constant, r : 1.1 and γ_0 : the shear strain in STZ ≈ 1) (from [184]).

Yang et al. found a remarkable correlation between the strength of BMGs in different alloy systems and their T_g normalized by their molar volume. They suggest an increase in T_g and decrease in the molar volume results in stronger glassy alloys. This correlation is depicted in Figure 2:32.

In conclusion, the increase of glass transition temperature and a decrease in molar volume results in stronger glass formers, concluding that the mechanical energy density for deformation is quite similar to thermal energy density for glass transition in BMGs [184].

Chapter 3

Development of a new family of phosphorous-free Pt-based bulk metallic glasses

Hamed Kazemi, Cyrill Cattin, Maïté Blank, Ludger Weber¹

Laboratory of Mechanical Metallurgy, Ecole polytechnique fédérale de Lausanne, EPFL,
CH-1015 Lausanne, Switzerland

¹corresponding author: ludger.weber@epfl.ch

H. Kazemi, C. Cattin, M. Blank, L. Weber, Development of a new family of phosphorous-free Pt-based bulk metallic glasses, Journal of Alloys and Compounds. 695 (2017) 3419–3428. doi:10.1016/j.jallcom.2016.12.017.

Contributions:

Hamed Kazemi: Alloy design, preparation and characterization, writing the manuscript.

Cyrill Cattin: Identifying the critical casting diameter for the alloy $\text{Pt}_{49.95}\text{B}_{24}\text{Si}_{6.4}\text{Ge}_3\text{Cu}_{16.65}$.

Maïté Blank: TEM analysis on the alloy $\text{Pt}_{49.95}\text{Si}_{9.4}\text{B}_{24}\text{Cu}_{15.65}\text{Ag}_1$.

Ludger Weber: Supervision, revision, correction and approving the manuscript.

Abstract

New BMGs exhibiting strong glass forming ability combined with high hardness have been developed based on the Pt-Si-B ternary system. The effects of partial substitution of platinum by transition metals of the group iron, cobalt, nickel, and copper, as well as the partial replacement of silicon by germanium on the melting temperature, T_m , the crystallization temperature, T_x , the glass transition temperature, T_g , and the hardness are investigated. Amongst the transition metals, nickel and copper were found to reduce the liquidus and the solidus temperatures of the Pt-Si-B near ternary eutectic composition, while cobalt and iron had no influence on the solidus temperature but raised the liquidus temperature significantly. Substitution of one fourth of platinum atoms by either nickel or copper increased the glass transition temperature by roughly 45 K and 65 K, respectively, with a concomitant increase in crystallization temperature of similar magnitude. For a series of alloys with the general formula $(\text{Pt}_{0.75}\text{Cu}_{0.25})_{66.6}\text{B}_{24}\text{Si}_{9.4-x}\text{Ge}_x$, increasing substitution of silicon by germanium ($x = 0 \dots 3$) led to a significantly increased crystallization temperature essentially by shifting the first of typically two crystallization peaks to higher temperatures, while the T_g was slightly lowered as x increased. This resulted in a marked widening of the supercooled liquid region, ΔT . Within this alloying series a general trend of increased hardness with increased T_g was observed.

1. Introduction

Platinum-based alloys are widely used in jewelry applications owing to their chemical inertness, aesthetic appearance, and recognized status as precious metal [1]. Compared to gold alloys, the high liquidus temperature of standard platinum grades (around 2000 K) renders processing more challenging. In particular, investment casting of platinum is limited to comparatively small volumes due to the temperature limitations of the investment refractory. In addition, platinum alloys for jewelry applications typically must fulfill purity requirements or hallmarking standards, e.g. Pt850, Pt900 or, most commonly, Pt950, corresponding to platinum weight fractions of 0.85 to 0.95, which, compared to gold hallmarking standards, e.g. Au750 (18kt) and Au585 (14kt), leaves less room for improving mechanical properties by alloying. Therefore, platinum alloys are typically somewhat softer than gold alloys and hence suffer from being easily scratched. To extend performance beyond what is obtained by standard alloying strategies for crystalline alloys [2], it has re-

cently been proposed to use platinum based bulk metallic glasses (BMGs) in jewelry applications [3]. Known platinum BMGs are based on the Pt-P binary system with some degree of substitution of platinum by transition metals [3–6].

Apart from a challenging metallurgy owed to the high level of phosphorus, these alloys suffer from some porosity hampering their use in applications with high esthetic requirements. Furthermore, due to their relatively low melting temperature and glass transition temperature, their hardness is only slightly higher than that of the hardest crystalline alloys [3,5]. Such Pt-P-based BMG's have been used for hot embossing (or nano-forming) of micro-components. The isotropic and defect-free structure (absence of grain boundaries) as well as superior mechanical properties of BMG's made them great candidates for the micro/nano-component fabrication [7]. For example, Kumar et al. [7] have demonstrated that nanopatterning of metallic glasses by hot embossing can generate feature sizes as small as 13 nm using Pt-P-based BMG. Similarly Saitome et al. [8] used Pt-P-based BMG's for producing optical components such as diffraction gratings (1 μm interval) and a hologram. These are just a few examples of the possible applications of Pt-based BMG's beyond jewelry and watch making.

Apart from phosphorus, several other elements form low-lying eutectics with $T_m < 1273\text{ K}$ on the platinum-rich side of their respective binary phase diagrams with platinum, i.e. As, Bi, B, Ge, Sb, Si, and Te, having in common that they are clustered around the metal/semimetal/non-metal transition and that the eutectic point in the binary is typically situated roughly between 20 and 40 at.-pct. of solute [9]. Figure 3:1 shows the composition and eutectic point of these binaries in one graph. It is to be noted that we have converted the atomic percentages to weight percentages. In most of these systems, amorphous metal formation has been reported for rapidly quenched alloys close to the eutectic point, except for bismuth and tellurium [10,11]. However, there is no tangible attempt in the literature to improve the glass forming ability of these binary systems to obtain bulk metallic glasses.

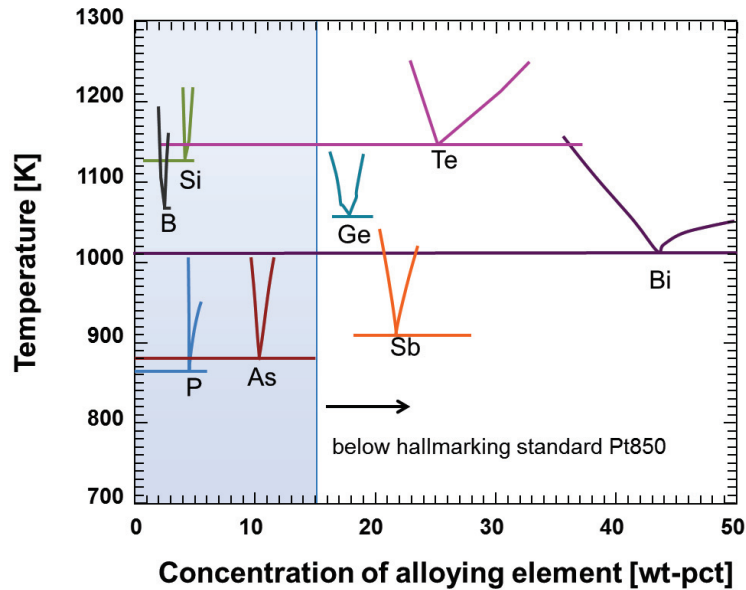


Fig. 3:1 Synopsis of the binary eutectic points of all alloying elements that have a melting point below 1273 K in the platinum-rich part of their respective binaries. The blue shaded area indicates the range of composition complying with the Pt850 hallmarking standard.

The present contribution presents an attempt to fill this gap by developing Pt-based bulk metallic glasses based on the Pt-Si-B ternary system. The rationale for this specific choice is three-fold:

- the expected atomic concentrations and relative size ratios correspond well to conditions identified by Miracle and co-workers [12–14] to be most suitable for bulk metallic glass formation;
- ternary amorphous alloys involving silicon and boron have been developed in the past e.g. in the Fe-Si-B, the Ni-Si-B and the Co-Si-B system [15–20]. For these three systems, the ternary eutectic point has typically been found to lay roughly 100-150 K below the average of the binary eutectics. This would lead to expect a ternary eutectic in the Pt-Si-B system at roughly 973 K, i.e. making a nice step towards the melting point of the already known Pt-P based BMGs;
- compliance with the limitations of the existing hallmarking standards for jewelry applications requires that the melting point depressants, i.e. the elements from the list given above, should be as light as possible in order to keep the weight fraction of platinum preferentially above 950/1000 or at least above 850/1000. As can be seen

from Figure 3:1, silicon and boron become fairly natural choices under these boundary conditions.

Once the low melting point regions in the ternary system are identified, the effect of partial substitution of the platinum by other transition metals as well as the substitution of silicon and boron by other metalloids will be discussed. Both approaches are common practice in platinum metal group (PMG) based bulk metallic glasses, e.g. the work by Schroers and coworkers [3,5] for substitution of the main constituent in Pt-P based BMGs, and work by Inoue et al. on the partial substitution of the metalloid in Pd-Cu-Si glasses [21]. In particular, we will discuss the significant influence of substitution on the glass transition temperature and on the hardness of the alloys.

2. Experimental Procedure

2.1. Materials and processing

Ingots were prepared by melting pure elements (Pt 99.9%, Si 99.99%, B 99.5%, Ni 99.5%, Cu 99.999%, Ge 98.5%, Co 99.998%, Ag 99.99%, Fe 99.98%) in a quartz tube under argon atmosphere (99.9999%). For compositions prone to solidify in an amorphous state, ribbons were produced by melt-spinning under argon atmosphere (99.9999%), with a linear speed at the surface of the copper disk of 26 ms^{-1} . Of the best glass-forming compositions cast samples in the form of rods with diameters varying from 0.75 to 5 mm and length between 20 and 40 mm were produced by suction casting in an arc-melter (MAM-1, Edmund Bühler GmbH, Hechingen, Germany) under argon (99.9999%) atmosphere. Prior to melting the ingots, the atmosphere was cleaned from residual oxygen by melting a small Ti droplet ($\approx 1 \text{ g}$). For some but not all of the alloys discussed here, the oxygen content was measured by inert gas fusion and was found to be systematically below 20 ppm and typically around 8 ppm. To improve homogenization, the billets were turned and remelted typically four times before being suction cast. For controlled crystallization, a thermally stabilized salt bath was used with temperature variation equal to $\pm 1 \text{ K}$.

2.2. Characterization

i) Structural analysis

The amorphous structure of the samples was verified using a Philips X'pert X-ray diffractometer equipped with a Cu-K α source. For melt spun ribbons XRD analysis was carried out on both the surface in contact with the copper wheel and the back. For the cast samples, sample surfaces were grinded with SiC paper and subsequently polished with 1 μ m diamond particles prior to diffraction analysis.

ii) Thermal analysis

Thermo-physical properties were investigated by a Differential Scanning Calorimeter (DSC Pegasus 404C Netzsch, Germany) under argon (99.9999%) flow, with a heating rate of 10 K/min in alumina crucibles. Solidus and liquidus temperatures were both measured on the first heating curve after glassy solidification. For amorphously solidifying compositions, glass transition temperatures were measured on the DSC curves as the inflection point of the step towards endothermic values. The crystallization temperature was measured by the onset of the exothermic peak upon heating.

iii) Transmission Electron Microscopy (TEM)

TEM analysis was carried out in a FEI Tecnai Osiris microscope at 200 kV. Electron-transparent samples with thicknesses varying between 30-70 nm were prepared by Ultramicrotomy. Ultramicrotomy was chosen as the preparation method particularly to avoid possible artifacts such as partial crystallization during ion milling as discussed by Sun et al. [22].

iv) Optical microscopy

Metallographic samples for optical microscopy were prepared by embedding the melt-spun ribbons or the suction cast rods in a hot mounting resin that was cured under pressure at 453 K, i.e. significantly below the glass transition temperature of any of the samples, cf. Table 3:1. After grinding on SiC paper down to P2500-mesh, the sample was polished on soft cloth with diamond particles of 6 and 1 μ m colloidal suspension, in presence of a mixture of soap, ethanol and distilled water as lubricant.

v) Mechanical analysis

Hardness measurements were carried out using a Gnehm FM300 microhardness tester on samples prepared for optical microscopy. The compression tests were carried out on as-cast samples of 2 mm diameter and 4 mm height on a Schenk RM600 Mechanical Testing Machine (Switzerland) equipped with a load cell of 100 kN. The test was conducted at a crosshead speed of 0.08 mms^{-1} corresponding to a nominal strain rate of 0.02 s^{-1} .

vi) Determination of the critical casting thickness

The critical copper mould casting thickness was assessed in two different ways: for the alloy with the largest difference, ΔT , between T_x and T_g , a conical sample was cast in a copper mould with an opening angle of 20° and the glassy to crystalline transition was assessed by measuring the microhardness along the axis of the cone. For about half of the quarternary or quinary alloys the critical casting thickness was qualitatively assessed by verifying the glassy nature of suction cast rods of 1 and 2 mm in diameter.

3. Results

3.1. Pt-Si-B ternary eutectic

A first series of alloys was prepared to identify the location of the ternary eutectic composition by covering the range between the two binary eutectics of $\text{Pt}_{77}\text{Si}_{23}$ and $\text{Pt}_{71}\text{B}_{29}$ (cf. Figure 3:2h) distributed on a slightly bent curve. The precise compositions as well as the data determined on the samples are listed in Table 3:1, in which also the characteristics of all other samples investigated in this work are listed. As it can be seen in the micrographs presented in Figure 3:2a-g, the microstructures close to the binary eutectics exhibit a significant amount of (facetted) primary phases embedded in a very finely dispersed eutectic. In contrast, for the alloy composition of $\text{Pt}_{73}\text{Si}_{12}\text{B}_{15}$ the microstructure is essentially composed of eutectic microstructure, cf. Figure 3:2d, albeit at two length scales: somewhat coarser cells embedded in finely dispersed eutectic.

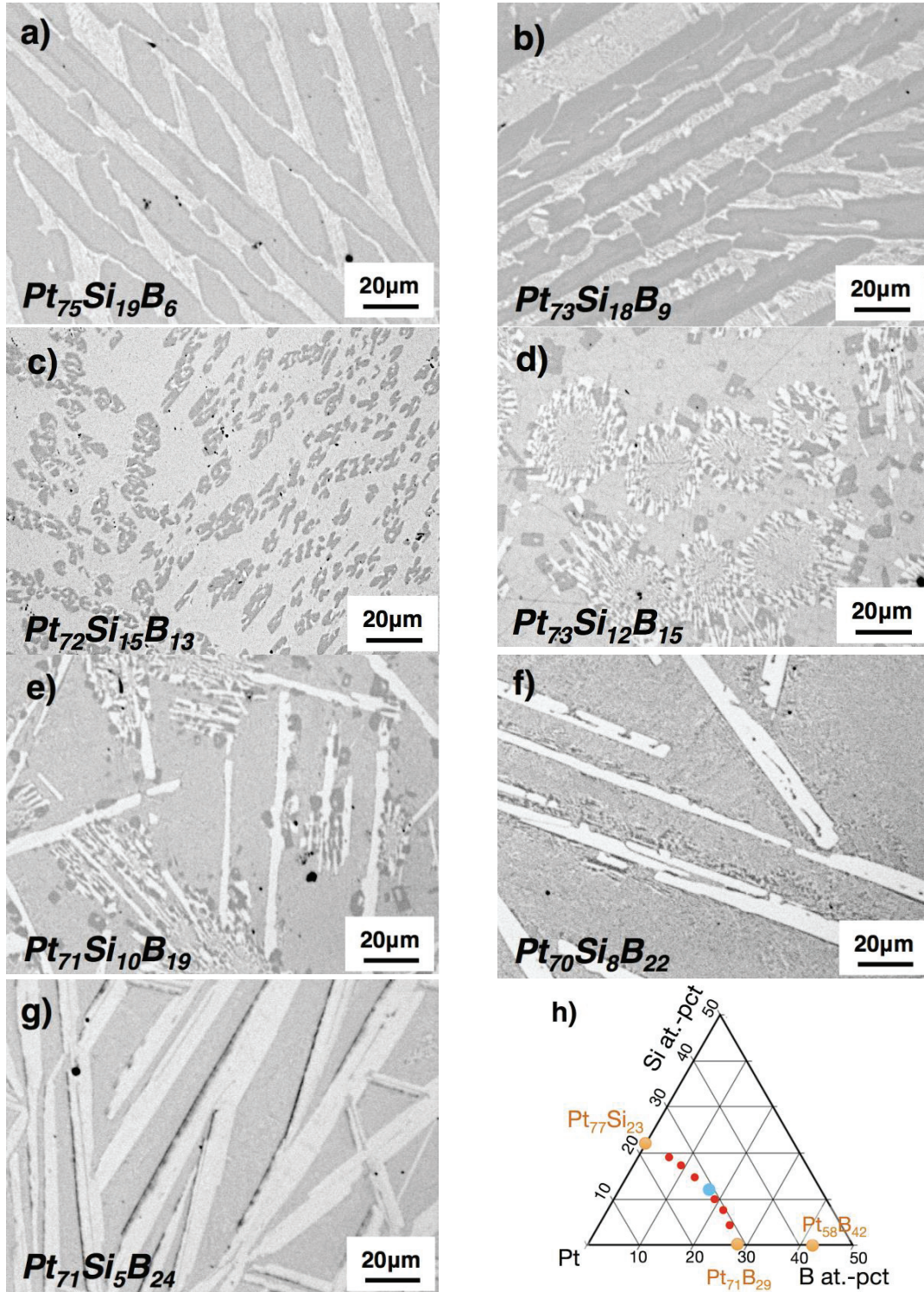


Fig. 3:2 a-g: Microstructures of the ternary alloys distributed on the bowed line between the binary eutectics as indicated in h).

Thermal analysis results of the same series shown in Figure 3:3 reveal that all alloys have a similar solidus temperature at around 973 K. For all but the $\text{Pt}_{73}\text{Si}_{12}\text{B}_{15}$ alloy the liquidus temperature was significantly higher than the solidus temperature and somewhere around the weighted average of the binary eutectic temperatures. In contrast, for the $\text{Pt}_{73}\text{Si}_{12}\text{B}_{15}$ alloy the DSC curve exhibited virtually a single peak upon heating indicating that the alloy was reasonably close to a hypothesized ternary eutectic composition.

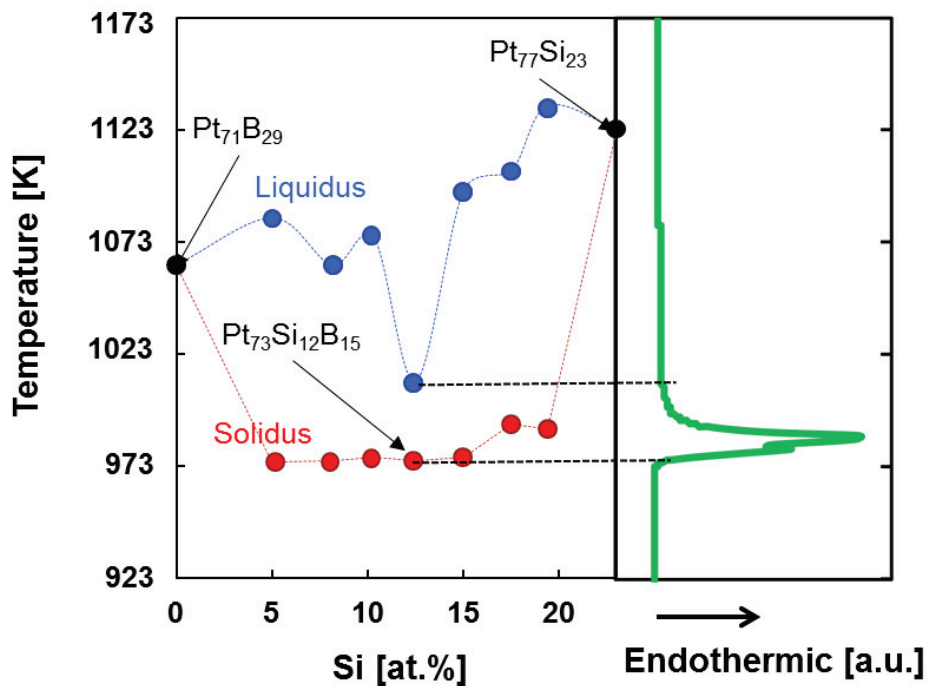


Fig. 3:3 Evolution of the solidus and liquidus temperatures of the alloys between the binary eutectics. The solidus temperature is fairly constant for all alloys while the liquidus temperature is lowest for the $\text{Pt}_{73}\text{B}_{15}\text{Si}_{12}$. The DSC curve to the right indicates how the liquidus and solidus temperatures were determined.

3.2. Effect of platinum substitution by transition metals

In a next step roughly one twentieth of the platinum was substituted by transition metals from the group $\text{TM}=\text{Cu}, \text{Ni}, \text{Fe}, \text{Co}$ in order to investigate the influence of those substitutions on melting. The solidus temperature was reduced by roughly 15-20 K by both copper and nickel while iron and cobalt did not exert any significant effect on the solidus temperature but raised instead the liquidus temperature significantly. The alloys in which platinum was partially substituted by nickel and copper could be made amorphous as 2-3 mm wide

and roughly 60 μm thick ribbons produced by melt spinning. The effect of substitution of up to one fourth of the platinum by Ni on the glass characteristics T_x , T_g , T_s and T_l are shown in Figure 3:4a.

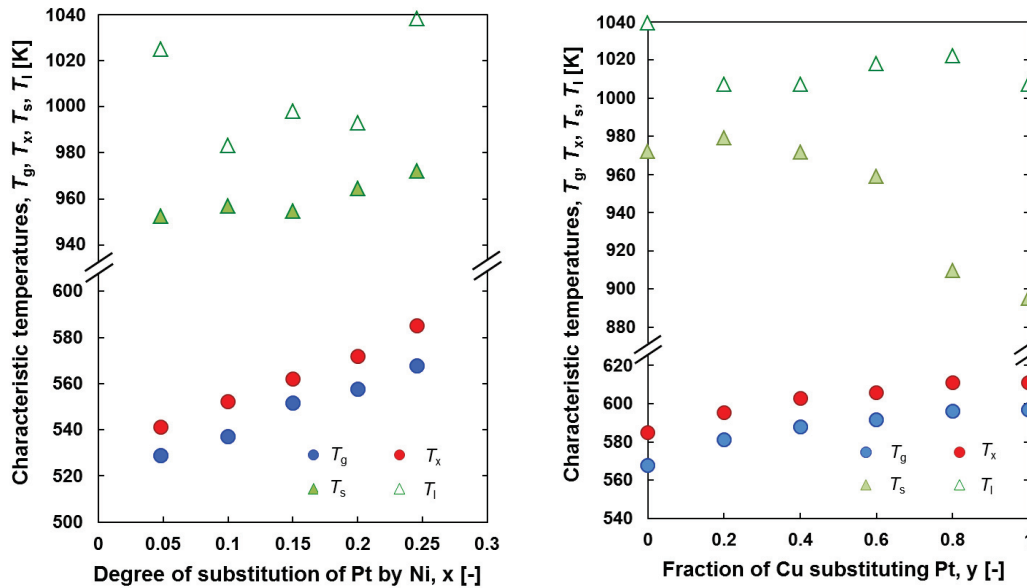


Fig. 3:4 Evolution of the characteristic temperatures for melt-spun alloys with a) the general formula $(\text{Pt}_{1-x}\text{Ni}_x)_{73}\text{B}_{15}\text{Si}_{12}$ and b) the general formula $(\text{Pt}_{0.75}(\text{Ni}_{1-y}\text{Cu}_y)_{0.25})_{73}\text{B}_{15}\text{Si}_{12}$.

Also shown in Figure 3:4b is the evolution of the same characteristics for a series of samples in which one fourth of platinum was substituted by a mixture of copper and nickel, going from only copper to only nickel as substitute. As indicated in Figure 3:2h there is a second eutectic in the Pt-B binary system at 42 at.-pct B. In order to explore the area between the approximate ternary eutectic and the binary Pt-42 at.-pct B eutectic, a series of compositions was devised in which the boron content was increased stepwise from 15 to 26 at.-pct accompanied by a stepwise reduction in silicon from 12 to roughly 9 at.-pct. The Cu:Pt ratio for this series was kept at 1:3. The DSC curves of the first heating after melt spinning are shown in Figure 3:5.

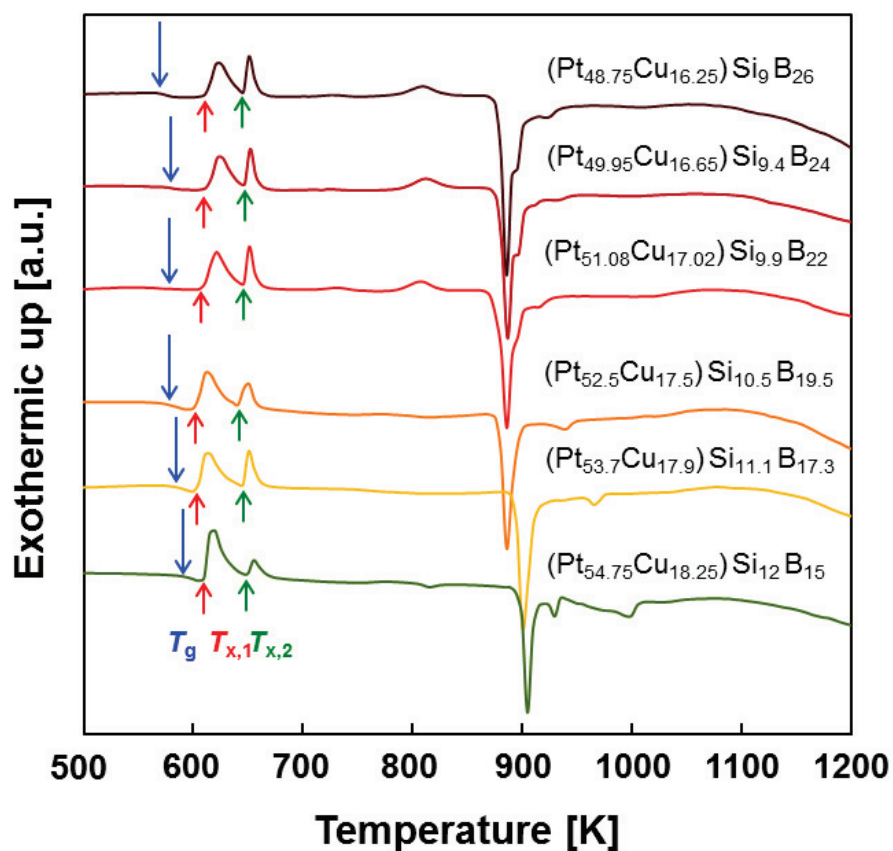


Fig. 3:5 DSC curves obtained upon heating at 10 Kmin^{-1} on melt-spun glassy samples lying in the eutectic trough. T_g , T_{x1} , and T_{x2} are shown by blue squares, red circles, and green circles, respectively.

Drawing from the work of Demetriou et al. [6] a small fraction (1 at.pct in global composition) of copper was replaced by silver, leading to a slight increase in crystallization temperature by 4 K and a reduction in solidus temperature by 5 K, while leaving T_g virtually unchanged. The interesting feature of a doubled crystallization peak, however, remained unaffected by the addition of silver. Based on the insignificant improvement brought by the 1 at.-pct addition of silver on glass forming ability and its cost in terms of compromising the compliance with the hallmarking standard, silver was excluded from the system in further series but the sample containing silver was used for TEM analysis.

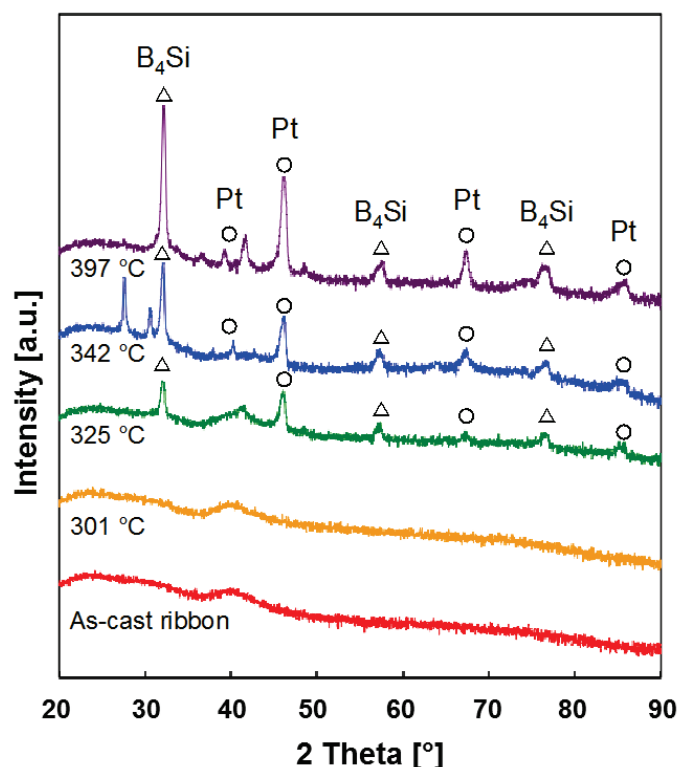


Fig. 3:6: XRD patterns of the alloy $\text{Pt}_{49.95}\text{Cu}_{15.65}\text{Ag}_1\text{Si}_{9.4}\text{B}_{24}$ after heat treatment in a salt-bath for 1 h at different temperatures (indicated to the right). During the first crystallization, face-centered cubic $\alpha\text{-Pt}$ and rhombohedral B_4Si are formed.

In order to identify the crystalline structure corresponding to the first and second crystallization peaks in the DSC pattern, melt-spun samples of the alloy $\text{Pt}_{49.95}\text{Cu}_{15.65}\text{Ag}_1\text{Si}_{9.4}\text{B}_{24}$ were annealed in a thermally stabilized salt bath at different temperatures in the super-cooled liquid region for 1 h. As shown in Figure 3:6, the first crystallization peak gradually disappears as the annealing temperature is increased. The glassy structure was characterized with XRD. The samples were subsequently characterized by HRTEM and SAED, in order to identify the crystalline phases. Figure 3:7a shows a typical HRTEM image of a sample annealed at 574 K, just one degree above the onset of the glass transition, giving evidence for a few ordered regions of nanometric size.

The crystalline structure of the phases formed during the first crystallization peak was investigated on the sample annealed at 598 K and 615 K for 1 h. The diffraction rings were pronounced enough such that two distinct phases could be indexed, cf. Figures 3:7b and 3:7c: first, an fcc phase with the lattice parameter of 3.93 Å, corresponding to $\alpha\text{-Pt}$ with an average crystal size of 3.66 nm deduced by Scherrer's formula based on the width of the

diffraction peak and, second, a rhombohedral phase corresponding to B_4Si . Traces of a third unknown phase were also found in the sample annealed at 615 K. The characterization of this phase by high energy X-ray will be reported elsewhere.

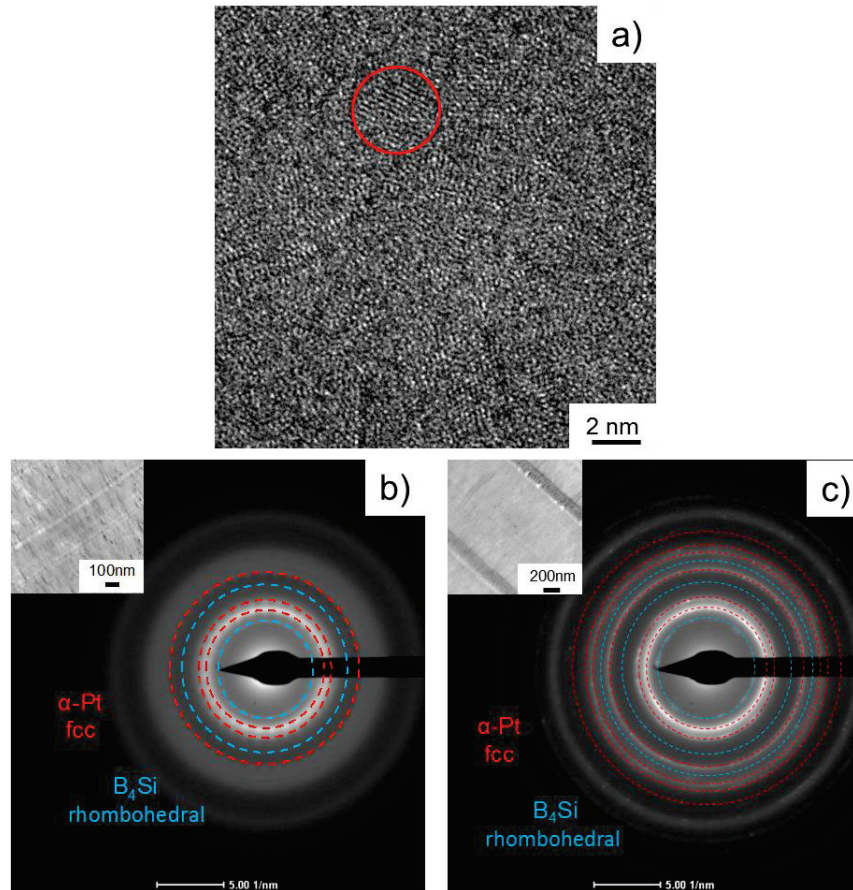


Fig. 3:7 Characterization of melt spun ribbons of the alloy $Pt_{49.95}Cu_{15.65}Ag_1Si_{9.4}B_{24}$
a) HRTEM image of the sample annealed at 574 K for 1 h; b) TEM diffraction image of a sample annealed at 598 K for 1 h; c) TEM diffraction image of a sample annealed at 615 K for 1 h.

3.3 Substitution of silicon by germanium

Further improvement of the thermal stability of the glass forming composition quantified by $\Delta T = T_x - T_g$ was aimed at by substituting part of the silicon atoms by germanium. This was motivated by the fact that germanium is electronically fairly similar to silicon and is itself also a powerful melting point depressant for platinum, cf. Figure 3:1. As can be seen in Figure 3:8, such substitution of silicon by germanium resulted in the gradual shift of the

first crystallization peak towards higher temperatures to the point that the two crystallization peaks coincide at 3 at.-pct of germanium.

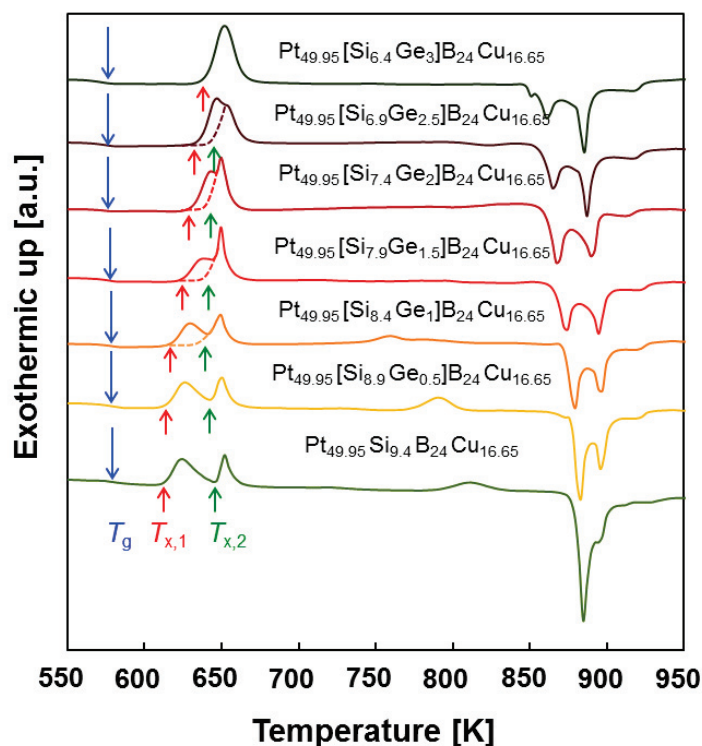


Fig. 3:8 DSC patterns of the alloys with the general formula of $\text{Pt}_{49.95}\text{Cu}_{16.65}\text{Si}_{9.4-x}\text{Ge}_x\text{B}_{24}$. The positive effect of substituting Si with Ge can be seen as widening of the super-cooled liquid region.

Concomitant to increasing T_x , partial substitution of silicon by germanium had the beneficial effect of also reducing T_g hence widening the super-cooled liquid region, which is typically taken as an indication of better glass forming ability [23,24].

As it has been shown above, the thermo-physical properties are closely linked to the composition. In an attempt to verify that the boron and copper contents fixed before substituting some of the silicon by germanium were still adequate, the boron and copper content was once more varied, always in exchange with platinum yet at a roughly fixed silicon and germanium content. The results of these series are shown in Figures 3:9a and 3:9b.

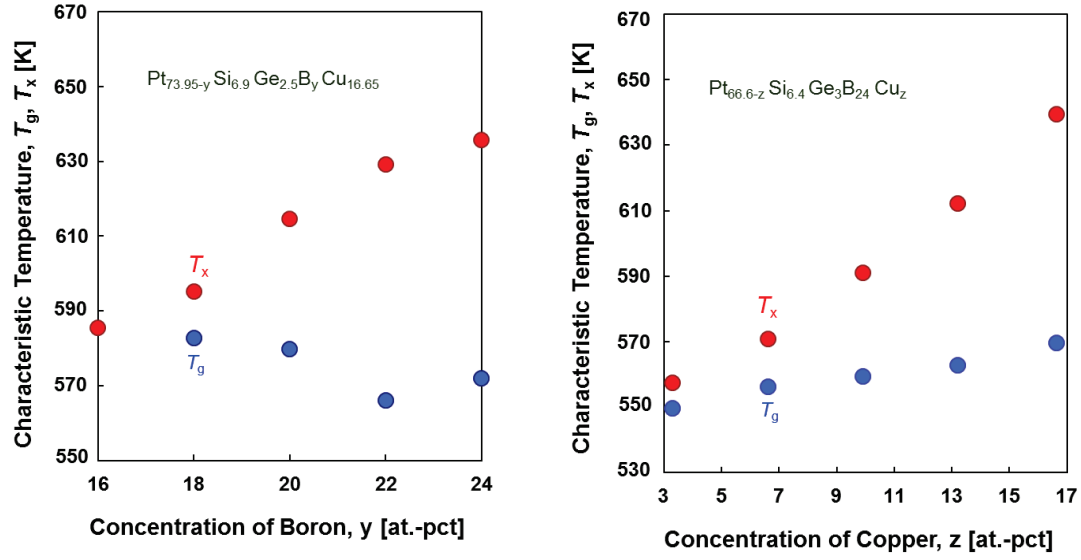


Fig. 3:9 Evolution of the characteristic temperatures, T_x and T_g , for a) an alloy of general composition $Pt_{73.95-y}Cu_{16.65}Si_{6.9}Ge_{2.5}B_y$ as a function of the boron concentration, y ; and b) an alloy of general composition $Pt_{66.6-z}Cu_zSi_{6.4}Ge_3B_{24}$ as a function of the copper concentration, z .

3.4 Mechanical properties

In order to make sure that the hardness values measured reflected well the mechanical behaviour of the metallic glasses produced and characterized in this work, a rod of the alloy $Pt_{49.95}B_{24}Si_{6.4}Ge_3Cu_{16.65}$ was copper-mould suction-cast with diameter 2 mm. The compression curves show essentially elastic behaviour with very limited plasticity up to a fracture stress of 1.83 ± 0.04 GPa and a compressive fracture strain of $2.8 \pm 0.2\%$ (each being an average of three samples). On some spare discs cut from the same rod, the microhardness was determined to be 576 ± 4 HV0.3 and it was further verified by XRD that the sample was fully glassy.

3.5 Critical casting thickness

The results of the critical casting thickness assessment are summarized in Table 3:2. Except for the sample $Pt_{49.95}B_{24}Si_{6.4}Ge_3Cu_{16.65}$ that was analyzed by casting a cone in a copper mould, all other samples were suction cast in rods of 1 and 2 mm diameter. The glassy nature was assessed by microhardness measurements in the center of the rod.

Microhardness values below 600 HV were taken as an indication of glassy structure. This threshold was derived from the evolution of the hardness along the center-line of the cone sample that showed a step function from roughly 550 HV to 750 HV when passing from the glassy into the crystalline region, cf. Fig. 3:10.

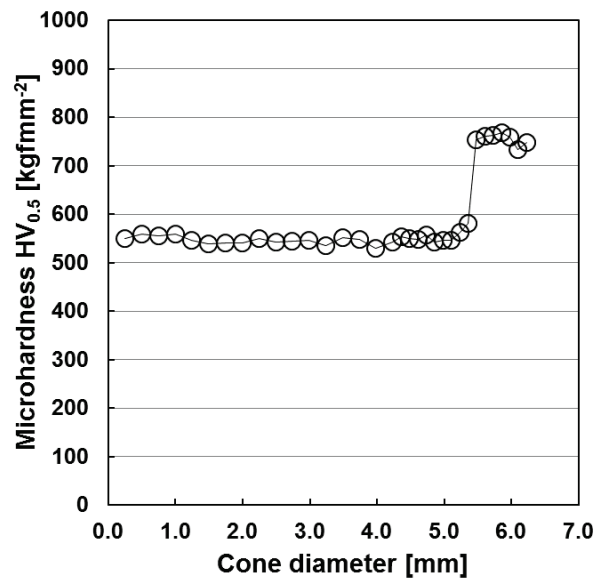


Fig. 3:10: Evolution of the microhardness along the central axis of a cone cast in a copper mold with opening of 20°. The microhardness increases significantly as soon as the critical diameter is reached, indicating that a hardness of 600 HV can be considered as a separation between amorphous and crystalline sample.

4. Discussion

4.1. Pt-Si-B ternary eutectic

The microstructures and the DSC measurements presented in Figures 3:2 and 3:3 suggest that the ternary system Pt-B-Si does have a ternary eutectic in the vicinity of the composition $\text{Pt}_{73}\text{B}_{15}\text{Si}_{12}$. The eutectic temperature is close to 973 K, and thus roughly 120 K below the average of the two binary eutectic temperatures. In this regard the Pt-Si-B system resembles the TM-Si-B ternaries (TM=Fe, Co, Ni). Beside the ternary eutectic there seems to be a low melting point trough in the direction of the second binary eutectic point in the Pt-B system, i.e. with reduced platinum and silicon content and increased boron content. However, the ternary alloys discussed here could not be obtained in fully amorphous structure.

4.2. Effect of substitution

As in similar studies on metallic glasses based on the Pt-P and the Pd-P system [5,25,26], substitution of some of the main constituent—platinum in the present case—by transition metals, notably nickel and copper, improves the glass formation ability of these low melting point alloys and they can be obtained in fully glassy state upon melt spinning. Most interestingly, however, Cu not only further lowers the melting point, but also significantly raises T_g , while Ni hardly reduced the liquidus temperature but also raised T_g , albeit less strongly than equal amounts of copper. If one extrapolates to $x=0$, i.e. no substitution of platinum by nickel in Figure 3:4a, one can estimate that the glass transition temperature for the ternary $Pt_{73}B_{15}Si_{12}$ should be around 520 K. In comparison, the alloy $Pt_{54.75}Cu_{18.25}B_{15}Si_{12}$ (corresponding to the alloy at $y=1$ in Figure 3:4b) has a T_g close to 600 K, an increase by 80K, while the liquidus temperature remained virtually unchanged. This highlights that in the search for improved glass forming ability, not only the evolution of the solidification temperature with composition should be considered but also the evolution of the glass transition temperature. It is worthwhile noting in Figure 3:9b however, that the influence of copper on the glass transition temperature is only about 30 K when substituting one quarter of the platinum atoms by copper in the alloys with higher boron and lower silicon content, i.e. from $Pt_{66.6}B_{24}Si_{6.4}Ge_3$ to $Pt_{49.95}Cu_{16.65}B_{24}Si_{6.4}Ge_3$ in which further some of the silicon is substituted by germanium. This difference can be separated in two parts: on the one hand it is clear from Figure 3:5 that increasing the boron-content and concomitantly reducing the silicon-content reduces the glass transition temperature for a fixed Pt:Cu ratio of 3:1. This reflects the fact that the interaction of boron with copper is probably weaker than the strong interaction of silicon with copper. On the other hand, replacing silicon by germanium further reduces the glass transition temperature, which would suggest also weaker interactions between copper and germanium than copper and silicon.

It is however worth noting that, if extrapolated to no copper substitution, T_g of the alloy $Pt_{66.6}B_{24}Si_{6.4}Ge_3$ would be around 545 K, i.e. 25 K higher than for $Pt_{73}B_{15}Si_{12}$. Such a trend to higher glass transition temperature with increased metalloid content has also been observed in Fe-Si-B and Co-Si-B metallic glasses [27].

4.3. Crystallization

Given the TEM and XRD results, i.e. Figures 3:6 and 3:7a-c, the first crystallization peak at lower temperatures corresponds to the formation of α -Pt and B_4Si while the second crystallization peak is due to an unknown complex phase whose characteristics could not be identified with standard XRD. The detailed determination of this phase is beyond the scope of this contribution. The results of high-energy XRD study will be presented in a companion paper. Precipitation of α -Pt and a compound such as B_4Si is similar to primary crystallization in Al-based metallic glasses [28–33], e.g. in $Al_{85}Ce_5Ni_8Co_2$ a simultaneous precipitation of α -Al and metastable $Al_{11}Ce_3$ intermetallic is observed. Similar occurrence of primary crystallization has already been observed in detail in the Fe-Si-B system where α -Fe nanocrystals are initially formed from the amorphous state [20,34–36].

In the case of the Pt-Si-B ternary system and the alloys shown in Figure 3:8, given that the first crystallization peak was attributed to the formation of α -Pt and B_4Si , it would seem natural that by replacing silicon with germanium the formation of the mentioned compounds is rendered more difficult. As seen from Figure 3:8, substitution of roughly a third of silicon with germanium results in the disappearance of the first crystallization peak. As mentioned above, besides increasing T_x , partial replacement of silicon by germanium had the additional effect of rapidly reducing T_g . Both lead to a widening of the super-cooled liquid region, usually an indication of better glass forming ability [23,24]. This observation is contrary to results reported by Estévez and Betancourt [37] for the Fe-Si-B system where substitution of silicon with germanium was found to be detrimental for the $Fe_{80}B_{10}Si_{10-x}Ge_x$ ($X=0-10$) alloy, reducing considerably the glass forming ability and the width of the super-cooled liquid region. These authors attributed the detrimental effect of substituting silicon with germanium on the glass forming ability to the formation of a less dense packed structure due to the larger atomic radius of germanium compared to silicon. This highlights the fact that while some analogies can be drawn between different systems, the details may vary significantly.

4.4. Mechanical properties

From the results reported above it can be concluded that most alloys analyzed here based on the ternary system Pt-B-Si and in particular the alloy $Pt_{49.95}Cu_{16.65}Si_{6.4}Ge_3B_{24}$ exhibit superior hardness and compression strength compared to existing Pt-P-based BMGs

whose hardness values remains typically below 420 HV. However, the compression stress-strain curve exhibits very little plasticity, opposite to the considerable plastic deformation observed in their phosphorous containing platinum-based BMGs [38]. According to Yang et al. [39] the hardness of a metallic glass is directly linked to its glass transition temperature. These authors suggested that both phenomena are facilitated by the collective atomic motion requiring sufficient energy to overcome the cohesive force between atoms, resulting in an increase of free volume. This energy can be in the form of mechanical work in the case of plastic deformation localized in shear bands or heat used to increase the temperature of the body. Both of these forms of energy will cause creation of free volume [40], [41].

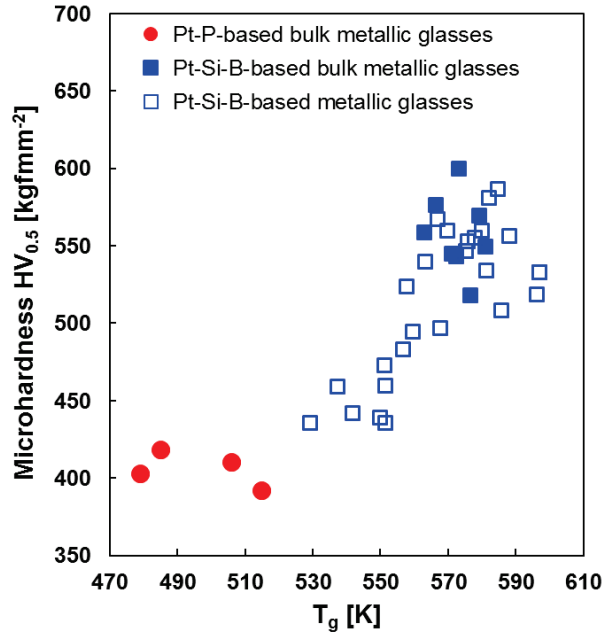


Fig. 3:11 Evolution of the hardness as a function of the glass transition temperature, T_g for samples based on the Pt-Si-B system (squares), and for their equivalents based on the Pt-P system (circles). Open symbols designate metallic glasses with a critical casting diameter smaller than 1 mm.

There is a critical level of free volume beyond which both the glass transition and the shear localization are activated. Upon appearance of both these phenomena atomic mobility is rapidly extended macroscopically. The main difference between the glass transition and the plastic deformation is the distribution of energy in the body. In the case of glass transition the heat covers the whole body of glassy solid whereas upon plastic deformation, mechanical energy is closely confined within the shear band. In both cases the atomic bond-

ing force to overcome is the same and the final status of the matter, i.e. reshuffled atoms, is similar [39]. The large variety of samples with T_g spanning a range from 520 to close to 600 K allows assessing such relationship as well as comparing with other platinum-based metallic glasses. This is done in Fig. 3:11. The data on Pt-P based systems come from Schroers and co-workers [3,5,6,42,43].

There is no clear separation in the data between metallic glasses (i.e. those with a critical diameter smaller than 1 mm) and those that form bulk metallic glasses. As can be seen, the alloys presented here show a consistent trend of increasing hardness with increasing T_g . The higher hardness observed in the alloys in the Pt-Si-B system can hence be connected to the systematically higher glass transition values of the alloys in this system compared to Pt-P-based alloys.

4.5 Critical casting thickness

Analyzing the data in Table 3:2, one can see that the critical diameter increases by and large with increasing ΔT . ΔT values larger than 40 K lead in all cases to critical casting thicknesses > 1 mm and are hence considered as being BMGs. Two out of twelve analyzed samples showed a critical casting thickness larger than 1 mm despite having a ΔT below 40 K. Hence, setting 40 K as a critical ΔT to obtain a BMG in this family of metallic glasses seems to be a good rule of thumb. This value is in the same ballpark as the values reported for phosphorous containing platinum-based BMGs with critical diameter about 1 mm reported Demetriou et al. [6], while higher ΔT values lead to significantly larger critical casting diameters [5]. We further note that most of the BMGs in the family presented here contain germanium, which reflects the strong effect of germanium on ΔT shown in Fig. 3:8.

5. Conclusions

A new family of phosphorous-free Pt-based BMGs was developed in the ternary system of Pt-Si-B. The composition showing the best glass forming ability was found to be $\text{Pt}_{49.95}\text{Cu}_{16.65}\text{Si}_{6.4}\text{Ge}_3\text{B}_{24}$, with a critical casting diameter of 5.3 mm and a super-cooled liquid region of 55 K. The following conclusions can be drawn:

- The ternary system Pt-Si-B contains a low lying ternary eutectic in the vicinity of the composition $\text{Pt}_{73}\text{B}_{15}\text{Si}_{12}$, indications in at.-pct, with a eutectic temperature of around 973 K.

- Similarly low melting points are encountered for compositions starting at the ternary eutectic and going towards the binary eutectic $\text{Pt}_{58}\text{B}_{42}$.
- The solidus temperatures can significantly be lowered by substituting some of the platinum by nickel and, especially, copper.
- The glass transition and crystallization temperatures are strongly affected by the composition. In particular, substituting Pt by Cu raises the glass transition temperature significantly, while substitution of silicon by germanium lowers the glass transition temperature.
- Substitution of some of the silicon by germanium shifts the primary crystallization peak to higher temperatures while the second crystallization peak remains unchanged.
- Primary crystallization of the glassy alloys in the Pt-Si-B system seems very similar to Al-based and Fe-based amorphous alloys. Analogous to Al-based metallic glasses, the crystallization proceeds by precipitation of $\alpha\text{-Pt}$ and B_4Si followed by formation of more complex phases at higher temperatures.

Alloys in the Pt-Si-B system systematically exhibit higher glass transition temperature and concomitantly higher hardness than their Pt-P-based counterparts. A hardness value of 550-580HV_{0.1-0.5} was achieved for the alloy $\text{Pt}_{49.95}\text{Cu}_{16.65}\text{Si}_{6.4}\text{Ge}_3\text{B}_{24}$ in the as-cast state the lower values were obtained for rapidly cooled (melt-spun) samples while the higher values were obtained in suction cast samples of 2 and 5 mm in diameter.

Composition [at.-pct.]	Fig.	State	Proc.	T _g [K]	T _x [K]	T _s [K]	T _i [K]	HV
Pt ₇₅ Si ₁₉ B ₆	2	c	qt	N/A	N/A	990	1134	463
Pt ₇₃ Si ₁₈ B ₉	2	c	qt	N/A	N/A	992	1105	460
Pt ₇₂ Si ₁₅ B ₁₃	2	c	qt	N/A	N/A	977	1096	486
Pt ₇₃ Si ₁₂ B ₁₅	2	c	qt	N/A	N/A	975	1011	470
Pt ₇₁ Si ₁₀ B ₁₉	2	c	qt	N/A	N/A	977	1075	440
Pt ₇₀ Si ₈ B ₂₂	2	c	qt	N/A	N/A	976	1063	435
Pt ₇₁ Si ₅ B ₂₄	2	c	qt	N/A	N/A	975	1084	375
Pt ₇₀ Si ₁₂ B ₁₅ Cu _{3.5}	text	c	qt	N/A	N/A	955	1000	482
Pt ₇₀ Si ₁₂ B ₁₅ Fe _{3.5}	text	c	qt	N/A	N/A	973	1141	541
Pt ₇₀ Si ₁₂ B ₁₅ Co _{3.5}	text	c	qt	N/A	N/A	970	1094	505
Pt _{69.5} Si ₁₂ B ₁₅ Ni _{3.5}	4a	g	ms	529	541	950	1025	436
Pt _{65.7} Si ₁₂ B ₁₅ Ni _{7.3}	4a	pc	ms	537	552	953	983	459
Pt _{62.05} Si ₁₂ B ₁₅ Ni _{10.95}	4a	g	ms	551	562	950	998	436
Pt _{58.4} Si ₁₂ B ₁₅ Ni _{14.6}	4a	pc	ms	558	572	962	993	524
Pt ₅₅ Si ₁₂ B ₁₅ Ni ₁₈	4a	g	ms	568	585	967	1041	497
Pt _{54.75} Si ₁₂ B ₁₅ Cu _{3.65} Ni _{14.6}	4b	g	ms	581	595	975	1008	534
Pt _{54.75} Si ₁₂ B ₁₅ Cu _{7.3} Ni _{10.95}	4b	g	ms	588	603	964	1040	556
Pt _{54.75} Si ₁₂ B ₁₅ Cu _{10.95} Ni _{7.3}	4b	g	ms	592	606	937	1020	N/A
Pt _{54.75} Si ₁₂ B ₁₅ Cu _{14.6} Ni _{3.65}	4b	g	ms	596	611	895	1036	519
Pt _{54.75} Si ₁₂ B ₁₅ Cu _{18.25}	4b	g	ms	597	611	889	1011	533
Pt _{48.75} Si ₉ B ₂₆ Cu _{16.25}	5	g	ms	574	613	877	936	581
Pt _{49.95} Si _{9.4} B ₂₄ Cu _{16.65}	5	g	ms	582	615	876	942	N/A
Pt _{51.08} Si _{9.9} B ₂₂ Cu _{17.02}	5	g	ms	571	611	875	931	N/A
Pt _{52.5} Si _{10.5} B _{19.5} Cu _{17.5}	5	g	ms	581	603	877	951	N/A
Pt _{53.7} Si _{11.1} B _{17.3} Cu _{17.9}	5	g	ms	589	604	891	976	N/A
Pt _{49.95} Si _{9.4} B ₂₄ Cu _{15.65} Ag ₁	6,7	g	ms	581	618	871	930	N/A
Pt _{49.95} Si _{8.9} B ₂₄ Cu _{16.65} Ge _{0.5}	8	g	ms	578	615	874	930	556
Pt _{49.95} Si _{8.4} B ₂₄ Cu _{16.65} Ge ₁	8	g	ms	577	619	870	930	518
Pt _{49.95} Si _{7.9} B ₂₄ Cu _{16.65} Ge _{1.5}	8	g	ms	576	626	865	931	553
Pt _{49.95} Si _{7.4} B ₂₄ Cu _{16.65} Ge ₂	8	g	ms	573	631	858	923	600
Pt _{49.95} Si _{6.9} B ₂₄ Cu _{16.65} Ge _{2.5}	8	g	ms	572	636	855	927	543
Pt _{49.95} Si _{6.4} B ₂₄ Cu _{16.65} Ge ₃	8	g	ms	570	640	848	927	560
Pt _{51.95} Si _{6.9} B ₂₂ Cu _{16.65} Ge _{2.5}	9a	g	ms	566	629	856	935	576

Pt _{53.95} Si _{6.9} B ₂₀ Cu _{16.65} Ge _{2.5}	9a	g	ms	580	615	870	951	560
Pt _{55.95} Si _{6.9} B ₁₈ Cu _{16.65} Ge _{2.5}	9a	g	ms	583	595	936	1015	531
Pt _{57.95} Si _{6.9} B ₁₆ Cu _{16.65} Ge _{2.5}	9a	g	ms	586	586	974	1080	509
Pt _{63.3} Si _{6.4} B ₂₄ Cu _{3.3} Ge ₃	9b	g	ms	550	557	941	1051	439
Pt _{59.99} Si _{6.4} B ₂₄ Cu _{6.61} Ge ₃	9b	g	ms	556	571	879	1047	484
Pt _{56.69} Si _{6.4} B ₂₄ Cu _{9.91} Ge ₃	9b	g	ms	560	591	931	1016	495
Pt _{53.38} Si _{6.4} B ₂₄ Cu _{13.22} Ge ₃	9b	g	ms	563	612	856	986	559
Pt _{49.95} Si _{6.4} B ₂₄ Cu _{16.65} Ge ₃		g	SC 2mm	576	638	846	928	576
Pt _{49.95} Si _{6.4} B ₂₄ Cu _{16.65} Ge ₃		g	SC 5mm	579	634	846	928	570

*for melt spun (ms), suction cast (sc), and quartz tube (qt) samples, hardness measurements were carried out using a load of 10 g, 100 g, and 1000 g, respectively.

Table 3:1 Composition, characteristic temperatures, and microhardness of all samples produced in this work.

Alloy	Used in...	d_c [mm]	ΔT [K]*	T_{rg}
Pt _{55.95} Si _{6.9} B ₁₈ Cu _{16.65} Ge _{2.5}	Fig.9a	1-2	12	0.57
Pt _{59.99} Si _{6.4} B ₂₄ Cu _{6.61} Ge ₃	Fig.9b	<1	15	0.53
Pt _{52.5} Si _{10.5} B _{19.5} Cu _{17.5}	Fig.5	2-5	22	0.61
Pt _{56.69} Si _{6.4} B ₂₄ Cu _{9.91} Ge ₃	Fig.9b	<1	31	0.55
Pt _{49.95} Si _{9.4} B ₂₄ Cu _{16.65}	Fig.5	<1	33	0.62
Pt _{48.75} Si ₉ B ₂₆ Cu _{16.25}	Fig.5	<1	39	0.61
Pt _{51.08} Si _{9.9} B ₂₂ Cu _{17.02}	Fig.5	1-2	40	0.61
Pt _{49.95} Si _{8.4} B ₂₄ Cu _{16.65} Ge ₁	Fig.8	2-5	42	0.62
Pt _{53.38} Si _{6.4} B ₂₄ Cu _{13.22} Ge ₃	Fig.9b	2-5	49	0.57
Pt _{49.95} Si _{7.4} B ₂₄ Cu _{16.65} Ge ₂	Fig.8	2-5	58	0.62
Pt _{51.95} Si _{6.9} B ₂₂ Cu _{16.65} Ge _{2.5}	Fig.9a	2-5	63	0.61
Pt _{49.95} Si _{6.4} B ₂₄ Cu _{16.65} Ge ₃	Fig.8	5.3	70	0.61

* ΔT values measured on melt spun samples

Table 3:2 Critical casting diameters of selected compositions of Table 1.

Acknowledgement

The authors wish to acknowledge financial support for this work by EPFL contract no. 535 627.

References:

- [1] pgm market report may 2015.pdf, <http://www.platinum.matthey.com/documents/new-item/pgm%20market%20reports/pgm%20market%20report%20may%202015.pdf> (accessed May 18, 2016).
- [2] B.T. Biggs, S.S. Taylor, E. van der Lingen, The Hardening of Platinum Alloys for Potential Jewellery Application, *Platin. Met. Rev.* 49 (2005) 2–15. doi:10.1595/147106705X24409.
- [3] J. Schroers, B. Lohwongwatana, W.L. Johnson, A. Peker, Precious bulk metallic glasses for jewelry applications, *Mater. Sci. Eng. -Struct. Mater. Prop. Microstruct. Process.* 449 (2007) 235–238. doi:10.1016/j.mesa.2006.02.301.
- [4] J. Schroers, W.L. Johnson, R. Busch, Crystallization kinetics of the bulk-glass-forming Pd₄₃Ni₁₀Cu₂₇P₂₀ melt, *Appl. Phys. Lett.* 77 (2000) 1158–1160. doi:10.1063/1.1289033.
- [5] J. Schroers, W.L. Johnson, Highly processable bulk metallic glass-forming alloys in the Pt–Co–Ni–Cu–P system, *Appl. Phys. Lett.* 84 (2004) 3666–3668. doi:10.1063/1.1738945.
- [6] M.D. Demetriou, M. Floyd, C. Crewdson, J.P. Schramm, G. Garrett, W.L. Johnson, Liquid-like platinum-rich glasses, *Scr. Mater.* 65 (2011) 799–802. doi:10.1016/j.scriptamat.2011.07.035.
- [7] G. Kumar, H.X. Tang, J. Schroers, Nanomoulding with amorphous metals, *Nature.* 457 (2009) 868–872. doi:10.1038/nature07718.
- [8] Y. Saotome, Y. Fukuda, I. Yamaguchi, A. Inoue, Superplastic nanoforming of optical components of Pt-based metallic glass, *J. Alloys Compd.* 434–435 (2007) 97–101. doi:10.1016/j.jallcom.2006.08.126.
- [9] Alloy Phase Diagram Database, (n.d.). <http://mio.asminternational.org/apd/index.aspx> (accessed September 8, 2016).
- [10] J.H. Harris, M.A. Tenhover, R.K. Grasselli, M.D. Ward, Electrolytic processes employing platinum based amorphous metal alloy oxygen anodes, US4781803 A, 1988. <http://www.google.ch/patents/US4781803> (accessed September 8, 2016).
- [11] M. El-Boragy, M. Ellner, B. Predel, Formation of Transition Metal-rich Glassy Phases in the Systems Ni–As, Pd–As, and Pt–As.[ZUR BILDUNG VON UEBERGANGSMETALLREICHEN GLASARTIGEN PHASEN IN DEN SYSTEMEN Ni–As, Pd–As UND Pt–As.], *ResearchGate.* 74 (1983) 545–548.
- [12] D. Miracle, O. Senkov, Topological criterion for metallic glass formation, *Mater. Sci. Eng. A.* 347 (2003) 50–58. doi:10.1016/S0921-5093(02)00579-8.
- [13] D.B. Miracle, The efficient cluster packing model – An atomic structural model for metallic glasses, *Acta Mater.* 54 (2006) 4317–4336. doi:10.1016/j.actamat.2006.06.002.
- [14] D.B. Miracle, On the universal model for medium-range order in amorphous metal structures, *J. Non-Cryst. Solids.* 317 (2003) 40–44. doi:10.1016/S0022-3093(02)01981-6.
- [15] B. Shen, A. Inoue, Glass Transition Behavior and Mechanical Properties of Ni–Si–B-Based Glassy Alloys, *Mater. Trans.* 44 (2003) 1425–1428. doi:10.2320/matertrans.44.1425.
- [16] T. Zhang, A. Inoue, Bulk Glassy Alloys in (Fe, Co, Ni)–Si–B System, *Mater. Trans.* 42 (2001) 1015–1018. doi:10.2320/matertrans.42.1015.
- [17] A. Inoue, A. Katsuya, K. Amiya, T. Masumoto, Preparation of Amorphous Fe–Si–B and Co–Si–B Alloy Wires by a Melt Extraction Method and Their Mechanical and Magnetic Properties, *Mater. Trans. JIM.* 36 (1995) 802–809. doi:10.2320/matertrans1989.36.802.
- [18] A. Asenjo, D. García, J.M. García, C. Prados, M. Vázquez, Magnetic force microscopy study of dense stripe domains in Fe–B/Co–Si–B multilayers and the evolution under an external applied field, *Phys. Rev. B.* 62 (2000) 6538–6544. doi:10.1103/PhysRevB.62.6538.
- [19] M. Vasquez, E. Ascasibar, A. Hernando, O.V. Nielsen, Co–Si–B and Fe–Co–B amorphous alloys: Induced anisotropy and various magnetic properties, *J. Magn. Magn. Mater.* 66 (1987) 37–44. doi:10.1016/0304-8853(87)90125-9.
- [20] T. Tokunaga, H. Ohtani, M. Hasebe, Thermodynamic evaluation of the phase equilibria and glass-forming ability of the Fe–Si–B system, *Calphad.* 28 (2004) 354–362. doi:10.1016/j.calphad.2004.11.004.

- [21] A. Inoue, T. Aoki, H. Kimura, Effect of B Addition on Extension of Supercooled Liquid Region before Crystallization in Pd–Cu–Si Amorphous Alloys, *Mater. Trans. JIM.* 38 (1997) 175–178. doi:10.2320/matertrans1989.38.175.
- [22] B.B. Sun, Y.B. Wang, J. Wen, H. Yang, M.L. Sui, J.Q. Wang, E. Ma, Artifacts induced in metallic glasses during TEM sample preparation, *Scr. Mater.* 53 (2005) 805–809. doi:10.1016/j.scriptamat.2005.06.007.
- [23] N. Chen, Y. Li, K.-F. Yao, Thermal stability and fragility of Pd–Si binary bulk metallic glasses, *J. Alloys Compd.* 504, Supplement 1 (2010) S211–S214. doi:10.1016/j.jallcom.2010.02.079.
- [24] A. Inoue, High strength bulk amorphous alloys with low critical cooling rates, *Mater Trans JIM.* 36 (1995) 866–875.
- [25] H.S. Chen, J.T. Krause, E. Coleman, Young's modulus and hardness of metallic (Pd1–xNi_x).835Si.165 glasses, *Scr. Metall.* 9 (1975) 787–789. doi:10.1016/0036-9748(75)90241-0.
- [26] H.. Chen, The glass transition temperature in glassy alloys: Effects of atomic sizes and the heats of mixing, *Acta Metall.* 22 (1974) 897–900. doi:10.1016/0001-6160(74)90056-X.
- [27] H.S. Chen, Glassy metals, *Rep. Prog. Phys.* 43 (1980) 353. doi:10.1088/0034-4885/43/4/001.
- [28] R.D. Sá Lisboa, C.S. Kiminami, Primary crystallization in amorphous Al₈₄Ni₈Co₄Y₃Zr₁ alloy, *J. Non-Cryst. Solids.* 304 (2002) 36–43. doi:10.1016/S0022-3093(02)01001-3.
- [29] J.H. Perepezko, R.J. Hebert, W.S. Tong, J. Hamann, H.R. Rösner, G. Wilde, Nanocrystallization Reactions in Amorphous Aluminum Alloys, *Mater. Trans.* 44 (2003) 1982–1992. doi:10.2320/matertrans.44.1982.
- [30] J. Hamann, W.S. Tong, H. Rösner, J.H. Perepezko, G. Wilde, Thermally Controlled Nanocrystallization in Amorphous Al Alloys, *Solid State Phenom.* 101–102 (2005) 259–264. doi:10.4028/www.scientific.net/SSP.101-102.259.
- [31] Á. Révész, G. Heunen, L.K. Varga, S. Suriñach, M.D. Baró, Real time synchrotron studies on amorphous Al₈₅Ce₅Ni₈Co₂ and Al₈₅Y₅Ni₈Co₂ alloys, *J. Alloys Compd.* 368 (2004) 164–168. doi:10.1016/j.jallcom.2003.07.021.
- [32] J.S. Blázquez, H. Dimitrov, J. Latuch, T. Kulik, Crystallization Kinetics of Al–Mn–Ni–(Co,Fe) Alloys, *Solid State Phenom.* 101–102 (2005) 265–268. doi:10.4028/www.scientific.net/SSP.101-102.265.
- [33] A. Inoue, Amorphous, nanoquasicrystalline and nanocrystalline alloys in Al-based systems, *Prog. Mater. Sci.* 43 (1998) 365–520. doi:10.1016/S0079-6425(98)00005-X.
- [34] A.R. Yavari, O. Drbohlav, Thermodynamics and Kinetics of Nanostructure Formation in Soft-Magnetic Nanocrystalline Alloys (Overview), *Mater. Trans. JIM.* 36 (1995) 896–902. doi:10.2320/matertrans1989.36.896.
- [35] J.C. Foley, D.R. Allen, J.H. Perepezko, Strategies for the development of nanocrystalline materials through devitrification, *Mater. Sci. Eng. A.* 226–228 (1997) 569–573. doi:10.1016/S0921-5093(97)80065-2.
- [36] K. Hono, K. Hiraga, Q. Wang, A. Inoue, T. Sakurai, The microstructure evolution of a Fe_{73.5}Si_{13.5}B₉Nb₃Cu₁ nanocrystalline soft magnetic material, *Acta Metall. Mater.* 40 (1992) 2137–2147. doi:10.1016/0956-7151(92)90131-W.
- [37] D.C. Estévez, I. Betancourt, Effect of germanium on the microstructure and the magnetic properties of Fe–B–Si amorphous alloys, *J. Non-Cryst. Solids.* 358 (2012) 1778–1782. doi:10.1016/j.jnoncrysol.2012.05.020.
- [38] J. Schroers, W.L. Johnson, Ductile Bulk Metallic Glass, *Phys. Rev. Lett.* 93 (2004) 255506. doi:10.1103/PhysRevLett.93.255506.
- [39] B. Yang, C.T. Liu, T.G. Nieh, Unified equation for the strength of bulk metallic glasses, *Appl. Phys. Lett.* 88 (2006) 221911. doi:10.1063/1.2206099.
- [40] A.. Argon, Plastic deformation in metallic glasses, *Acta Metall.* 27 (1979) 47–58. doi:10.1016/0001-6160(79)90055-5.
- [41] F. Spaepen, Homogeneous flow of metallic glasses: A free volume perspective, *Scr. Mater.* 54 (2006) 363–367. doi:10.1016/j.scriptamat.2005.09.046.
- [42] J.-Y. Suh, B. Lohwongwatana, C.M. Garland, R.D. Conner, W.L. Johnson, D. Suh, Novel thermo-plastic bonding using a bulk metallic glass solder, *Scr. Mater.* 59 (2008) 903–908. doi:10.1016/j.scriptamat.2008.06.055.
- [43] B.A. Legg, J. Schroers, R. Busch, Thermodynamics, kinetics, and crystallization of Pt_{57.3}Cu_{14.6}Ni_{5.3}P_{22.8} bulk metallic glass, *Acta Mater.* 55 (2007) 1109–1116. doi:10.1016/j.actamat.2006.09.024.

Chapter 4

Effects of partial crystallization in Pt-Si-B-based bulk metallic glasses on glass transition and crystallization of the remaining amorphous matrix

Hamed Kazemi¹, Cyrill Cattin¹, Gilles Hodel^{1,2}, Tatiana Pachova¹ and Ludger Weber^{1,*}

¹Laboratory of Mechanical Metallurgy, Ecole polytechnique fédérale de Lausanne, EPFL, CH-1015 Lausanne, Switzerland

²now at Novelis, Route des laminoirs 15, CH-3960 Sierre, Switzerland

*corresponding author

H. Kazemi, C. Cattin, G. Hodel, T. Pachova, L. Weber, Effects of partial crystallization in Pt-Si-B-based bulk metallic glasses on glass transition and crystallization of the remaining amorphous matrix, Journal of Non-Crystalline Solids. 460 (2017) 66–73. doi:10.1016/j.jnoncrysol.2017.01.025.

Contributions:

Hamed Kazemi: Development of the alloy $\text{Pt}_{49.95}\text{B}_{24}\text{Si}_{6.4}\text{Ge}_3\text{Cu}_{16.65}$, Initial study of the influence of crystallization on the hardness and thermophysical properties, SEM-EDX microscopy, writing the manuscript.

Cyrill Cattin: Supervision, designing of the experiments, revising and correcting of the manuscript.

Gilles Hodel: Investigation of the influence of crystallization on the hardness and compressive strength.

Tatiana Pachova: Investigation of the influence of crystallization on thermophysical and physical properties.

Ludger Weber: Supervision, revising, correcting and approving the manuscript.

Abstract

The influence of partial crystallization on the evolution of the characteristic temperatures, i.e. of the glass transition and the onset of crystallization, the density, and the mechanical properties of the bulk metallic glass $\text{Pt}_{49.95}\text{Si}_{6.4}\text{B}_{24}\text{Ge}_3\text{Cu}_{16.65}$ is investigated. Partial crystallization is introduced by annealing the alloy in a stabilized salt bath at 350°C and for different times and quantified by the residual heat of crystallization as measured in differential scanning calorimetry. It is found that the crystalline regions are enriched in platinum and the remaining amorphous phase is enriched in copper. The evolution of T_g and T_x of the remaining amorphous phase can be quantitatively linked to the degree of copper enrichment of the amorphous phase as crystallization advances. Hardness increases steadily with the degree of crystallization from 570 HV in the as-cast state to 750 HV in the fully crystallized state. In contrast, compressive strength drops steadily with increasing crystallinity due to increasing brittleness.

1. Introduction

Bulk metallic glasses are complex alloys produced by rapid quenching of metallic melts. The potential for glass formation rather than crystallization upon cooling from the melt is limited to a restricted number of alloy compositions obeying in general certain criteria in terms of interactions of the alloying elements, atomic size relations and enhanced stability of the liquid phase compared to solid phases, as e.g. formulated by the “golden rules” of Inoue [1]. The glassy state is however kinetically stabilized and, hence, metastable and can be transformed in a more stable state by crystallization [1]. Besides annealing at temperatures above the glass transition temperature, T_g , other phenomena have been reported to lead to crystallization, namely irradiation [2–4], mechanical deformation [5–10] and dealloying [11].

Bulk metallic glasses exhibit interesting mechanical properties high hardness, high yield strength and a large elastic strain range, making them particularly interesting as elastic energy storage materials as, e.g., in Golf clubs or springs of mechanical watches [12,13]. Their elastic deformation capacity is enhanced both by the increase in yield strength and the reduction in Young’s modulus of the glassy state compared to its crystalline counterpart.

Partial crystallization can be used as a tool to introduce very small crystallites into otherwise homogenous glasses, producing a combination of amorphous matrix with uniformly

distributed crystals [14]. By controlled partial crystallization it is possible to modify the mechanical and physical properties of BMGs. Often partial crystallization leads also to higher ductility since the crystals act as obstacles for the propagation of shear bands which leads to multiplication of the latter and more homogeneous deformation [15–17]. In some glass formers partial crystallization results in a significant increase in hardness, e.g. Al–Ni–Y and Al–Gd–Fe. This is attributed to the formation of the finely distributed α -Al phase during crystallization [18,19]. The same improvement of hardness upon crystallization has also been observed in Fe-TM-Si-B systems (TM: Transition Metal) [14,20]. The mechanical properties of partially crystallized BMGs depend on the size, the composition, the volume fraction and the morphology of the crystalline phases that form from the glassy matrix.

The increase in hardness upon partial crystallization is governed by two phenomena; firstly, a phase mixture or composite effect and, in the event that the crystalline phase has not the same composition as the amorphous phase, secondly, a gradual compositional change of the remaining amorphous phase leading to changes in the matrix properties [21,22]. It has even been shown by Zhong et al. [23] for an $\text{Al}_{86}\text{Ni}_{11.67}\text{Y}_{2.23}$ alloy that the enrichment of nickel and yttrium in the remaining amorphous matrix upon primary crystallization of α -Al nano-phase is the predominant contribution to increased hardness.

The influence of annealing and ensuing partial crystallization has been investigated in precious-metal based BMGs [24,25]. These precious-metal based BMGs (e.g. $\text{Au}_{50}\text{Cu}_{25.5}\text{Ag}_{7.5}\text{Si}_{17}$, $\text{Pt}_{60}\text{Cu}_{16}\text{Co}_2\text{P}_{22}$ and $\text{Pd}_{35}\text{Pt}_{15}\text{Cu}_{30}\text{P}_{20}$) unanimously showed an increase in hardness upon partial crystallization, with the Pt-P-based glassy alloy showing up to 54% of increase compared to the as-cast hardness of 420 HV [24]. Partial crystallization was also found to introduce fragility to $\text{Pt}_{60}\text{Cu}_{16}\text{Co}_2\text{P}_{22}$, observed by crack formation during indentation [25]. Recently, a new Pt-based BMG has been developed in the ternary Pt-Si-B system, namely $\text{Pt}_{49.95}\text{Si}_{6.4}\text{B}_{24}\text{Ge}_3\text{Cu}_{16.65}$ (Chapter 3). The detailed description of its development process is given in the previous chapter. Compared to Pt-P-based glassy alloys, the Pt-Si-B based alloys are significantly harder, exhibiting 570 HV in the as-cast state. For this alloy the process of crystallization, the resulting crystalline phases, and the effect of partial crystallization have not been reported so far.

In the event that the remaining amorphous matrix is enriched in certain alloying elements, the characteristic temperatures of the amorphous phase should also evolve according to the new composition. While the phenomenon of partitioning of alloying elements in the

crystallization of metallic glasses has been studied on various systems [26–30] the effect on the characteristic temperatures have received much less attention so far and, to our knowledge, no attempt has been made to describe this effect quantitatively.

In the present contribution we hence investigate the influence of partial crystallization on the partitioning of alloying elements between the crystalline and the amorphous phase in $\text{Pt}_{49.95}\text{Si}_{6.4}\text{B}_{24}\text{Ge}_3\text{Cu}_{16.65}$ and its effect on the evolution of the characteristic temperatures of glass transition, T_g , and onset of crystallization, T_x . We further report the evolution of density, hardness and compressive strength as a function of the degree of crystallization for this alloy.

2. Experimental methods

2.1. Materials

Ingots were prepared by mixing pure elements (Pt 99.9%, Si 99.99%, B 99.5%, Ni 99.5%, Cu 99.999%, Ge 98.5%) in a quartz tube under argon atmosphere (99.9999%) melted by induction heating. In order to investigate glass formation, glassy ribbons were produced by melt-spinning under argon atmosphere (99.9999%), with a linear speed of the copper disk of 26 m/s. Cast samples in the form of rods were produced in an arc-melter with oxygen-gettered argon atmosphere (99.9999%) by suction casting into copper molds. Samples were melted and turned four times before casting. The mass of the ingot after melting was compared to the sum of the melted-in ingredients to verify that the nominal composition was actually obtained. Differences of less than 1 mg were accepted. The oxygen content in the alloys was measured by Inert gas fusion and was found to be consistently inferior to 20 ppm and typically around 8 ppm.

It should be noted that the arc-melter did not allow any direct measurement of the melt temperature before casting and any such measurement would have been affected by the strong temperature gradients present between the face exposed to the plasma and the face in contact with the copper chill. The temperature of the melt before casting might however influence the cooling rate and thus the time necessary to achieve a given degree of crystallization in each individual cast sample can slightly vary.

2.2. Annealing in stabilized salt bath

For controlled crystallization, a thermally stabilized salt bath was used; this was held at 350 ± 1 °C. All further analyses were carried out on a continuously treated set of samples i.e. pieces from as-cast rods were cut, then the whole rod was annealed for a given time, a sample disk was cut from the rod, and the remainder heat treated further, and so on. This made sure that the measured differences came essentially from the differences in heat treatment and not from casting-to-casting differences, cf. above. Indeed, it had been observed previously that the propensity to crystallization would vary slightly from one casting to the next by an amount that was non-negligible compared to the variations introduced by each step of the annealing treatment, cf. insert in Fig. 4:1. For each heat treatment condition at least three samples were prepared for the analyses. Different measures such as T_g , T_x , or density correspond to a mean between the samples for a given treatment time and the vertical error bars represent the standard deviation on those values. The horizontal bars represent the range of the sample's possible crystallinity degree for a given annealing time measured based on three to five samples subjected to the same treatment.

2.3. Characterization techniques

- General sample preparation

The suction-cast rods or parts thereof used in the characterization techniques described below were typically ground with SiC emery paper down to a grit size of F1200 and then polished on a deep cloth (Struers MD-NAP) with 1 μ m diamond paste.

- Structural analysis

The glassy structure of the samples was assessed by X-ray diffraction using an X'pert Philips machine equipped with a Cu K_α source. The working voltage was 40 kV and the current 45 mA. For melt spun ribbons XRD analysis was carried out on both the surface in contact with the copper wheel and the back. For the cast samples analysis was performed on polished cross-sections.

2.3.1. Thermal analysis

Thermo-physical properties were investigated by Differential Scanning Calorimetry (DSC Pegasus 404C Netzsch, Germany) under argon (99.9999%) flow, with a heating rate of 10 K/min in alumina crucibles. Glass transition temperatures were measured on the DSC

curves as the inflection point of the step towards the endothermic values. The crystallization temperature was measured by the onset of the exothermic peak upon heating. Solidus and liquidus onset temperatures were both measured on the heating curve.

2.3.2. Scanning electron microscopy (SEM)

Micrographs were made using a FEI XLF30 microscope equipped with an Oxford instruments INCASynergy 350 detector for EDX analysis. The EDX point analyses were carried out with a voltage of 20 kV. Each measurement was carried out 4 times, and the average values are presented.

- Mechanical analysis

Hardness measurements were carried out using a Gnehm FM300 microhardness device with 500 g load. Compression tests were carried out samples of 5 mm diameter and 10 mm height on a Schenk universal testing machine equipped with a 100 kN load-cell. The samples were machined to well-defined geometry. Beside the as-cast samples some samples were annealed in a stabilized salt bath at 350°C for various times to obtain a range of degrees of crystallization. The strain rate was set to 0.02 1/s.

- Density

Density was measured by the Archimedes method on samples with a typical volume of 0.01 cm³. The procedure used lead to a typical uncertainty of 0.05 g/cm³.

3. Experimental results

3.1. Partial crystallization during annealing

The amorphous nature of the as cast samples has been confirmed by XRD for the melt-spun ribbons and the suction-cast rods. Figure 4:1 shows a typical example of a DSC curve of a 2 mm cast rod of alloy Pt_{49.95}Si_{6.4}B₂₄Ge₃Cu_{16.65} in as-cast and partially crystallized state. The ratio of the crystallization enthalpy, i.e. the area under the exothermic peak upon heating in DSC, between the annealed sample, ΔH_x , and the as-cast sample, ΔH_0 , can be used as an indicator of the remaining amorphous volume fraction, 1-X. The volume percentage of crystallized material, X, can then be calculated as

$$X = \frac{\Delta H_0 - \Delta H_x}{\Delta H_0}. \quad (4.1)$$

Due to the lack of precise temperature control in suction casting using the arc-melter, the enthalpy of crystallization was measured for all castings from which samples were used in this research. The enthalpy of crystallization was found to be $40.65 \text{ J/g} \pm 0.25 \text{ J/g}$ hence comforting the use of Eq. (4.1) from one casting to another. Nevertheless, the temperature time history in producing the samples might still have varied slightly, due to the lack of direct temperature control in the arc-melter. Thus, the time necessary to achieve a given degree of crystallization in each individual cast sample was observed to vary slightly. Typical variations in crystallization kinetics from one sample to another of the same composition are depicted in the diagram inserted in Figure 4:1.

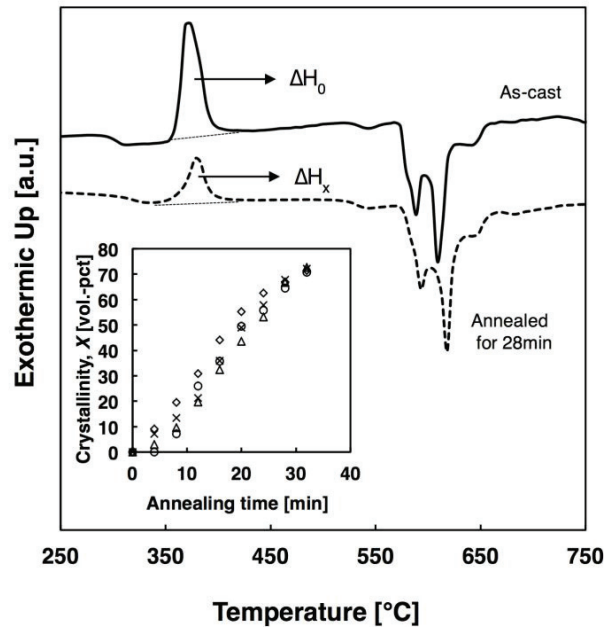


Figure 4:1 The DSC pattern of the as-cast and partially crystallized 2 mm rods of alloy $\text{Pt}_{49.95}\text{Si}_{6.4}\text{B}_{24}\text{Ge}_3\text{Cu}_{16.65}$ produced by arc-melter. The variation of the crystallization time for different samples with the same composition is also shown in the insert.

3.2. Mechanical properties

As can be seen in Figure 4:2, the hardness increases steadily with the degree of crystallinity.

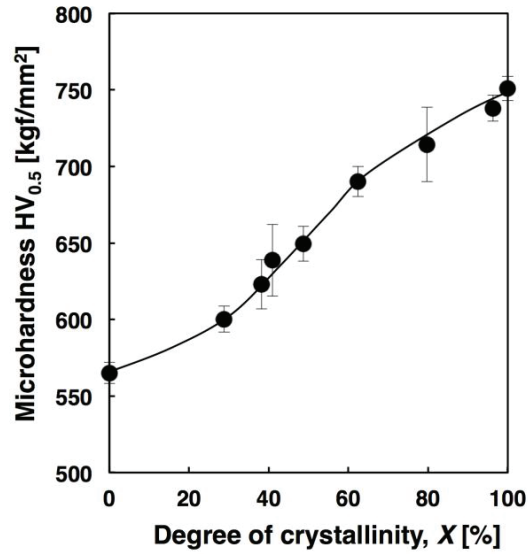


Figure 4:2 Evolution of the hardness as a function of the degree of crystallinity measured on 2 mm rods. Data points are mean values of 5 measurements and vertical error bars correspond to one standard deviation

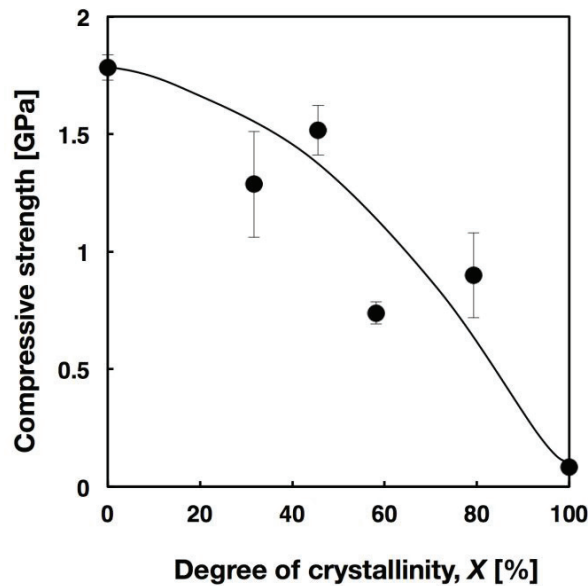


Figure 4:3 Evolution of the compressive strength as a function of the degree of crystallinity measured on cylinders of 5 mm diameter. Each data point corresponds to the mean value of three tests and the vertical error bar is the calculated standard deviation.

On the other hand, Figure 4:3 shows the evolution of the ultimate compressive strength as a function of the degree of crystallization. In contrast to the hardness which keeps going up as crystallinity increases, the compressive strength decreases. We note that the com-

pression curves of the various samples were fairly linear stress-strain diagrams with in essence only elastic deformation

3.3. Physical and thermophysical properties

In Figure 4:4 the evolution of density with the degree of crystallinity is shown. In total the density increases by 1.7% from a fully glassy to fully crystalline state. The significant error bars are due to the fact that the samples had rather low volume and indicate the standard deviation of three independent measurements of density.

Figure 4:5 shows the evolution of the characteristic temperatures of the amorphous phase as a function of the degree of crystallinity. It is interesting to note that the glass transition temperature is quite steadily increasing while the crystallization temperature is slightly decreasing at the beginning and then raising more or less parallel to the glass transition temperature.

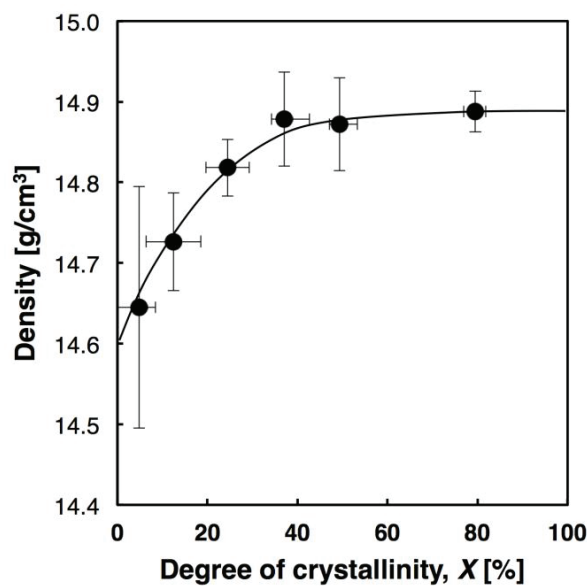


Figure 4:4 Evolution of the density as a function of the degree of crystallinity. The horizontal error bar corresponds to the variation of crystallinity for a given annealing time on the same rod, while the vertical error bar corresponds to the standard deviation calculated over five measurements.

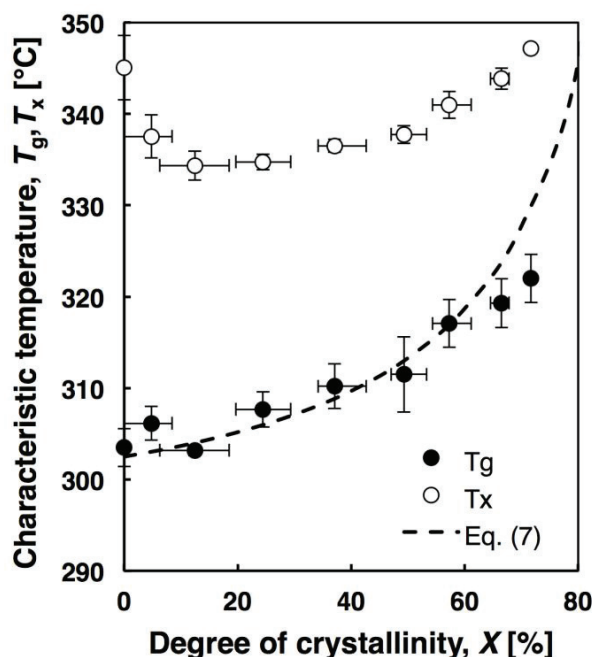


Figure 4:5 Evolution of T_g and T_x as a function of the degree of crystallinity for the partially crystallized samples. The horizontal error bar corresponds to the range of crystallinity for a given annealing time on the same rod, cf. Figure 4:1, while the vertical error bar corresponds to the standard deviation calculated for three measurements.

3.4. Microstructural and compositional analysis

Figure 4:6 shows back-scattered electron microscopy images of the $\text{Pt}_{49.95}\text{Si}_{6.4}\text{B}_{24}\text{Ge}_3\text{Cu}_{16.65}$ alloy at different stages of crystallization. The first observation is that the crystalline phase is richer in heavy atoms, creating a clear contrast in the BSE-mode. As the crystallization advances, the remaining glassy phase gets continuously darker, which indicates that the amorphous phase is enriched in alloying elements at the expense of platinum. The intensity and the brightness of the BSE micrographs are normalized so that the intensity of the gray-white spectrum can be used for a qualitative estimation of the average atomic number of the elements constituting the different phases. For a quantitative investigation of the distribution of the solute atoms during crystallization, EDX elemental mapping of the microstructure at 64% of crystallinity was conducted. These results are shown in Figure 4:7.

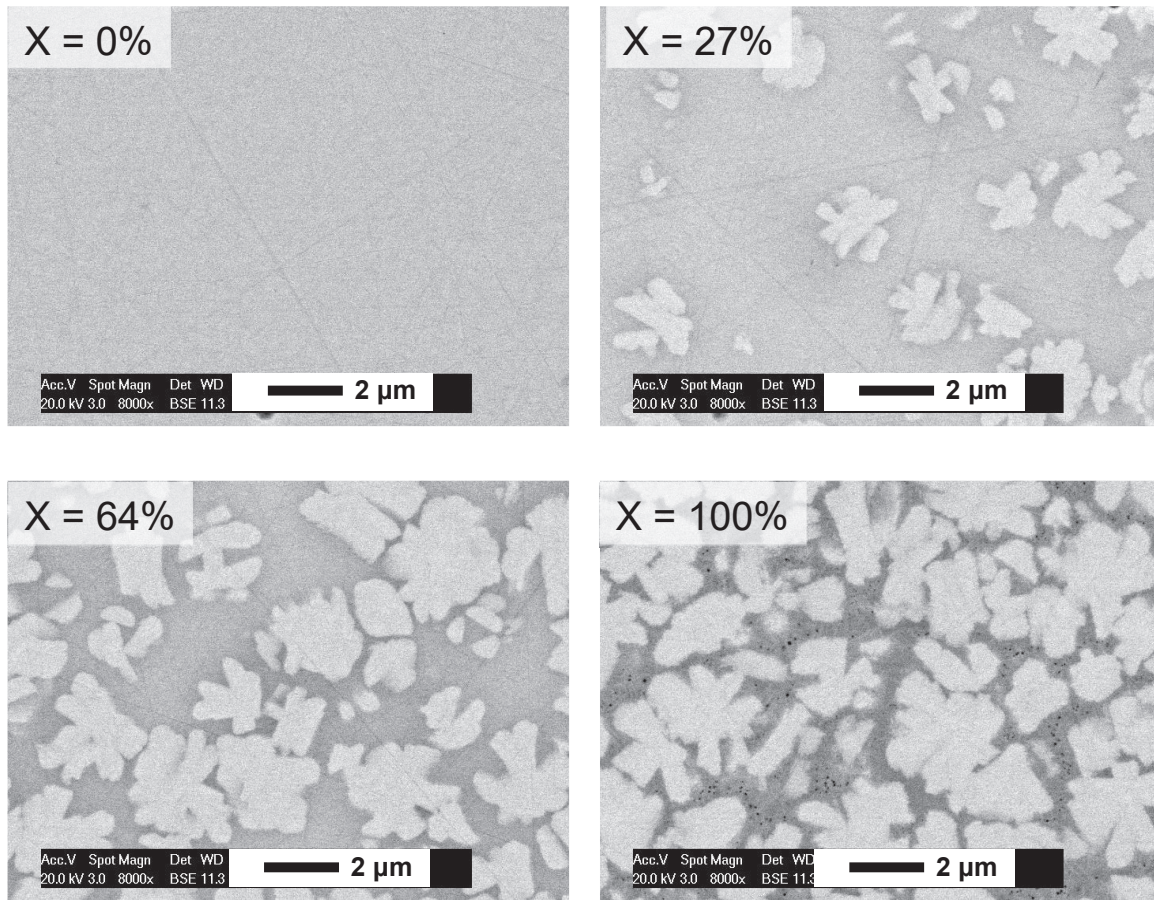


Figure 4:6 Back-scattered electron images of partially crystallized samples prepared from 5 mm rods of alloy $\text{Pt}_{49.95}\text{Si}_{6.4}\text{B}_{24}\text{Ge}_3\text{Cu}_{16.65}$ produced by suction casting in an arc-melter. The images are taken under 20 kV of acceleration voltage and the contrast and brightness is normalized for all images.

The most important contrast can be observed for the inhomogeneous distribution of platinum and copper: the crystalline phases appearing as lighter regions in BSE images (e.g. Figure 4:6) are richer in platinum and poor in copper whereas the remaining glassy regions show a more pronounced presence of copper and are relatively poorer in platinum. No contrast can be observed for the distribution of the alloying elements silicon, boron and germanium between the crystalline and the remaining glassy phase.

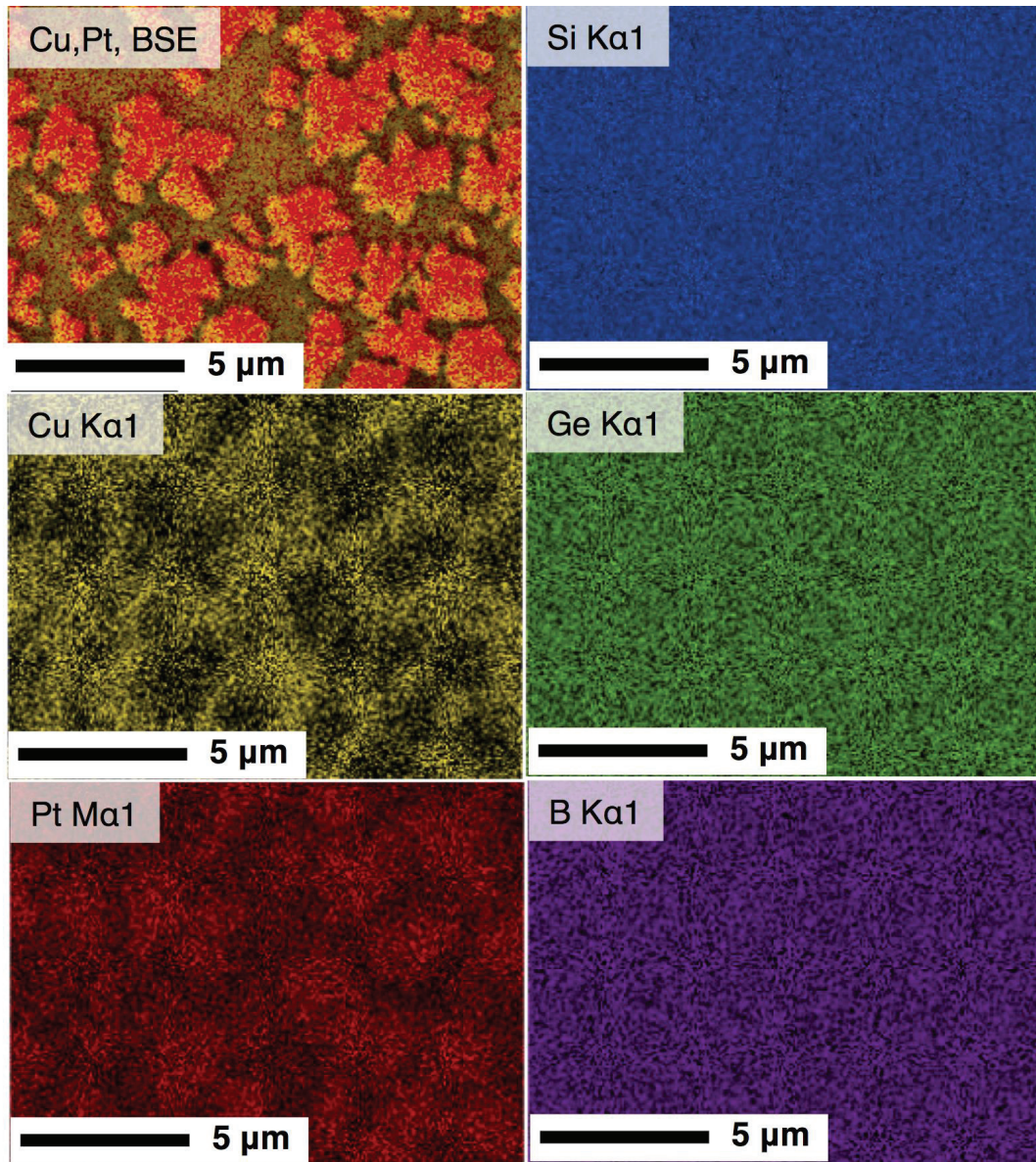


Figure 4:7 EDX elemental mapping of samples prepared from 5 mm rods of alloy $\text{Pt}_{49.95}\text{Si}_{6.4}\text{B}_{24}\text{Ge}_3\text{Cu}_{16.65}$ with 64% of crystallinity. The images are produced under 20 kV of acceleration voltage.

4. Discussion

4.1. Link between residual enthalpy of crystallization and degree of crystallinity

In view of the quite significant elemental partitioning of copper and platinum between the crystallized and the amorphous regions it might be called in question whether the specific heat of crystallization is the same for the first volume fractions of crystallized material as for the last. To validate our hypothesis that ΔH_x is indeed a good measure for the quantity

of remaining amorphous phase, a series of alloys with varying Cu:Pt ratios between 0.33 and 0.67 were produced, the remainder of alloys being kept fixed, and their enthalpy of crystallization was measured, yielding ΔH_0 values of 40.1, 36.5, 38.8, 40.6 J/g for Cu:Pt ratios of 0.33, 0.43, 0.54, 0.67, respectively. The crystallization enthalpy did hence not vary by more than $\pm 5\%$ around the mean value, being slightly lower in the middle of the range of Cu:Pt ratios investigated. This led us to be confident that the degree of crystallinity is indeed well estimated by the residual enthalpy of crystallization, and that we are, if anything, rather overestimating the crystallinity in the beginning and underestimating it towards the end. Furthermore, high-energy X-ray diffraction for detailed structural analysis of the not yet identified complex crystalline phase, which is beyond the scope of the present contribution, gave as a side effect support to the degree of crystallization measured by DSC.

4.2. Evolution of mechanical properties with increasing crystallinity

With the caveat concerning the measurement of the degree of crystallinity discussed above, the microhardness increases steadily with the volume fraction of crystalline phase. With a typical diagonal of the indentation of 35-41 μm the hardness measured is to be taken as a composite value for amorphous phase containing crystalline particles. Such composites, in cases where the phase contrast between the two phases is rather small, do often behave not far from the rule of mixture, i.e. they show a fairly linear transition between the two values characterizing the two phases. Considering that the contiguity of the phases changes from amorphous matrix with crystalline inclusions to crystalline network with amorphous islands as crystallization proceeds, a slightly sigmoidal evolution as experimentally observed can be rationalized.

Our data are in general agreement with effects of crystallization reported for Al-based [14,18,19,23,31], Zr-based [16,17,32–34], Au-based, Pd-based and finally Pt-P-based alloys [24,25]. The increase in the hardness can be attributed to two concomitant phenomena; firstly, to the formation of crystalline phases with higher hardness, and secondly, to the continuous evolution of the composition of the remaining amorphous phase.

It is at first sight surprising that the evolution of the compressive strength with crystallinity is exactly opposite to that of the microhardness. This is rationalized by the observation that (partially) crystallized samples are typically significantly more brittle than their amorphous

counterparts. Indeed, as mentioned before the samples show in essence only elastic deformation and break catastrophically once a shear band develops. Hence, the reduced compressive strength is rather an indication for pre-existing defects in combination with a reduced fracture toughness of the crystalline phase that lead to catastrophic failure at reduced compressive stress as the crystalline volume fraction increases. Similar observations of embrittlement upon crystallization have been observed in the Pt-P system by formation of cracks during indentation [24], and in $\text{Zr}_{57}\text{Cu}_{20}\text{Al}_{10}\text{Ni}_8\text{Ti}_5$ [35]. In these alloys, when crystals form from the amorphous phase they are well dispersed and might even act as obstacles against the advance of shear bands, which is one of the mechanisms responsible for the improvement of the toughness and ductility upon partial crystallization [36]. Yet by the increase in their volume fraction, crystals percolate resulting in a rapid drop in the toughness and compressive strength [37]. In the alloy studied here, no improvement in strength nor in toughness due to crystallization has been observed. Rather, the compression strength is already reduced at a degree of crystallinity as low as 27% and continues to decrease as crystallinity increases. This does not mean that at very low degrees of crystallinity there might not be a small increase in strength and/or toughness. We simply do not have any experimental evidence for this at this time.

4.3. Density change upon crystallization

The change in density from the fully amorphous to the fully crystalline state was found to be on the order of 1.7%. This is significantly less than what is typical for pure metals, but rather high for a metallic glass. Indeed, typical BMGs exhibit density changes from 0.5 to 1.5% [38]. It is also further observed that the density does not increase proportionally with the volume fraction of crystalline phase, cf. Figure 4:4. This can be rationalized by the significant partitioning of alloying elements, in particular copper and platinum as shown in Figure 4:7. The continuous enrichment of copper in the residual amorphous phase may lead to an amorphous phase that has significantly lower shrinkage than the amorphous phase of nominal (and initial) composition. A detailed understanding on how the glass characteristics are affected by the copper and platinum content is hence required and discussed in the following.

4.4. Local compositional variation upon crystallization

As was clearly shown in Figures 4:6 and 4:7, crystallization leads to a partitioning of the constituting elements between the crystalline and the amorphous phase. Interestingly, it is not the light and small elements that seem to partition but rather the large and heavy ones, i.e. platinum and copper. The main shortcoming in elemental mapping by EDX is the inherent difficulty in quantitatively mapping light elements such as boron, and for this element the partitioning cannot be quantified by EDX. As a corollary, atomic concentrations from point analysis will always be summed up to 100 per cent by the EDX system with significant uncertainty due to the inaccurate quantification of the light elements, particularly boron. Hence, the concentrations of copper and platinum as determined by EDX cannot be taken at their face value. However, the ratio of atomic concentrations of copper and platinum should be rather precise (the ZAF correction due to boron should not affect the signals of those elements).

This was verified with a series of four glassy alloys covering a range of Cu:Pt ratio of 0.33 to 0.67 for which the measured Cu:Pt ratio was within a few percent of the nominal value. The range was chosen such that the lowest Cu:Pt ratio i.e. 0.33 corresponded to the base alloy, while the highest Cu:Pt ratio of 0.67 was set to yield about a similar increase in T_g , presumed to be due to the Cu-partitioning, as observed in the partially crystallized samples, cf. Figure 4:5. For the following discussion we define the Cu:Pt atomic concentration ratio as ξ . To evaluate the Cu-enrichment at different stages of partial crystallization, EDX point analysis has been carried out under 20 kV voltage for locally measuring ξ in the remaining amorphous phase as well as in the crystalline regions. EDX point analysis was carried out on the same samples used for the elemental mapping, cf. Figures 4:6 and 4:7. The result of the EDX point analysis is shown in Figure 4:8,

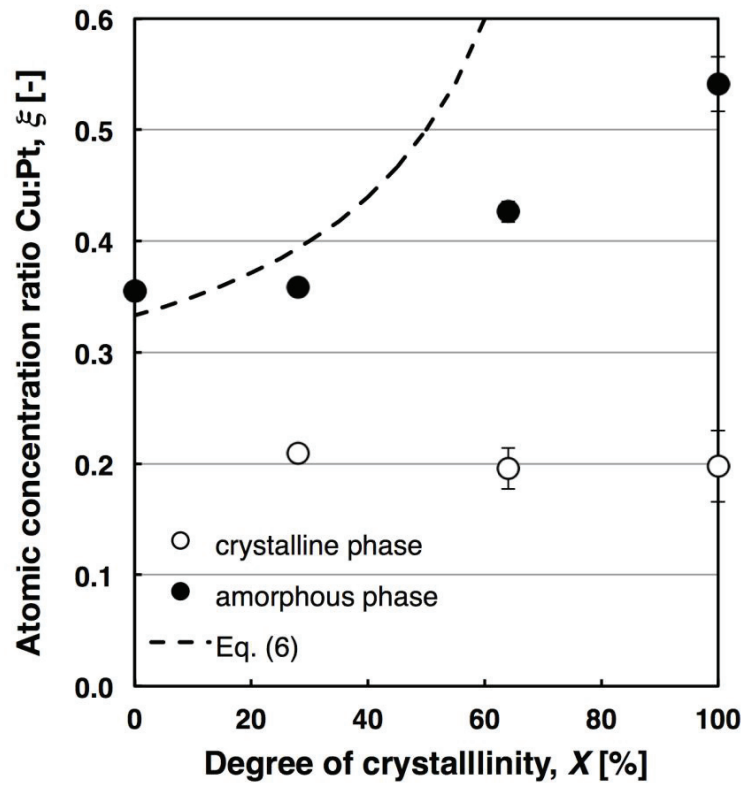


Figure 4:8 Evolution of Cu:Pt measured by EDX point analysis on crystalline and glassy regions. Each point corresponds to the mean value calculated for four measurements under 20 kV of acceleration voltage. The point of the amorphous phase at 100% crystallinity is measured at places in the middle between the visible crystallites

In Figure 4:8 each data point is the average of four point measurements. As it can be seen, partial crystallization increasingly enriches the remaining amorphous phase in copper, while the crystalline phase with lower copper content maintains almost a constant ξ -value. The initial Cu:Pt ratio measured for the amorphous alloy in Figure 9 is slightly higher than the nominal composition of the alloy ($\xi = 1/3$ in $\text{Pt}_{49.95}\text{Si}_{6.4}\text{B}_{24}\text{Ge}_3\text{Cu}_{16.65}$).

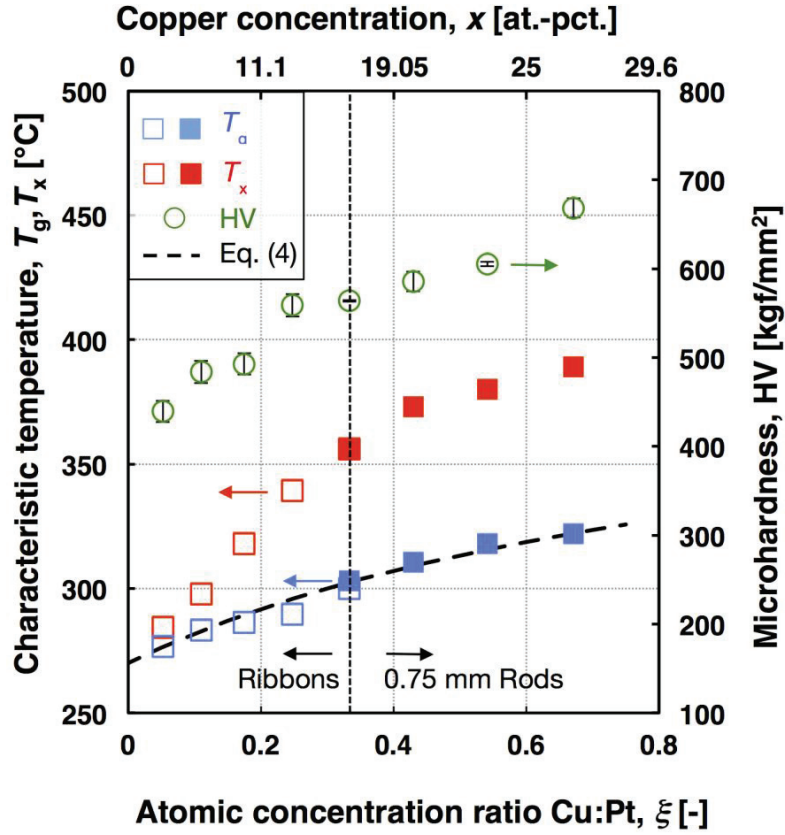


Figure 4:9 Evolution of T_g and T_x as a function of the Cu:Pt-ratio in alloys with the general formula $\text{Pt}_{66.6-x}\text{Si}_{6.4}\text{B}_{24}\text{Ge}_3\text{Cu}_x$. The empty data points are measurements done on melt-spun ribbons and full data points are measured on 0.75 mm cast rods. The hardness values are shown as round data points and the vertical error bar corresponds to one standard deviation of five measurement. To facilitate readability, the (non-linear) scale of copper concentration, x , as introduced in the general composition formula of the alloy series is also indicated at the top.

4.5. Evolution of the characteristic temperatures, T_g and T_x

The observed evolution of the characteristic temperatures, T_g and T_x of the residual amorphous phases are considered to be linked to the changes in chemical composition of the residual amorphous phase, cf. Figure 4:7. In order to proceed to a quantitative verification, a series of alloys was produced with the general formula $\text{Pt}_{66.6-x}\text{Si}_{6.4}\text{B}_{24}\text{Ge}_3\text{Cu}_x$ for which the characteristic temperatures in the fully amorphous state T_g and T_x were determined. The results of this series are shown in Figure 4:9 as a function of ξ . Note that on the secondary ordinate, the x values of the general composition formula for selected Cu:Pt ratios are indicated as well. It can clearly be seen that the characteristic temperatures increase

with increasing ξ , in qualitative agreement with the hypothesis formulated based on Figures 4:5 and 4:7. To establish the quantitative confirmation we note that the glass transition temperature of the series shown in Figure 4:9 can be approximated as a function of the copper concentration, x_{Cu}^a , by

$$T_g [^{\circ}C] = 270 + 1.95x_{Cu}^a \quad (4.2)$$

Under the assumption that the sum of the atomic concentrations of copper and platinum remains stable at 66.6 at.-pct (in other words that there is no change in concentration in the metalloid content as suggested by the elemental mapping in Figure 4:7), we can express the copper concentration as a function of ξ as

$$x_{Cu}^a = \frac{66.6\xi}{(1+\xi)} \quad (4.3)$$

and, hence,

$$T_g [^{\circ}C] = 270 + 1.95 \frac{66.6\xi}{(1+\xi)}. \quad (4.4)$$

The values corresponding to Eq. (4.4) are indicated by the dashed line in Figure 4:9. With the result from Figure 4:8, i.e. that ξ is roughly constant at around 0.2 in the crystalline phase, i.e., $x_{Cu}^c = 11.1$ at.-pct., and again assuming that the atomic concentrations of copper and platinum sum up to 66.6 at.-pct., we can predict the evolution of the copper concentration in the residual amorphous phase, x_{Cu}^a , and the Cu:Pt ratio in the amorphous phase, ξ^a , as

$$x_{Cu}^a [\text{at.-pct}] = \frac{x_{Cu}^{\text{tot}} - x_{Cu}^c X}{(1-X)} = \frac{16.65 - 11.1X}{(1-X)} \quad (4.5)$$

and

$$\xi^a = \frac{x_{Cu}^a}{(1-x_{Cu}^a)} \quad (4.6)$$

The predictions of Eq. (4.6) are shown as dashed line in Figure 4:8. It seems that Eq. (4.6) overestimates the enrichment of copper in the amorphous phase. However, as the copper is likely not distributed completely homogeneously in the remaining amorphous phase, the

measurements taken far from the moving crystallization interfaces may indeed be lower than the average in the amorphous phase. Secondly, especially at high levels of crystallization it is very difficult to find a spot that is larger than the interaction volume of the EDX system in the amorphous matrix, let alone to be sure that the subsurface volume is fully amorphous. Hence, there are good reasons why the measured copper concentration in the amorphous phase is less than what would be predicted by Eq. (4.6).

The combination of Eqs. (4.2) and (4.5) leads to a prediction of the evolution of T_g as a function of the degree of crystallinity:

$$T_g [^{\circ}\text{C}] = 270 + 1.95 \frac{16.65 - 11.1X}{(1 - X)} \quad (4.7)$$

which is also shown as dashed line in Figure 4:5. As the predictions of Eq. (4.7) are in good agreement with the observed evolution of the glass transition temperature, the rationalization provided, i.e. that the changes in T_g are due to copper enrichment in the remaining amorphous phase, is not only qualitatively but also quantitatively satisfactory.

In closing, we note that while the effects of crystallization on physical and mechanical properties have been described in some detail, the nature of the crystalline phase proved to be rather complicated and had to be determined by synchrotron X-ray diffraction. A detailed account of this characterization will be given elsewhere.

5. Conclusion

The influence of partial crystallization on thermophysical and mechanical properties of the alloy $\text{Pt}_{49.95}\text{Si}_{6.4}\text{B}_{24}\text{Ge}_3\text{Cu}_{16.65}$ was evaluated. The following conclusions can be drawn:

- The hardness increased steadily from 570 to 750 HV with degree of crystallinity while the compressive strength decreased due to reduced toughness with increasing crystallinity.
- The glass transition temperature of the remaining amorphous matrix increased from 302 to 322°C with increasing degree of crystallinity.
- The crystals formed at first are somewhat depleted in copper and enriched in platinum while EDX mapping did not show any significant redistribution of the other alloying elements.

- The evolution in glass transition temperature of the remaining amorphous matrix can be quantitatively rationalized by the change in Cu:Pt ratio in the amorphous phase as crystallization advances.

Acknowledgements

The authors wish to acknowledge financial support for this work by EPFL contract no. 535 627.

References:

- [1] C. Suryanarayana, A. Inoue, *Bulk Metallic Glasses*, CRC Press, 2010.
- [2] T. Nagase, T. Sanda, A. Nino, W. Qin, H. Yasuda, H. Mori, Y. Umakoshi, J.A. Szpunar, MeV electron irradiation induced crystallization in metallic glasses: Atomic structure, crystallization mechanism and stability of an amorphous phase under the irradiation, *J. Non-Cryst. Solids*. 358 (2012) 502–518. doi:10.1016/j.jnoncrysol.2011.11.010.
- [3] T. Nagase, Y. Umakoshi, Temperature dependence in density-fluctuation-induced crystallization in metallic glass by MeV electron irradiation, *Intermetallics*. 18 (2010) 1803–1808. doi:10.1016/j.intermet.2010.02.044.
- [4] T. Nagase, T. Hosokawa, Y. Umakoshi, Temperature dependence of MeV-electron-irradiation-induced nanocrystallization in Zr–Pt metallic glass, *Intermetallics*. 18 (2010) 767–772. doi:10.1016/j.intermet.2009.12.003.
- [5] Z. Yan, Y. Hu, K. Song, F. Dai, J. He, J. Eckert, Vickers-indentation-induced crystallization in a metallic glass, *Appl. Phys. Lett.* 106 (2015) 101909. doi:10.1063/1.4915109.
- [6] Z. Yan, K. Song, Y. Hu, F. Dai, Z. Chu, J. Eckert, Localized crystallization in shear bands of a metallic glass, *Sci. Rep.* 6 (2016) 19358. doi:10.1038/srep19358.
- [7] M.C. Gao, R.E. Hackenberg, G.J. Shiflet, Deformation-Induced Nanocrystal Precipitation in Al-Base Metallic Glasses, *Mater. Trans.* 42 (2001) 1741–1747. doi:10.2320/matertrans.42.1741.
- [8] J.-J. Kim, Y. Choi, S. Suresh, A.S. Argon, Nanocrystallization During Nanoindentation of a Bulk Amorphous Metal Alloy at Room Temperature, *Science*. 295 (2002) 654–657. doi:10.1126/science.1067453.
- [9] N. Boucharat, R. Hebert, H. Rösner, R. Valiev, G. Wilde, Nanocrystallization of amorphous Al₈₈Y₇Fe₅ alloy induced by plastic deformation, *Scr. Mater.* 53 (2005) 823–828. doi:10.1016/j.scriptamat.2005.06.004.
- [10] B. Lohwongwatana, J. Schroers, W.L. Johnson, Strain Rate Induced Crystallization in Bulk Metallic Glass-Forming Liquid, *Phys. Rev. Lett.* 96 (2006) 75503. doi:10.1103/PhysRevLett.96.075503.
- [11] P. Rizzi, F. Scaglione, L. Battezzati, Nanoporous gold by dealloying of an amorphous precursor, *J. Alloys Compd.* 586, Supplement 1 (2014) S117–S120. doi:10.1016/j.jallcom.2012.11.029.
- [12] M.F. Ashby, A.L. Greer, Metallic glasses as structural materials, *Scr. Mater.* 54 (2006) 321–326. doi:10.1016/j.scriptamat.2005.09.051.
- [13] E. Axinte, Metallic glasses from “alchemy” to pure science: Present and future of design, processing and applications of glassy metals, *Mater. Des.* 35 (2012) 518–556. doi:10.1016/j.matdes.2011.09.028.
- [14] K. Lu, Nanocrystalline metals crystallized from amorphous solids: nanocrystallization, structure, and properties, *Mater. Sci. Eng. R Rep.* 16 (1996) 161–221. doi:10.1016/0927-796X(95)00187-5.
- [15] C. Fan, A. Inoue, Ductility of bulk nanocrystalline composites and metallic glasses at room temperature, *Appl. Phys. Lett.* 77 (2000) 46–48. doi:10.1063/1.126872.
- [16] C. Fan, C. Li, A. Inoue, V. Haas, Deformation behavior of Zr-based bulk nanocrystalline amorphous alloys, *Phys. Rev. B*. 61 (2000) R3761–R3763. doi:10.1103/PhysRevB.61.R3761.
- [17] D.V. Louzguine-Luzgin, G.Q. Xie, S. Gonzales, J.Q. Wang, K. Nakayama, J.H. Perepezko, A. Inoue, Nano-crystallization behavior of Zr–Cu–Al bulk glass-forming alloy, *J. Non-Cryst. Solids*. 358 (2012) 145–149. doi:10.1016/j.jnoncrysol.2011.08.026.

- [18] H. Chen, Y. He, G.J. Shiflet, S.J. Poon, Mechanical properties of partially crystallized aluminum based metallic glasses, *Scr. Metall. Mater.* 25 (1991) 1421–1424. doi:10.1016/0956-716X(91)90426-2.
- [19] Y.-H. Kim, A. Inoue, T. Masumoto, Ultrahigh Tensile Strengths of Al₈₈Y₂Ni₉M₁ (M=Mn or Fe) Amorphous Alloys Containing Finely Dispersed fcc-Al Particles, *Mater. Trans. JIM.* 31 (1990) 747–749. doi:10.2320/matertrans1989.31.747.
- [20] X.D. Liu, J.T. Wang, Z.Q. Hu, B.Z. Ding, Structure and properties of Fe-based nanocrystalline alloys containing a small amount of transition elements, *Mater. Sci. Eng. A.* 169 (1993) L17–L19. doi:10.1016/0921-5093(93)90616-M.
- [21] J. Eckert, J. Das, S. Pauly, C. Duhamel, Mechanical properties of bulk metallic glasses and composites, *J. Mater. Res.* 22 (2007) 285–301. doi:10.1557/jmr.2007.0050.
- [22] A.L. Greer, Partially or fully devitrified alloys for mechanical properties, *Mater. Sci. Eng. A.* 304–306 (2001) 68–72. doi:10.1016/S0921-5093(00)01449-0.
- [23] Z.C. Zhong, X.Y. Jiang, A.L. Greer, Ninth International Conference on Rapidly Quenched and Metastable Materials Micro structure and hardening of Al-based nanophase composites, *Mater. Sci. Eng. A.* 226 (1997) 531–535. doi:10.1016/S0921-5093(97)80062-7.
- [24] S. Cardinal, J. Qiao, J.M. Pelletier, H. Kato, Bulk metallic glasses based on precious metals: Thermal treatments and mechanical properties, *Intermetallics.* 63 (2015) 73–79. doi:10.1016/j.intermet.2015.04.003.
- [25] S. Cardinal, J.M. Pelletier, M. Eisenbart, U.E. Klotz, Influence of crystallinity on thermo-process ability and mechanical properties in a Au-based bulk metallic glass, *Mater. Sci. Eng. A.* 660 (2016) 158–165. doi:10.1016/j.msea.2016.02.078.
- [26] D.R. Allen, J.C. Foley, J.H. Perepezko, Nanocrystal development during primary crystallization of amorphous alloys, *Acta Mater.* 46 (1998) 431–440. doi:10.1016/S1359-6454(97)00279-6.
- [27] K.F. Kelton, T.K. Croat, A.K. Gangopadhyay, L.-Q. Xing, A.L. Greer, M. Weyland, X. Li, K. Rajan, Mechanisms for nanocrystal formation in metallic glasses, *J. Non-Cryst. Solids.* 317 (2003) 71–77. doi:10.1016/S0022-3093(02)02004-5.
- [28] K. Hono, D.H. Ping, M. Ohnuma, H. Onodera, Cu clustering and Si partitioning in the early crystallization stage of an Fe_{73.5}Si_{13.5}B₉Nb₃Cu₁ amorphous alloy, *Acta Mater.* 47 (1999) 997–1006. doi:10.1016/S1359-6454(98)00392-9.
- [29] K. Kajiwarra, M. Ohnuma, T. Ohkubo, D.H. Ping, K. Hono, APFIM/TEM/SAXS studies of early stage crystallization of a Zr_{52.5}Cu_{17.9}Ni_{14.6}Al₁₀Ti₅ metallic glass, *Mater. Sci. Eng. A.* 375–377 (2004) 738–743. doi:10.1016/j.msea.2003.10.087.
- [30] Y. Zhang, K. Hono, A. Inoue, T. Sakurai, APFIM studies of nanocrystalline microstructural evolution in Fe-Zr-B(-Cu) amorphous alloys, *Mater. Sci. Eng. A.* 217 (1996) 407–413. doi:10.1016/S0921-5093(96)10285-9.
- [31] X.Y. Jiang, Z.C. Zhong, A.L. Greer, Ninth International Conference on Rapidly Quenched and Metastable Materials Particle-size effects in primary crystallization of amorphous Al-Ni-Y alloys, *Mater. Sci. Eng. A.* 226 (1997) 789–793. doi:10.1016/S0921-5093(96)10732-2.
- [32] G. Kumar, D. Rector, R.D. Conner, J. Schroers, Embrittlement of Zr-based bulk metallic glasses, *Acta Mater.* 57 (2009) 3572–3583. doi:10.1016/j.actamat.2009.04.016.
- [33] S. Xie, E.P. George, Hardness and shear band evolution in bulk metallic glasses after plastic deformation and annealing, *Acta Mater.* 56 (2008) 5202–5213. doi:10.1016/j.actamat.2008.07.009.
- [34] G. Wang, J. Shen, Q.H. Qin, J.F. Sun, Z.H. Stachurski, B.D. Zhou, Investigation of deformation behavior of Zr-Ti-Ni-Cu-Be bulk metallic glass containing nanocrystals, *J. Mater. Sci.* 40 (2005) 4561–4569. doi:10.1007/s10853-005-3081-6.
- [35] L.Q. Xing, C. Bertrand, J.-P. Dallas, M. Cornet, Nanocrystal evolution in bulk amorphous Zr₅₇Cu₂₀Al₁₀Ni₈Ti₅ alloy and its mechanical properties, *Mater. Sci. Eng. A.* 241 (1998) 216–225. doi:10.1016/S0921-5093(97)00489-9.
- [36] C. Fan, C. Li, A. Inoue, V. Haas, Deformation behavior of Zr-based bulk nanocrystalline amorphous alloys, *Phys. Rev. B.* 61 (2000) R3761–R3763. doi:10.1103/PhysRevB.61.R3761.
- [37] S. Gravier, L. Charleux, A. Mussi, J.J. Blandin, P. Donnadieu, M. Verdier, Mechanical behaviour of nanocomposites derived from zirconium based bulk amorphous alloys, *J. Alloys Compd.* 434–435 (2007) 79–83. doi:10.1016/j.jallcom.2006.08.113.
- [38] Z. Zhang, L. Xia, R.J. Wang, B.C. Wei, M.X. Pan, W.H. Wang, Structural evolution and property changes in Nd₆₀Al₁₀Fe₂₀Co₁₀ bulk metallic glass during crystallization, *Appl. Phys. Lett.* 81 (2002) 4371–4373. doi:10.1063/1.1525053.

Chapter 5

Synchrotron radiation X-ray diffraction study of crystallization in Pt-Si-B-Ge-Cu bulk metallic glass

(Submitted to Journal of alloys and compounds)

Hamed Kazemi^a, Cyrill Cattin^a, Alla Arakcheeva^{b,c} and Ludger Weber^a,

^a Laboratory of Mechanical Metallurgy, Ecole Polytechnique Fédérale de Lausanne, EPFL,
CH-1015 Lausanne, Switzerland

^b Phase Solutions Ltd., Ch. des Mésanges 7, 1012 Lausanne, Switzerland

^c Laboratory of Nanostructures and Novel Electronic Materials, Ecole Polytechnique
Fédérale de Lausanne, EPFL, CH-1015 Lausanne, Switzerland

Contributions:

Hamed Kazemi: Development of the alloy $\text{Pt}_{49.95}\text{B}_{24}\text{Si}_{6.4}\text{Ge}_3\text{Cu}_{16.65}$, Sample preparation, SEM-EDX microscopy, writing the manuscript.

Cyrill Cattin: Supervision, designing of the experiments, revising and correcting the manuscript.

Alla Arakcheeva: Synchrotron radiation X-ray diffraction analysis.

Ludger Weber: Supervision, revising, correcting and approving the manuscript.

Abstract

The study of crystallization in the amorphous alloy $\text{Pt}_{49.95}\text{Cu}_{16.65}\text{Si}_{6.4}\text{Ge}_3\text{B}_{24}$, using synchrotron radiation x-ray diffraction resulted in identification of a new hexagonal phase with the lattice parameters of $8.973(1) \text{ \AA}$, $c = 2.959(1) \text{ \AA}$. The formation of the main hexagonal crystalline phase is also accompanied by precipitation of $\alpha\text{-Pt}$. Despite exhibiting a clear glass transition and a supercooled liquid region in the DSC analysis, the 5 mm as-cast sample was found to contain short-range ordered domains with the same hexagonal structure in the range of 2-3 nm in size. By increasing the degree of crystallinity, the hexagonal lattice parameter decreased while the size of the ordered domains in the remaining glassy matrix increased to 8 nm. The decrease of the hexagonal unit cell volume is attributed to approaching a densely packed equilibrium state while the apparent decrease in crystallite size according to Scherrer's formula is interpreted as a widening of the peaks due to compositional variation of the crystallized domains caused by the rejection of copper atoms into the glassy matrix resulting in a gradual enrichment of the matrix in copper which eventually also crystallizes.

1. Introduction

Bulk metallic glasses are a rather new family of multicomponent alloys produced by rapid cooling of glass forming liquid into an amorphous solid. Quenched metallic glasses are metastable by nature and tend to crystallize to more energetically favorable crystalline structures [1]. The most direct indication of the thermal stability of a metallic glass is the difference between the glass transition temperature, T_g , where mobility of the atoms sets in, and the temperature of crystallization, T_x , characterizing the ease of nucleation and growth of the more stable crystalline phases. Crystallization in metallic glasses can be categorized in three main groups, polymorphic [2], eutectic, and primary crystallization [3]. In the polymorphic crystallization the composition of the crystalline phases is close to the general composition of the initial amorphous parent phase, while in the eutectic and primary crystallization, the composition of the crystalline phases are different from the matrix. In the case of the latter, crystallization of the glassy matrix results in variation of composition of the remaining glassy phase [4].

In polymorphic and eutectic transformation, the rate of the crystal growth shows only little dependence on time in the very early stages of growth, due to the Gibbs-Thomson effect.

In later stages the crystallites grow at constant speed until they impinge on other crystals. On the other hand, in primary crystallization the process is diffusion-controlled, due to difference in the chemical composition between the parent phase and the crystallites. This slows down the grain growth, and nucleation is dominant leading to crystals that are smaller compared to systems that crystallize through eutectic or polymorphic crystallization [5]. In the case of metallic glasses crystallizing through primary crystallization, annealing above T_g is a rather straightforward method for producing nanostructured materials. On the other hand, crystalline nuclei can also form due to insufficient cooling rate, yet do not lead to fully crystalline material due to slow growth kinetics.

Typical values reported for sizes of nano-crystals formed from the amorphous parent phase upon annealing above T_g are in the range of 5 to 50 nm and a volume fraction of 30-80% corresponding to a mean particle density of 10^{22} - 10^{25} m⁻³ [3]. A well-documented class of metallic glasses crystallizing through primary crystallization are Al-based metallic glasses [6].

According to the “confusion principle”, a term coined by Greer [7], the number of possible crystalline structures (which are energetically roughly equally favorable) increases by adding different atomic species, leading to increased complexity of the system. The crystallization is then more likely to be frustrated upon rapid cooling [7]. This gives rise to formation of complex and often unknown crystalline structures in multicomponent glassy alloys. To analyze such complex crystals at small size, synchrotron X-ray diffraction is a powerful tool [8–13]. Recently, a new platinum-based bulk metallic glass has been developed with the composition of Pt_{49.95}Cu_{16.65}Si_{6.4}Ge₃B₂₄ [14]. This alloy was found to be glassy when suction-cast into a rod of 5mm diameter. It further was found that upon annealing the hardness of this alloy increased from 570 HV in the as-cast state to 750 HV in the crystalline state [15]. Furthermore, backscattered electron microscopy as well as EDX elemental mapping showed that the crystalline phases forming from the glassy structure are relatively richer in platinum and have reduced copper content while the remaining glassy phase is enriched in copper [15]. The other elements did not show any preferential partitioning between the crystalline and the amorphous phase. While this was well quantified for silicon and germanium, the statement has to be taken with a grain of salt in the case of boron that is inherently difficult to quantify by EDX [15].

The aim of this work is therefore to characterize and identify the crystalline phases forming upon crystallizing from the glassy state using synchrotron X-ray diffraction. Such characterization is done on the same 5 mm suction-cast ingots of the alloy $\text{Pt}_{49.95}\text{Cu}_{16.65}\text{Si}_{6.4}\text{Ge}_3\text{B}_{24}$ studied previously [15].

2. Experimental procedures

Ingots of the alloy $\text{Pt}_{49.95}\text{Cu}_{16.65}\text{Si}_{6.4}\text{Ge}_3\text{B}_{24}$ were synthesized by initially melting the highly pure elements (Pt 99.9%, Si 99.99%, B 99.5%, Cu 99.999%, Ge 98.5%) in a quartz tube under argon atmosphere (99.9999%). The ingot was then transferred into an arc-melter. Prior to melting the ingot a zirconium droplet was remelted to getter the residual oxygen in the atmosphere. The ingots were then melted, turned and re-melted four times, and finally suction cast into a 5 mm water-cooled Cu mold. Discs of 2 mm thickness were cut and mirror polished using as final step 1 μm diamond particles. The oxygen content of the ingots was determined using inert-gas analysis (LECO TC, LECO St. Joseph) and was found to be systematically below 20 ppm with a typical value of 8 ppm. For partially crystallizing the samples, annealing was carried out in a stabilized salt bath at 350 °C with a maximum temperature variation of ± 1 °C. The degree of crystallinity was determined by measuring the crystallization enthalpy upon heating using a Differential Scanning Calorimeter (DSC, Pegasus 404C Netzsch, Germany) under argon (99.9999%) flow, with a heating rate of 10 K/min in alumina crucibles. The crystallization enthalpy of the partially crystallized samples, ΔH_x , and that of the as-cast samples, ΔH_0 , was used to calculate as the degree of crystallinity, X by

$$X = \frac{\Delta H_0 - \Delta H_x}{\Delta H_0} \quad (5.1)$$

The experimental synchrotron radiation XRD data were obtained from the Swiss-Norwegian beam-line (Phil Pattison, SNBL/ESRF, Grenoble). Partially crystallized samples analyzed with the full-profile XRD technique were in the shape of discs with the diameter of 5 mm and thickness of 2 mm. The diffraction images were recorded at room temperature using an incident X-ray beam with a cross section of 0.3 mm x 0.3 mm. The incident angle was approximately 4 degrees. The wavelength $\lambda = 0.6776$ Å was selected using a double-crystal monochromator. The PILATUS-2M pixel detector was used for the recording. The area detector image was integrated to produce a one-dimensional powder pat-

tern, showing the diffracted intensity as a function of the scattering angle 2θ . In order to precisely calibrate the sample-to-detector distance, the beam center on the detector, and other parameters such as detector tilt, a pattern from a reference sample of LaB_6 was collected immediately before taking the measurements. The experimental lattice parameter of the LaB_6 cubic unit cell, $a = 4.15496(4) \text{ \AA}$, is equal to the value $a = 4.1549(1) \text{ \AA}$, found by Ning et Fleming [16]. The JANA2006 program package [17] was used for all computations.

3. Results

3.1. Thermal analysis

Figure 5:1 shows the DSC curves of the samples of the alloy $\text{Pt}_{49.95}\text{Cu}_{16.65}\text{Si}_{6.4}\text{Ge}_3\text{B}_{24}$ annealed for various times at 350°C to achieve, respectively, 0%, 27%, 60% and 98% of crystallinity. The influence of crystallinity on the thermophysical and mechanical properties of partially crystallized alloys have been communicated in a companion paper [15].

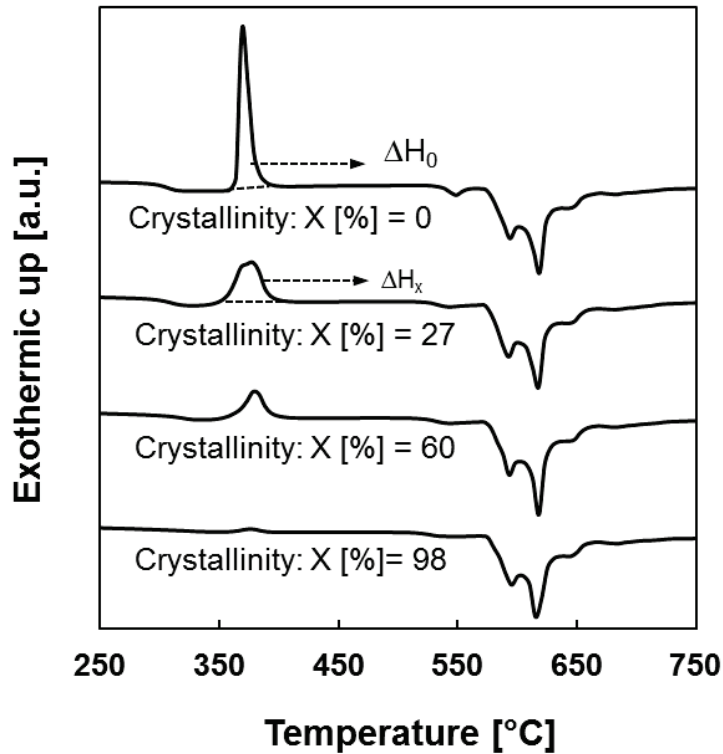


Figure 5:1 The DSC pattern of the as-cast and partially crystallized samples from suction-cast samples of 5 mm diameter of the alloy $\text{Pt}_{49.95}\text{Cu}_{16.65}\text{Si}_{6.4}\text{Ge}_3\text{B}_{24}$. The values of crystallinity are measured by comparing the enthalpy of crystallization of annealed samples to that of as-cast sample.

3.2. XRD analysis of amorphous and partially crystallized samples

The X-ray diffraction patterns obtained for the samples with 0%, 27%, 60% and 98% of crystallinity are shown in Figure 5:2. Their diffraction maxima can be indexed on the basis of hexagonal lattice parameters $a = 8.973 \text{ \AA}$ and $c = 2.959 \text{ \AA}$. This indicates a single phase, whose symmetry is identical at all stages of crystallization. The as-cast sample does not show a regular wide bump but rather a somewhat structured broad diffraction profile typical for nanocrystalline materials. Its two very broad maxima correspond to the strongest maxima of the partially crystallized samples.

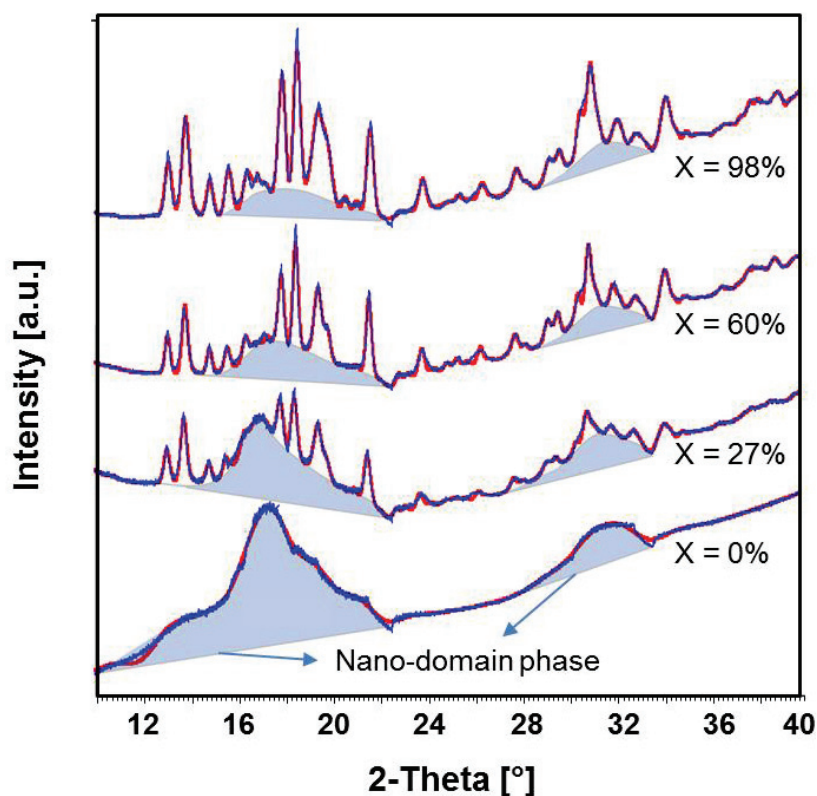


Figure 5:2 The X-ray diffraction patterns of partially crystallized samples of the alloy $\text{Pt}_{49.95}\text{Cu}_{16.65}\text{Si}_{6.4}\text{Ge}_3\text{B}_{24}$ obtained by synchrotron HE-XRD.

3.3. Determination of the structure of the crystalline phase

For determining the atomic positions in the hexagonal crystalline phase, the sample exhibiting the highest degree of crystallinity of 98% was used. The basic structural model was

obtained using the Superflip option of the JANA2006 program package [17]. The final crystal structure has been achieved after many cycles of Rietveld refinement and Fourier summations. The unit cell parameters, space group and the main characteristics of the structure determination and refinement are listed in Table 5:1. The XRD profile and its fit are shown in Figure 5:3. The structure is a close analogue of $\text{Zn}_3\text{Pt}_9\text{B}_{3.86}$ [18] (crystallographic parameters available in [19]). The atomic parameters are listed in Table 5:2. The structure is illustrated in Figure 5:4 as a set of its projections.

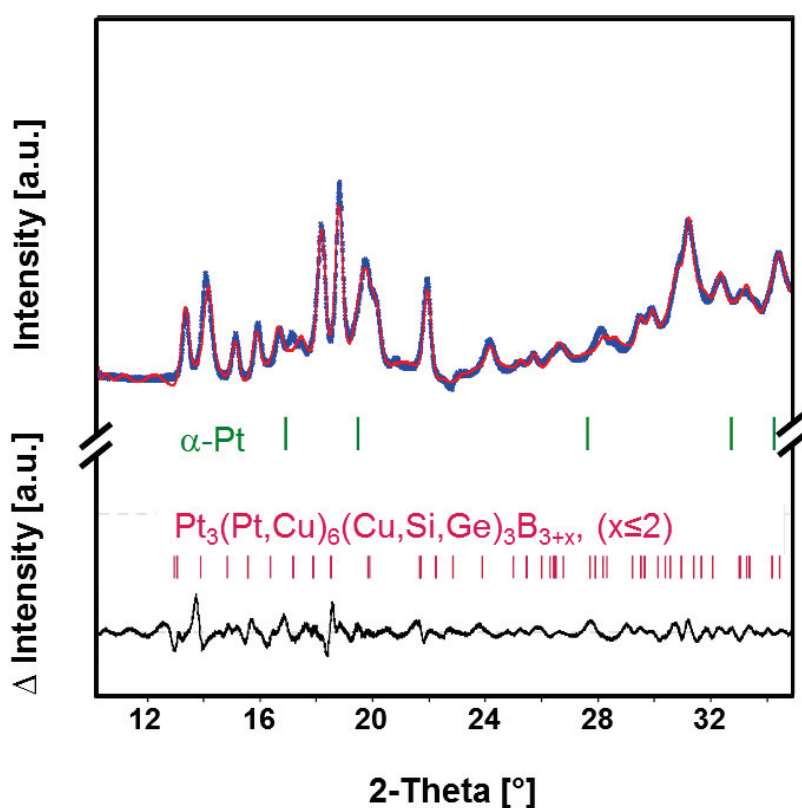


Figure 5:3 The XRD profile of the $\text{Pt}_{49.95}\text{Cu}_{16.65}\text{Si}_{6.4}\text{Ge}_3\text{B}_{24}$ sample with 98% of crystallinity. The blue line and red line, respectively, correspond to experimental values and the calculated profile. Green and red vertical marks indicate the positions of Bragg reflections for $\alpha\text{-Pt}$ and $\text{Pt}_3(\text{Pt,Cu})_6(\text{Cu,Si,Ge})_3\text{B}_{3+x}$ ($x \leq 2$), respectively. The difference profile is shown in the bottom.

The atomic positions of the structure model are well defined. However, the site occupation can only be given approximately. Two positions of platinum atoms have been detected in the model. One of them (Pt in Table 5:2) is certainly fully occupied by platinum atoms. Another one is "lighter", i.e. platinum is partially substituted by a lighter element. Copper

was proposed for that substitution, so that the occupation platinum 83(1)% + copper 17(1)% was refined for this position ((Pt,Cu) in Table 5:2).

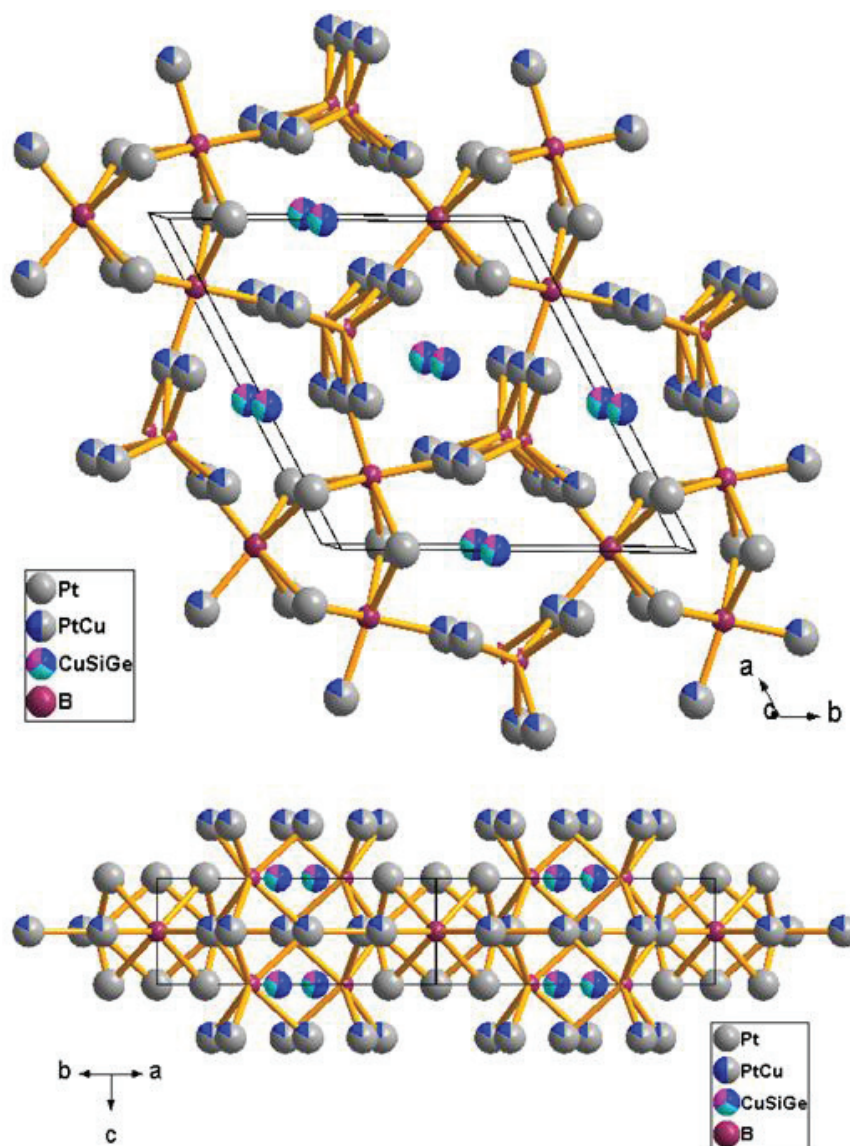


Figure 5:4 The *ab* structure projection of the $\text{Pt}_3(\text{Pt}_{0.833}\text{Cu}_{0.1667})_6(\text{Cu}_{0.54}\text{Si}_{0.3}\text{Ge}_{0.16})_3\text{B}_{3.84}$ model. The fully occupied positions are shown.

Two positions for boron atoms have been detected in the model. One of them (B1 in Table 5:2) is certainly fully occupied by boron atoms. Another one (B2 in Table 5:2) shows a smaller occupation. This is similar to the partial occupation (43(9)%) of this position in the analogous structure of $\text{Zn}_3\text{Pt}_9\text{B}_{3.86}$. A refined value of 42(5)% has been obtained for this

position in the final model. Beyond positions of platinum and boron, only one additional position for copper, silicon, or germanium atoms ((Cu,Si,Ge) in Table 2) is present in the model. The refined composition of this position is Cu 54(1)% + Si 30(1)% + Ge 16(1)% (Table 5:2).

Composition	$\text{Pt}_3(\text{Pt}_{0.833}\text{Cu}_{0.1667})_6(\text{Cu}_{0.54}\text{Si}_{0.3}\text{Ge}_{0.16})_3\text{B}_{3.84}$
	(= $\text{Pt}_{50.5}\text{Cu}_{16.5}\text{Si}_{5.7}\text{Ge}_{3}\text{B}_{24.3}$)
Cell settings	Hexagonal
Space group	<i>P</i>-62<i>m</i> (No. 189)
<i>a</i>, <i>c</i> (Å)	8.973(10), 2.959(4)
Structure analogous	$\text{Zn}_3\text{Pt}_9\text{B}_{3.86}$
Refinement <i>R</i> , <i>wR</i> (observed) (%) <i>R</i> , <i>wR</i> (all) (%) <i>GOF</i> <i>R_P</i> , <i>wR_P</i> (%) Source of atomic scattering factors	2.86, 4.40
	2.86, 4.40
	7.65
	2.26, 3.12
	<i>International Tables for X-ray Crystallography</i> (1992, Vol. C, Tables 4.2.6.8 and 6.1.1.1.) [17]

Table 5:1 Structure characteristics of $\text{Pt}_3(\text{Pt,Cu})_6(\text{Cu,Si,Ge})_3\text{B}_{3+x}$, ($x \leq 2$) and details of the structure refinement in the sample with 98% of crystallinity.

Position	Wyckoff symbol	Occupation*	x	y	z
Pt	3f	Pt 100%	0.171(4)	0	0
(Pt,Cu)	6k	Pt 83(1)% + Cu 17(1)%	0.459(6)	0.264(4)	0.5
(Cu,Si,Ge)	3f	Cu 54(1)% + Si 30(1)% + Ge 16(1)%	0.43(2)	0	0
B1	3g	B 100%	0.79(10)	0	0.5
B2	2c	B 42(5)%	$\frac{1}{3}$	$\frac{2}{3}$	0

Table 2: Atomic parameters in Pt_3 for the main crystalline phase $(\text{Pt,Cu})_6(\text{Cu,Si,Ge})_3\text{B}_{3+x}$, ($x \leq 2$). Space group is *P*-62*m*; lattice parameters: *a* = 8.973(10), *c* = 2.959(4) Å in the sample with crystallinity of 98%.

As a conclusion, the model composition can be given as $\text{Pt}_3(\text{Pt,Cu})_6(\text{Cu,Si,Ge})_3\text{B}_{3+x}$, ($x \leq 2$). The refined composition taking into account the chemical analysis is $\text{Pt}_3(\text{Pt}_{0.83}\text{Cu}_{0.17})_6(\text{Cu}_{0.54}\text{Si}_{0.3}\text{Ge}_{0.16})_3\text{B}_{3.84}$. Expanded to 100 at.-pct this corresponds to $\text{Pt}_{50.5}\text{Cu}_{16.5}\text{Si}_{5.7}\text{Ge}_3\text{B}_{24.3}$, which is fairly close to the nominal composition $\text{Pt}_{49.95}\text{Cu}_{16.65}\text{Si}_{6.4}\text{Ge}_3\text{B}_{24}$

3.4. Evolution of the crystalline average domain size upon crystallization

The hexagonal unit cell parameters $a = 8.973(1) \text{ \AA}$ and $c = 2.959(1) \text{ \AA}$ (Table 5:1) found in the sample with the highest crystallinity (98%) have been taken as the starting ones for fitting the XRD profiles of the samples exhibiting 0%, 27% and 60% crystallinity. Their profiles have been refined on the basis of the Le-Bail decomposition taking into account the crystalline and nano-domain fractions of the hexagonal phase and the α -Pt traces. The contribution of each fraction was estimated by the Rietveld refinement for each sample. The structural model of the same chemical composition was used to fit both the crystalline and nano-domain glassy matrix. The Gaussian function was applied for the profile approximation of the Bragg peaks used for the mean domain size estimation according to Scherrer's formula. The experimental characteristics, i.e., full width at half maximum, $\text{FWHM} = B_{\text{obs}}$, θ angle, along with the instrumental effect, $B_{\text{std}} = 0.098$ of the device, shape factor $K = 0.9$ and the wavelength $\lambda = 0.6776 \text{ \AA}$ are used for the calculation of the mean domain size D :

$$D = \frac{K\lambda}{\frac{\pi}{180}(B_{\text{obs}}^2 - B_{\text{std}}^2)^{1/2} \cos \theta} \quad (5.2)$$

The contribution of the lattice strain to the line broadening is about 5% of B_{obs} in the analyzed samples. This contribution affects the mean size value below the estimation accuracy of 0.5 nm.

Sample crystallinity* [vol.-pct.]	Phase Vol. fractions	Lattice parameters [Å] Unit cell volume, V [Å ³] Crystallographic density, dx [g/cm ³]	Mean size of domains [nm]
98%	MP cryst 83(5)%	$a = 8.973(1)$, $c = 2.959(1)$ $V = 206.3$ $dx = 14.72$	17.6(5)
	MP nano 12(5)%	$a = 9.05(1)$, $c = 3.11(1)$ $V = 220.7$ $dx = 13.77$	8.1(5)
	Pt 5(2)%	$a = 3.970(5)$ $V = 62.7$ $dx = 20.66$	7.1(5)
60%	MP cryst 57(5)%	$a = 8.990(1)$, $c = 2.971(1)$ $V = 208.2$ $dx = 14.603$	27.4(5)
	MP nano 38(5)%	$a = 9.05(1)$, $c = 3.11(1)$ $V = 220.7$ $dx = 13.77$	7.4(5)
	Pt 5(2)%	$a = 3.973(7)$ $V = 62.7$ $dx = 20.66$	10.7(5)
27%	MP cryst 27(5)%	$a = 8.998(2)$, $c = 2.990(1)$ $V = 209.6$ $dx = 14.48$	17.2(5)
	MP nano 68(5)%	$a = 9.05(1)$, $c = 3.11(1)$ $V = 220.7$ $dx = 13.77$	6.4(5)
	Pt 5(2)%	$a = 3.973(7)$ $V = 62.7$ $dx = 20.66$	16.6(5)
As-cast	MP nano	$a = 9.05(1)$, $c = 3.11(1)$; $V = 220.7$ $dx = 13.77$	2-3

* based on DSC measurements

Table 5:3 Details of the mean domain size estimation using reflection (300) for samples exhibiting nominally 0%, 27%, 60% and 98% of crystallinity of the alloy

Pt_{49.95}Cu_{16.65}Si_{6.4}Ge₃B₂₄. LaB₆ is used as a standard for calculating the domain sizes according to Eq. (5.2).

The log-normal distribution function was used for the estimation of the domain size distribution:

$$F(x) = \frac{1}{x\sigma\sqrt{2\pi}} \exp\left(\frac{-\left(\ln\left(\frac{x}{m}\right)\right)^2}{2\sigma^2}\right) \quad (5.3)$$

where $m = D$ has been used as an approximation of the median domain size; and σ has been taken from the profile fit of each single experimental reflection taken after subtraction of the background and the correction for the strain effect. The result of the fitting for determining the mean size of domains at different degrees of crystallinity is presented in Table 5:3. The main crystalline phase (MP) whose fraction increases linearly with the degree of crystallinity is the hexagonal phase.

4. Discussion

4.1. General XRD analysis of amorphous and partially crystallized samples

The detailed analysis of the XRD pattern in Figure 5:2 reveals that the pattern of the as cast state can be interpreted as a nano-domain state of the same lattice as found for the phase after (partial) crystallization, despite the fact that the DSC fingerprint was clearly glassy. On the other hand, the relative quantities of crystalline and nano-domain contribution to the XRD pattern indicated in Table 5:3 have been determined independently of the DSC results but both agree very well, which comforts the view that the nano-domain phase is indeed the phase that gives a glass-like signal in DSC.

The detailed XRD pattern in Figure 5:2 is well accounted for by the hexagonal phase, the lattice description of which is given in Table 5:1. We note in passing that some weak reflections (i.e. the difference between the red and the blue curve in Figure 5:2, e.g. at $2\theta=16^\circ$) could not be explained by the hexagonal phase but were identified as being due to traces of α -Pt with a measured lattice parameter $a = 3.973(7)$ Å. This parameter is reasonably close to the values of 3.92 - 3.94 Å published for platinum and can be considered as an internal standard (together with the external standard of LaB_6) for the estimation of the lattice parameters of the new compound. The fact that the lattice parameter measured for α -Pt is somewhat larger than that of bulk platinum indicates the dilatation of the fcc-lattice supposedly due to solid solution of other alloying elements present in α -Pt, albeit literature reports rather a reduction of lattice parameter for solid solutions of copper, sili-

con, [20] and boron in platinum [21], while for germanium no data are available. Nevertheless, similar observations have been reported in the primary crystallization of Al-Ni-Y alloys, where the α -Al phase exhibits a larger lattice parameter indicating a supersaturated solid solution containing Y and Ni atoms [22].

4.2. Evolution of the lattice parameter in the crystalline and the nano-domain phase

From Table 5:3 one can glean that at all stages of crystallization the mean domain size of the freshly formed crystalline phase is consistently larger than that of the glassy nano-domain matrix. Interestingly, the fraction of the α -Pt phase remains at 5% yet its domain size decreases as crystallization advances.

Three general trends shown in Figure 5a can be observed in the evolution of the unit cell volumes and the mean size of the domains presented in Table 5:3. First, the mean nano-domain size of the remaining glassy phase increases from 2-3 nm to 8.1 nm in the sample from 0 to 98% of crystallinity, secondly, the mean crystallite size in the crystalline material first increases and then decreases again, and thirdly, by increasing the degree of crystallinity, the unit cell volume of the hexagonal crystalline phase decreases.

The increase of the nano-domain size stands to reason since the mobility of the atoms above T_g is sufficient to facilitate coarsening, i.e. the larger nano-domains grow at the expense of the smaller ones. Similar reasoning can also be applied to the initial increase of the crystalline grains. The subsequent decrease in apparent crystallite size from the sample with 60% crystallinity to that with 98% crystallinity is opposite to expectation. We propose the following rationalization: the crystallite size is deduced from Scherrer's formula in which the widening of the diffraction peaks is entirely attributed to the effect of crystallite size. However, in the material at hand, crystallization has been observed to lead to a significant partitioning of copper to the remaining glassy matrix [15].

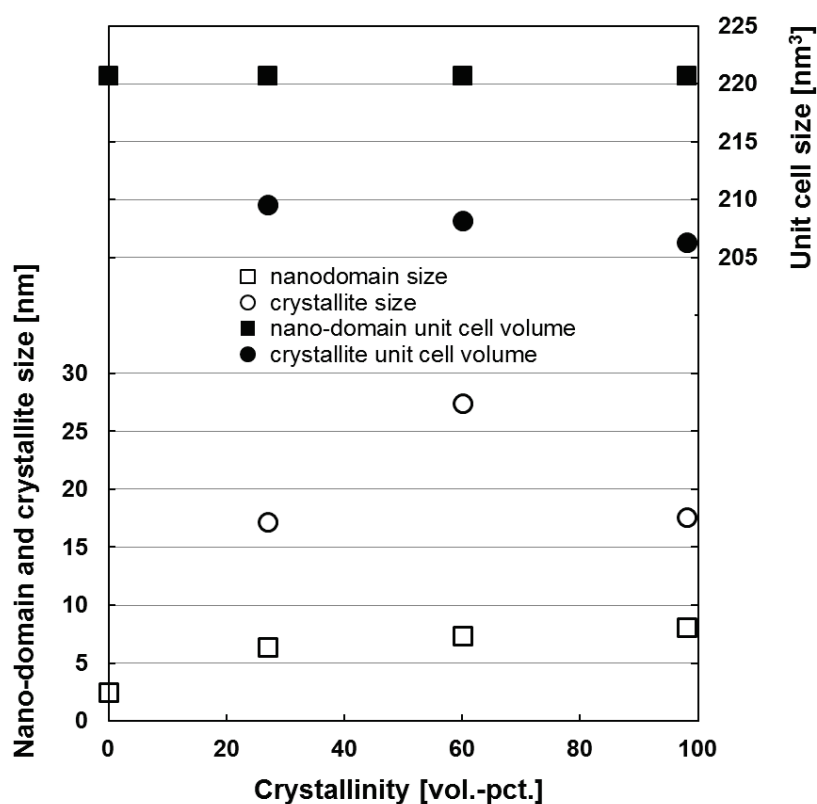


Figure 5:5 a) The evolution of the lattice cell volume and apparent crystallite or nano-domain size of the main hexagonal crystalline phase and the remaining nano-domain glassy matrix (values taken from Table 5:3); b) back-scattered electron mode SEM picture of growing crystalline domains of a sample with 27 vol.-pct. crystallinity. The rejection of copper leads to the contrast between crystalline and remaining glassy nano-domain regions.

Indeed, EDX analysis showed that the ratio of Cu:Pt in the remaining glassy phase increased gradually from 1:3 to 2:5, roughly, upon complete crystallization of the sample caused by copper rejection from the hexagonal crystalline phase into the glassy matrix during crystallization. Since the regions enriched in copper eventually crystallize as well, the crystallites formed last are significantly enriched in copper, which is expected to have an effect on the lattice parameters of these crystallites. Such slight decrease in average lattice parameter is indeed observed, cf. Table 5:3. The latter could, however, also be due to a reshuffling of atoms to adopt positions and elemental distributions of lowest energy in a supposedly shallow energy landscape, the degree of which depends on the time spent in the crystalline state. In either case, this leads to a contribution to the widening of the diffraction peaks due to fluctuations in composition or atom arrangements, which superposes

on an, on physical grounds, expected reduction in peak width due to increased crystallite size. The relative contribution of the composition variation or the degree of approaching the lowest energy can, however, not be separated. Since the width of the peak is entirely attributed to the effect of crystallite size, the deduced crystallite size at 98% crystallinity is smaller than for the 60% crystallinity sample. The real mean crystallite size is hence expected to be larger than the values indicated in Table 5:3. This would also explain why the crystalline domains that can be observed by back scattered electron mode in the SEM, cf. Figure 5:5b, are significantly larger, i.e. in the μm range, than the apparent grain size calculated by Scherrer's formula.

With the increase in copper content in the remaining glassy phase, the lattice parameters of the nano-domain phase would also be expected to evolve. Although this cannot be ascertained, cf. Table 5:3 and Figure 5:5a, it is possible that such an evolution is still physically the case, because the small and diffuse contribution of the nano-domain phase to the overall XRD profile in the partially or close to fully crystalline state does simply not allow for extracting such an evolution for the nano-domain phase. The lattice parameter indications of the nano-domain phase for the partially and close to fully crystalline samples are those deduced for the fully glassy state and need therefore be taken with a grain of salt. But even the lattice parameter of the fully glassy state has to be regarded as indicative with regard to the difference between measured density of the as cast sample, i.e. 14.65 gcm^{-3} , and the crystallographic density of the nano-domain phase given as 13.77 gcm^{-3} in Table 5:3. On the other hand, the density of the 98% crystalline sample of 14.95 gcm^{-3} measured by Archimedes' principle, corresponds well with a mixture of 95% of crystalline hexagonal phase of crystallographic density of 14.77 gcm^{-3} and 5 vol.-pct. of platinum at a density of roughly 21 gcm^{-3} .

5. Conclusions

- A new hexagonal crystalline structure with lattice parameters of $a = 8.973(1) \text{ \AA}$ and $c = 2.959(1) \text{ \AA}$ was found to be forming upon crystallization in the alloy $\text{Pt}_{49.95}\text{Cu}_{16.65}\text{Si}_{6.4}\text{Ge}_3\text{B}_{24}$. This new phase is a close analogous structure to $\text{Zn}_3\text{Pt}_9\text{B}_{3.86}$.
- The 5mm as-cast sample exhibited a clear glass transition and a relatively wide supercooled liquid region in DSC pattern, yet the synchrotron HE-XRD showed that

this glass contained nano-size ordered domains of 2-3 nm in size as estimated via Scherrer's formula.

- The size of the nano-domains in the glassy phase increase from approximately 2-3 nm to 8 nm as the degree of crystallinity increased.
- By increasing the degree of crystallinity, the lattice parameters of the freshly crystallized hexagonal phase decreased slightly. Such decrease was attributed to compositional variations due to copper rejection in early stages of crystallization or to re-shuffling into lower energy distributions in a shallow energy landscape progressing with time.

Acknowledgments

The authors wish to acknowledge financial support for this work by EPFL contract no. 535 627. We are grateful Swiss–Norwegian Beam Lines (ESRF, Grenoble) for beamtime and to Philip Pattison (SNBL, ESRF) for the X-ray diffraction experiments.

References:

- [1] J. Schroers, Processing of Bulk Metallic Glass, *Adv. Mater.* 22 (2009) 1566–1597. doi:10.1002/adma.200902776.
- [2] U. Köster, J. Meinhardt, NATO-Advanced Research Workshop on Undercooled Metallic Melts: Properties, Solidification and Metastable Phases Crystallization of highly undercooled metallic melts and metallic glasses around the glass transition temperature, *Mater. Sci. Eng. A.* 178 (1994) 271–278. doi:10.1016/0921-5093(94)90553-3.
- [3] M.T. Clavaguera-Mora, N. Clavaguera, D. Crespo, T. Pradell, Crystallisation kinetics and microstructure development in metallic systems, *Prog. Mater. Sci.* 47 (2002) 559–619. doi:10.1016/S0079-6425(00)00021-9.
- [4] A. Inoue, Amorphous, nanoquasicrystalline and nanocrystalline alloys in Al-based systems, *Prog. Mater. Sci.* 43 (1998) 365–520. doi:10.1016/S0079-6425(98)00005-X.
- [5] C. Fan, C. Li, A. Inoue, Nanocrystal composites in Zr–Nb–Cu–Al metallic glasses, *J. Non-Cryst. Solids.* 270 (2000) 28–33. doi:10.1016/S0022-3093(00)00078-8.
- [6] A.L. Greer, Partially or fully devitrified alloys for mechanical properties, *Mater. Sci. Eng. A.* 304–306 (2001) 68–72. doi:10.1016/S0921-5093(00)01449-0.
- [7] A.L. Greer, Confusion by design, *Publ. Online* 25 Dec. 1993 Doi101038366303a0. 366 (1993) 303–304. doi:10.1038/366303a0.
- [8] N. Zheng, G. Wang, L. c. Zhang, M. Calin, M. Stoica, G. Vaughan, N. Mattern, J. Eckert, In situ high-energy x-ray diffraction observation of structural evolution in a Ti-based bulk metallic glass upon heating, *J. Mater. Res.* 25 (2010) 2271–2277. doi:10.1557/jmr.2010.0298.
- [9] Y.E. Kalay, I. Kalay, J. Hwang, P.M. Voyles, M.J. Kramer, Local chemical and topological order in Al–Tb and its role in controlling nanocrystal formation, *Acta Mater.* 60 (2012) 994–1003. doi:10.1016/j.actamat.2011.11.008.
- [10] N. Mattern, U. Kühn, A. Concustell, A. Schöps, M.D. Baro, J. Eckert, Phase Separation and Crystallization in Cu–Zr Metallic Glasses, *Mater. Trans.* 48 (2007) 1639–1643. doi:10.2320/matertrans.MJ200708.
- [11] E. Matsumura, T. Ichitsubo, J. Saida, S. Kohara, H. Ohsumi, Structural study of Zr-based metallic glasses, *J. Alloys Compd.* 434–435 (2007) 119–120. doi:10.1016/j.jallcom.2006.08.141.

- [12] X.M. Shi, X.D. Wang, Q. Yu, Q.P. Cao, D.X. Zhang, J. Zhang, T.D. Hu, L.H. Lai, H.L. Xie, T.Q. Xiao, J.Z. Jiang, Structure alterations in Al-Y-based metallic glasses with La and Ni addition, *J. Appl. Phys.* 119 (2016) 114904. doi:10.1063/1.4944653.
- [13] M.J. Kramer, M. Xu, Y.Y. Ye, D.J. Sordellet, J.R. Morris, Phase Stability and Transformations in the $Zr_{20}Ni_{80}Cu_{1-x}$ Amorphous System, *Metall. Mater. Trans. A.* 39 (2007) 1847–1856. doi:10.1007/s11661-007-9309-0.
- [14] H. Kazemi, C. Cattin, M. Blank, L. Weber, Development of a new family of phosphorous-free Pt-based bulk metallic glasses, *J. Alloys Compd.* (Submitted).
- [15] H. Kazemi, C. Cattin, G. Hodel, T. Pachova, L. Weber, Effect of partial crystallization in Pt-Si-B-based bulk metallic glasses on glass transition and crystallization of the remaining amorphous matrix, *J. Non-Cryst. Solids.* (Submitted).
- [16] G. Ning, R.L. Flemming, Rietveld refinement of LaB₆: data from μ XRD, *J. Appl. Crystallogr.* 38 (2005) 757–759. doi:10.1107/S0021889805023344.
- [17] V. Petříček, M. Dušek, L. Palatinus, Crystallographic Computing System JANA2006: General features, *Z. Für Krist. - Cryst. Mater.* 229 (2014) 345–352. doi:10.1515/zkri-2014-1737.
- [18] K. Petry, W. Klunzer, W. Jung, Some Zinc and Gallium Transition-Metal Borides with New Channel Structures - $Zn_3Pt_9B_4$, $Ga_2.7Ir_9B_5$ and $Ga_3Pt_9B_4$, *Z. Krist.* 209 (1994) 151–156. doi:10.1524/zkri.1994.209.2.151.
- [19] E. Prince, ed., *International Tables for Crystallography: Mathematical, physical and chemical tables*, 1st ed., International Union of Crystallography, Chester, England, 2006. <http://it.iucr.org/Cb/> (accessed August 15, 2016).
- [20] W.B. PEARSON, *A Handbook of lattice spacings and structures of metals and alloys*, Pergamon Press, Northern Ireland, 1964.
- [21] H. Brodowsky, H. Sagunski, Thermodynamic Properties of Pt-B Solid-Solutions, *Berichte Bunsen-Ges.-Phys. Chem. Chem. Phys.* 87 (1983) 803–805.
- [22] Y.-H. Kim, A. Inoue, T. Masumoto, Ultrahigh Tensile Strengths of $Al_{88}Y_2Ni_9M_1$ ($M=Mn$ or Fe) Amorphous Alloys Containing Finely Dispersed fcc-Al Particles, *Mater. Trans. JIM.* 31 (1990) 747–749. doi:10.2320/matertrans1989.31.747.

Chapter 6

Influence of rare earth and group IIIA elements and fluxing on the thermophysical properties of a Pt-Si-B-Ge-Cu bulk metallic glass

(Submitted to Materials and Designs)

Hamed Kazemi, Cyrill Cattin, Mathilde Taconnet de Perrot, Aigoul Schreier, and Ludger Weber

Laboratory of Mechanical Metallurgy, Ecole Polytechnique Fédérale de Lausanne, EPFL,
CH-1015 Lausanne, Switzerland

Contributions:

Hamed Kazemi: Development of the alloy $\text{Pt}_{49.95}\text{B}_{24}\text{Si}_{6.4}\text{Ge}_3\text{Cu}_{16.65}$, initial investigation of the influence of scandium addition and fluxing on the thermophysical properties of a Pt-Si-B-Ge-Cu bulk metallic glass, XRD analysis, writing the manuscript.

Cyrill Cattin: Supervision, designing of the experiments, revising and correcting the manuscript.

Mathilde Taconnet de Perrot: preparation and characterization of the alloys series containing Ho and Sc.

Aigoul Schreier: preparation and characterization of the alloys series containing rare earth (RE) and group IIIA elements.

Ludger Weber: Supervision, revising, correcting and approving the manuscript.

Abstract

The effect of minor addition of rare earth (RE) and group IIIA elements on the glass forming ability of a platinum-based bulk metallic glass with the general formula $\text{Pt}_{49.95}\text{Cu}_{16.65-1}(\text{RE or IIIA})_1\text{Si}_{6.4}\text{Ge}_3\text{B}_{24}$ (RE = Sm, Ho, Tb, Gd, and Dy; IIIA = Sc and Y) was investigated. All elements substituted by 1 at.-pct. for copper increased the glass transition temperature, T_g , between 6 and 17 °C with a similar effect on the crystallization temperature, T_x , except for yttrium, for which the crystallization temperature decreased significantly. For a copper-mold casting diameter of 2 mm, only dysprosium, scandium, and holmium led to fully amorphous samples and concomitant reduced liquidus temperature, T_l , while for the other elements, except for yttrium, T_l increased and the samples were partially crystalline. Microhardness increased slightly with increasing T_g . It is further shown that by introducing as little as 100 ppm of scandium the oxygen level in the alloy can be reduced from around 15 ppm to below 5 ppm, yet without any effect on T_g , and notably not on T_x . Fluxing with B_2O_3 , on the other hand, proved to be ineffective in reducing the oxygen content of the base alloy, and left all characteristic temperatures unchanged.

1. Introduction

Owing to their unique combination of properties, bulk metallic glasses (BMGs) have emerged as a promising class of advanced technical materials. BMGs are commonly isotropic at a length scale beyond some tenth of nm. The consequence of the absence of long-range periodicity is the absence of lattice defects such as dislocations or grain boundaries, leading to a superior yield strength and hardness, combined with a reduced Young's modulus, making them capable of storing more elastic energy than their crystalline counterparts. This has been exploited in high-end golf clubs and is considered interesting for springs in mechanical watches, for example [1], [2]. Other more recent applications have been found in producing micro/nano components by thermoplastic forming of BMG's [3], [4]. Difficulties in processing of BMGs has hampered their widespread application due to the dependence of their properties on both the composition and the processing parameters [1], [2], [5]–[7]. One particular challenge in BMG processing is to limit the oxygen content, which strongly affects both the glass forming ability (GFA) and the mechanical properties, particularly in titanium and zirconium based BMGs [8]–[10], but also in palladium or platinum based alloys [11]–[13]. Oxide particles or other impurities tend to serve

as potential heterogeneous sites, favoring crystallization and thus reducing the GFA [14]–[18]. One of the most common methods for reducing the oxygen content and eliminating the heterogeneous nucleation sites is fluxing with B_2O_3 [12], [19]. The effect of fluxing can be significant, e.g. in $Pt_{57.3}Cu_{14.6}Ni_{5.3}P_{22.8}$, where fluxing increases the critical casting diameter from 6 mm to up to 20 mm [20]. It has also been found that fluxing of $Pd_{77.5}Si_{16.5}Cu_6$ with B_2O_3 led to a reduction in oxygen content from 3.5 to 1.4 ppm concomitant with a significant increase in ductility and an enlargement of the supercooled liquid region from 45 °C in the non-fluxed alloy to 76 °C in the fluxed alloy [12]. Besides reducing the oxygen content, fluxing with B_2O_3 may also lead to a compositional change by either i) pick-up of boron by reducing boron oxide under evolution of oxygen gas, ii) pick-up of boron and loss of another alloying element to the fluxing liquid by an exchange reaction, or iii) loss in one or several of the alloying elements by dissolution into boron oxide without oxygen pick-up. The required excess in oxygen for the latter process is either provided by working under oxygen atmosphere or by precipitation of elemental boron. Compositional variation has been reported for fluxing of the alloy $Pd_{77.5}Si_{16.5}Cu_6$ with B_2O_3 at temperatures above 1030 °C [13]. In this study, boron pick-up of 0.7 and 1.4 at.-pct. has been reported, leading to a reduction of the GFA. It has however not been reported whether this pick-up was according to process i) or ii) listed above, i.e. whether this was simple boron pick-up or an exchange reaction with concomitant reduction of the silicon content. The latter is known to have a very strong effect on GFA of Pd-Si-Cu alloys [21]. Interestingly enough, Inoue et al. found that substitution of silicon with boron in the alloy $Pd_{76}Si_{18-x}Cu_6B_x$ [22] increased the width of the supercooled liquid region up to $x \leq 3$ with ensuing strong reduction in the GFA for $x > 3$. Given the somewhat higher initial silicon content in the work of Inoue et al. [22], it could be that the main factor affecting the GFA in both cases was a reduction in the silicon content below a critical value of around 15 at.-pct..

Increased oxygen content in the alloy $Zr_{57}Nb_5Al_{10}Cu_{15.4}Ni_{12.6}$ was found to significantly reduce the ductility of the alloy due to the formation of oxides [23]. Similar observations have been made for other zirconium-based glassy alloys [23]–[25]. Due to their reactivity, zirconium-based alloys cannot be fluxed with B_2O_3 , yet the oxygen content of these alloys can be considerably reduced by minor addition of oxygen-scavenging elements with higher affinity to oxygen compared to the elements present in the BMG [9], [23]. Rare earth (RE) and group IIIA elements are capable of forming highly stable oxides making them suitable candidates for this task. It has been reported that the addition of as little as 2 at.-pct. of

yttrium in both zirconium- and iron-based alloys significantly increases the GFA [26]–[28]. Furthermore, the addition of 300 to 600 ppm of scandium to $\text{Zr}_{52.5}\text{Al}_{10}\text{Ti}_5\text{Cu}_{17.9}\text{Ni}_{14.6}$ was found to increase the critical casting diameter from 4.5 to 12 mm [29]. Besides oxygen scavenging, the minor addition of RE or group IIIA metals may also alter the atomic topology of the system due to their large atomic radii. Atoms with large radii are difficult to incorporate in crystalline phases otherwise made of smaller atoms; hence, crystallization of competing crystalline structures upon quenching is hampered and glass formation is favored instead [28], [28] Similar improving effects of addition of oxygen scavengers have also been found in Fe-Cr-Mo-C-B glassy alloys [30].

Recently, a new family of Pt-based BMGs based on the ternary Pt-Si-B system has been presented [31]. These alloys offer relatively good GFA and high hardness. $\text{Pt}_{49.95}\text{Cu}_{16.65}\text{Si}_{6.4}\text{Ge}_3\text{B}_{24}$, for example, exhibits a critical casting diameter larger than 5 mm, and, when copper mold cast to this size, is characterized by a glass transition temperature, T_g , of 307 °C and a width of the supercooled liquid region of 54 K (cf. Table 6:1). Typical oxygen levels were on the order of 20 ppm. Based on the reported effectiveness of B_2O_3 fluxing on Pt-P-based BMGs, fluxing might also be a promising route to reduce oxygen levels in the $\text{Pt}_{49.95}\text{Cu}_{16.65}\text{Si}_{6.4}\text{Ge}_3\text{B}_{24}$. Furthermore, RE or IIIA elements are expected to act efficiently as oxygen scavengers but might also affect the characteristic temperatures and mechanical properties by their effect on topology due to their large size. Hence, in this work an attempt is made to separate these two effects by studying the effectiveness of fluxing with B_2O_3 as well as the addition of minor substitution of copper by RE and group IIIA elements for reducing the oxygen content. For the RE and group IIIA on the example of scandium we show that, at low oxygen content certainly, oxygen scavenging is decoupled from the concomitant influence on the thermophysical and mechanical properties.

2. Experimental procedures

2.1. Materials

Ingots were prepared by mixing pure elements (Pt 99.9, Si 99.99, B 99.5, Cu 99.999, Ge 98.5, purity indications in wt.-pct.) under argon atmosphere (argon 6.0 = 99.9999% Ar) in quartz tubes. The substitution elements, i.e. the RE metals samarium, holmium, gadolinium, dysprosium, and terbium, as well as the group IIIA elements scandium and yttrium, were > 98.5 wt.-pct pure and were added in an arc-melter (MAM-1, Edmund Buehler

GmbH, Hechingen, Germany) under oxygen-gettered argon 6.0 atmosphere. The samples were homogenized by turning and re-melting four times in the arc-melter. Cylindrical samples with 0.75 and 2 mm in diameter were produced by suction casting.

A series of alloys was produced with the general composition $\text{Pt}_{49.95}\text{Cu}_{16.65-1}(\text{M})_1\text{Si}_{6.4}\text{Ge}_3\text{B}_{24}$ (in at.-pct.) with $\text{M} = \text{Sm}, \text{Ho}, \text{Gd}, \text{Dy}, \text{Tb}, \text{Sc}, \text{and Y}$ (and $\text{M} = \text{Cu}$ for the unsubstituted base alloy). For reasons that will become apparent in the following, holmium and scandium were selected for a second series of alloys, in which a range of substitution from 0.5 to 4 at.-pct. for equal amounts of copper was covered. One more sample was prepared with only 100 ppm of scandium to separate the oxygen scavenging effect from the effect of scandium content on the atomic topology of the alloy.

2.2. Characterization techniques

2.2.1. Structural analysis

An X'pert Philips X-ray diffractometer equipped with a Cu-K_α source was used to analyze the structure of the samples. Analyzed surfaces were grinded with SiC paper and polished down to 1 μm using diamond particles. The working voltage and the anode current were 40 kV and 45 mA, respectively.

2.2.2. Thermal analysis

The characteristic temperatures and the enthalpy of crystallization were obtained under argon 6.0 flow at a heating rate of $10 \text{ K}\cdot\text{min}^{-1}$, using a Differential Scanning Calorimeter (DSC Pegasus 404C Netzsch, Germany) equipped with alumina crucibles. T_g was measured on the DSC curve as the inflection point of the step towards the endothermic values, while the crystallization temperature, T_x , designates the onset of the exothermic peak upon heating and was taken as the intersection of the tangent to the plateau before the exothermic rise and the tangent to the exothermic rise up to half maximum. Solidus and liquidus temperatures were both measured upon heating as the onset (T_s) and the end (T_l) of the endothermic deviations characterizing melting.

2.2.3. Mechanical analysis

Hardness measurements were carried out using a Gnehm FM300 microhardness tester. The sample surfaces were grinded with SiC paper and polished down to 1 μm using diamond particles. Reported values are averages of at least five measurements.

2.3. Fluxing with B_2O_3

B_2O_3 (99.98%, Sigma Aldrich, Germany) powder was heated to 1100 $^{\circ}\text{C}$ in a graphite crucible, using a vacuum induction furnace. The molten boron oxide was kept at that temperature and under vacuum for 25 hours to remove traces of humidity. The final vacuum was 10^{-5} mbar. A graphite crucible was used because trials of fluxing the alloy $\text{Pt}_{49.95}\text{Cu}_{16.65}\text{Si}_{6.4}\text{Ge}_3\text{B}_{24}$ in zirconia, alumina, and fused-silica (quartz) crucibles resulted in chemical reactions between the alloy and the crucibles. The temperature, measured with a K-type thermocouple at 2 mm from the liquid, was then lowered to 300 $^{\circ}\text{C}$ to allow for adding a homogenized ingot into the crucible. The furnace was then closed; the atmosphere was purged five times with argon. The temperature was increased to 1150 $^{\circ}\text{C}$, and fluxing was carried out under vacuum for 40 hours. After 6 hours of fluxing the vacuum level was typically better than 10^{-4} mbar and during the 40 hours of fluxing, the variation of temperature was within ± 5 $^{\circ}\text{C}$. Subsequently the temperature was lowered to 1100 $^{\circ}\text{C}$ and the alloy was gravity cast in a copper mold (cast diameter of 5 mm) while maintaining the vacuum. The temperature of the copper mold measured with a second K-type thermocouple was 50 $^{\circ}\text{C}$ prior to casting. For the reference sample without fluxing, the homogenized ingot was simply melted in a graphite crucible under intermediate vacuum of 10^{-5} mbar and cast at 1100 $^{\circ}\text{C}$.

The oxygen level in the alloys was measured using an inert gas analysis system (LECO TC, carried out at the certified lab of Cendres et Métaux, Bienne/Biel, Switzerland). The quantitative detection level of oxygen concentration for the inert gas analysis was 5 ppm and values below this were to be considered only qualitative.

2.4. Annealing in a stabilized salt bath

In order to compare the crystallization kinetics of the most promising RE/IIIA-containing alloy, samples were subjected to a crystallization treatment in a stabilized salt bath at roughly 5 $^{\circ}\text{C}$ below T_x as obtained by DSC at a heating rate of 10 Kmin^{-1} . In order to pre-

vent effects due to sample-to-sample variations, the analyses were conducted on discs that were cut from the same cylindrical sample: the cylinder was repeatedly removed after fixed times from the salt bath, three roughly 1 mm thick disc samples were cut off and the cylinder was put back in the salt bath to continue its crystallization treatment. On each sample, hardness and a DSC curve were measured. Hence the values for T_g , and T_x correspond to an average of the samples for a certain treatment time, while the hardness values are averages of at least five measurements on each of the three samples. The vertical error bars represent the standard deviation on all values.

3. Results

3.1. XRD analysis

The XRD spectra of the samples with 1 at.-pct. of copper substituted by scandium, yttrium, and the RE-elements specified above are shown in Figure 6:1. Substitution of copper by scandium, holmium and dysprosium does not affect the glassy nature of the base alloy, whereas samarium, yttrium, terbium, and gadolinium led to partially crystalline samples when copper mould suction cast in 2 mm rods.

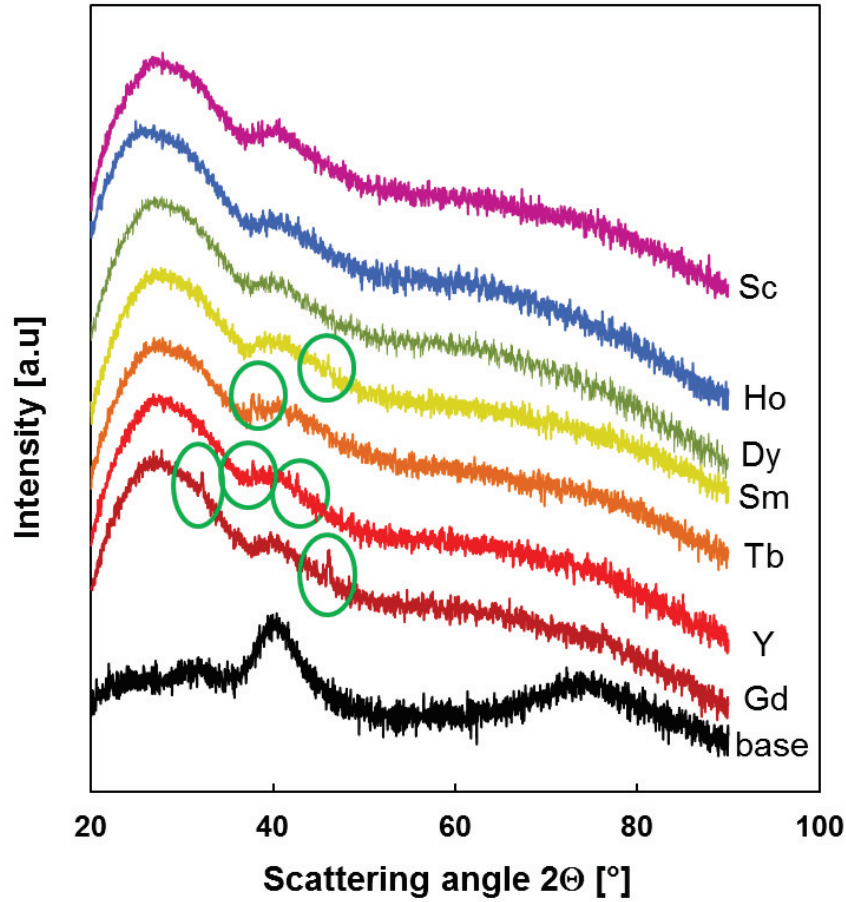


Figure 6:1 Overview of the XRD signals for the alloys with a general formula of $\text{Pt}_{49.95}\text{Cu}_{15.65}\text{M}_1\text{Si}_{6.4}\text{Ge}_3\text{B}_{24}$, where $\text{M} = \text{Sm}, \text{Tb}, \text{Dy}, \text{Ho}, \text{Gd}, \text{Sc}, \text{Y}$, or Cu (no substitution). The samples with dysprosium, holmium, scandium, and copper show no sign of crystallization, while the substitution of copper with gadolinium, samarium, terbium, or yttrium leads to partial crystallization.

3.2. Effect of substituting copper by IIIA and RE elements on characteristic temperatures

The precise compositions as well as the data determined on the samples are listed in Table 1. The characteristic temperatures T_g , T_x , T_s , and T_l of the samples with 1 at.-pct. of IIIA and RE elements substituted for 1 at.-pct. of copper are given in Figure 6:2. As can be seen, the T_g is systematically higher than for the sample without substitution, the increase going from 3 °C for the sample containing samarium to 11 °C for the sample with dysprosium. On the other hand, T_x evolves fairly parallel to the T_g , except for yttrium, which led to a significantly lower T_x . Given the fairly strong effect of these substitution elements on T_g ,

the two most promising substitution elements, i.e. scandium and holmium selected for their large $\Delta T (= T_x - T_g)$ and high T_g were analyzed in more detail.

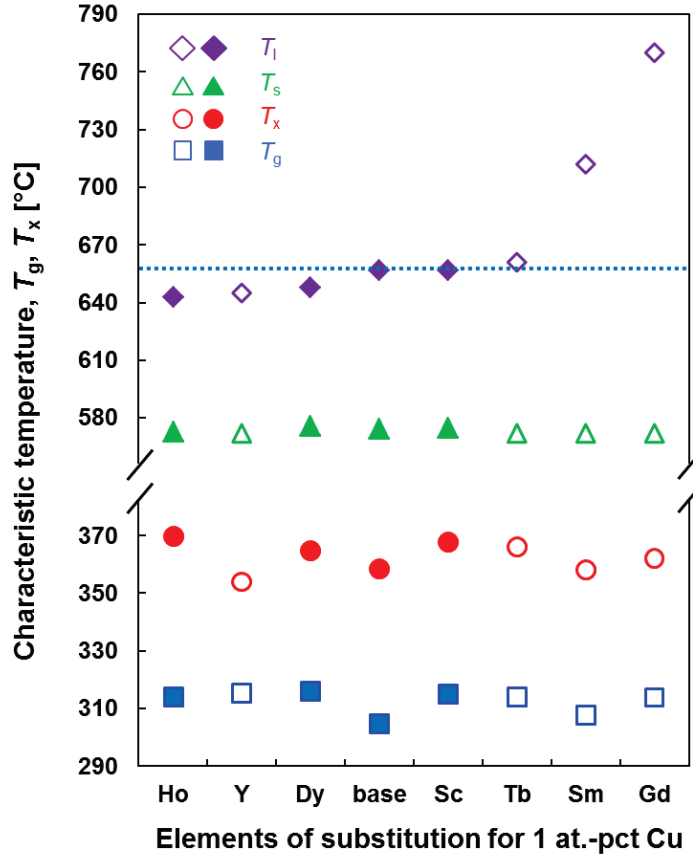


Figure 6:2 T_g , T_x , T_s , and T_i values of 2 mm wide copper mold cast cylinders with a general formula of $\text{Pt}_{49.95}\text{Cu}_{15.65}\text{M}_1\text{Si}_{6.4}\text{Ge}_3\text{B}_{24}$, where M = Sm, Tb, Dy, Ho, Gd, Sc, Y, or Cu (no substitution). Full data points represent fully glassy samples, while empty data points stand for partially crystalline samples.

The evolution of the characteristic temperatures of base alloys with substitution of equal amounts of copper by 0.5 to 4 at.-pct. of scandium and holmium in 2 mm diameter samples suction cast in a copper mold are shown in Figure 6:3. The rise in T_g and T_x is fairly steady with a level of substitution up to about 2 at.-pct. and then drops sharply as partial crystallization upon casting sets in.

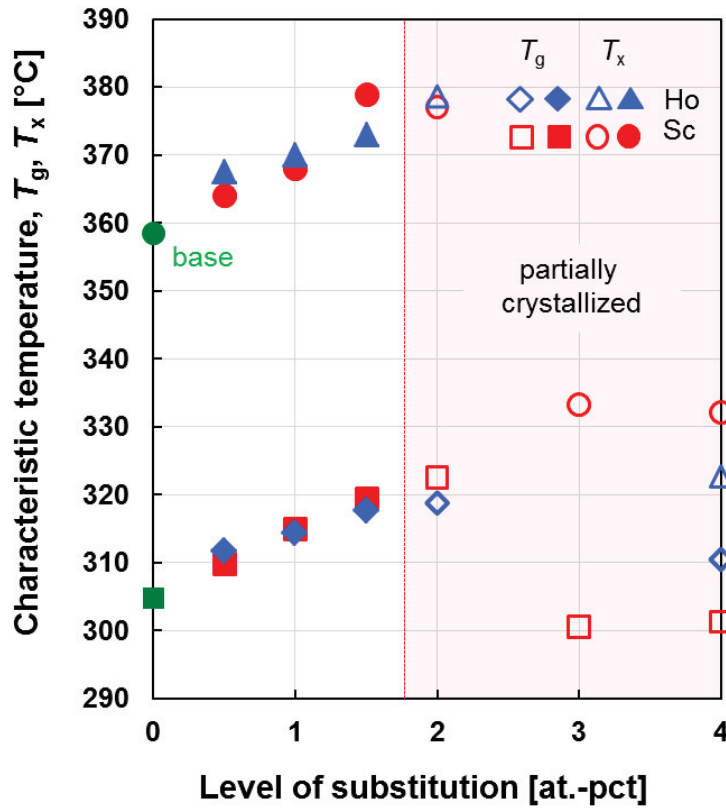


Figure 6:3 T_g and T_x values of 2 mm wide copper mold cast cylinders with a general formula of $\text{Pt}_{49.95}\text{Cu}_{16.65-x}\text{M}_x\text{Si}_{6.4}\text{Ge}_3\text{B}_{24}$ where $\text{M} = \text{Sc}$ or Ho , as a function of the degree of substitution, x . Full data points represent fully glassy samples, empty data points stand for partially crystalline samples.

The partial crystallization manifests itself also in the evolution of microhardness in this series shown in Figure 6:4: after a gentle increase with the level of substitution up to 2 at.-pct., the hardness increases strongly at higher levels of substitution due to partial crystallization, as previously observed in this class of BMGs.

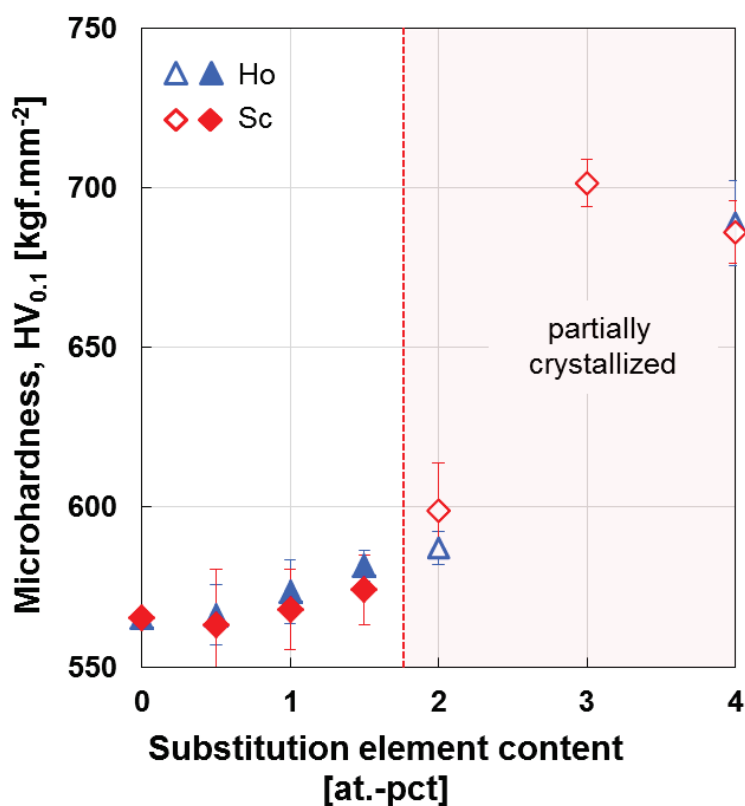


Figure 6:4 Microhardness of 2 mm wide copper mold cast cylinders with a general formula of $Pt_{49.95}Cu_{16.65-x}M_xSi_{6.4}Ge_3B_{24}$, where $M = Sc$ or Ho , as a function of the degree of substitution, x . The data points are mean values of at least five measurements, with the standard deviation indicated as vertical error bars.

The evolution of the enthalpy of crystallization as a function of the degree of substitution is shown in Figure 6:5. Scandium and holmium lower strongly the enthalpy of crystallization without significant discontinuity as partial crystallization sets in above a substitution level of 1.5 - 2 at.-pct..

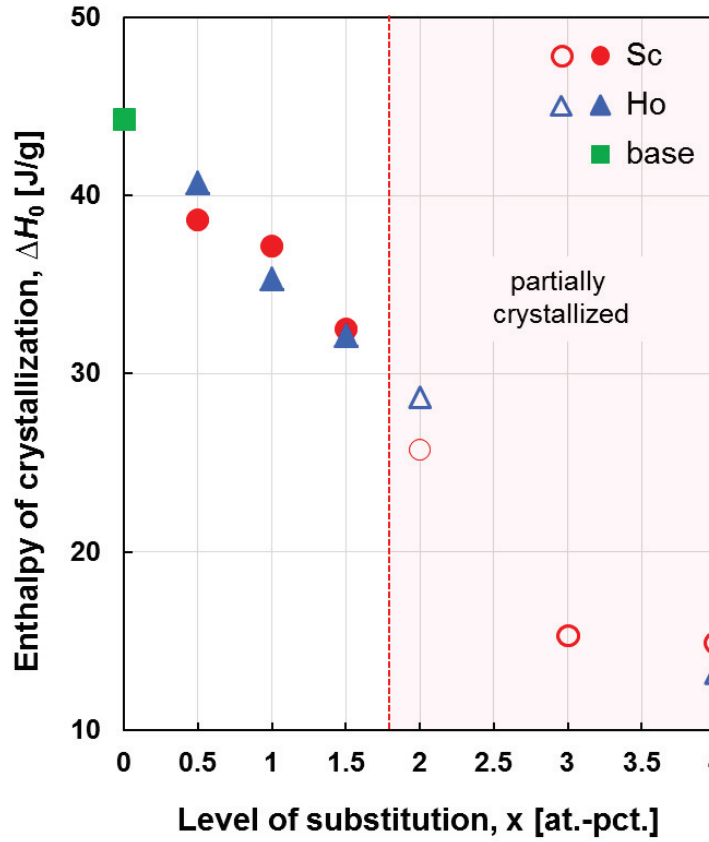


Figure 6:5 Evolution of the enthalpy of crystallization, ΔH , as a function of degree of substitution of copper, x , by scandium or holmium, showing a steadily decreasing value without discontinuity as partial crystallization sets in.

3.3. Influence of scandium addition on the hardening behavior during crystallization

As reported previously [32], [33] for the unsubstituted base alloy $\text{Pt}_{49.95}\text{Cu}_{16.65}\text{Si}_{6.4}\text{Ge}_3\text{B}_{24}$, the hardness increases from 570 HV in the as-cast state to 750 HV in fully crystallized alloy. The increase of hardness is attributed to the formation of hexagonal crystals, and the concomitant enrichment of the remaining glassy state in copper [32], [33]. Figure 6:6 shows the influence of the addition of 1 at.-pct. scandium on the increase of the hardness upon isothermal partial crystallization at 370 °C. The degree of crystallinity, X , is determined by comparing the remaining enthalpy of crystallization, ΔH_x , to the enthalpy of crystallization of the fully amorphous sample, ΔH_0 :

$$X = \frac{\Delta H_0 - \Delta H_x}{\Delta H_0} \quad (6.1)$$

As can be seen, the increase of the hardness happens sooner in the sample without scandium compared to the sample with modified composition. The final hardness of both alloys remains fairly similar upon complete crystallization.

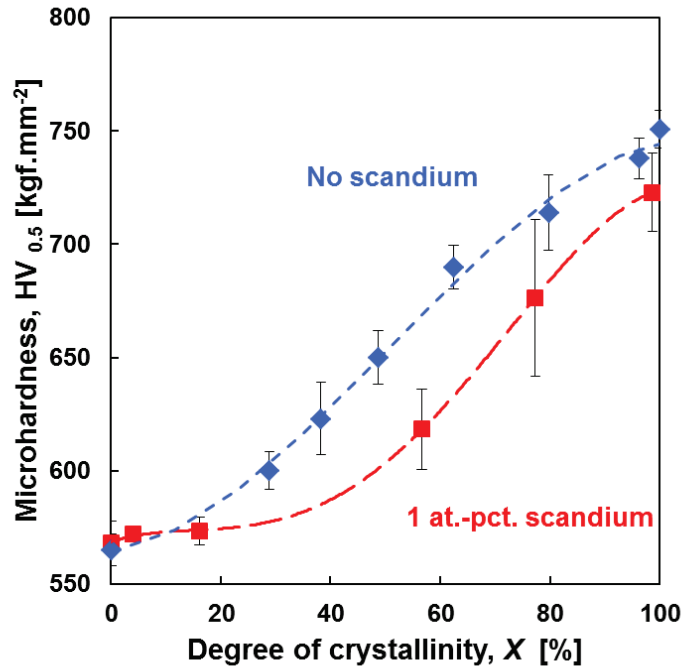


Figure 6:6 Evolution of microhardness with the degree of crystallinity, X , in $\text{Pt}_{49.95}\text{Cu}_{16.65}\text{Si}_{6.4}\text{Ge}_3\text{B}_{24}$, as well as in $\text{Pt}_{49.95}\text{Cu}_{15.65}\text{Sc}_1\text{Si}_{6.4}\text{Ge}_3\text{B}_{24}$. The samples were 2 mm wide cylinders obtained by copper mold casting. Both samples were annealed a few degrees below the respective onset of crystallization temperatures.

3.4. Characteristic temperatures before and after fluxing with B_2O_3

Figure 7 shows the DSC patterns of the fluxed alloy $\text{Pt}_{49.95}\text{Cu}_{16.65}\text{Si}_{6.4}\text{Ge}_3\text{B}_{24}$ and that of the as-cast sample. Each of the mentioned temperatures in Figure 6:7 is an average value of that particular characteristic temperature obtained for three separately processed, fluxed, and cast samples. The DSC curves look essentially the same with the characteristic temperatures at, within typical variability, identical values.

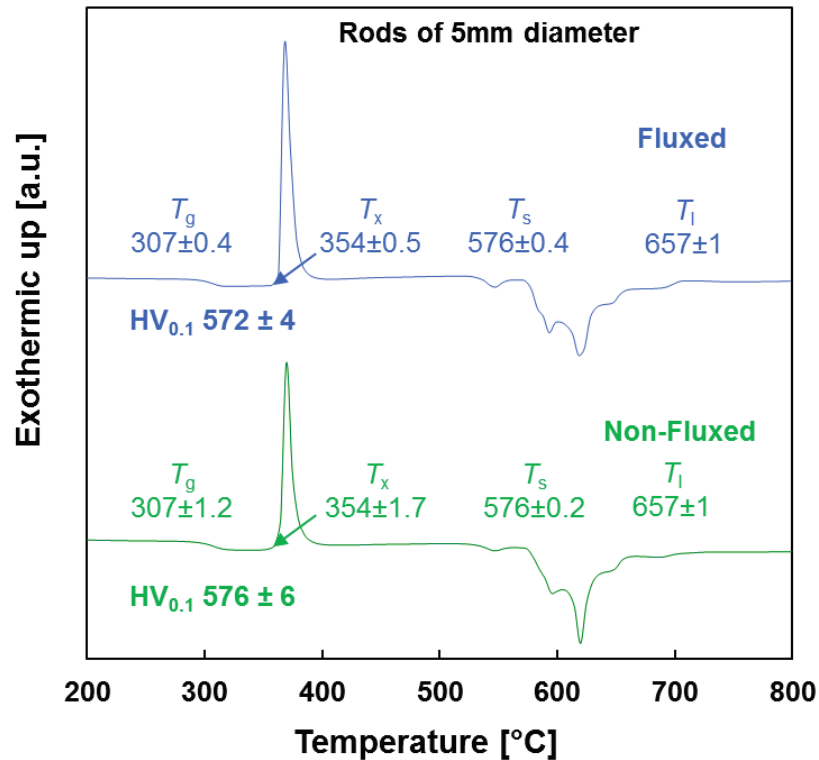


Figure 6:7 Comparison of DSC patterns of fluxed and non-fluxed $Pt_{49.95}Cu_{16.65}Si_{6.4}Ge_3B_{24}$. The samples were 5 mm wide cylinders obtained by copper mold casting, and the heating rate during DSC characterization was $10\text{ K}\cdot\text{min}^{-1}$. (The difference of T_g and T_x compared to 2 mm wide samples of the same alloy (cf. Figure 2) is due to relatively smaller cooling rate in 5 mm wide sample)

3.5. Oxygen content before and after fluxing with B_2O_3 as well as before and after oxygen scavenging by scandium

Since fluxing with boron oxide had no effect on the characteristic temperatures, a small quantity of scandium was added to scavenge oxygen. Two scandium concentrations were chosen to this end: 100 ppm and 1 at.-pct.. As before, scandium substitutes equal amounts of copper leading to the general formula of $Pt_{49.95}Cu_{16.65-x}Sc_xSi_{6.4}Ge_3B_{24}$. The DSC patterns of the two scandium containing alloys are shown in Figure 6:8, together with the DSC curves of the base alloy.

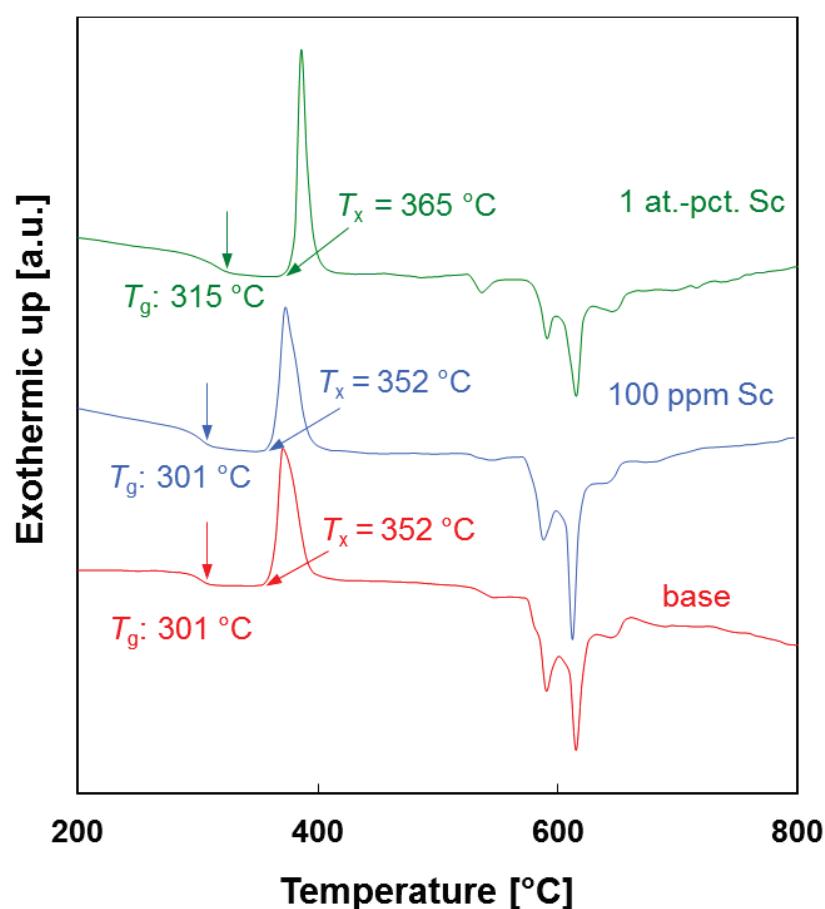


Figure 6:8 DSC patterns of glassy rods of 0.75 mm diameter of the scandium-containing alloys with general formula $\text{Pt}_{49.95}\text{Cu}_{16.65-x}\text{Sc}_x\text{Si}_{6.4}\text{Ge}_3\text{B}_{24}$ for substitution levels, x , of 0, 100 ppm and 1 at.-pct. (Likewise cf. Figure 6:7, the higher cooling rate in 0.75 mm wide samples have resulted in slightly different T_g and T_x compared to 2 mm wide samples cf. Figure 6:2)

The result of the oxygen content measurement carried out on the scandium-containing samples as well as the fluxed and cast samples are presented in Figure 6:9. As can be seen, scandium successfully scavenges oxygen from the system to levels below the quantitative detection limit of the inert gas fusion analyzer used for this study (5 ppm) and this reduction is achieved for as little as 100 ppm of scandium. The unsubstituted samples either cast directly or fluxed with B_2O_3 before casting both exhibit oxygen contents close to 20 ppm.

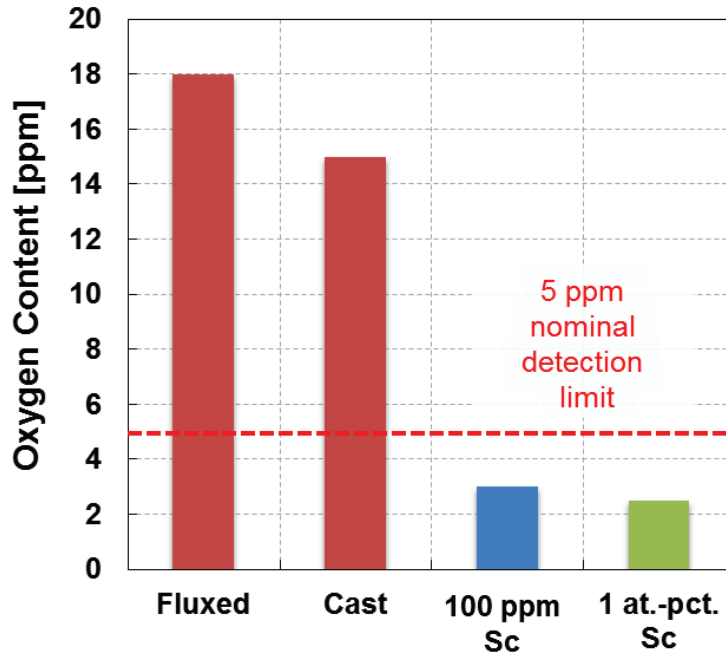


Figure 6:9 Comparison of oxygen content of the fluxed and non-fluxed samples of $\text{Pt}_{49.95}\text{Cu}_{16.65}\text{Si}_{6.4}\text{Ge}_3\text{B}_{24}$ compared to the scandium-containing alloys with the general formula $\text{Pt}_{49.95}\text{Cu}_{16.65-x}\text{Sc}_x\text{Si}_{6.4}\text{Ge}_3\text{B}_{24}$.

4. Discussion

4.1. Effect of substitution on characteristic temperatures

The increase in T_g and T_x brought about by the addition of RE and group IIIA elements studied here is all the more remarkable since they achieve this increase while substituting copper, which has for itself already a significant effect on T_g and T_x (on the order of 2 K per at.-pct., cf. Reference [30]). Since these minor additions act on T_g and T_x simultaneously, and since in a given class of BMGs the hardness scales fairly proportionally with T_g [34], these minor additions can be used to fine tune the properties of the BMG. As can be seen in Figure 3, the range of substitution that can be exploited is rather limited, i.e. roughly 2 at.-pct. for scandium and holmium. Nevertheless, the improvement in hardness is on the order of 30 $\text{HV}_{0.1}$, which is quite significant.

We also note that for the two substitution elements studied in some detail here, i.e. scandium and holmium, the solidus and liquidus temperatures were either not affected or reduced by the substitution at the level of 1 at.-pct., cf. Table 6:1. Inversely, substituting 1 at.-pct. of copper with terbium, samarium and gadolinium led to an increase in liquidus

temperature, cf. Figure 6:2, and consequently the samples were partially crystalline upon suction casting to 2 mm diameter. In the case of the sample containing yttrium, the lower GFA i.e. smaller critical cast diameter is rationalized by the smaller supercooled liquid region. The importance of the liquidus temperature is further highlighted by the loss of the fully amorphous structure at substitution of copper by scandium and holmium at 2 at.-pct. and above: for these substitution levels, the liquidus temperature is significantly higher than for the base alloy and this effect apparently outweighs the concomitant increase in T_g leading to a reduced GFA [35].

As suggested by Ponnambalam et al. [30], [36] the improving effect of incorporating elements with large atomic radius can be explained by the theory of atomic level stress induced during glass formation [37]. According to Senkov et al. [38], the atomic radius of scandium, holmium, and platinum are respectively 0.1641 nm, 0.17661 nm, and 0.1387 nm [38]. Thus, it is possible that the presence of scandium and holmium atoms with their larger atomic radii increases the strain in the lattice and favors the formation of glassy phase, and hence improves the thermal stability. This is the case only as long the formation of primary phases can be avoided.

4.2. Characteristic temperatures before and after fluxing with B₂O₃

As can be seen from Figure 6:7, there is no significant difference between the DSC curve of non-fluxed and fluxed samples, and the characteristic temperatures remain unchanged upon fluxing with B₂O₃. Given the kinetics of purification, the time of the fluxing process was chosen as long as possible, i.e. 40 h, comparable to fluxing times mentioned in the literature [39]. Hence, it seems that fluxing with boron oxide is not able to improve or bring about any change on the thermal fingerprint, i.e. T_g , T_x , T_s , and T_l , of the glassy alloy. Likewise, as can be seen from Figure 9, fluxing does not significantly change the oxygen content in the present alloy. Furthermore the hardness measurements on the fluxed sample and cast sample were respectively 572 ± 4 and 576 ± 6 HV_{0.1}, hence showing no significant difference.

In the cases where fluxing is successful in reducing the oxygen content, such as for the alloy Pd₇₆Si₁₈Cu₆, the most probable oxide compound that forms is silicon oxide, which exhibits a relatively higher affinity to oxygen [12]. For Pt_{49.95}Cu_{16.65}Si_{6.4}Ge₃B₂₄, however,

the Ellingham diagram [40] shows that, among the probable alloying elements forming oxides, i.e., silicon, germanium and boron, boron has the highest oxygen affinity. Thus, if the main oxide heterogeneities are B-containing compounds fluxing with the same boron-containing oxide compound might only occur if the oxides float to the surface and are absorbed in the fluxing agent, but the fluxing agent will not be able to create a chemical potential gradient that reduces the oxides in situ. Hence, by fluxing it cannot be verified whether or not the reduction of the oxygen content has a beneficial effect on the GFA of the base alloy investigated here.

4.3. Oxygen levels before and after fluxing and oxygen scavenging

The analysis of the oxygen level for the fluxed and the two scandium containing alloys allows for deducing that the oxygen level as such, when lowered from above 15 ppm to below 5 ppm, has no observable effect on the characteristic temperatures of the alloy. It should be noted that the initial oxygen content in noble metal based alloys such as platinum or palladium are inherently lower (tens of ppm) compared to reactive systems such as Zr-based alloys with higher oxygen contents (hundreds of ppm) [29]. The same level of oxygen reduction is obtained when added as little as 100 ppm of scandium or as much as 1 at.-pct. of scandium; hence, it can be deduced that the increase in T_g and T_x is solely due to the presence of the large scandium atoms and not an effect linked to the oxygen content. This stands to reason in as much that oxygen in the form of oxides is not expected to have any effect on the glass transition. In turn, if one considers the difference between T_x and T_g essentially as a measure for the mobility of atoms, a parallel shift in T_g and T_x due to minor alloying with RE and group IIIA elements stands also to reason and would be a sign that the crystallization process is essentially not affected by minor alloying. This is roughly obeyed by all alloying additions, except for yttrium where the crystallites present after suction casting may be such that they facilitate further crystallization. However, we currently do not have an explanation why yttrium is acting in this way.

5. Conclusions

From the results and the discussion presented above the following conclusions are drawn:

- Rare earth and group IIIA elements have a strongly increasing effect both on the glass transition and the crystallization temperature in BMGs with the general formu-

la $\text{Pt}_{49.95}\text{Cu}_{16.65-x}\text{M}_x\text{Si}_{6.4}\text{Ge}_3\text{B}_{24}$ with $\text{M} = \text{Y}, \text{Sc}, \text{Sm}, \text{Dy}, \text{Tb}, \text{Gd}, \text{and Ho}$, provided they can be produced in fully amorphous form.

- Whether or not the substitutions for copper lead to fully amorphous structures seems to be linked to the effect of the substitution on the liquidus temperature.
- For additions of scandium and holmium of up to 1.5 at.-pct. 2 mm diameter rods could be obtained fully amorphous by suction casting in a copper mold.
- An oxygen content in the range between roughly 3 and 20 ppm has no effect neither on the T_g nor on the T_x in the alloys studied here
- Prolonged fluxing (40h @ 1150 °C) in B_2O_3 was found to be ineffective in reducing the oxygen content in the alloy $\text{Pt}_{49.95}\text{Cu}_{16.65}\text{Si}_{6.4}\text{Ge}_3\text{B}_{24}$.
- As little as 100 ppm of scandium can effectively reduce the oxygen content in metallic glass from above 15 ppm to below the detection limit of the inert gas analyzer used for oxygen content measurement, i.e. 5 ppm.

Composition [at.-pct.]	State*	Proc.	T _g [°C]	T _x [°C]	T _s [°C]	T _l [°C]	ΔH [J/g]	HV _{0.1/0.5} [kgfmm ⁻²]
Pt _{49.95} Cu _{16.65} Si _{6.4} Ge ₃ B ₂₄	g	2 mm cast	305	359	574	657	44	565
Pt _{49.95} Cu _{15.65} Sm ₁ Si _{6.4} Ge ₃ B ₂₄	pc	2 mm cast	308	358	572	712	39	562
Pt _{49.95} Cu _{15.65} Gd ₁ Si _{6.4} Ge ₃ B ₂₄	pc	2 mm cast	314	362	572	770	37	538
Pt _{49.95} Cu _{15.65} Tb ₁ Si _{6.4} Ge ₃ B ₂₄	pc	2 mm cast	314	366	572	661	39	556
Pt _{49.95} Cu _{15.65} Sc ₁ Si _{6.4} Ge ₃ B ₂₄	g	2 mm cast	315	368	575	657	37	568
Pt _{49.95} Cu _{15.65} Y ₁ Si _{6.4} Ge ₃ B ₂₄	pc	2 mm cast	315	354	572	645	36	548
Pt _{49.95} Cu _{15.65} Dy ₁ Si _{6.4} Ge ₃ B ₂₄	g	2 mm cast	316	365	576	648	35	557
Pt _{49.95} Cu _{15.65} Ho ₁ Si _{6.4} Ge ₃ B ₂₄	g	2 mm cast	314	370	573	643	35	574
Pt _{49.95} Cu _{16.15} Sc _{0.5} Si _{6.4} Ge ₃ B ₂₄	g	2 mm cast	310	364	578	657	39	563
Pt _{49.95} Cu _{15.15} Sc _{1.5} Si _{6.4} Ge ₃ B ₂₄	g	2 mm cast	320	379	575	720	32	574
Pt _{49.95} Cu _{14.65} Sc ₂ Si _{6.4} Ge ₃ B ₂₄	pc	2 mm cast	323	377	588	810	26	599
Pt _{49.95} Cu _{13.65} Sc ₃ Si _{6.4} Ge ₃ B ₂₄	pc	2 mm cast	301	333	591	842	15	701
Pt _{49.95} Cu _{12.65} Sc ₄ Si _{6.4} Ge ₃ B ₂₄	pc	2 mm cast	301	330	589	870	15	686
Pt _{49.95} Cu _{16.15} Ho _{0.5} Si _{6.4} Ge ₃ B ₂₄	g	2 mm cast	312	367	577	657	41	566
Pt _{49.95} Cu _{15.15} Ho _{1.5} Si _{6.4} Ge ₃ B ₂₄	g	2 mm cast	318	373	571	713	32	582
Pt _{49.95} Cu _{14.65} Ho ₂ Si _{6.4} Ge ₃ B ₂₄	pc	2 mm cast	319	379	569	721	29	587
Pt _{49.95} Cu _{12.65} Ho ₄ Si _{6.4} Ge ₃ B ₂₄	pc	2 mm cast	311	323	572	844	13	689
Pt _{49.95} Cu _{16.65} Si _{6.4} Ge ₃ B ₂₄	g	5 mm cast	307	354	575	657	41	576
Pt _{49.95} Cu _{16.65} Si _{6.4} Ge ₃ B ₂₄	g	5 mm fluxed cast	307	354	575	657	42	572
Pt _{49.95} Cu _{16.64} Sc _{0.01} Si _{6.4} Ge ₃ B ₂₄	g	0.75 mm cast	301	357	574	657	42	560
Pt _{49.95} Cu _{16.65} Si _{6.4} Ge ₃ B ₂₄	g	0.75 mm cast	301	357	575	657	43	557
Pt _{49.95} Cu _{15.65} Sc ₁ Si _{6.4} Ge ₃ B ₂₄	g	0.75 mm cast	315	370	576	657	37	569

* g and pc stand for glassy and partially crystalline, respectively.

Table 6:1 Chemical composition, characteristic temperatures, and microhardness of all Pt-Cu -Si-Ge-B-based samples produced in this work. The characteristic temperatures were measured upon the first heating from the glassy state.

Acknowledgements

The authors wish to acknowledge financial support for this work by EPFL contract no. 535 627.

References:

- [1] M. F. Ashby and A. L. Greer, "Metallic glasses as structural materials," *Scr. Mater.*, vol. 54, no. 3, pp. 321–326, Feb. 2006.
- [2] E. Axinte, "Metallic glasses from 'alchemy' to pure science: Present and future of design, processing and applications of glassy metals," *Mater. Des.*, vol. 35, pp. 518–556, Mar. 2012.
- [3] Y. Saotome, Y. Fukuda, I. Yamaguchi, and A. Inoue, "Superplastic nanoforming of optical components of Pt-based metallic glass," *J. Alloys Compd.*, vol. 434–435, pp. 97–101, May 2007.
- [4] G. Kumar, H. X. Tang, and J. Schroers, "Nanomoulding with amorphous metals," *Nature*, vol. 457, no. 7231, pp. 868–872, Feb. 2009.
- [5] W. H. Wang, C. Dong, and C. H. Shek, "Bulk metallic glasses," *Mater. Sci. Eng. R Rep.*, vol. 44, no. 2–3, pp. 45–89, Jun. 2004.
- [6] H. S. Chen, "Glassy metals," *Rep. Prog. Phys.*, vol. 43, no. 4, pp. 353–432, Apr. 1980.
- [7] J. Schroers, "Processing of Bulk Metallic Glass," *Adv. Mater.*, vol. 22, no. 14, pp. 1566–1597, Dec. 2009.
- [8] G. J. Hao, Y. Zhang, J. P. Lin, Y. L. Wang, Z. Lin, and G. L. Chen, "Bulk metallic glass formation of Ti-based alloys from low purity elements," *Mater. Lett.*, vol. 60, no. 9–10, pp. 1256–1260, May 2006.
- [9] W. PENG and Y. ZHANG, "Micro-alloying of yttrium in Zr-based bulk metallic glasses," *Prog. Nat. Sci. Mater. Int.*, vol. 21, no. 1, pp. 46–52, Feb. 2011.
- [10] G. Hao, F. Ren, Y. Zhang, and J. Lin, "Role of yttrium in glass formation of Ti-based bulk metallic glasses," *Rare Met.*, vol. 28, no. 1, pp. 68–71, Feb. 2009.
- [11] J. Schroers and W. L. Johnson, "Ductile Bulk Metallic Glass," *Phys. Rev. Lett.*, vol. 93, no. 25, p. 255506, Dec. 2004.
- [12] D. Granata, E. Fischer, V. Wessels, and J. F. Löffler, "Fluxing of Pd–Si–Cu bulk metallic glass and the role of cooling rate and purification," *Acta Mater.*, vol. 71, pp. 145–152, Jun. 2014.
- [13] D. Granata, E. Fischer, V. Wessels, and J. F. Löffler, "The detrimental effect of flux-induced boron alloying in Pd–Si–Cu bulk metallic glasses," *Appl. Phys. Lett.*, vol. 106, no. 1, p. 11902, Jan. 2015.
- [14] N. Chen *et al.*, "Flux-induced structural modification and phase transformations in a Pd₄₀Ni₄₀Si₄P₁₆ bulk-glassy alloy," *Acta Mater.*, vol. 58, no. 18, pp. 5886–5897, Oct. 2010.
- [15] J. Schroers, Y. Wu, and W. L. Johnson, "Heterogeneous influences on the crystallization of Pd₄₃Ni₁₀Cu₂₇P₂₀," *Philos. Mag. A*, vol. 82, no. 6, pp. 1207–1217, Apr. 2002.
- [16] J. J. Wall *et al.*, "Heterogeneous nucleation in a glass-forming alloy," *Appl. Phys. Lett.*, vol. 92, no. 24, p. 244106, Jun. 2008.
- [17] S. Mukherjee, Z. Zhou, J. Schroers, W. L. Johnson, and W. K. Rhim, "Overheating threshold and its effect on time–temperature–transformation diagrams of zirconium based bulk metallic glasses," *Appl. Phys. Lett.*, vol. 84, no. 24, pp. 5010–5012, Jun. 2004.
- [18] Z. Liu *et al.*, "Pronounced ductility in CuZrAl ternary bulk metallic glass composites with optimized microstructure through melt adjustment," *AIP Adv.*, vol. 2, no. 3, p. 32176, Sep. 2012.
- [19] H. Kui, A. Greer, and D. Turnbull, "Formation of Bulk Metallic-Glass by Fluxing," *Appl. Phys. Lett.*, vol. 45, no. 6, pp. 615–616, 1984.
- [20] B. A. Legg, J. Schroers, and R. Busch, "Thermodynamics, kinetics, and crystallization of Pt_{57.3}Cu_{14.6}Ni_{5.3}P_{22.8} bulk metallic glass," *Acta Mater.*, vol. 55, no. 3, pp. 1109–1116, Feb. 2007.
- [21] H. S. Chen and D. Turnbull, "Formation, stability and structure of palladium-silicon based alloy glasses," *Acta Metall.*, vol. 17, no. 8, pp. 1021–1031, Aug. 1969.
- [22] A. Inoue, T. Aoki, and H. Kimura, "Effect of B Addition on Extension of Supercooled Liquid Region before Crystallization in Pd–Cu–Si Amorphous Alloys," *Mater. Trans. JIM*, vol. 38, no. 2, pp. 175–178, 1997.
- [23] R. D. Conner, R. E. Maire, and W. L. Johnson, "Effect of oxygen concentration upon the ductility of amorphous Zr₅₇Nb₅Al₁₀Cu_{15.4}Ni_{12.6}," *Mater. Sci. Eng. A*, vol. 419, no. 1–2, pp. 148–152, Mar. 2006.

- [24] J. Eckert, N. Mattern, M. Zinkevitch, and M. Seidel, "Crystallization Behavior and Phase Formation in Zr–Al–Cu–Ni Metallic Glass Containing Oxygen," *Mater. Trans. JIM*, vol. 39, no. 6, pp. 623–632, 1998.
- [25] A. Gebert, J. Eckert, and L. Schultz, "Effect of oxygen on phase formation and thermal stability of slowly cooled Zr₆₅Al_{7.5}Cu_{17.5}Ni₁₀ metallic glass," *Acta Mater.*, vol. 46, no. 15, pp. 5475–5482, Sep. 1998.
- [26] Z. P. Lu, C. T. Liu, and W. D. Porter, "Role of yttrium in glass formation of Fe-based bulk metallic glasses," *Appl. Phys. Lett.*, vol. 83, no. 13, pp. 2581–2583, Sep. 2003.
- [27] W. H. Wang, "Roles of minor additions in formation and properties of bulk metallic glasses," *Prog. Mater. Sci.*, vol. 52, no. 4, pp. 540–596, May 2007.
- [28] Z. P. Lu and C. T. Liu, "Role of minor alloying additions in formation of bulk metallic glasses: A Review," *J. Mater. Sci.*, vol. 39, no. 12, pp. 3965–3974, 2004.
- [29] A. A. Kündig *et al.*, "Influence of low oxygen contents and alloy refinement on the glass forming ability of Zr_{52.5}Cu_{17.9}Ni_{14.6}Al₁₀Ti₅," *Mater. Trans.*, vol. 43, no. 12, pp. 3206–3210, 2002.
- [30] V. Ponnambalam, S. J. Poon, and G. J. Shiflet, "Fe-based bulk metallic glasses with diameter thickness larger than one centimeter," *J. Mater. Res.*, vol. 19, no. 5, pp. 1320–1323, 2004.
- [31] H. Kazemi, C. Cattin, M. Blank, and L. Weber, "Development of a new family of phosphorous-free Pt-based bulk metallic glasses," *J. Alloys Compd.*
- [32] H. Kazemi, C. Cattin, G. Hodel, T. Pachova, and L. Weber, "Effect of partial crystallization in Pt-Si-B-based bulk metallic glasses on glass transition and crystallization of the remaining amorphous matrix," *J. Non-Cryst. Solids*. (Submitted)
- [33] H. Kazemi, C. Cattin, A. Arakcheeva, and L. Weber, "Synchrotron radiation X-ray diffraction study of crystallization in Pt-Si-B-Ge-Cu bulk metallic glass." (Submitted)
- [34] B. Yang, C. T. Liu, and T. G. Nieh, "Unified equation for the strength of bulk metallic glasses," *Appl. Phys. Lett.*, vol. 88, no. 22, p. 221911, May 2006.
- [35] D. Turnbull, "Under what conditions can a glass be formed?," *Contemp. Phys.*, vol. 10, no. 5, pp. 473–488, 1969.
- [36] V. Ponnambalam, S. J. Poon, and G. J. Shiflet, "Fe–Mn–Cr–Mo–(Y,Ln)–C–B (Ln = Lanthanides) bulk metallic glasses as formable amorphous steel alloys," *J. Mater. Res.*, vol. 19, no. 10, pp. 3046–3052, 2004.
- [37] T. Egami and Y. Waseda, "Atomic size effect on the formability of metallic glasses," *J. Non-Cryst. Solids*, vol. 64, no. 1–2, pp. 113–134, Apr. 1984.
- [38] O. N. Senkov and D. B. Miracle, "Effect of the atomic size distribution on glass forming ability of amorphous metallic alloys," *Mater. Res. Bull.*, vol. 36, no. 12, pp. 2183–2198, Oct. 2001.
- [39] K.-F. Yao, Y.-Q. Yang, and N. Chen, "Mechanical properties of Pd–Cu–Si bulk metallic glass," *Intermetallics*, vol. 15, no. 5–6, pp. 639–643, May 2007.
- [40] D. R. Gaskell, *Introduction to the Thermodynamics of Materials, Fifth Edition*. CRC Press, 2008.

Chapter 7 Processing of BMGs

In this chapter a brief overview of the processing equipment constructed and used during this thesis is presented.

The main principle in fabrication of glassy alloys is avoiding uncontrolled crystallization. Therefore, understanding the kinetics of crystallization process in BMG forming alloys is necessary to develop fabrication processes. Furthermore, BMG's are one of the most sensible families of materials to processing parameters and composition. Schroers [186] in his review article presented a succinct review of the different processing methods of BMG's.

Parameters such as oxygen content or purity of the primary ingredients can significantly alter the physical and mechanical properties of glassy alloys [186–190]. Examples of this close dependence can be found in the significant influence of impurities such as oxygen on glass forming ability or mechanical properties of palladium or platinum based alloys [96,105,191]. Furthermore, oxide particles or other impurities tend to serve as potential heterogeneous sites, favoring crystallization thus reducing the glass forming ability [103,104,106,192,193].

Without exception, the alloy preparation for glassy alloys is done either under protective atmosphere or under vacuum. Often, the alloy production is decoupled from the quenching process needed for glass formation. Commonly for the alloys without problematic alloying elements such as phosphorous, the primary ingredients are brought to a relatively high temperature so the elements are incorporated in the liquid phase. For phosphorous containing alloys, the latter can be added through a pre-alloy or via powder metallurgy. The preparation methods of the ingots for BMG's can be categorized as following (inspired by [194]).

Equipment	Maximum temperature	Temperature control / measure	Short-comings
Resistive Furnace	1200 °C	Thermocouple controlled	Low maximum temperature, lack of agitation and mixing,
Arc melting	3000 °C	Impossible	High temperature gradient, no control of temperature, no low-vapor pressure materials
Gas pressure casting	1200 °C	Pyrometer	Reaction with crucible (Quartz, Graphite, Boron-nitride)
Injection casting	1200 °C or 3000 °C Depending on the crucible	Pyrometer	Reaction with crucible (Quartz, Graphite, Boron-nitride)
Melt spinning	3000 °C Depending on the crucible	Pyrometer	Not for bulk materials, reaction with crucible (Quartz, Graphite, Boron-nitride)

Table 7:1 Summary of possible fabrication methods for processing of BMG's (after [194].)

One of the critical steps in preparation of the alloys is choosing the appropriate crucible materials. Table 7:2 presents some of the choices of crucible materials as well as their service temperatures and particular issues that should be taken into consideration when using them. Most of the components of these crucibles are refractory compounds such as stable oxide. A practical approach for choosing the right crucible is to compare the stability of the oxide of the alloying elements with that of the refractory materials used in the crucible. This information can be obtained using Ellingham's diagram [195] as a first estimate. Affinity of the element forming the oxide to the melt must be considered as well.

Material	Chemical composition	Service Temperature	Shortcomings
Graphite	Carbon	<3000 °C	May cause carbon intake (e.g. in Fe, Ni-based BMG) or reaction (Si)
Alumina	Al ₂ O ₃	<2000 °C	Reaction with Boron, Zr or more stable oxide formers
Zirconia	ZrO ₂ (often containing Yttria)	<1500 °C	Cannot be used for alloys containing rare-earth metals
Boron-Nitride	BN	Depending on the reactions	Reaction with Al at 1050°C, Si at 1500 or Fe, Ni, Co at 1500 °C
Quartz	SiO ₂	1400 °C	Si uptake in the case of Palladium-based alloys, reaction with more stable oxide formers
Pyrex	SiO ₂ +B ₂ O ₃ Na ₂ O+Al ₂ O ₃	<850 °C	Low thermal stability.

Table 7:2 Different crucible materials and their respective properties (data from [196]).

As it was mentioned before it is of utmost importance that the melting and mixing of the ingredients be done under protective atmosphere preferably in the presence of an oxygen getter such as Zr or Ti using high purity Argon (99.9999%).

The alloy preparation and production during this project was carried out according to the sequence shown in Figure 7:1. In the following sections each of these production methods as well as the alloy preparation step are briefly discussed.

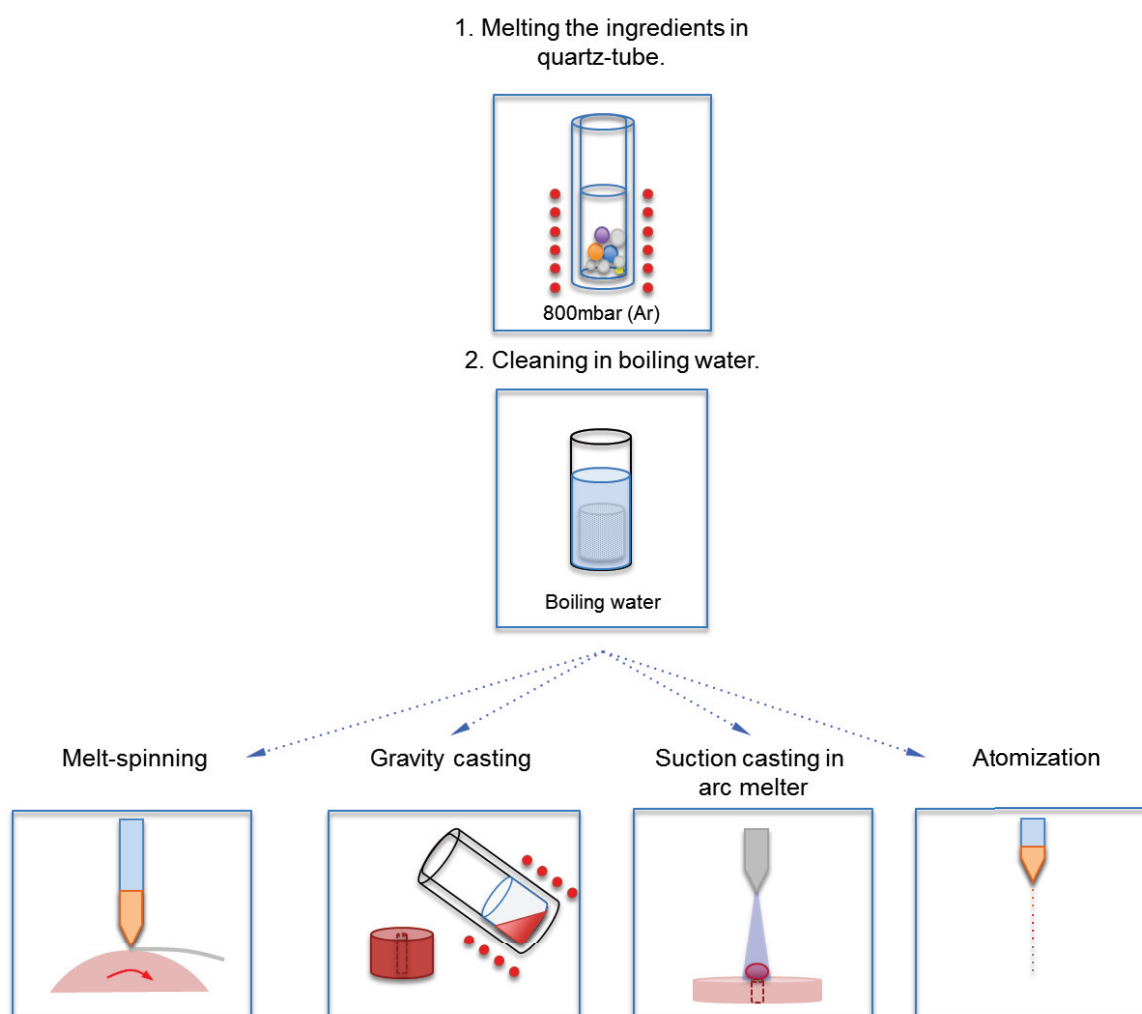


Figure 7:1 Alloy preparation and BMG production routes.

a. Alloy Preparation

Table 7:3 shows the purity of the alloying elements used during this project. The mass measurement for the constituents of the alloys was done with a precision of 0.001 g using a Mettler-Toledo PM400 balance.

The ingredients with the desired proportion were put in a quartz tube. The quartz tube has been rinsed with ethanol before manipulation and dried with pressurized air. Vacuum of 0.5mbar was then applied to clear the atmosphere, followed by purging with argon (purity $\geq 99.99\%$) pressure of 500mbar, giving a 1000x dilution factor to oxygen present in the atmosphere. The vacuum and purge steps were repeated for 5 times. Finally, the atmosphere of quartz tube was sealed under 800mbar of argon.

Element	Purity	Provider	Country	Remarks
Pt	99.99%.	Metalor Technologies SA	Switzerland	No element present by more than 16ppm.
B	99.5%.	ABCR GmbH&Co.KG	Germany	Boron in crystalline form.
Si	99.99%	Alfa Aesar GmbH&Co.KG	Germany	Polycrystalline
Ni	99.5%.	Alfa Aesar GmbH&Co.KG	Germany	
Cu	99.999%	Fluka AG	Switzerland	
Ag	99.99%.	Argor Heraeus	Switzerland	
Fe	99.98%	Alfa Aesar GmbH&Co.KG	Germany	
Ge	98.5%.	Fluka AG	Switzerland	Puriss grade.
Co	99.998%	JMC Co. Ltd.	Japan	Metal in form of rods.
Sc	99.99%	Cerac Inc.	U.S.A.	Chunks
Te	99.9%	Nucor Co.	U.S.A.	Powder
Dy	99.9%	Nucor Co.	U.S.A.	Powder
Gd	99.9%	Nucor Co.	U.S.A.	Powder
Sm	99.9%	Nucor Co.	U.S.A.	Powder
Ho	99.9%	Nucor Co.	U.S.A.	Powder

Table 7:3 Different first materials and their respective purity.

In the next step, the alloy was melted using an induction apparatus. The magnetic field provided by the induction unit agitated the melt, which enhances the mixing, and improves the homogeneity of the ingot. After the final melting the sample was left to cool down by natural convection air-cooling. The quartz tube was then broken to extract the alloy sample.

The mass variation of alloy ingredients and the final ingot prepared in this method was typically on the order of 0.001g. Thus, the superior precision, led to the decision of choosing

this process as the main alloy preparation method for all samples. Given that the element most susceptible to oxidation is Boron, often a very minor presence of oxygen leads to formation of B_2O_3 , which sticks to the wall of the quartz tube. Since B_2O_3 can be dissolved in boiling water all retracted ingots from the quartz tube were washed in boiling water to remove the undesired byproducts of melting.

b. Melt spinning

A melt spinner apparatus (LMM-EPFL, provided originally by Swissmetal Holding Ltd, Switzerland) equipped with a Copper-Beryllium alloy disc (Diameter=25cm, thickness=2 cm) has been used. The disc rotates at 1960 round/min, approximately corresponding to surface speed of 26m/s. The cooling rate in this method is dependent on parameters of the system such as the disc speed and the velocity of metal injection or the heat transfer rate through the disc, however an approximated value for cooling rate is tentatively 10^6 K/s [197]. The chamber of the melt spinner has been put under vacuum and purged 3 times before each process. Helium with 99.996% purity has been used as purging gas. Melting was done by an induction copper coil module attached to a solid-state induction generator, Type-TQ (Radyne Ltd. England).

The first efforts using small quantities of alloy (≤ 6 g) in large crucible were not consistently successfully due to lack of coupling for the induction coil, and absence of any quantified measure of the exact temperature of the metal before injection. This problem was solved by adding a piece of graphite to the system for providing the coupling. In order to avoid breaking the quartz tubes due to thermal dilatation difference between quartz and graphite, the gap between the quartz tube and graphite piece was filled with alumina wool of 1mm thickness. The general design of combined crucibles is shown in Figure 7:2.

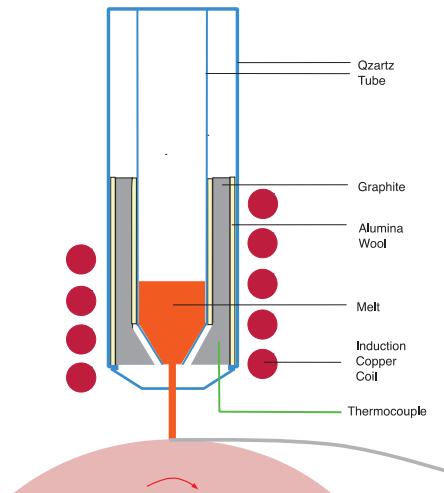


Figure 7:2 The configuration of the crucible and the induction coils used for melt spinning.

Thanks to the thermocouple implanted in the graphite piece, by adjusting the supplied electrical power to the system, the temperature of metal could be closely controlled and monitored before injection. For the melt spinning samples produced by the combination of crucibles, the temperature before injecting the metal was set to 1050°C.

c. Gravity casting

The gravity casting was carried out in a Balzer-Pfieffer induction-casting system as shown in Figure 7:3.

The casting temperature was measured by a thermocouple planted in the graphite crucible and the vacuum level was 10^{-5} mbar. Before heating the samples, the atmosphere was purged 5 times using Argon (99.9999%).



Figure 7:3 Balzer-Pfeiffer induction-casting system.

d. Arc-melting

An arc melter is a useful tool in preparing small quantities of alloys under protective atmospheres. It also gives the opportunity to suction casting alloys into different diameters. Figure 7:4 shows the MAM 1 arc-melter made by Edmund Buehler, Germany, used for producing suction cast samples during this thesis.

Besides using high purity protective gas and multiple purges, an oxygen getter of Zr or Ti was always melted for at least 15 seconds before melting the ingot. The casting was done under 1 bar of Ar (99.9999%).

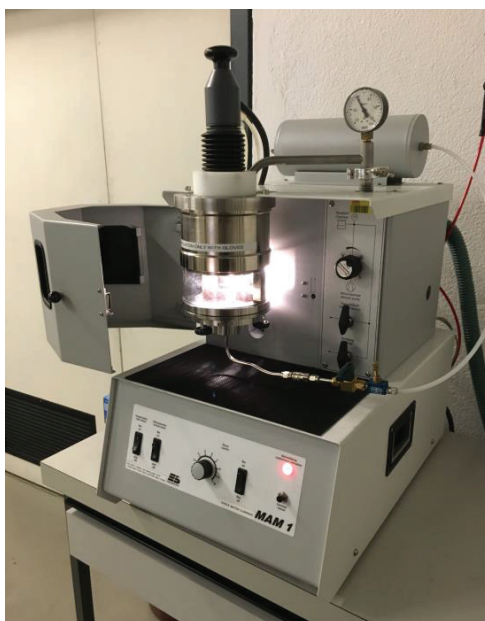


Figure 7:4 MAM 1 machine used for suction casting samples.

e. Atomization

i. Formation of droplets

The atomizer developed in the laboratory of mechanical metallurgy (LMM, EPFL) in the framework of this thesis is based on the production of droplets travelling in gaseous medium in the present case high purity helium. Standard atomizing equipment uses high relative velocity between the liquid phase and the gas phase to disintegrate the liquid stream. The high relative velocity can be generated by forced gas flow through nozzles hitting the

liquid stream or by ejecting small liquid droplets from a rotating disc. The atomizer built in LMM shown in Figure 7:5 is based on injecting a continuous flow of liquid metal into static helium medium. The liquid decomposes into small droplets due to the Rayleigh instability, cf. Figure 7:6.

As shown in Figure 7:5, the path of the droplets is vertical and the flow can be considered as a falling jet. Thanks to both gravity and the injection pressure, the liquid jet falls in a cylindrical form until a critical value at which it disintegrates into droplets.

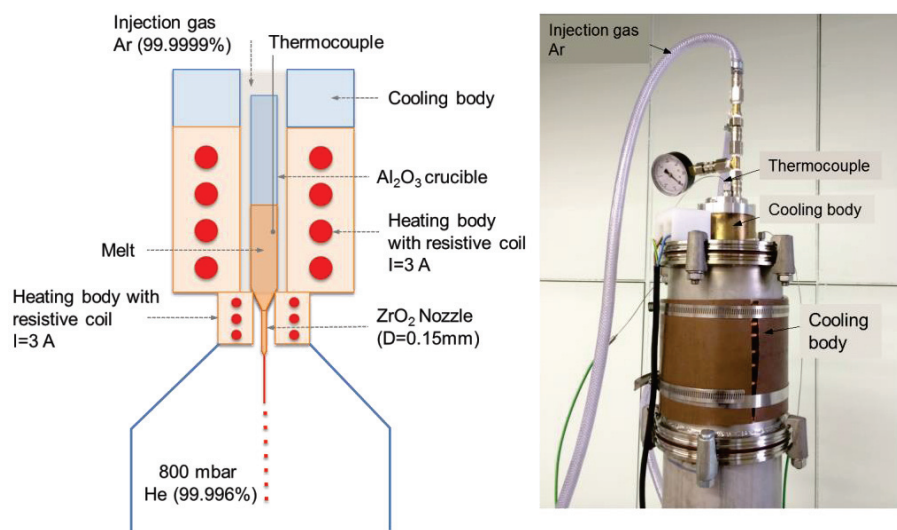


Figure 7:5 Schematic heating module of the atomizer.

Given the higher proportion of the surface energy per volume in thinner jets, they are more likely to disintegrate [198].

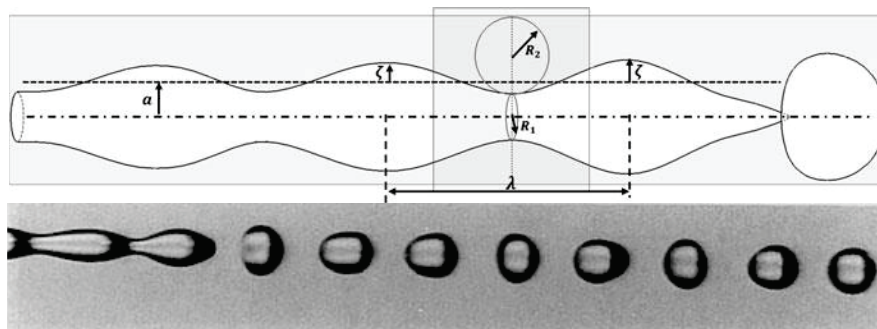


Figure 7:6 Upper image liquid column transformations according to Laplace law. Bottom image Uniform breakup of a water jet with diameter of 0.27 mm and velocity of 2.9 m/s subject to disturbance wavelength to diameter ratio of 4.6 (from [198]).

Instability analysis proves that the jet is stable for all angular disturbances; on the other hand axial disturbances make the jet unstable [198]. These axial disturbances give rise to

the variations of the radii of the liquid column. From Young-Laplace equation the pressure difference can be written as:

$$\Delta P = \gamma \left(\frac{1}{R_1} + \frac{1}{R_2} \right) \quad (7.1)$$

Figure 7:6 shows where the parameters in Eq. (3.1) intervene.

From Young-Laplace equation Eq. (7.1), by decreasing the radius of the thinner part, the pressure difference increases. The pressure gradient can be equally increased by increasing the surface tension γ . This pressure gradient pushes the fluid flow from the thinner section (R_2 , in Figure 7.6) to the larger section of the jet. Such transfer continues until the ultimate separation and disintegration of the jet takes place. Intuitively, the droplet formed from this disintegration, becomes spherical to minimize the high surface energy which is typical of molten metals [198].

Three energies are present in the process of atomization: surface energy, kinetic energy and energy loss due to friction. The shape of the liquid column with periodically changing radius could be described by a wave with a defined wavelength. For each of that wavelength, one principal droplet is formed. The size of the droplets and their size distribution is also a function of the size and shape of the nozzle [198]. According to standard theory for round nozzles, the droplets are expected to have a diameter roughly twice the diameter of the nozzle through which the liquid has passed.

The cooling of the droplets is in part by radiation and in part by convection. To optimize the heat transfer a good thermal conducting gas is preferable, which is why we have been using helium in our apparatus. The outlet velocity and hence the overpressure of the liquid must be selected carefully such that the exit speed of the liquid at the nozzle is smaller than the free falling speed of a sphere of the size expected from the nozzle diameter. If the exit speed is higher than the free falling speed, the liquid column gets squeezed and its diameter gets larger, leading to larger particles with lower rate of cooling (and the need for a longer distance to fall to reach fully solid state, since the heat extraction rate is proportional to the surface while the heat content is proportional to the volume).

The driving force for disintegration of the fluid is provided by the kinetic energy of the fluid in contact with the static medium (here He). Thus atomization of molten metals inherently requires the transfer of energy from the atomization medium to the molten metal and the creation of a large amount of surface area. The energy transferred from the atomization

medium (e.g. He) to the molten metal in the form of surface energy for unit mass of powder produced. The relative velocity between the liquid and the gas is one of the most important parameters determining the particle size. For a given geometry of nozzle, particle size is a function of the pressure of the atomizing media, and the melt flow rate which itself is determined by the gas injection pressure. For producing amorphous alloys through atomization considering the cooling rate for the solidification of the droplets is of utmost importance.

ii. Cooling and solidifying of droplets

Given the relatively small sizes of the atomized powder, normally having a Biot number much smaller than 0.1 ($B_i = hL_c/k_b$ h : heat transfer coefficient, $L_c = \text{Volume/surface}$ and k_b : thermal conductivity of the body.) the gradient of temperature within the particle is negligible and the temperature can be considered constant in the particle [198]. The cooling rate and the solidification time can be respectively written as Eq. (7.2) and Eq. (7.3) [198]:

$$\rho_d V_d C_{pd} \frac{dT_d}{dt} = -A_d (q_h + q_m + q_r) \quad (7.2)$$

where the subscript d denotes the particle properties (liquid or solid), C_{pd} the heat capacity, ρ_d the density, T_d the temperature, V_d the volume, and A_d the surface. The symbols q_h , q_m , and q_r denote the heat fluxes (per unit area) caused by the convective heat transfer, the convective mass transfer, and the thermal radiation, respectively. Upon further development of Eq. (7.2) (Page 332 of [198]) one can derive Eq. (7.3)

$$t = \frac{V\rho C_p}{Ah} \ln \left[\frac{T_\infty - T_s}{T_\infty - T_i} \right] \quad (7.3)$$

Where V is the volume, ρ the density, C_p the heat capacity, A the surface area, h the heat transfer coefficient, T_∞ the temperature infinitely far away from the droplet, T_s the solidus temperature and T_i the temperature at the moment the droplet enters in contact with the fluid [198].

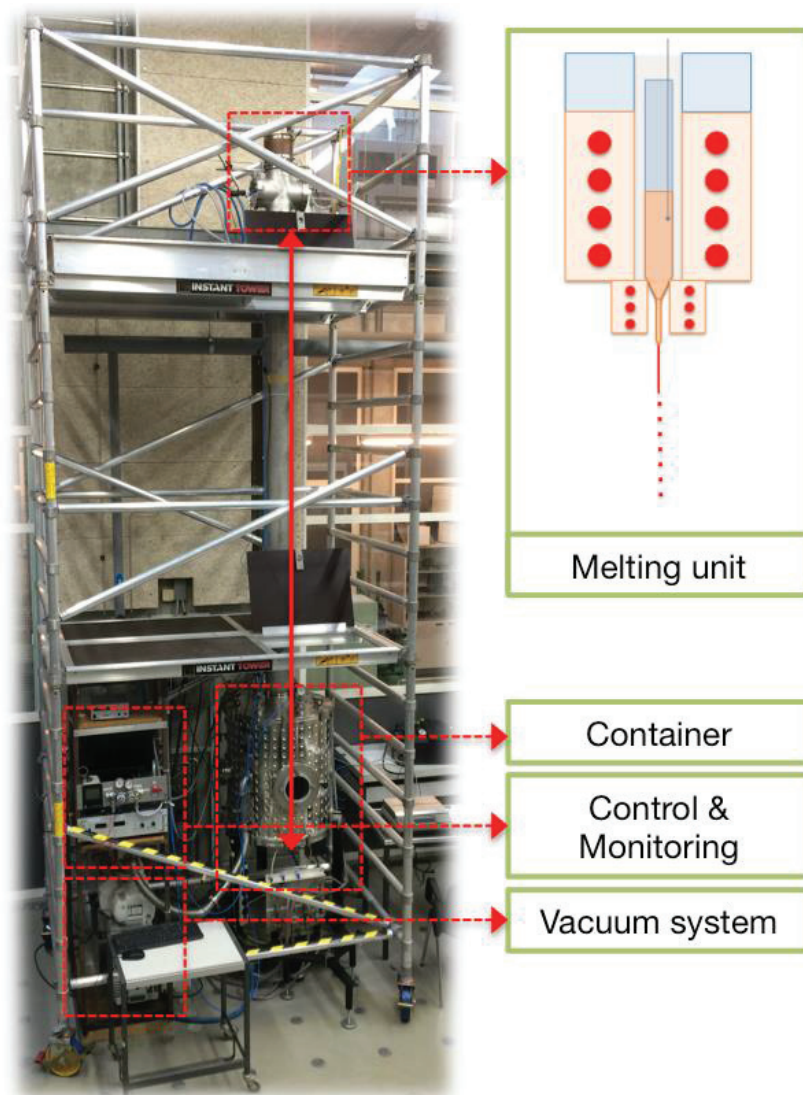


Figure 7:7 The atomizer developed in Laboratory of Mechanical Metallurgy (LMM, EPFL).
Figure 7:5 shows more details on the melting unit.

For crystalline alloys, as soon as crossing the solidus temperature, provided enough undercooling is provided, the molten droplet solidifies. Yet in the case of glass forming alloys it is necessary to reduce the temperature below the glass transition temperature. In the case of the alloys studied in this project, the T_g is commonly between 250 °C and 330 °C, so the time of flight before the impact with the container should be long enough so the temperature is reduced below the typical glass transition. Figure 7:7 shows the atomizer developed in Laboratory of Mechanical Metallurgy (LMM, EPFL).

The design of the atomizer is such that all of the components that come into contact with the melt are exchangeable so there will be no cross-contamination from one alloy to an-

other. Figure 3:8 shows an example of sieved particle 400 to 450 μm of the alloy $\text{Pt}_{49.95}\text{Si}_{6.4}\text{B}_{24}\text{Ge}_3\text{Cu}_{16.65}$ as well as the DSC pattern corresponding to the same sample batch.

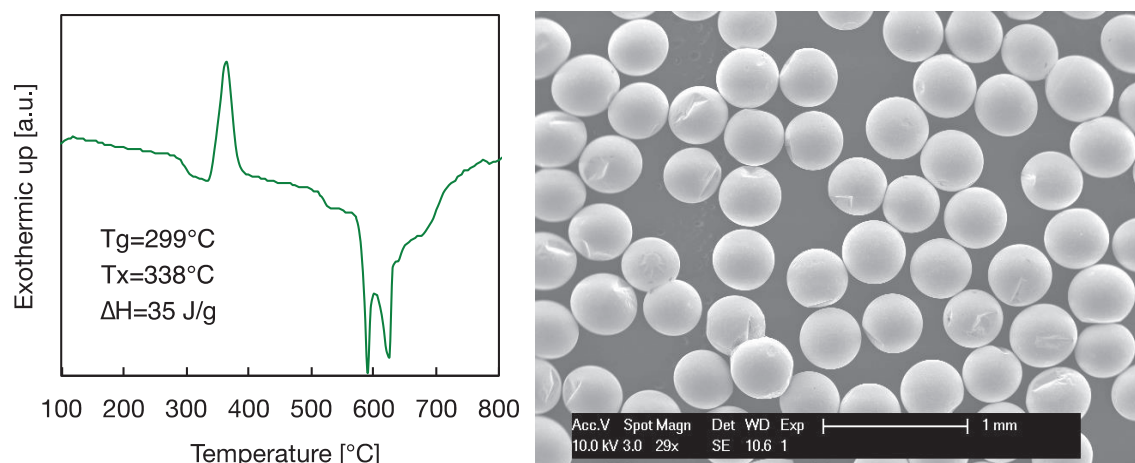


Figure 7:8 Particle of the alloy $\text{Pt}_{49.95}\text{Si}_{6.4}\text{B}_{24}\text{Ge}_3\text{Cu}_{16.65}$ with the particle size between 400 to 450 μm as well as the DSC pattern corresponding to the same sample.

f. Forming in the supercooled liquid region

For producing and forming of BMG's, the importance of avoiding crystallization has already been mentioned. Schroers [186] in his review article on thermoplastic forming (TPF) of BMG's has discussed the different aspects of this technology. He suggests *“Continuation of the rapid proliferation of BMG technology hinges on material costs and the advancement of TPF-based processing methods for commercial adaptation. [...] To appreciate their full range of attractive properties as a structural material, BMGs should, however, be used in geometries where at least one dimension is comparable with the processing zone. Resolving these issues might result in a societal impact of BMGs similar in magnitude to that of thermoplastics in the 20th century.”*

Ashby and Greer [187] suggest different application fields for BMG's as structural materials such as Springs, Tools, fashion items and MEMS. The features that these applications have in common are the high dimensional precision requirement and often complexity of geometry. Schroers [186] proposes that thermoplastic forming in supercooled liquid region can be the ultimate solution to produce parts as strong as metallic alloys with the same processability of plastics. Thermoplastic forming of BMG's can be described schematically as shown in Figure 7:9.

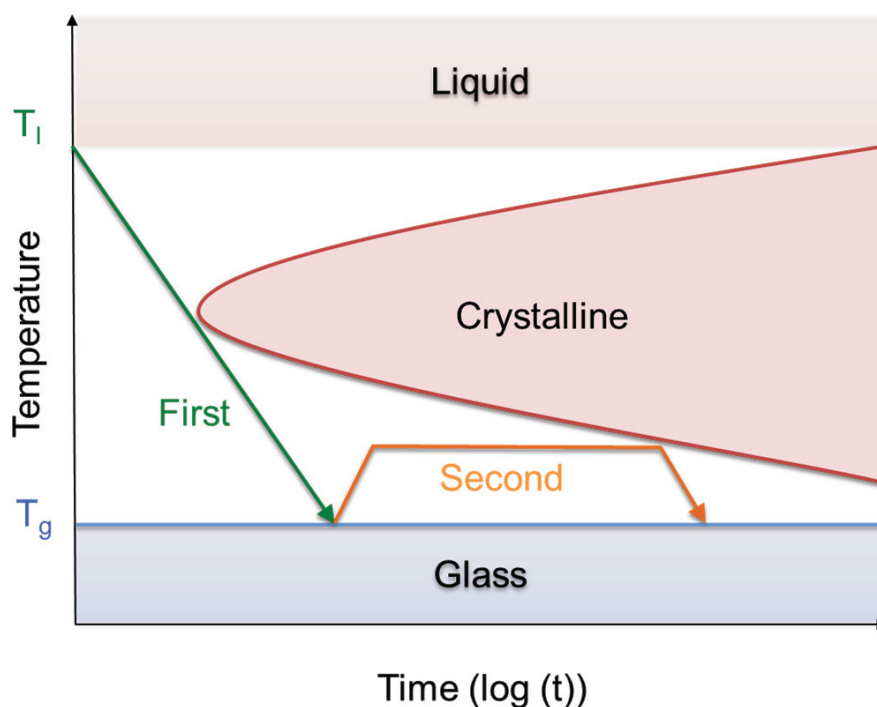


Figure 7:9 Producing BMG by rapid cooling and avoiding crystallization (First). Thermo-plastic forming in the supercooled liquid region ($T_g < T < T_x$) (Second). (drawn after [186])

As it can be seen in Figure 7:9, by avoiding the nose of crystallization T-T-T curve glass is formed in a metastable status. By heating the alloy above the T_g there is a rapid decrease in the viscosity down to values as low as 10^8 Pa·s, which becomes comparable to plastics above their T_g . The main idea of TPF-based forming is decoupling the first and second steps shown in Figure 7:9 and forming the metallic glasses from glassy feedstock [186]. This method can be compared to direct casting of BMG's into the final shape using die-casting or suction casting. As mentioned before, glass formers tend to be close to eutectic compositions with rather low-lying liquidus temperatures.

This is especially interesting for adopting the existing die casting solutions for aluminum, in order to produce BMG's. Furthermore, the solidification shrinkage in BMG formers is relatively small compared to crystalline alloys, e.g. upon solidification of Zr-based BMG the volume change is in the order of only 0.5% [199].

Schroers [199] suggests that in order to develop the processing parameters for TPF-based processing, one may consider creeping flow conditions. By doing so, no slip conditions are assumed, i.e., zero velocity of the liquid at the channel/liquid interface and a Reynolds

number of 0. Under these conditions, the formability of a BMG in the SCLR can be quantified using the Hagen–Poiseuille Equation [199]:

$$p = 32v \cdot \eta \frac{L}{d^2} \quad (7.4)$$

where p is the pressure level to move a liquid with viscosity η , at a velocity v , through a channel of thickness d and length L . The maximum time available for the forming process is limited by t_{onset} , i.e. the onset time of crystallization. By substituting $v = L/t_{\text{onset}}$ in Equation (7.4) one can write the maximum length that can be filled without crystallization [199]:

$$L = \sqrt{\frac{p \cdot t_{\text{onset}} \cdot d^2}{32\eta}} \quad (7.5)$$

Looking at Eq. (7.5) the filling length can be used to quantify the isothermal formability of BMGs in their SCLR. Thus, the formability depends on the viscosity and the filling time given by t_{onset} [186].

In this thesis upon achieving the first samples with the glassy structure with at least one dimension larger than 1 mm the viscosity was measured using parallel plate rheometry (Eq. 7.6). The viscosity, η , can be extracted at fixed load, F , from the position, h , vs. time, t , curve

$$\eta = -\frac{2Fh^3}{3\pi a^4 \frac{dh}{dt}} \quad (7.6)$$

where a the radius and $\frac{dh}{dt}$ is the rate of height change.

This method for measuring the viscosity is particularly useful in the vicinity of crystallization temperature in the super-cooled liquid region. The shortcoming of such method is that the measured viscosity is a function of the aspect ratio. However, for the aspect ratio smaller than 0.25 the measure viscosity can be considered as the equilibrium viscosity within the precision of the measurement [200].

Figure 7:10 depicts the evolution of viscosity as a function of temperature in the super-cooled liquid region for the alloy $\text{Pt}_{49.95}\text{Si}_{6.4}\text{B}_{24}\text{Ge}_3\text{Cu}_{16.65}$. It can be seen that the variation between two tests with identical aspect ratio is greater than the difference due to the effect of the aspect ratio. Interestingly, the viscosity decreases with the increase of temperature and upon approaching T_x , the viscosity increases rapidly due to formation of crystalline phases.

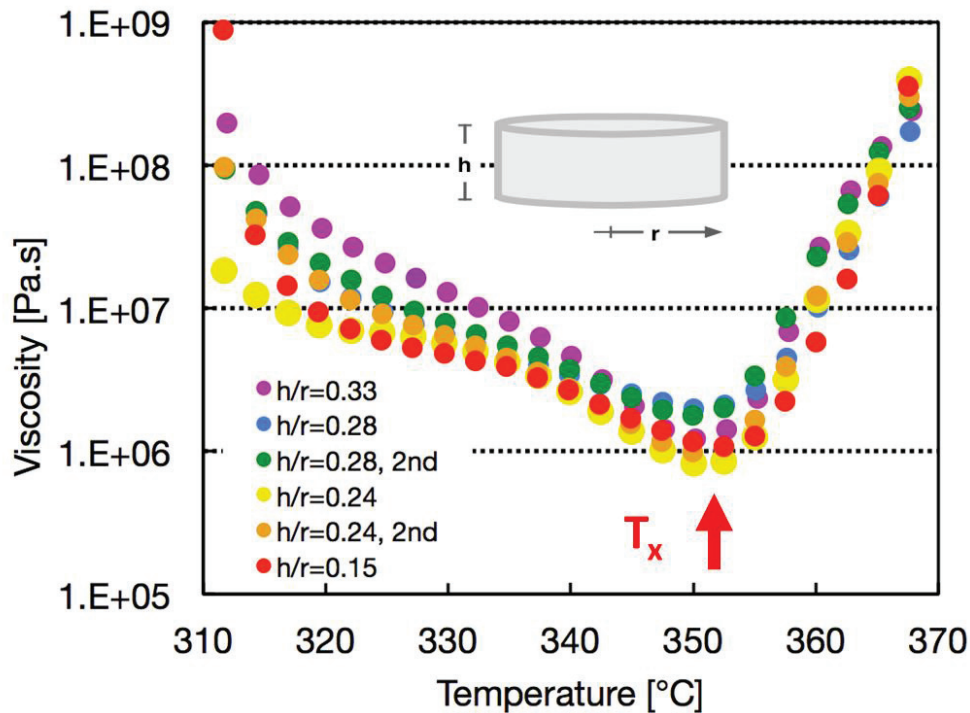


Figure 7:10 the evolution of viscosity in the super cooled liquid region. Measurement was carried out using a parallel plate rheometry in a TMA, on cast discs of 2mm diameter of alloy $\text{Pt}_{49.95}\text{Si}_{6.4}\text{B}_{24}\text{Ge}_3\text{Cu}_{16.65}$.

g. Fabrication of a watch case by thermoplastic forming

One of the objectives and as a matter of fact challenges set for this project was to produce a specific watchcase from the alloy $\text{Pt}_{49.95}\text{Si}_{6.4}\text{Ge}_3\text{B}_{24}\text{Cu}_{16.65}$ using thermoplastic forming in the supercooled liquid region similar to the one shown in Schroers review article [186].

Given the dimensions of the watch case direct casting was out of question. Furthermore, considering the highly detailed geometry of the watchcase, it was decided to produce the part initially by thermoplastic forming and later achieve the final shape through machining. Figure 7:11 shows the final geometry of the watchcase included within the shape produced by thermoplastic forming.

The general concept for producing the watch case through thermoplastic forming involves: i) casting plates of the alloy $\text{Pt}_{45.95}\text{Si}_{6.4}\text{B}_{24}\text{Ge}_3\text{Cu}_{16.65}$ while maintaining the glassy structure and ii) filling a mould cavity as shown in Figure 7:12 and 7:13 via a combination of extrusion and injection. The choice of the shape of the feedstock was aimed to minimize the interface compared to other possible forms such as pellets or powder. Briefly, the process

involves heating the mould (machined from DIN 1.4305 equivalent to AISI 304 for rapid machining) to the desired temperature inside a furnace, removing the mould from the furnace inserting the discs-shaped feedstock and then hydraulic pressing. Once the cross head of the press is at arrest and before the temperature of the feedstock approaches T_x the mould is cooled down in water.

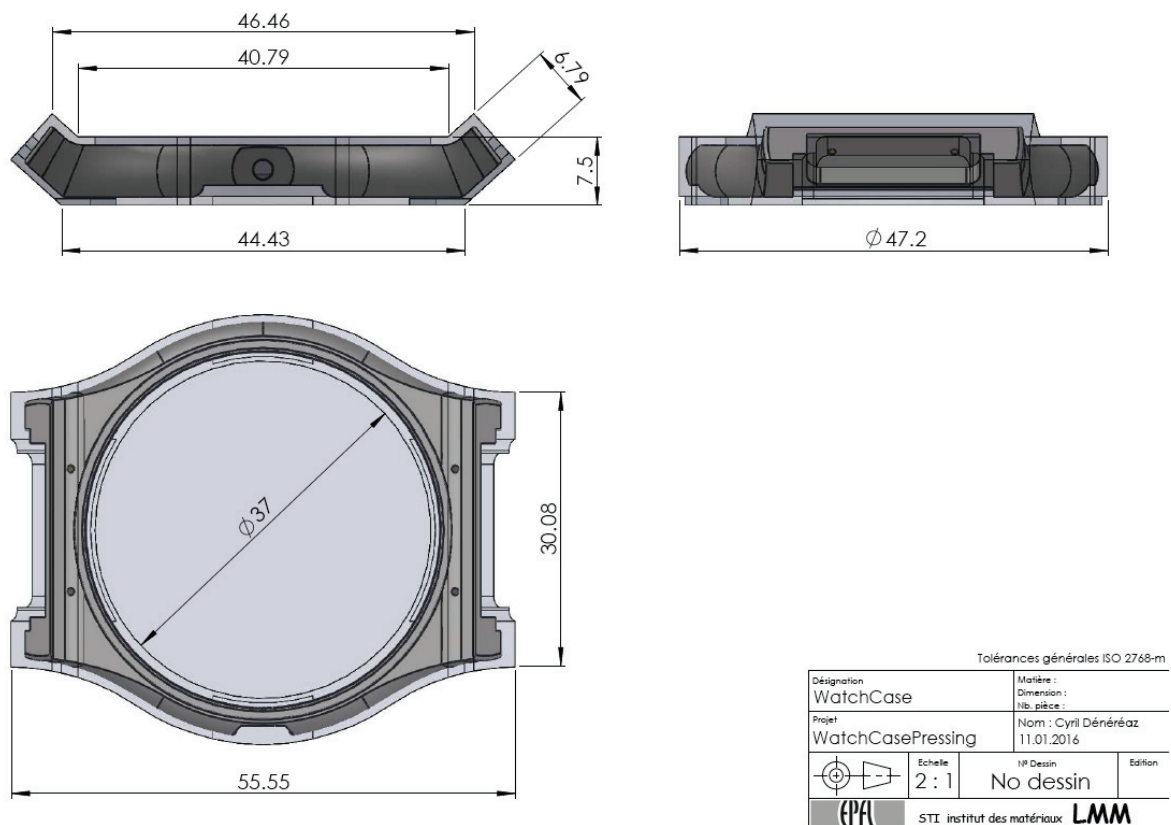


Figure 7:11 The final shape of the watch case compared to the near-final shape of the produced part.



The different production steps for producing the work piece are schematically shown in Figure 7:14. The production of the glassy feedstock for thermoplastic forming in the super-cooled liquid region is done following these steps (Figure 7:14, 1 to 4):

1. Mixing of ingredients and melting with induction in sealed quartz tube.
2. Induction melting of ingredients in quartz crucible to produce ingots of 10 to 30 g.
3. Cleaning the ingot in boiling water to remove the possible traces of B_2O_3 .
4. Arc-melting of ingots to add rare-earth metals (e.g. Sc) and further homogenize the ingots.
5. Induction melting of homogenized ingots in graphite crucible
6. Copper mould casting of discs of diameter 36 mm and thickness 3 mm.

For alloy $Pt_{45.95}Si_{6.4}B_{24}Ge_3Cu_{16.65}$ in general, going from step 1 to step 4, by induction melting ingredients directly in graphite crucible has proven to be not possible due to formation of 'precipitates', i.e. inhomogeneous dissolution of B and/or Ge. Steps 2 and 4 are therefore necessary for the production of homogeneous feedstock material.

As shown in Figure 7:14, the primary glassy materials are in the form of cast discs with diameter of 35 mm and thickness of 3.5 mm. These discs are cast into copper mould under protective atmosphere (Ar 99.9999%) using the Balzer-Pfeiffer casting machine shown in Figure 7:3. Temperature is recorded by means of a type K thermocouple inserted into the rim at the bottom of the graphite crucible, roughly 2 mm from the inside wall of the crucible. The following steps are performed: i) Heating of metal to 1100 °C at constant induction power of 4 kW; ii) Hold at 1100 °C for 2 min iii) Cooling to 1075 °C at constant induction power of 0.5 kW; iv) Cooling to 1050 °C at 0 kW and tilt-casting into copper mould at 1050 °C. A typical feedstock disc exhibits one or two visually distinct areas (of slightly reduced thickness), cf. Figure 7:15.

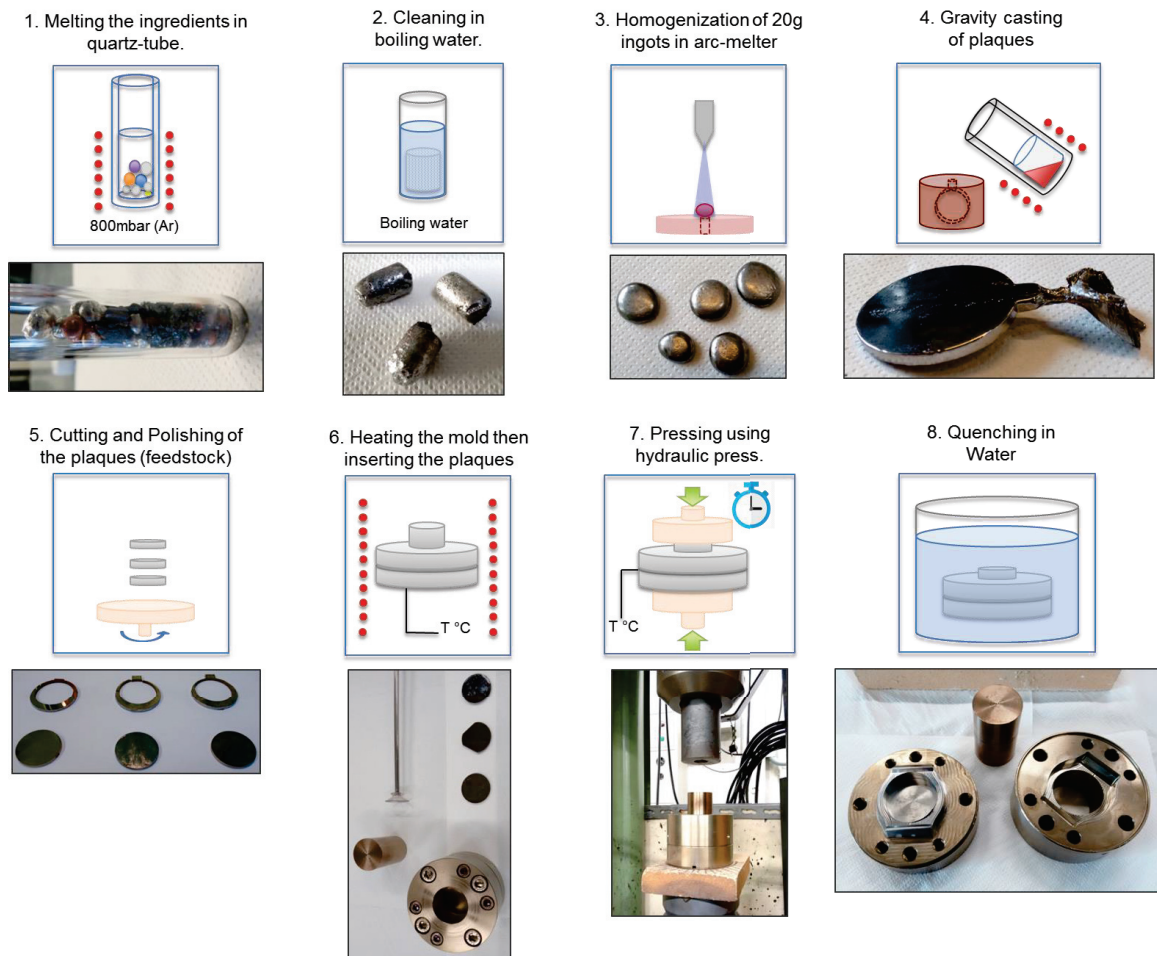


Figure 7:14 Different steps in production of watch-case shown in Figure 7:11.

To ensure that the entire work piece is glassy samples are cut from bulk at different zones of the disc and DSC and hardness measurements are carried out. Given the strong influence of crystallinity on hardness, the latter is used as an indication of the glassy state of the discs. Micro-hardness, DSC and XRD experiments have shown that feedstock discs produced according to the above protocol were fully glassy, and that those distinct areas were due to time-delayed solidification during form-filling, i.e. liquid metal running around already solidified but amorphous spots, and not due to partial crystallization during solidification.

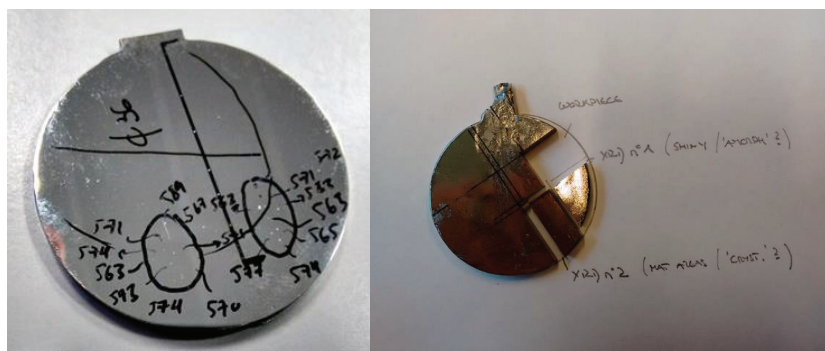


Figure 7:15 Typical glassy discs after casting. The discs are characterized by hardness and DSC measurement on the surface as well as samples cut from the bulk.

For preparing the glassy feedstock for thermoplastic forming, the surfaces of the discs are grinded with SiC paper and polished with 6 μm diamond particles.

The thermoplastic forming is done according to the following steps (Figure 7:14, 6 to 8):

1. Preheating of assembled mould and piston in oven. Temperature recorded on outer surface of assembled mould.
2. Removing of preheated mould from oven.
3. Adding of feedstock (3 discs of $d = 36 \text{ mm}$ and $t = 3 \text{ mm}$), one on top of the other, using a suction tool. Temperature of feedstock recorded on side in contact with bottom part of mould.
4. Closing of mould by adding piston.
5. Mounting of set-up onto moulding press.
6. Thermoplastic forming by applying compressive force and monitoring displacement of piston.
7. Fast cooling in H_2O bath once feedstock temperature recording approached T_x .

During the whole process the temperature of the mould is monitored thanks to a thermocouple inserted into the mould as shown in Figure 7:16. The same figure also shows the assembly of the mould as well as the final shape of the work piece produced by extrusion of the glassy materials in the supercooled liquid region.

The critical criterion for designing the mould is to make sure that the whole cavity of the work piece is filled by the flowing supercooled liquid after being subject to shear due to

extrusion. This is important to get rid of the interfaces between the three cast disc feed-stock.

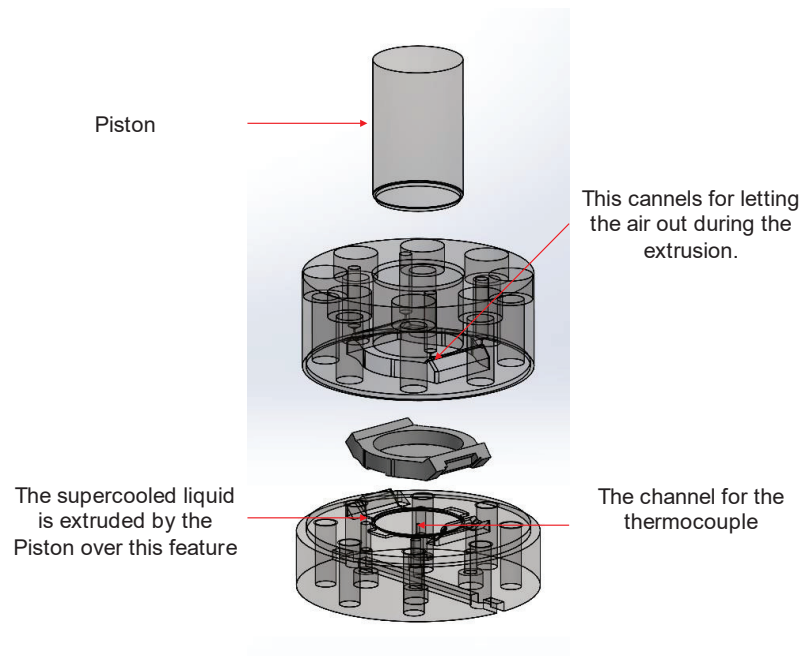


Figure 7:16 The assembly of the mould and the shape of the final work piece.

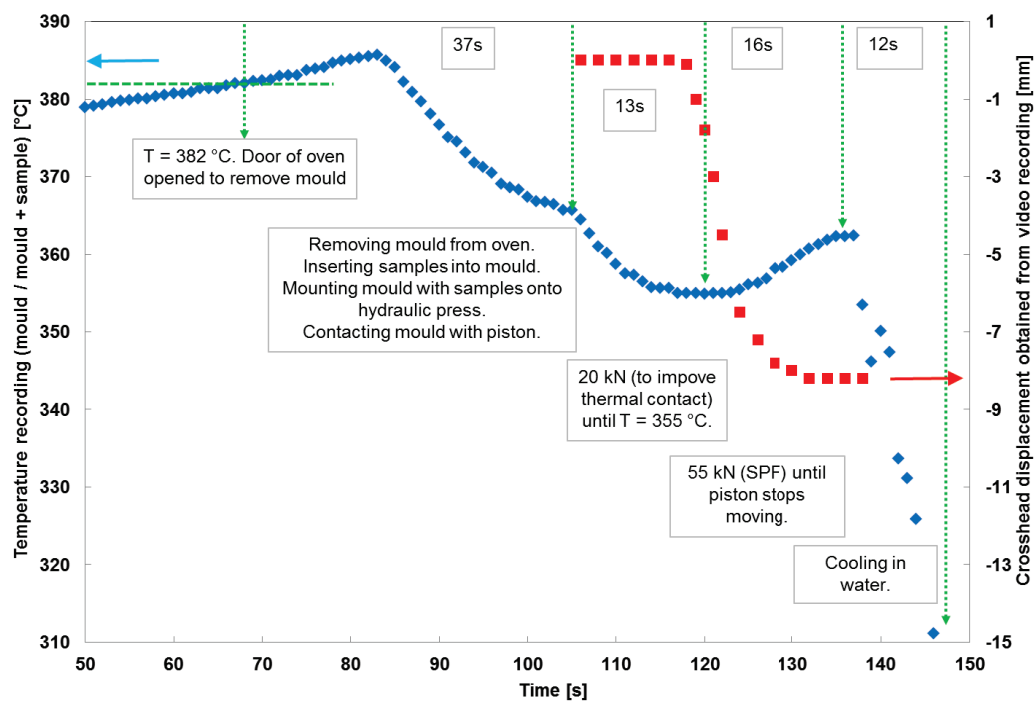


Figure 7:17 The temperature of the mould/sample during thermoplastic forming and the crosshead displacement of the hydraulic obtained by video recording.

Efforts have been directed towards quantifying the thermoplastic forming process by detecting the position of the piston (crosshead) as well as the temperature of the glassy feedstock during the whole process. Two curves can be obtained for the thermoplastic forming as shown in Figure 7:17.

After cooling the mould in water and achieving room temperature, the mould is opened as shown in Figure 7:18. Interestingly, as it can be seen in Figure 7:18, the surface details produced by this method are very precisely the machining marks on the mould. This is not further surprising as the hydrostatic pressure in the viscous metal is on the order of 20 MPa a pressure corresponding to a surface curvature of $0.1\ \mu\text{m}$, assuming a characteristic surface tension of $1\ \text{J/m}^2$. This is also highlighted by many articles on TPF formed microcomponents. Furthermore, the XRD and optical microscopy analysis showed that the work piece is entirely glassy and there are no traces of the initial interfaces between the cast plates.

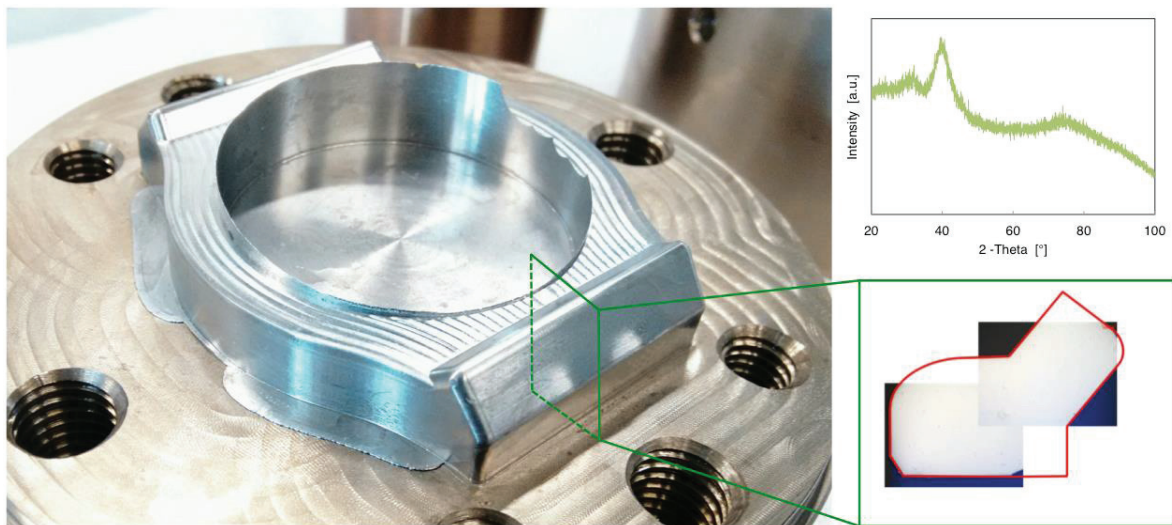


Figure 7:18 The final result of the forming in supercooled liquid region. The XRD pattern is done on the section outlined by a red line.

h. Laser surface treatment

It was previously shown that partial crystallization leads to a significant increase of hardness but also causes loss of ductility in the alloy $\text{Pt}_{49.95}\text{Si}_{6.4}\text{Ge}_3\text{B}_{24}\text{Cu}_{16.65}$ (Chapter 4). Laser surface treatment is a method to locally introduce crystallization only on the surface while maintaining the bulk in the glassy phase for retaining its superior ductility. For doing so, a Nanosecond pulsed laser by PyroPhotonics Lasers Inc. as shown in Figure 7:20 was used.



Figure 7:19 Nanosecond pulsed laser by PyroPhotonics Lasers Inc. used for surface treatment of the alloy $\text{Pt}_{49.95}\text{Si}_{6.4}\text{Ge}_{2.5}\text{B}_{24}\text{Cu}_{15.8}\text{Sc}_{0.85}$.

The laser lines scan for introducing partial crystallization was done on the cast slabs of 3.5 mm thickness from the alloy $\text{Pt}_{49.95}\text{Si}_{6.4}\text{Ge}_{2.5}\text{B}_{24}\text{Cu}_{15.8}\text{Sc}_{0.85}$. The average power of the laser was 25 W, the pulsed length was set to 600 ns with a repetition rate of 100 kHz. The line scans were done with an under focus of 10 mm from the focal point of the laser, i.e. the focal point of the laser was above the metal surface and the processing speeds were chosen as 1.8, 2, 3 and 4 mm/s. Figure 7:21 shows the SE-SEM image of the line scan done with 3 mm/s speed.

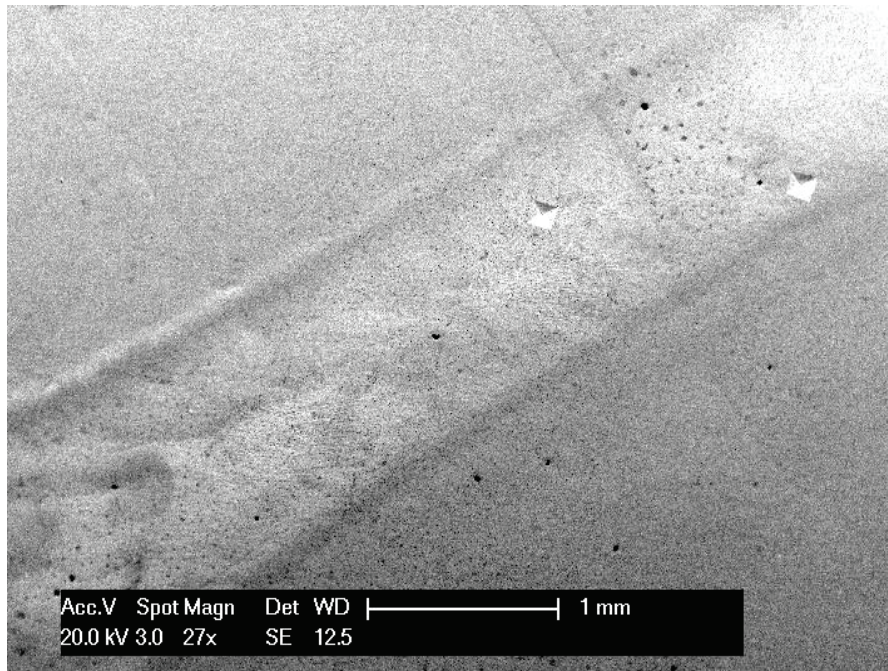


Figure 7:20 The secondary electron image of the line scan done on the sample of the alloy $\text{Pt}_{49.95}\text{Si}_{6.4}\text{Ge}_{2.5}\text{B}_{24}\text{Cu}_{15.8}\text{Sc}_{0.85}$. The hardness indentations done under the load of 50g are also visible on the top right.

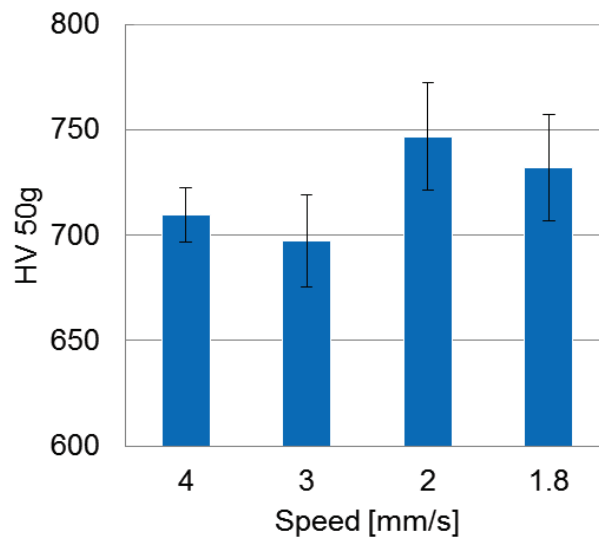


Figure 7:21 The hardness measurements done on the surface of the treated area, the indentations are similarly done as shown in Figure 7:20.

There is a clear increase of the hardness upon surface treatment with the laser, cf. Figure 7:23. Similar increase of hardness has been observed elsewhere in glassy systems [201].

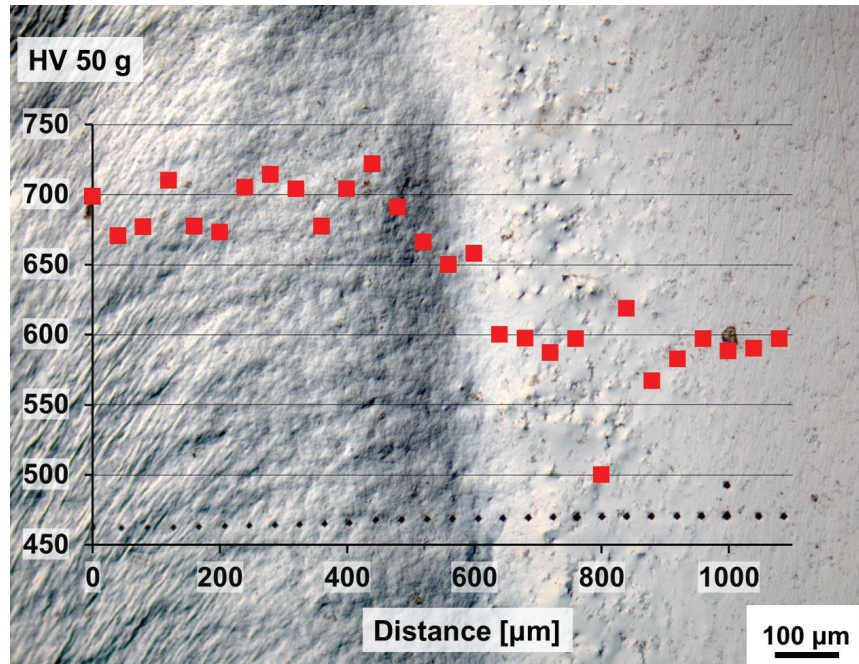


Figure 7:21 The hardness increase in the surface treatment by laser done at the speed of 5 mm/s.

To achieve crystallization and avoid vitrification of the surface the cooling rate should be low enough. For this initial pilot study the parameters for laser surface treatment were acquired experimentally. Unfortunately the thermal conductivity of the alloy $\text{Pt}_{49.95} \text{Si}_{6.4} \text{Ge}_{2.5} \text{B}_{24} \text{Cu}_{15.8} \text{Sc}_{0.85}$ is not yet measured directly yet a rough estimation can be made based on the Wiedemann-Franz law describing the correlation of electrical and thermal conductivities. The electrical conductivity of cast disc of 3.5 mm thickness from alloy $\text{Pt}_{49.95} \text{Si}_{6.4} \text{Ge}_{2.5} \text{B}_{24} \text{Cu}_{15.8} \text{Sc}_{0.85}$ was measured using a SigmaTest 2.069 which uses induced Eddy current to measure the electrical resistivity. The average value of 10 measurements of electrical conductivity was $0.493 \pm 0.002 \cdot 10^6 \text{ S/m}$. Using the correlation shown by Terada et al. [202] for Pt-Ni and Pt-V alloys, as well as the Wiedemann-Franz law, a thermal conductivity of 5 to 6 W/mK can be expected for this alloy.

After surface treatment with the laser for superficial hardening, commonly, a post-processing step such as final polishing or machining might be necessary, it is hence important to know the depth of the hardening induced by the partial crystallization. Figure 7:23 shows the hardening depth of the surface treatment lines whose measures of surface hardness was shown previously in Figure 7:21.

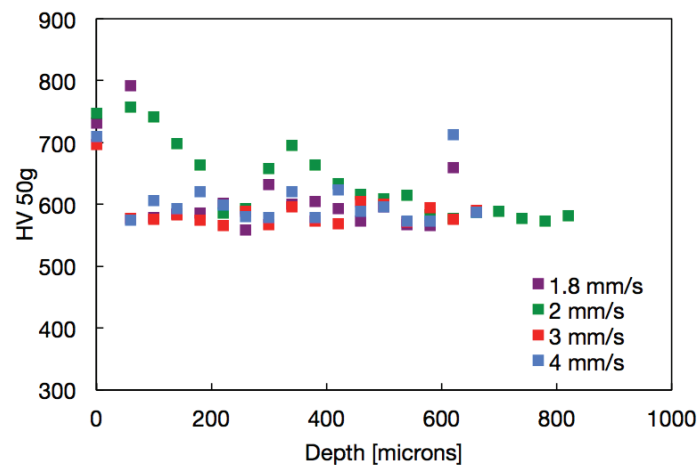


Figure 7:22 The depth of hardening of the line scan surface treatment by laser shown in Figure 7:23, every data point represent an individual hardness indentation.

Interestingly, the line scan done by the speed of 2 mm/s shows rather higher hardness values down to the depth of 150 microns. For confirming the depth of hardening for the line scans done under 2 mm/s more data point was obtained at each depth. The result is presented in Figure 7:23.

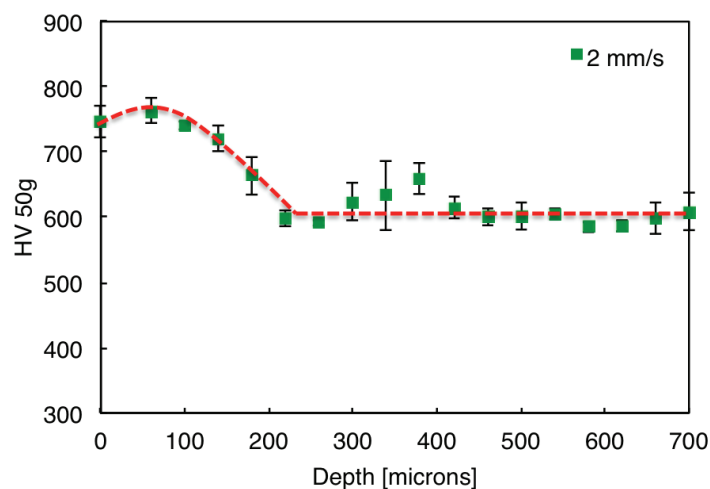


Figure 7:23 The depth of the hardening done with the speed of 2 mm/s. Each data point is the mean value of 5 indentations at the same depth while the error bars correspond to the standard deviation calculated for the 5 measures.

As it can be seen in Figure 7:23, the scan speed of 2 mm/s creates a hard surface of at least 100 microns which gives enough margins for surface finishing and further materials removal of 50-70 microns.

Chapter 8 Miscellaneous

In this chapter, various subjects studied during this project, which did not lead to a publication but are self-standing elements of this work, are briefly presented.

a. Influence of Mn-addition on glass formation

It is often assumed that the glass transition temperature in bulk metallic glasses (BMG) is merely a shallow function of composition. Evidence has been found for several metallic glasses derived from quaternary $(\text{Pt}+\text{TM})_{66}\text{B}_{24}(\text{Si}+\text{Ge})_{10}$ systems exhibiting strong changes of T_g (from 570 K to 650K) with varying the type of TM(=transition metal) used. A particularly strong modifier of T_g is manganese. Compared to the transition-metal-free glass transition temperature of about 540 K substitution of one fourth of the platinum by manganese changes the glass transition temperature by over 100 K, i.e. ≈ 6 K/at.-pct. We note in passing that this value is larger than for other transition metals, e.g. Ni (1.8 K/at.-pct) and Cu (3 K/at.-pct), but much less than the values observed in Chapter 6 for group 3A and rare earth elements where values of 10 to 20 K/at.-pct were observed. The reduced glass transition temperature remained virtually unchanged over a wide range of compositions, since incorporation of manganese simultaneously increased the glass transition and melting temperature in the $\text{Pt}_{49.95}\text{Si}_{6.4}\text{Ge}_{2.5}\text{B}_{24}[\text{Cu}_{1-x}\text{Mn}_x]_{16.65}$, ($x=0\ldots 0.6$) Figure 8:1 shows the variations of the characteristic temperatures namely T_g , T_x and T_m as the function of the degree of the substitution of Cu with Mn in the alloys with the general formula of $\text{Pt}_{49.95}\text{Si}_{6.4}\text{Ge}_{2.5}\text{B}_{24}[\text{Cu}_{1-x}\text{Mn}_x]_{16.65}$, ($x=0\ldots 0.6$). By increasing the Mn content and the consequent increase of the T_g , the hardness is also increased as shown in Figure 8:2. As can be seen, by increasing the substitution of the Cu content by Mn all characteristics temperatures increase. Yet the increase of the T_g is more pronounced compared to that of T_x resulting in a reduction of the width of the supercooled liquid region. Furthermore, both T_s (T_m) and T_l increase by adding Mn to the system, which is also an indication of deviating from the optimal glass forming composition. Hence, despite its desirable effect on the

glass transition temperature, manganese has a strongly negative effect on the processing window to be used in these alloys.

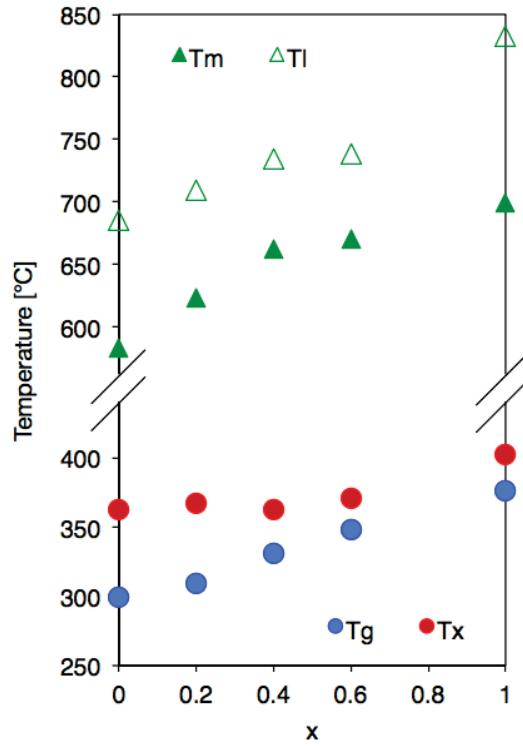


Figure 8:1 Evolution of T_g , T_x and T_m and T_l as the function of the degree of substitution of the Cu with Mn, in suction cast $d=1$ mm rods of the alloy $Pt_{49.95} Si_{6.4} Ge_{2.5} B_{24} [Cu_{1-x}Mn_x]_{16.65}$, ($x=0\ldots 0.6$).

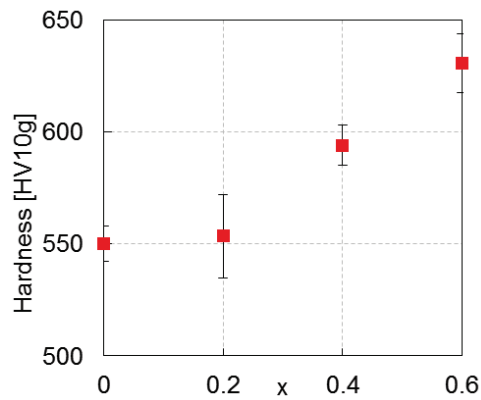


Figure 8:2 Evolution of the hardness as the function of the degree of substitution of the Cu with Mn in the alloy with the general formula of $Pt_{49.95} Si_{6.4} Ge_{2.5} B_{24} [Cu_{1-x}Mn_x]_{16.65}$, ($x=0\ldots 0.6$), in suction cast $d=1$ mm rods.

Furthermore given that the substitution of Cu with Mn can significantly increase the T_g , its influence on the activation energies of glass transition and crystallization is evaluated. these evaluations are based on Kissinger's formalism [203,204]:

$$\ln \frac{T_{g,x}^2}{\beta} = \frac{E_{g,x}}{RT_{g,x}} + \text{const} \quad (8.1)$$

where β is the heating rate and $E_{g,x}$ either the activation energy of glass transition or crystallization. By plotting the $\ln \frac{T_{g,x}^2}{\beta}$ versus $\frac{1000}{T_{g,x}}$, a straight line with the slope proportional to the effective activation energy can be obtained. The activation energies for glass transition and crystallization for two alloys evolve as shown in Figure 8:3 to the right:

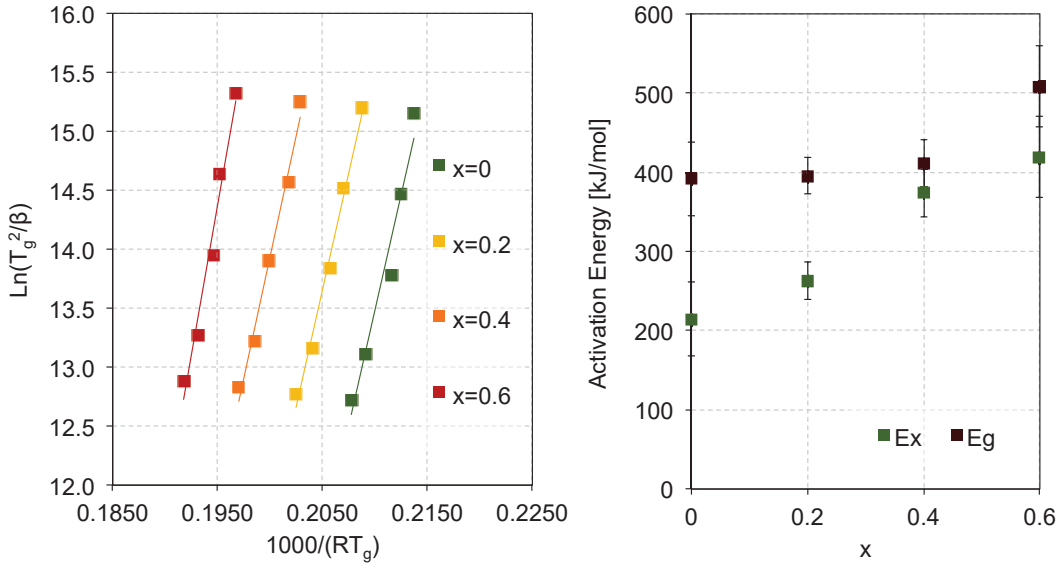


Figure 8:3 Activation energies of glass transition (E_g) and crystallization (E_x) as the function of substitution of the Cu with Mn in the alloys with the general formula of $\text{Pt}_{49.95}\text{Si}_{6.4}\text{Ge}_{2.5}\text{B}_{24}[\text{Cu}_{1-x}\text{Mn}_x]_{16.65}$, ($x=0\ldots0.6$).

As can be seen, E_g and E_x both increase by the increase of respectively T_g and T_x . This is in line with the observations by Qin and McKenna [205] for a wide range of glass formers.

To further explore the influence of the composition on the mechanical properties resulting from the shift of T_g to higher temperatures by incorporating Mn, a series of compression testes has been carried out to explore the deformation behavior at relatively low strain rate of nominally $2 \cdot 10^{-4} \text{s}^{-1}$. The compression tests have been carried out on suction cast cylinders of 1 mm diameter and 2 mm height. Figure 8:4 shows the set-up for carrying out the compression tests at intermediate temperatures. Heating plates were used for increasing the temperature. The thermocouples were placed inside the steel heating plates at 1 mm

of the surface. For homogenizing the temperature across the sample, when the plates touch the sample there is a dwelling time of 3 minutes before starting the test.

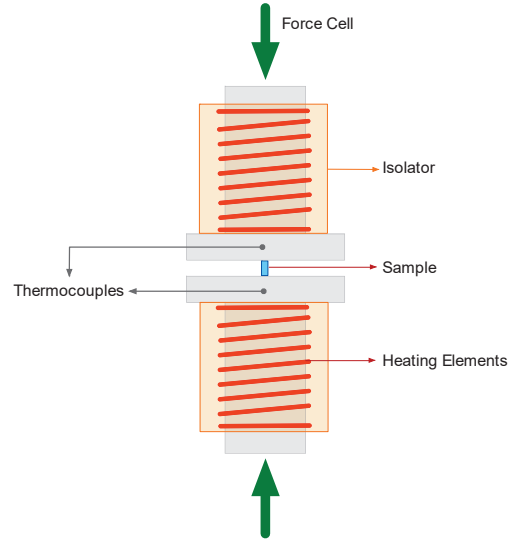


Figure 8:4 The set-up for carrying out the compression tests at intermediate temperatures.

Two typical diagrams showing the evolution of compressive response by increasing the temperature are presented. As it can be seen at 0.85-0.9 T_g there is transition from inhomogeneous flow characterized by formation of localized shear bands to the homogenous flow regime.

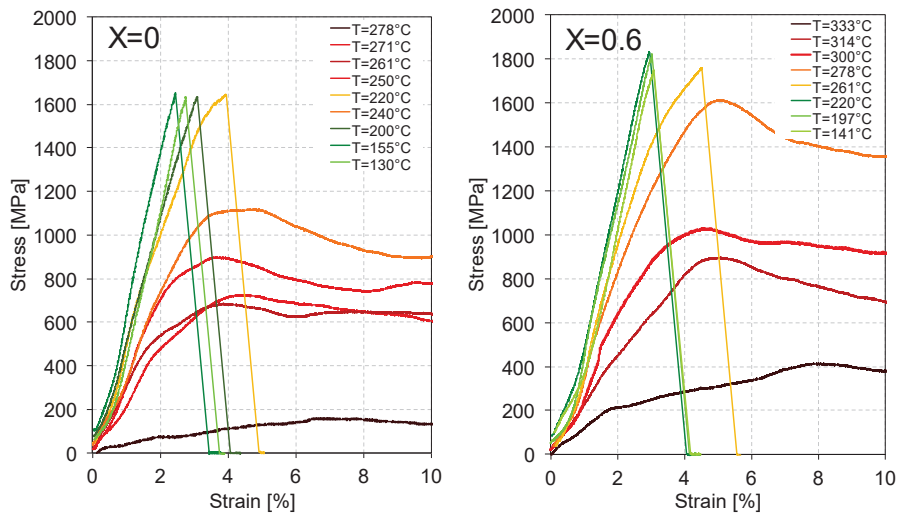


Figure 8:5 Compression test at intermediate temperatures for two alloys belonging with the general formula of $\text{Pt}_{49.95} \text{Si}_{6.4} \text{Ge}_{2.5} \text{B}_{24} [\text{Cu}_{1-x}\text{Mn}_x]_{16.65}$, ($x=0, 0.6$).

As expected, by normalizing the compressive strength to the compressive strength at 100°C and the test temperature to T_g all the data points collapse on roughly the same curve.

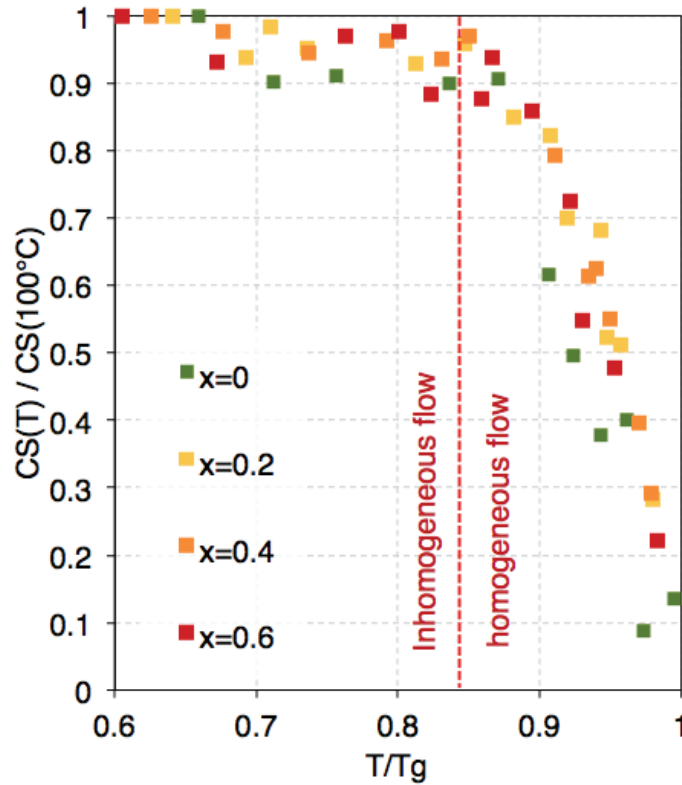


Figure 8:6 Normalized compressive strength as a function of different test temperatures, carried out on the samples with the general formula of $\text{Pt}_{49.95}\text{Si}_{6.4}\text{Ge}_{2.5}\text{B}_{24}[\text{Cu}_{1-x}\text{Mn}_x]_{16.65}$, ($x=0\ldots0.6$).

For the strain rate employed here the transition between the inhomogeneous and homogeneous flow is hence situated between $0.85\text{--}0.9T_g$ which corresponds to the threshold presented by Spaepen [180,206] in the characteristic deformation map for amorphous metals.

b. Formation of Boron-rich primary phases

It has been observed that by decreasing the cooling rate and casting alloys with diameters larger 4mm diameter there is often formation of primary phases. These phases can be seen in Figure 8:7. Looking at the BSE images shown in Figure 8:7, it can be deduced that there is a significant presence of light elements in the composition of this dark primary phases. The lightest elements present in the composition of this alloys are namely boron and silicon.

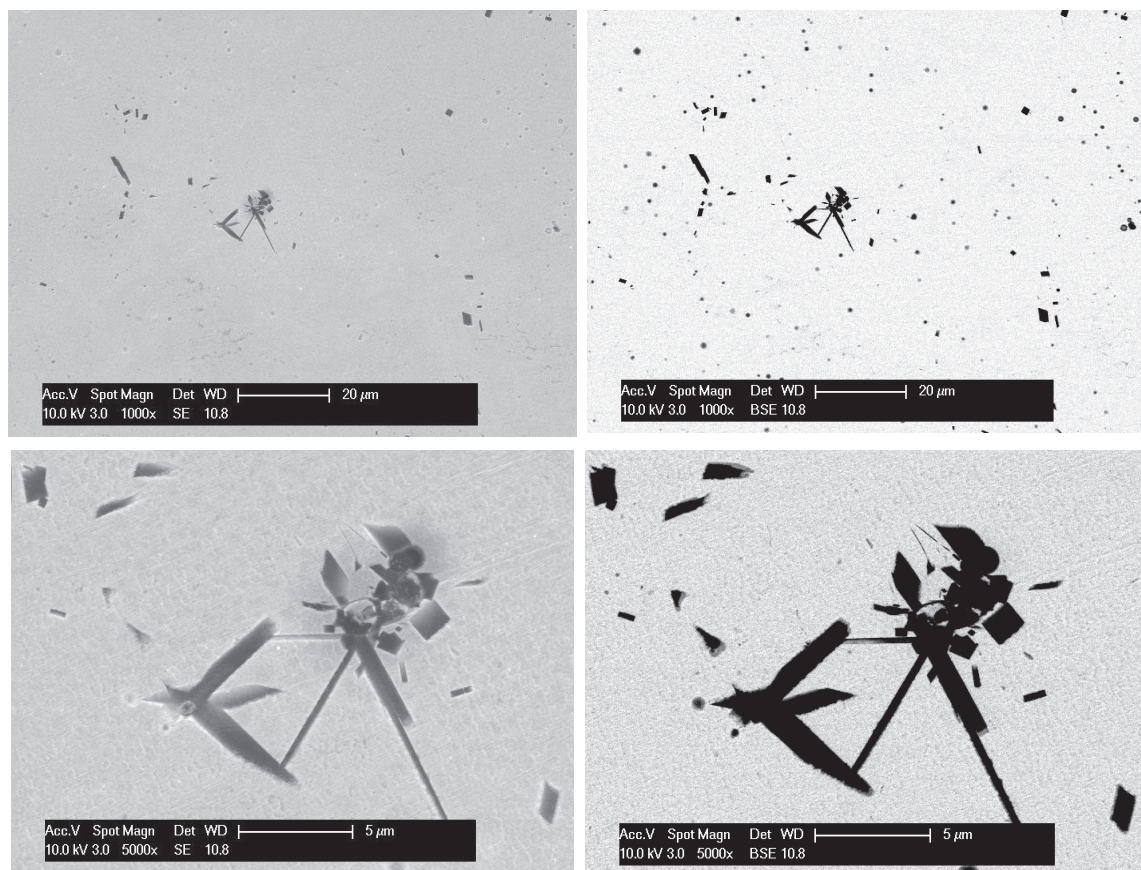


Figure 8:7 SEM micrographs of the as-cast 5 mm cast rod of the alloy $\text{Pt}_{49.95}\text{Si}_{6.4}\text{B}_{24}\text{Ge}_3\text{Cu}_{16.65}$.

Interestingly enough, during crystallization the shape or the quantity of these primary precipitates remained the same as shown in the example of the alloy $\text{Pt}_{45.95}\text{Si}_{6.4}\text{B}_{24}\text{Ge}_3\text{Cu}_{16.65}$ with 64% crystallinity.

EDX elemental mapping, cf. Figure 8:8, confirmed that the primary phases appearing dark in BSE images taken for the as-cast sample of the alloy $\text{Pt}_{49.95}\text{Cu}_{16.65}\text{Si}_{6.4}\text{B}_{24}\text{Ge}_3$ are rich in boron. Given the rather positive enthalpy of mixing between copper and boron [207], a possible explanation for formation of these boron-rich phases upon casting is the rejection of boron atoms from the homogenous liquid due to the presence of Cu. For investigating the composition of these primary phases characterization with NanoSIMS (Nano- Secondary Ion Mass Spectroscopy) was carried out in the Laboratory of for Biological Geochemistry (LGB), EPFL. The NanoSIMS 50L used for this analysis is a dynamic, double-focusing, magnetic-sector, multi-collecting ion probe, using Cs^+ ions [208]. Figure 8:9 shows schematically the set-up the CAMECA NanoSIMS in LGB, EPFL.

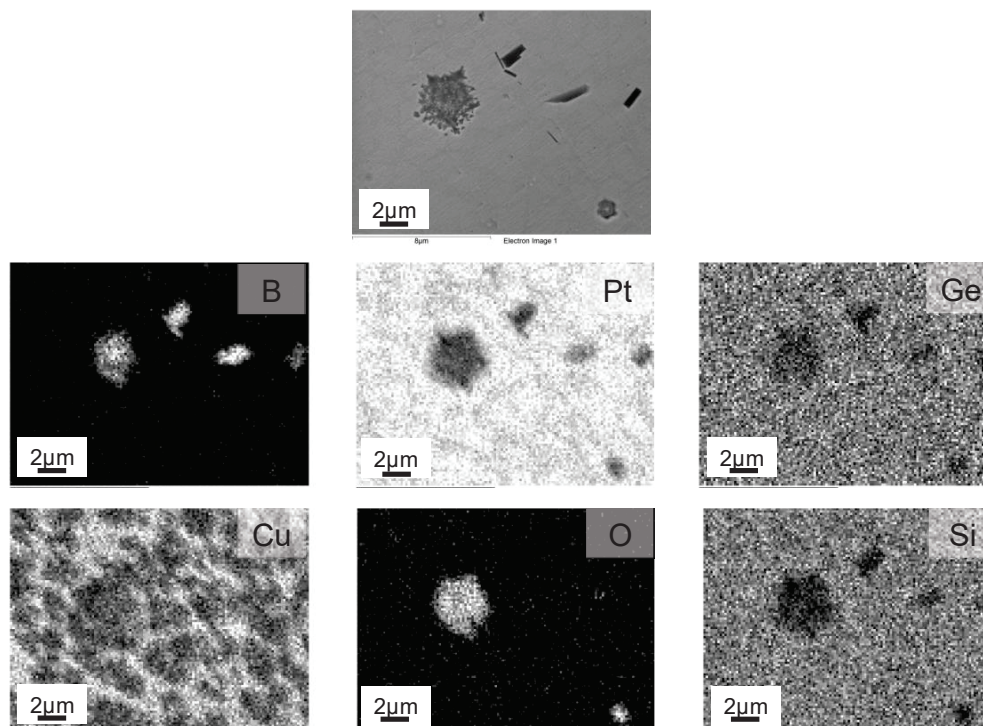


Figure 8:8 EDX elemental mapping of the 5 mm cast rod of the alloy $\text{Pt}_{49.95}\text{Si}_{6.4}\text{B}_{24}\text{Ge}_3\text{Cu}_{16.65}$ with 64% of crystallinity.

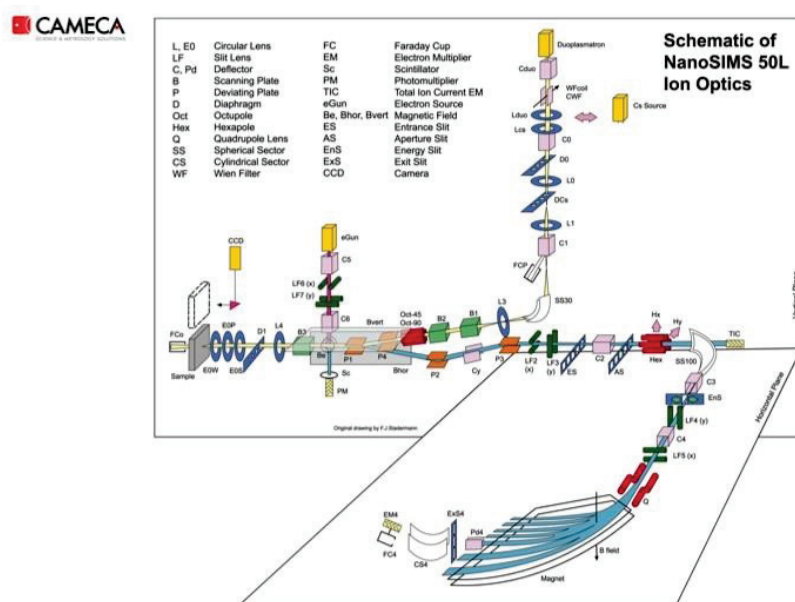


Figure 8:9 The NanoSIMS N50L is equipped with a multi-collector system that allows simultaneous collection of up to 7 different isotopes. Images or maps can be generated from the lightest elements, such as H (e.g. D/H ratios), C ($^{13}\text{C}/^{12}\text{C}$ ratios), N ($^{15}\text{N}/^{14}\text{N}$ ratios), O (e.g. $^{18}\text{O}/^{16}\text{O}$ ratios) to the heaviest elements like uranium (From [208]).

The Nano SIMS was configured to detect ^{11}B , ^{28}Si , ^{63}Cu , ^{72}Ge and ^{194}Pt isotopes, and was calibrated with pure samples of these elements prior to analysis. Nano-SIMS characterization of these primary boron-rich phases revealed the presence of silicon in the latter. As can be clearly seen in Figure 8:10, silicon and boron are both present in these primary phases formed upon quenching of the liquid in the alloy $\text{Pt}_{45.95}\text{Si}_{6.4}\text{B}_{24}\text{Ge}_3\text{Cu}_{16.65}$. The main limitation of such characterization with Nano-SIMS is qualitative nature of measurements and the impossibility of translating the number of counts to the actual atomic concentration of alloying elements.

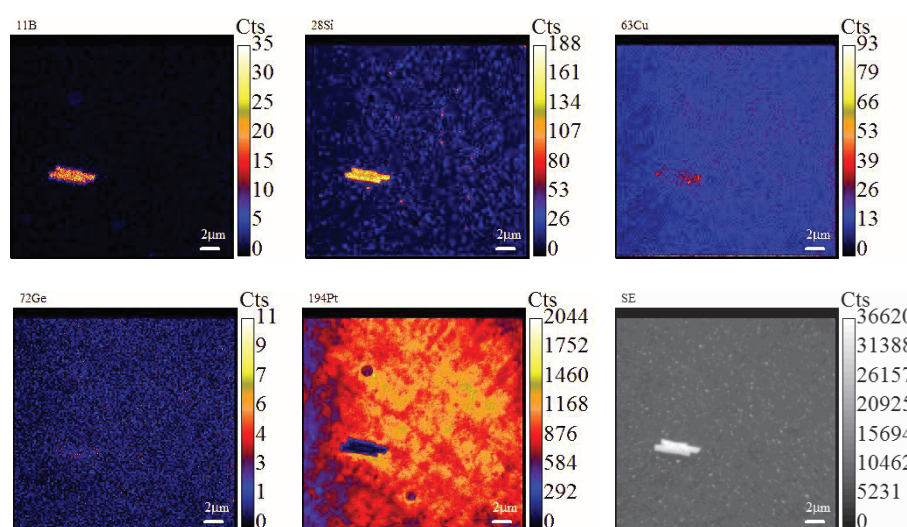


Figure 8:10 Nano-SIMS characterization of the B-rich primary phase. The sample belongs to the 5 mm suction cast rod of the alloy $\text{Pt}_{49.95}\text{Si}_{6.4}\text{B}_{24}\text{Ge}_3\text{Cu}_{16.65}$.

Furthermore, the ease of detaching ions from a certain phase is a function of the composition and the atomic bonding of that particular phase [209–211]. So it is possible that a lighter phase with weak atomic bonding shows a higher number of counts for a certain element compared to a phase with a stronger atomic bonding yet lower concentration.

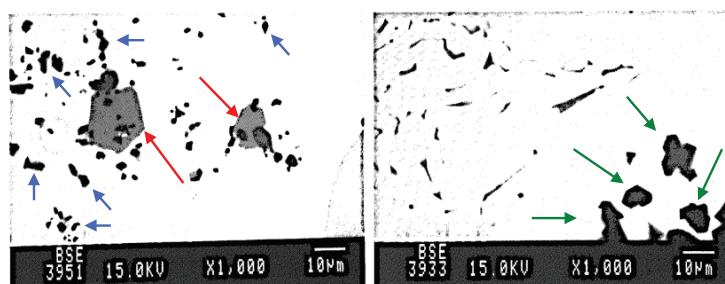


Figure 8:11 (left) Backscattered electron image of a Si-rich sample with 15 at.-pct. of boron annealed 1401 °C, small dark crystals shown by blue arrows are SiB_6 and larger gray crystals shown by red arrows are SiB_3 . (right) Si-rich sample with 8 at.-pct. of boron annealed at 1390 °C, dark crystals shown by green arrows are SiB_6 (From [212]).

This is called the matrix effect. The matrix effect aside, NanoSIMS is a powerful tool that proves the presence of boron and silicon in primary Boron-rich phase, but falls short of telling the exact composition of this phase. Aselage [212] has observed silicon borides with similar shape and morphology in arc melted silicon-boron alloys. The examples of silicon borides are shown in Figure 8:11.

Aselage [212] suggests that by looking at images shown in Figure 8:11, that the SiB_3 crystal indicated by blue arrows surround the many SiB_6 shown by red arrows, showing that SiB_6 was present at higher temperatures and that SiB_3 grew during cooling. He also suggests that the more stable form of Silicon boride is SiB_6 .

One of the important parameters in formation of these boron-rich primary phases is the slow cooling rate especially in the samples with higher cast diameter. One of the slowest cooling rates that can be achieved during our work was applied to the samples subject to DSC. There, the cooling rate is imposed by the machine and is equal to 10 K/min. Figure 8:12 shows the BSE images taken from the sample of the alloy $\text{Pt}_{49.95}\text{Si}_{6.4}\text{B}_{24}\text{Ge}_3\text{Cu}_{16.65}$ subject to slow cooling in the DSC.

The sizes of the boron-rich primary phases are much larger compared to the size of their counterparts produced by casting. It is also shown that the boron-rich dark phases are formed within the inter-dendritic fine eutectic phase and confined by the bright Pt-rich primary phases.

Interestingly but not surprisingly, such boron-rich primary phases are not present in the melt-spun ribbons, as shown in Figure 8:13.

More investigation is needed to understand the mechanism of formation of these boron-rich primary phases in the cast samples of the alloy $\text{Pt}_{49.95}\text{Si}_{6.4}\text{B}_{24}\text{Ge}_3\text{Cu}_{16.6}$.

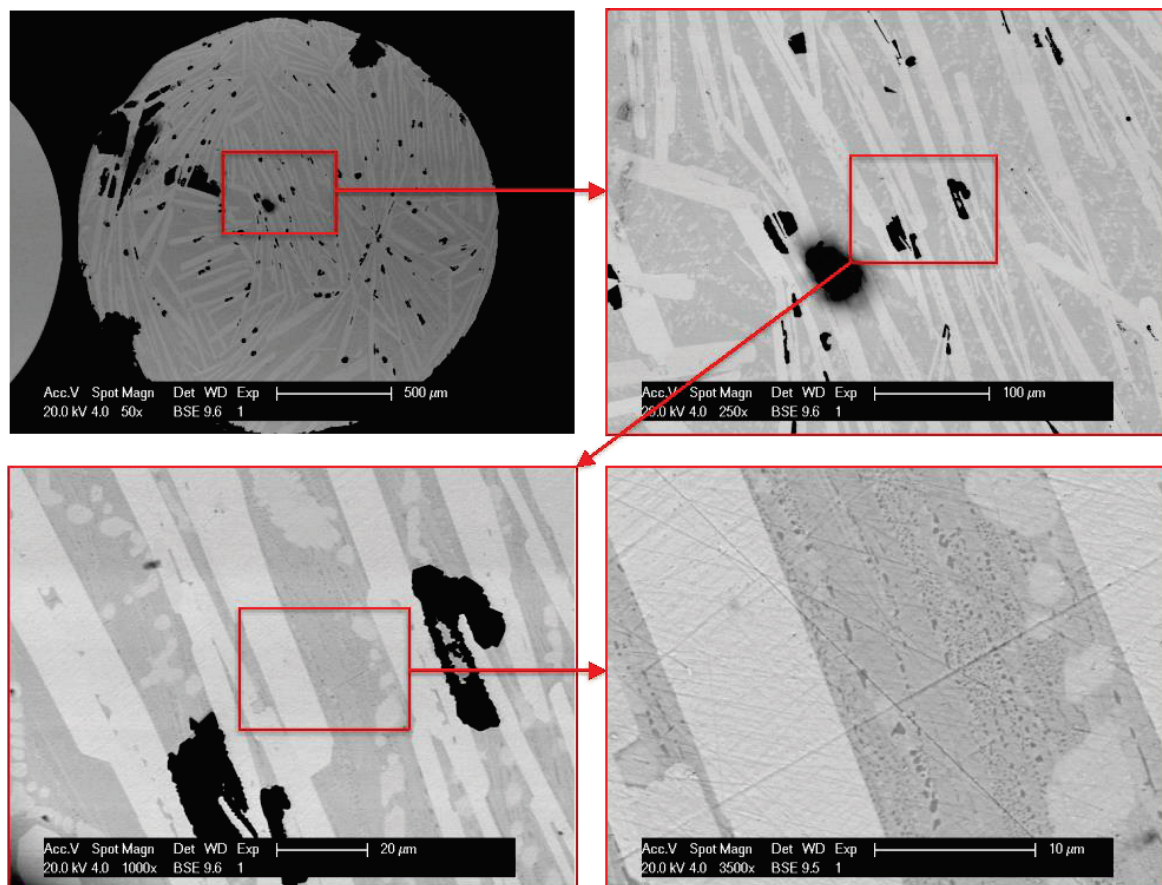


Figure 8:12 BSE images taken from the ingot sample of the alloy $\text{Pt}_{49.95}\text{Si}_{6.4}\text{B}_{24}\text{Ge}_3\text{Cu}_{16.65}$ cooled down from 1200 $^{\circ}\text{C}$ at 10 K/min.

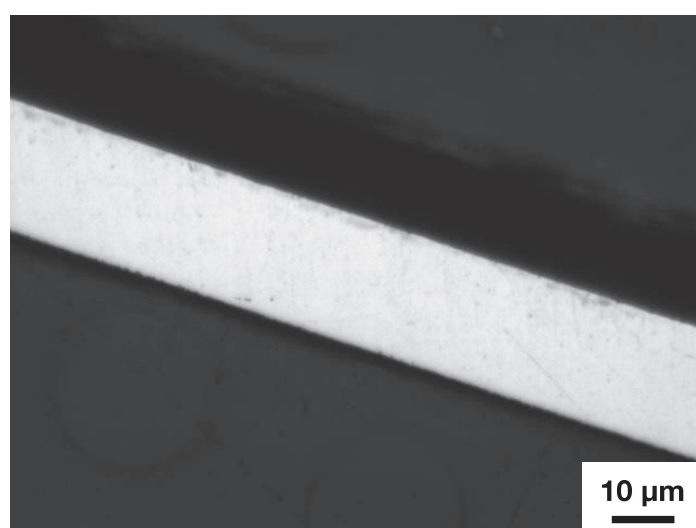


Figure 8:13 Optical microscopy of Melt-spun ribbon of the alloy $\text{Pt}_{49.95}\text{Si}_{6.4}\text{B}_{24}\text{Ge}_3\text{Cu}_{16.65}$

Chapter 9 Conclusions and perspectives

a. Achieved results

The following items briefly present the conclusions achieved during different sections of this thesis.

A new family of phosphorous-free Pt-based BMGs was developed in the ternary system of Pt-Si-B. The composition showing the best glass-forming ability was found to be $\text{Pt}_{49.95}\text{Cu}_{16.65}\text{Si}_{6.4}\text{Ge}_3\text{B}_{24}$, with a casting diameter of at least 5 mm and a super-cooled liquid region of 55 K. The following conclusions can be derived for the alloy development part of the thesis:

- The ternary system Pt-Si-B contains a low lying ternary eutectic in the vicinity of the composition $\text{Pt}_{73}\text{B}_{15}\text{Si}_{12}$, indications in at.-pct, with a eutectic temperature of around 973 K.
- Similarly low melting points are encountered for compositions starting at the ternary eutectic and going towards the binary eutectic $\text{Pt}_{58}\text{B}_{42}$.
- The solidus temperatures can significantly be lowered by substituting some of the platinum by nickel and, especially, copper.
- The glass transition and crystallization temperatures are strongly affected by the composition. In particular, substituting platinum by copper raises the glass transition temperature significantly, while substitution of silicon by germanium lowers the glass transition temperature. With the exception of Ge and B which decrease the T_g other alloying elements such as Cu, Ni, Y, Sc, Tb, Gd, Dy, Ho, Sm and Mn tend to increase the T_g .
- Primary crystallization of the glassy alloys in the Pt-Si-B system is very similar to Al-based and Fe-based amorphous alloys. Analogous to Al-based metallic glasses, the

crystallization proceeds by precipitation of α -Pt followed by formation of more complex phases at higher temperatures.

- Substitution of some of the silicon by germanium shifts the primary crystallization peak to higher temperatures while the second crystallization peak remains unchanged.
- Alloys in the Pt-Si-B system systematically exhibit higher glass transition temperature and concomitantly higher hardness than their Pt-P-based counterparts. A hardness value of 576 ± 4 HV0.3 was achieved for the alloy $\text{Pt}_{49.95}\text{Cu}_{16.65}\text{Si}_{6.4}\text{Ge}_3\text{B}_{24}$ in the as-cast state.

The influence of partial crystallization on thermophysical and mechanical properties of the alloy $\text{Pt}_{49.95}\text{Si}_{6.4}\text{B}_{24}\text{Ge}_3\text{Cu}_{16.65}$ was evaluated. The following conclusions can be drawn:

- The hardness increased steadily from 570 to 750 HV with degree of crystallinity while the compressive strength decreased due to reduced toughness with increasing crystallinity.
- The glass transition temperature of the remaining amorphous matrix increased from 302 to 322°C with increasing degree of crystallinity.
- The crystals formed at first are somewhat depleted in copper and enriched in platinum while EDX mapping did not show any significant redistribution of the other alloying elements.
- The evolution in glass transition temperature of the remaining amorphous matrix can be quantitatively rationalized by the change in Cu:Pt ratio in the amorphous phase as crystallization advances.
- A new hexagonal crystalline structure with lattice parameters of $a = 8.973(1)$ Å and $c = 2.959(1)$ Å was found to be forming upon crystallization in the alloy $\text{Pt}_{49.95}\text{Si}_{6.4}\text{B}_{24}\text{Ge}_3\text{Cu}_{16.65}$. This new phase is a close analogous structure to $\text{Zn}_3\text{Pt}_9\text{B}_{3.86}$.
- The 5mm as-cast sample exhibited a clear glass transition and a relatively wide super-cooled liquid region in DSC pattern, yet the HE-XRD showed that this glass contained nano-size ordered domains of 2-3 nm in size as estimated via Scherrer's formula.
- By increasing the degree of crystallinity, the lattice parameters of the freshly crystallized hexagonal phase decreased slightly. Such decrease was attributed to the rejection of Cu atoms from the crystalline solid solution into the glassy matrix, albeit the fi-

nal evidence of an increasing lattice parameter in the nano-domain phase by enrichment in copper could not be provided by the present data.

- The size of the nano-domains in the glassy phase increase from approximately 2-3 nm to 8 nm as the degree of crystallinity increased.

Concerning the influence of oxygen content and the alloy optimization by minor addition of rare-earth and group 3A elements the following conclusions were drawn:

- Prolonged fluxing (40h) with B_2O_3 was found to be ineffective in reducing the oxygen content in the alloy $Pt_{49.95}Si_{6.4}B_{24}Ge_3Cu_{16.65}$.
- Alternatively, the oxygen content in the alloy $Pt_{49.95}Si_{6.4}B_{24}Ge_3Cu_{16.65}$ was reduced by minor addition of rare-earth metal (REM) namely Sc below the detection limit of the In-ert Gas analyzer (5 ppm) of the used for oxygen content measurement.
- Upon reduction of the oxygen content and the measurement of the thermo-physical properties it became evident that such properties are not sensible to oxygen content in the range of 5-20 ppm.
- Alloy optimization in the alloys with the general formula of $Pt_{49.95}Si_{6.4}B_{24}Ge_3Cu_{16.65-x}REM_x$, by addition of both Sc and Ho was found to have a strong increasing influence on the glass transition and crystallization temperature. By addition of 2 at.% of Sc and Ho the T_g was increased respectively by 18 °C and 14 °C and the T_x respectively by 23 °C and 20 °C.
- As it has been observed previously [30], the increase of the T_g results in an increase of the hardness of the glassy alloys. Such phenomenon has been observed in the case of the alloys containing Ho and Sc whose hardness increases almost linearly by the increase of their respective glass transition temperature.

b. Future development

- For further development of the full potential of thermoplastic forming in the super-cooled liquid region, efforts should be focused to produce parts more similar to the final shape of the piece to considerably reduce the cost of machining.

- Surface treatment by laser is a powerful tool to introduce architecture of material properties within the same work piece. The laser can be used to vitrify the crystalline surface or crystallize the glass.
- The composition and the structure of Boron-rich primary phases appearing in the cast samples due to insufficient cooling rate should be further investigated. This can be done by transmission electron microscopy (TEM) and specially Electron Energy Loss Spectroscopy (EELS).
- The local measurement of hardness by nanoindentation and producing nano-hardness maps of partially crystallized samples can be an interesting subject. This is specially the case when those maps are compared with the EDX-mapping showing the distribution of alloying elements.
- Given the interesting mechanical properties as well as the inherent chemical inertness of these Pt-Si-B-based BMG's there is a possibility to use them in micro/nano fabrication.

References

- [1] pgm market report may 2015.pdf, <http://www.platinum.matthey.com/documents/new-item/pgm%20market%20reports/pgm%20market%20report%20may%202015.pdf> (accessed May 18, 2016).
- [2] B.T. Biggs, S.S. Taylor, E. van der Lingen, The Hardening of Platinum Alloys for Potential Jewellery Application, *Platin. Met. Rev.* 49 (2005) 2–15. doi:10.1595/147106705X24409.
- [3] G. Ainsley, Platinum Investment Casting Alloys, *PlatinumMetalsRev.* 22 (1978).
- [4] C. Mshumi, C. Lang, Strengthening of Platinum-5 wt.% Copper by Heat Treatment, *Platinum Metals Review.* 51 (2007) 78–82. doi:10.1595/147106707X187173.
- [5] L.A. Cornish, R. Süß, A. Douglas, L.H. Chown, L. Glaner, The Platinum Development Initiative: Platinum-Based Alloys for High Temperature and Special Applications: Part I, *Platinum Metals Review.* 53 (2009) 2–10. doi:10.1595/147106709X393299.
- [6] P. Hill, N. Adams, T. Biggs, P. Ellis, J. Hohls, S. Taylor, I. Wolff, Platinum alloys based on Pt–Pt3Al for ultra-high temperature use, *Materials Science and Engineering: A.* 329–331 (2002) 295–304. doi:10.1016/S0921-5093(01)01577-5.
- [7] T. Biggs, M.J. Witcomb, L.A. Cornish, Martensite-type transformations in platinum alloys, *Materials Science and Engineering: A.* 273–275 (1999) 204–207. doi:10.1016/S0921-5093(99)00371-8.
- [8] A. Douglas, P.J. Hill, T. Murakumo, L.A. Cornish, R. Süß, The Platinum Development Initiative: Platinum-Based Alloys for High Temperature and Special Applications: Part II, *Platinum Metals Review.* 53 (2009) 69–77. doi:10.1595/147106709X434040.
- [9] L.A. Cornish, R. Süß, L.H. Chown, L. Glaner, The Platinum Development Initiative: Platinum-Based Alloys for High Temperature and Special Applications: Part III, *Platinum Metals Review.* 53 (2009) 155–163. doi:10.1595/147106709X464371.
- [10] G. Normandeau, Practical Applications of Heat Treatable Platinum, IMPERIAL SMELTING & REFINING CO. OF CANADA LTD. (1998).
- [11] W. Weber, K. Zimmermann, H.-H. Beyer, Surface-hardened objects of alloys of platinum and palladium and method for ..., 5518556, 1996. <http://www.google.ch/patents?id=GDMbAAAAEBAJ> (accessed June 5, 2012).
- [12] J. Schroers, B. Lohwongwatana, W.L. Johnson, A. Peker, Precious bulk metallic glasses for jewelry applications, *Materials Science and Engineering: A.* 449–451 (2007) 235–238. doi:10.1016/j.msea.2006.02.301.
- [13] M.D. Demetriou, M. Floyd, C. Creadson, J.P. Schramm, G. Garrett, W.L. Johnson, Liquid-like platinum-rich glasses, *Scripta Materialia.* 65 (2011) 799–802. doi:10.1016/j.scriptamat.2011.07.035.
- [14] A. Inoue, Stabilization of metallic supercooled liquid and bulk amorphous alloys, *Acta Materialia.* 48 (2000) 279–306. doi:10.1016/S1359-6454(99)00300-6.
- [15] J. Schroers, Processing of Bulk Metallic Glass, *Advanced Materials.* 22 (2009) 1566–1597. doi:10.1002/adma.200902776.
- [16] J. Schroers, The superplastic forming of bulk metallic glasses, *JOM.* 57 (2005) 35–39. doi:10.1007/s11837-005-0093-2.
- [17] H. Okamoto, Pt–Si (Platinum–Silicon), *J. Phase Equilib. Diffus.* 32 (2011) 394–395. doi:10.1007/s11669-011-9915-9.
- [18] H. Okamoto, B–Pt (Boron–Platinum), *Binary Alloy Phase Diagrams.* 1 (1990).
- [19] M. Vasquez, E. Ascasibar, A. Hernando, O.V. Nielsen, Co–Si–B and Fe–Co–B amorphous alloys: Induced anisotropy and various magnetic properties, *Journal of Magnetism and Magnetic Materials.* 66 (1987) 37–44. doi:10.1016/0304-8853(87)90125-9.
- [20] I.W. Donald, H.A. Davies, T. Kemény, The effect of Pt-group metal additions on the thermal stability of Fe- and Ni-based glassy alloys, *Journal of Non-Crystalline Solids.* 50 (1982) 351–358. doi:10.1016/0022-3093(82)90095-3.
- [21] T. Tokunaga, H. Ohtani, M. Hasebe, Thermodynamic evaluation of the phase equilibria and glass-forming ability of the Fe–Si–B system, *Calphad.* 28 (2004) 354–362. doi:10.1016/j.calphad.2004.11.004.
- [22] K. Hono, K. Hiraga, Q. Wang, A. Inoue, T. Sakurai, The microstructure evolution of a Fe_{73.5}Si_{13.5}B₉Nb₃Cu₁ nanocrystalline soft magnetic material, *Acta Metallurgica et Materialia.* 40 (1992) 2137–2147. doi:10.1016/0956-7151(92)90131-W.
- [23] J.C. Foley, D.R. Allen, J.H. Perepezko, Strategies for the development of nanocrystalline materials through devitrification, *Materials Science and Engineering: A.* 226–228 (1997) 569–573. doi:10.1016/S0921-5093(97)80065-2.
- [24] A. Inoue, A. Katsuya, K. Amiya, T. Masumoto, Preparation of Amorphous Fe–Si–B and Co–Si–B Alloy Wires by a Melt Extraction Method and Their Mechanical and Magnetic Properties, *Materials Transactions, JIM.* 36 (1995) 802–809. doi:10.2320/matertrans1989.36.802.
- [25] A. Asenjo, D. García, J.M. García, C. Prados, M. Vázquez, Magnetic force microscopy study of dense stripe domains in Fe–B/Co–Si–B multilayers and the evolution under an external applied field, *Phys. Rev. B.* 62 (2000) 6538–6544. doi:10.1103/PhysRevB.62.6538.
- [26] M. Vasquez, E. Ascasibar, A. Hernando, O.V. Nielsen, Co–Si–B and Fe–Co–B amorphous alloys: Induced anisotropy and various magnetic properties, *Journal of Magnetism and Magnetic Materials.* 66 (1987) 37–44. doi:10.1016/0304-8853(87)90125-9.
- [27] I.W. Donald, H.A. Davies, T. Kemény, The effect of Pt-group metal additions on the thermal stability of Fe- and Ni-based glassy alloys, *Journal of Non-Crystalline Solids.* 50 (1982) 351–358. doi:10.1016/0022-3093(82)90095-3.
- [28] D.H. Xu, G. Duan, W.L. Johnson, C. Garland, Formation and properties of new Ni-based amorphous alloys with critical casting thickness up to 5 mm, *Acta Mater.* 52 (2004) 3493–3497. doi:10.1016/j.actamat.2004.04.001.
- [29] D.B. Miracle, W.S. Sanders, O.N. Senkov, The influence of efficient atomic packing on the constitution of metallic glasses, *Philosophical Magazine.* 83 (2003) 2409–2428. doi:10.1080/1478643031000098828.

-
- [30] D.B. Miracle, The efficient cluster packing model – An atomic structural model for metallic glasses, *Acta Materialia*. 54 (2006) 4317–4336. doi:10.1016/j.actamat.2006.06.002.
 - [31] D.B. Miracle, Efficient local packing in metallic glasses, *Journal of Non-Crystalline Solids*. 342 (2004) 89–96. doi:10.1016/j.jnoncrysol.2004.05.017.
 - [32] D.B. Miracle, On the universal model for medium-range order in amorphous metal structures, *Journal of Non-Crystalline Solids*. 317 (2003) 40–44. doi:10.1016/S0022-3093(02)01981-6.
 - [33] O.N. Senkov, D.B. Miracle, Effect of the atomic size distribution on glass forming ability of amorphous metallic alloys, *Materials Research Bulletin*. 36 (2001) 2183–2198. doi:10.1016/S0025-5408(01)00715-2.
 - [34] W. Weber, K. Zimmermann, H.-H. Beyer, Surface-hardened objects of alloys of platinum and palladium and method for ..., 5518556, 1996. <http://www.google.ch/patents?id=GDMbAAAAEBAJ> (accessed June 5, 2012).
 - [35] G. Ainsley, Platinum Investment Casting Alloys, *PlatinumMetalsRev.* 22 (1978).
 - [36] H.S. Chen, Composition dependence of the glass transition temperatures of Pd-Ni-P and Pt-Ni-P glasses, *Journal of Non-Crystalline Solids*. 12 (1973) 333–338. doi:10.1016/0022-3093(73)90005-7.
 - [37] H. Chen, Thermodynamic considerations on the formation and stability of metallic glasses, *Acta Metallurgica*. 22 (1974) 1505–1511. doi:10.1016/0001-6160(74)90112-6.
 - [38] amorphous solid | physics, *Encyclopedia Britannica*. <http://www.britannica.com/science/amorphous-solid> (accessed May 18, 2016).
 - [39] K. Binder, W. Kob, *Glassy Materials and Disordered Solids: An Introduction to Their Statistical Mechanics*, World Scientific, 2011.
 - [40] S. Schneider, Bulk metallic glasses, *J. Phys.: Condens. Matter*. 13 (2001) 7723. doi:10.1088/0953-8984/13/34/316.
 - [41] W. Klement, R.H. Willens, P. Duwez, Non-crystalline Structure in Solidified Gold–Silicon Alloys, *Nature*. 187 (1960) 869–870. doi:10.1038/187869b0.
 - [42] A. Inoue, Stabilization of metallic supercooled liquid and bulk amorphous alloys, *Acta Materialia*. 48 (2000) 279–306. doi:10.1016/S1359-6454(99)00300-6.
 - [43] A.L. Greer, Confusion by design, , Published Online: 25 December 1993; | doi:10.1038/366303a0. 366 (1993) 303–304. doi:10.1038/366303a0.
 - [44] D.. Miracle, O.. Senkov, Topological criterion for metallic glass formation, *Materials Science and Engineering: A*. 347 (2003) 50–58. doi:10.1016/S0921-5093(02)00579-8.
 - [45] H.. Chen, Thermodynamic considerations on the formation and stability of metallic glasses, *Acta Metallurgica*. 22 (1974) 1505–1511. doi:10.1016/0001-6160(74)90112-6.
 - [46] D. Turnbull, Under what conditions can a glass be formed?, *Contemporary Physics*. 10 (1969) 473–488. doi:10.1080/00107516908204405.
 - [47] O.N. Senkov, D.B. Miracle, Description of the fragile behavior of glass-forming liquids with the use of experimentally accessible parameters, *Journal of Non-Crystalline Solids*. 355 (2009) 2596–2603. doi:10.1016/j.jnoncrysol.2009.09.020.
 - [48] H.A. Davies, J.B. Hull, The formation, structure and crystallization of non-crystalline nickel produced by splat-quenching, *J Mater Sci*. 11 (n.d.) 215–223. doi:10.1007/BF00551430.
 - [49] Y.J. Kim, R. Busch, W.L. Johnson, A.J. Rulison, W.K. Rhim, Experimental determination of a time–temperature–transformation diagram of the undercooled Zr₄₁.2Ti₁₃.8Cu₁₂.5Ni₁₀.0Be₂₂.5 alloy using the containerless electrostatic levitation processing technique, *Applied Physics Letters*. 68 (1996) 1057–1059. doi:doi:10.1063/1.116247.
 - [50] O.N. Senkov, Correlation between fragility and glass-forming ability of metallic alloys, *Phys. Rev. B*. 76 (2007) 104202. doi:10.1103/PhysRevB.76.104202.
 - [51] J. Bernal, Bakerian Lecture 1962 - Structure of Liquids, *Proc. R. Soc. Lond. A-Math. Phys. Sci.* 280 (1964) 299–+. doi:10.1098/rspa.1964.0147.
 - [52] D. Miracle, O.. Senkov, A geometric model for atomic configurations in amorphous Al alloys, *Journal of Non-Crystalline Solids*. 319 (2003) 174–191. doi:10.1016/S0022-3093(02)01917-8.
 - [53] O.N. Senkov, J.M. Scott, D.B. Miracle, Composition range and glass forming ability of ternary Ca–Mg–Cu bulk metallic glasses, *Journal of Alloys and Compounds*. 424 (2006) 394–399. doi:10.1016/j.jallcom.2006.01.104.
 - [54] O.N. Senkov, D.B. Miracle, Description of the fragile behavior of glass-forming liquids with the use of experimentally accessible parameters, *Journal of Non-Crystalline Solids*. 355 (2009) 2596–2603. doi:10.1016/j.jnoncrysol.2009.09.020.
 - [55] O.N. Senkov, D.B. Miracle, Effect of the atomic size distribution on glass forming ability of amorphous metallic alloys, *Materials Research Bulletin*. 36 (2001) 2183–2198. doi:10.1016/S0025-5408(01)00715-2.
 - [56] D.B. Miracle, On the universal model for medium-range order in amorphous metal structures, *Journal of Non-Crystalline Solids*. 317 (2003) 40–44. doi:10.1016/S0022-3093(02)01981-6.
 - [57] D.B. Miracle, The efficient cluster packing model – An atomic structural model for metallic glasses, *Acta Materialia*. 54 (2006) 4317–4336. doi:10.1016/j.actamat.2006.06.002.
 - [58] T. Egami, Y. Waseda, Atomic size effect on the formability of metallic glasses, *Journal of Non-Crystalline Solids*. 64 (1984) 113–134. doi:10.1016/0022-3093(84)90210-2.
 - [59] O.N. Senkov, J.M. Scott, D.B. Miracle, Composition range and glass forming ability of ternary Ca–Mg–Cu bulk metallic glasses, *Journal of Alloys and Compounds*. 424 (2006) 394–399. doi:10.1016/j.jallcom.2006.01.104.
 - [60] D.. Miracle, O.. Senkov, A geometric model for atomic configurations in amorphous Al alloys, *Journal of Non-Crystalline Solids*. 319 (2003) 174–191. doi:10.1016/S0022-3093(02)01917-8.

-
- [61] E.R. Arata, F.H. Dalla Torre, J.F. Löffler, Identification of bulk metallic glass-forming compositions in La-based systems using ultrahigh gravitational acceleration, *Acta Materialia*. 56 (2008) 651–658. doi:10.1016/j.actamat.2007.10.026.
- [62] J.F. Löffler, S. Bossuyt, A. Peker, W.L. Johnson, Eutectic isolation in Mg-Al-Cu-Li(-Y) alloys by centrifugal processing, *Philosophical Magazine*. 83 (2003) 2797–2813. doi:10.1080/1478643031000122152.
- [63] E.M. Gossett, E.B. Scanley, Y. Liu, Y. Li, Z. Liu, S. Sohn, J. Schroers, C. Broadbridge, T.C. Schwendemann, Computational Nanocharacterization for Combinatorially Developed Bulk Metallic Glass, *Int. J. Hi. Spe. Ele. Syst.* 24 (2015) 1520012. doi:10.1142/S0129156415200128.
- [64] J. Liu, Y. Liu, P. Gong, Y. Li, K.M. Moore, E. Scanley, F. Walker, C.C. Broadbridge, J. Schroers, Combinatorial exploration of color in gold-based alloys, *Gold Bull.* 48 (2015) 111–118. doi:10.1007/s13404-015-0167-z.
- [65] S. Ding, Y. Liu, Y. Li, Z. Liu, S. Sohn, F.J. Walker, J. Schroers, Combinatorial development of bulk metallic glasses, *Nat Mater.* 13 (2014) 494–500. doi:10.1038/nmat3939.
- [66] C.A. Angell, K.L. Ngai, G.B. McKenna, P.F. McMillan, S.W. Martin, Relaxation in glassforming liquids and amorphous solids, *Journal of Applied Physics*. 88 (2000) 3113–3157. doi:10.1063/1.1286035.
- [67] J.S. Langer, Theories of glass formation and the glass transition, *Rep. Prog. Phys.* 77 (2014) 42501. doi:10.1088/0034-4885/77/4/042501.
- [68] W. Kauzmann, The Nature of the Glassy State and the Behavior of Liquids at Low Temperatures., *Chem. Rev.* 43 (1948) 219–256. doi:10.1021/cr60135a002.
- [69] H.. Chen, The glass transition temperature in glassy alloys: Effects of atomic sizes and the heats of mixing, *Acta Metallurgica*. 22 (1974) 897–900. doi:10.1016/0001-6160(74)90056-X.
- [70] A. Inoue, High strength bulk amorphous alloys with low critical cooling rates, *Mater Trans JIM*. 36 (1995) 866–875.
- [71] Z.P. Lu, C.T. Liu, Y. Wu, H. Tan, Y. Li, G.L. Chen, Composition effects on glass-forming ability and its indicator γ , *Intermetallics*. 16 (2008) 410–417. doi:10.1016/j.intermet.2007.12.002.
- [72] Z.P. Lu, H. Bei, C.T. Liu, Recent progress in quantifying glass-forming ability of bulk metallic glasses, *Intermetallics*. 15 (2007) 618–624. doi:10.1016/j.intermet.2006.10.017.
- [73] S. Venkataraman, B. Bartusch, C. Mickel, K.B. Kim, J. Das, S. Scudino, M. Stoica, D.J. Sordet, J. Eckert, Metallic glass formation in the Cu₄₇Ti₃₃Zr₁₁Ni₈Si₁ alloy, *Materials Science and Engineering: A*. 444 (2007) 257–264. doi:10.1016/j.msea.2006.08.089.
- [74] O.N. Senkov, Correlation between fragility and glass-forming ability of metallic alloys, *Phys. Rev. B*. 76 (2007) 104202. doi:10.1103/PhysRevB.76.104202.
- [75] O.N. Senkov, Correlation between fragility and glass-forming ability of metallic alloys, *Phys. Rev. B*. 76 (2007) 104202. doi:10.1103/PhysRevB.76.104202.
- [76] P. Desre, I. Ansara, P. Cremer, J.C. Joud, Concentration fluctuations diagram in undercooled liquid and glass forming ability. Application to the Fe₇₅Si₂₅B system, *Calphad*. 13 (1989) 89–96. doi:10.1016/0364-5916(89)90044-8.
- [77] F. Schwartz, J. Bigot, The Influence of the Substitution of Metallic Elements on the Thermal-Stability and Magnetic-Properties of Amorphous Fe-B-Si Alloys, *Materials Science and Engineering*. 99 (1988) 39–42. doi:10.1016/0025-5416(88)90287-X.
- [78] I.W. Donald, H.A. Davies, Ni-Si-B metallic glasses with high metalloid contents, *Journal of Materials Science*. 15 (1980) 2939–2941. doi:10.1007/BF00550570.
- [79] T. Kanomata, Y. Sato, Y. Sugawara, S. Aburatani, H. Kimura, T. Kaneko, A. Inoue, T. Masumoto, Heat capacity of Pd-Si, Ni-Si-B and Zr-based metallic glasses, *Sci. Rep. Res. Inst. Tohoku Univ. Ser. A-Phys. Chem. Metall.* 43 (1997) 89–95.
- [80] O. Haruyama, K. Tatsugawa, T. Sugimoto, N. Asahi, Structural-Analysis of Amorphous Ni₇₇Si_xB_{23-x} (x=3 or 13) and Ni₇₇.5Si_{7.9}B_{14.6} Alloys by X-Ray-Diffraction, *J. Mater. Sci. Lett.* 10 (1991) 1261–1262. doi:10.1007/BF00720940.
- [81] M. Baro, N. Clavaguera, S. Surinach, The Crystallization Process of Ni₇₈Si₈B₁₄ Amorphous-Alloys, *Materials Science and Engineering*. 97 (1988) 333–336. doi:10.1016/0025-5416(88)90068-7.
- [82] T. Komatsu, Y. Tanaka, R. Yokota, K. Matusita, Correlation Between Electrical-Properties and Thermal-Stability in Ni-Si-B Metallic Glasses, *J. Mater. Sci.* 22 (1987) 2185–2191. doi:10.1007/BF01132958.
- [83] I.W. Donald, H.A. Davies, The influence of composition on the formation and stability of Ni-Si-B metallic glasses, *Journal of Materials Science*. 15 (1980) 2754–2760. doi:10.1007/BF00550543.
- [84] M. Hagiwara, A. Inoue, T. Masumoto, Production of amorphous CoSiB and CoMSiB (M \equiv Group IV – VIII transition metals) wires by a method employing melt spinning into rotating water and some properties of the wires, *Materials Science and Engineering*. 54 (1982) 197–207. doi:10.1016/0025-5416(82)90114-8.
- [85] F. Schwartz, J. Bigot, The Influence of the Substitution of Metallic Elements on the Thermal-Stability and Magnetic-Properties of Amorphous Fe-B-Si Alloys, *Materials Science and Engineering*. 99 (1988) 39–42. doi:10.1016/0025-5416(88)90287-X.
- [86] I.W. Donald, H.A. Davies, Ni-Si-B metallic glasses with high metalloid contents, *Journal of Materials Science*. 15 (1980) 2939–2941. doi:10.1007/BF00550570.
- [87] Z.P. Lu, C.T. Liu, Role of minor alloying additions in formation of bulk metallic glasses: A Review, *Journal of Materials Science*. 39 (2004) 3965–3974. doi:10.1023/B:JMSC.0000031478.73621.64.
- [88] A. Inoue, T. Aoki, H. Kimura, Effect of B Addition on Extension of Supercooled Liquid Region before Crystallization in Pd-Cu-Si Amorphous Alloys, *Materials Transactions, JIM*. 38 (1997) 175–178. doi:10.2320/matertrans1989.38.175.

-
- [89] H. Choi-Yim, R. Busch, W.L. Johnson, The effect of silicon on the glass forming ability of the Cu₄₇Ti₃₄Zr₁₁Ni₈ bulk metallic glass forming alloy during processing of composites, *Journal of Applied Physics*. 83 (1998) 7993–7997. doi:10.1063/1.367981.
- [90] H. Choi-Yim, D. Xu, W.L. Johnson, Ni-based bulk metallic glass formation in the Ni–Nb–Sn and Ni–Nb–Sn–X (X = B, Fe, Cu) alloy systems, *Applied Physics Letters*. 82 (2003) 1030–1032. doi:10.1063/1.1544434.
- [91] O.N. Senkov, D.B. Miracle, A topological model for metallic glass formation, *Journal of Non-Crystalline Solids*. 317 (2003) 34–39. doi:10.1016/S0022-3093(02)01980-4.
- [92] W.H. Wang, Roles of minor additions in formation and properties of bulk metallic glasses, *Progress in Materials Science*. 52 (2007) 540–596. doi:10.1016/j.pmatsci.2006.07.003.
- [93] H. Kui, A. Greer, D. Turnbull, Formation of Bulk Metallic-Glass by Fluxing, *Appl. Phys. Lett.* 45 (1984) 615–616. doi:10.1063/1.95330.
- [94] O. Haruyama, T. Watanabe, K. Yuki, M. Horiuchi, H. Kato, N. Nishiyama, Thermodynamic approach to glass-forming ability of water-quenched Pd–P-based and Pt₆₀Ni₁₅P₂₅ bulk metallic glasses, *Phys. Rev. B*. 83 (2011). doi:10.1103/PhysRevB.83.064201.
- [95] X. Yang, X. Ma, Q. Li, S. Guo, The effect of Mo on the glass forming ability, mechanical and magnetic properties of FePC ternary bulk metallic glasses, *Journal of Alloys and Compounds*. 554 (2013) 446–449. doi:10.1016/j.jallcom.2012.11.170.
- [96] D. Granata, E. Fischer, V. Wessels, J.F. Löffler, The detrimental effect of flux-induced boron alloying in Pd–Si–Cu bulk metallic glasses, *Applied Physics Letters*. 106 (2015) 11902. doi:10.1063/1.4905174.
- [97] I. Seki, D.V. Louzguine-Luzgin, T. Takahashi, H. Kimura, A. Inoue, Suppression of Crystallization in Ti-Based Alloys by Fluxing, *Materials Transactions*. 52 (2011) 458–463. doi:10.2320/matertrans.MBW201001.
- [98] K.F. Yao, F. Ruan, Y.Q. Yang, N. Chen, Superductile bulk metallic glass, *Appl. Phys. Lett.* 88 (2006). doi:10.1063/1.2187516.
- [99] A. Inoue, N. Nishiyama, H. Kimura, Preparation and Thermal Stability of Bulk Amorphous Pd₄₀Cu₃₀Ni₁₀P₂₀ Alloy Cylinder of 72 mm in Diameter, *Materials Transactions, JIM*. 38 (1997) 179–183. doi:10.2320/matertrans1989.38.179.
- [100] J.S. Yu, Y.Q. Zeng, T. Fujita, T. Hashizume, A. Inoue, T. Sakurai, M.W. Chen, On the effect of impurities in metallic glass formation, *Applied Physics Letters*. 96 (2010) 141901. doi:10.1063/1.3373528.
- [101] A.J. Drehman, A.L. Greer, Kinetics of crystal nucleation and growth in Pd₄₀Ni₄₀P₂₀ glass, *Acta Metallurgica*. 32 (1984) 323–332. doi:10.1016/0001-6160(84)90105-6.
- [102] J. Schroers, W.L. Johnson, Highly processable bulk metallic glass-forming alloys in the Pt–Co–Ni–Cu–P system, *Applied Physics Letters*. 84 (2004) 3666–3668. doi:10.1063/1.1738945.
- [103] J.J. Wall, C.T. Liu, W.-K. Rhim, J.J.Z. Li, P.K. Liaw, H. Choo, W.L. Johnson, Heterogeneous nucleation in a glass-forming alloy, *Applied Physics Letters*. 92 (2008) 244106. doi:10.1063/1.2948861.
- [104] J. Schroers, Y. Wu, W.L. Johnson, Heterogeneous influences on the crystallization of Pd₄₃Ni₁₀Cu₂₇P₂₀, *Philosophical Magazine A*. 82 (2002) 1207–1217. doi:10.1080/01418610208240026.
- [105] D. Granata, E. Fischer, V. Wessels, J.F. Löffler, Fluxing of Pd–Si–Cu bulk metallic glass and the role of cooling rate and purification, *Acta Materialia*. 71 (2014) 145–152. doi:10.1016/j.actamat.2014.03.008.
- [106] N. Chen, L. Gu, G.Q. Xie, D.V. Louzguine-Luzgin, A.R. Yavari, G. Vaughan, S.D. Imhoff, J.H. Perepezko, T. Abe, A. Inoue, Flux-induced structural modification and phase transformations in a Pd₄₀Ni₄₀Si₄P₁₆ bulk-glassy alloy, *Acta Materialia*. 58 (2010) 5886–5897. doi:10.1016/j.actamat.2010.07.003.
- [107] G. Hao, F. Ren, Y. Zhang, J. Lin, Role of yttrium in glass formation of Ti-based bulk metallic glasses, *Rare Metals*. 28 (2009) 68–71. doi:10.1007/s12598-009-0013-7.
- [108] V. Ponnambalam, S.J. Poon, G.J. Shiflet, Fe-based bulk metallic glasses with diameter thickness larger than one centimeter, *Journal of Materials Research*. 19 (2004) 1320–1323. doi:10.1557/JMR.2004.0176.
- [109] V. Ponnambalam, S.J. Poon, G.J. Shiflet, Fe–Mn–Cr–Mo–(Y, Ln)–C–B (Ln = Lanthanides) bulk metallic glasses as formable amorphous steel alloys, *Journal of Materials Research*. 19 (2004) 3046–3052. doi:10.1557/JMR.2004.0374.
- [110] W.H. Wang, Roles of minor additions in formation and properties of bulk metallic glasses, *Progress in Materials Science*. 52 (2007) 540–596. doi:10.1016/j.pmatsci.2006.07.003.
- [111] Z. p. Lu, C. t. Liu, X. z. Wang, Minor additions of Sn in a bulk glass-forming Fe-based system, *Journal of Materials Research*. 21 (2006) 3180–3186. doi:10.1557/jmr.2006.0388.
- [112] R.D. Conner, R.E. Maire, W.L. Johnson, Effect of oxygen concentration upon the ductility of amorphous Zr₅₇Nb₅Al₁₀Cu_{15.4}Ni_{12.6}, *Materials Science and Engineering: A*. 419 (2006) 148–152. doi:10.1016/j.msea.2005.12.009.
- [113] G. Hao, F. Ren, Y. Zhang, J. Lin, Role of yttrium in glass formation of Ti-based bulk metallic glasses, *Rare Metals*. 28 (2009) 68–71. doi:10.1007/s12598-009-0013-7.
- [114] H.S. Chen, Glassy metals, *Rep. Prog. Phys.* 43 (1980) 353. doi:10.1088/0034-4885/43/4/001.
- [115] A. van den Beukel, J. Sietsma, The glass transition as a free volume related kinetic phenomenon, *Acta Metallurgica et Materialia*. 38 (1990) 383–389. doi:10.1016/0956-7151(90)90142-4.
- [116] A. Niikura, A. Tsai, A. Inoue, T. Masumoto, Chemical structural relaxation-induced embrittlement in amorphous Mg₇₀Cu₂₀Y alloys, *Journal of Non-Crystalline Solids*. 159 (1993) 229–234. doi:10.1016/0022-3093(93)90227-O.
- [117] J. Lewandowski, Effects of Annealing and Changes in Stress State on Fracture Toughness of Bulk Metallic Glass, *Materials Transactions*. 42 (2001) 633–637.
- [118] G. Kumar, D. Rector, R.D. Conner, J. Schroers, Embrittlement of Zr-based bulk metallic glasses, *Acta Materialia*. 57 (2009) 3572–3583. doi:10.1016/j.actamat.2009.04.016.

-
- [119] G. Kumar, M. Ohnuma, T. Furubayashi, T. Ohkubo, K. Hono, Thermal embrittlement of Fe-based amorphous ribbons, *Journal of Non-Crystalline Solids*. 354 (2008) 882–888. doi:10.1016/j.jnoncrysol.2007.08.001.
 - [120] O. Haruyama, Y. Nakayama, R. Wada, H. Tokunaga, J. Okada, T. Ishikawa, Y. Yokoyama, Volume and enthalpy relaxation in Zr₅₅Cu₃₀Ni₅Al₁₀ bulk metallic glass, *Acta Materialia*. 58 (2010) 1829–1836. doi:10.1016/j.actamat.2009.11.025.
 - [121] A. van den Beukel, J. Sietsma, The glass transition as a free volume related kinetic phenomenon, *Acta Metallurgica et Materialia*. 38 (1990) 383–389. doi:10.1016/0956-7151(90)90142-4.
 - [122] C.J. Gilbert, R.O. Ritchie, W.L. Johnson, Fracture toughness and fatigue-crack propagation in a Zr–Ti–Ni–Cu–Be bulk metallic glass, *Applied Physics Letters*. 71 (1997) 476–478. doi:10.1063/1.119610.
 - [123] T.W. Wu, F. Spaepen, Small angle X-ray scattering from an embrittling metallic glass, *Acta Metallurgica*. 33 (1985) 2185–2190. doi:10.1016/0001-6160(85)90179-8.
 - [124] W.H. Jiang, F.X. Liu, H. Choo, P.K. Liaw, Effect of Structural Relaxation on Mechanical Behavior of a Zr-Based Bulk-Metallic Glass, *Materials Transactions*. 48 (2007) 1781–1784. doi:10.2320/matertrans.MJ200734.
 - [125] F.E. Luborsky, J.L. Walter, Stability of amorphous metallic alloys, *Journal of Applied Physics*. 47 (1976) 3648–3650. doi:10.1063/1.323173.
 - [126] O. Haruyama, A. Inoue, Free volume kinetics during sub-T_g structural relaxation of a bulk Pd₄₀Ni₄₀P₂₀ metallic glass, *Applied Physics Letters*. 88 (2006) 131906. doi:10.1063/1.2189833.
 - [127] D. Deng, A.S. Argon, Structural relaxation and embrittlement of Cu₅₉Zr₄₁ and Fe₈₀B₂₀ glasses, *Acta Metallurgica*. 34 (1986) 2011–2023. doi:10.1016/0001-6160(86)90260-9.
 - [128] C.J. Gilbert, R.O. Ritchie, W.L. Johnson, Fracture toughness and fatigue-crack propagation in a Zr–Ti–Ni–Cu–Be bulk metallic glass, *Applied Physics Letters*. 71 (1997) 476–478. doi:10.1063/1.119610.
 - [129] G. Kumar, D. Rector, R.D. Conner, J. Schroers, Embrittlement of Zr-based bulk metallic glasses, *Acta Materialia*. 57 (2009) 3572–3583. doi:10.1016/j.actamat.2009.04.016.
 - [130] J. Lewandowski, Effects of Annealing and Changes in Stress State on Fracture Toughness of Bulk Metallic Glass, *Materials Transactions*. 42 (2001) 633–637.
 - [131] W.H. Jiang, F.X. Liu, H. Choo, P.K. Liaw, Effect of Structural Relaxation on Mechanical Behavior of a Zr-Based Bulk-Metallic Glass, *Materials Transactions*. 48 (2007) 1781–1784. doi:10.2320/matertrans.MJ200734.
 - [132] C. Suryanarayana, A. Inoue, *Bulk Metallic Glasses*, CRC Press, 2010.
 - [133] T. Nagase, T. Sanda, A. Nino, W. Qin, H. Yasuda, H. Mori, Y. Umakoshi, J.A. Szpunar, MeV electron irradiation induced crystallization in metallic glasses: Atomic structure, crystallization mechanism and stability of an amorphous phase under the irradiation, *Journal of Non-Crystalline Solids*. 358 (2012) 502–518. doi:10.1016/j.jnoncrysol.2011.11.010.
 - [134] T. Nagase, Y. Umakoshi, Temperature dependence in density-fluctuation-induced crystallization in metallic glass by MeV electron irradiation, *Intermetallics*. 18 (2010) 1803–1808. doi:10.1016/j.intermet.2010.02.044.
 - [135] T. Nagase, T. Hosokawa, Y. Umakoshi, Temperature dependence of MeV-electron-irradiation-induced nanocrystallization in Zr–Pt metallic glass, *Intermetallics*. 18 (2010) 767–772. doi:10.1016/j.intermet.2009.12.003.
 - [136] Z. Yan, Y. Hu, K. Song, F. Dai, J. He, J. Eckert, Vickers-indentation-induced crystallization in a metallic glass, *Applied Physics Letters*. 106 (2015) 101909. doi:10.1063/1.4915109.
 - [137] Z. Yan, K. Song, Y. Hu, F. Dai, Z. Chu, J. Eckert, Localized crystallization in shear bands of a metallic glass, *Scientific Reports*. 6 (2016) 19358. doi:10.1038/srep19358.
 - [138] M.C. Gao, R.E. Hackenberg, G.J. Shiflet, Deformation-Induced Nanocrystal Precipitation in Al-Base Metallic Glasses, *Materials Transactions*. 42 (2001) 1741–1747. doi:10.2320/matertrans.42.1741.
 - [139] J.-J. Kim, Y. Choi, S. Suresh, A.S. Argon, Nanocrystallization During Nanoindentation of a Bulk Amorphous Metal Alloy at Room Temperature, *Science*. 295 (2002) 654–657. doi:10.1126/science.1067453.
 - [140] N. Boucharat, R. Hebert, H. Rösner, R. Valiev, G. Wilde, Nanocrystallization of amorphous Al₈₈Y₇Fe₅ alloy induced by plastic deformation, *Scripta Materialia*. 53 (2005) 823–828. doi:10.1016/j.scriptamat.2005.06.004.
 - [141] B. Lohwongwatana, J. Schroers, W.L. Johnson, Strain Rate Induced Crystallization in Bulk Metallic Glass-Forming Liquid, *Phys. Rev. Lett.* 96 (2006) 75503. doi:10.1103/PhysRevLett.96.075503.
 - [142] P. Rizzi, F. Scaglione, L. Battezzati, Nanoporous gold by dealloying of an amorphous precursor, *Journal of Alloys and Compounds*. 586, Supplement 1 (2014) S117–S120. doi:10.1016/j.jallcom.2012.11.029.
 - [143] T. Nagase, T. Sanda, A. Nino, W. Qin, H. Yasuda, H. Mori, Y. Umakoshi, J.A. Szpunar, MeV electron irradiation induced crystallization in metallic glasses: Atomic structure, crystallization mechanism and stability of an amorphous phase under the irradiation, *Journal of Non-Crystalline Solids*. 358 (2012) 502–518. doi:10.1016/j.jnoncrysol.2011.11.010.
 - [144] A.R. Yavari, K. Georgarakis, J. Antonowicz, M. Stoica, N. Nishiyama, G. Vaughan, M. Chen, M. Pons, Crystallization during Bending of a Pd-Based Metallic Glass Detected by X-Ray Microscopy, *Phys. Rev. Lett.* 109 (2012) 85501. doi:10.1103/PhysRevLett.109.085501.
 - [145] K.M. Flores, R.H. Dauskardt, Local heating associated with crack tip plasticity in Zr–Ti–Ni–Cu–Be bulk amorphous metals, *Journal of Materials Research*. 14 (1999) 638–643. doi:10.1557/JMR.1999.0642.
 - [146] Z. Yan, W. Hao, Y. Hu, K. Song, M. Stoica, S. Scudino, J. Eckert, Evidence for viscous flow nature in Zr₆₀Al₁₅Ni₂₅ metallic glass subjected to cold rolling, *Applied Physics Letters*. 103 (2013) 21907. doi:10.1063/1.4813497.
 - [147] A. Argon, Plastic deformation in metallic glasses, *Acta Metallurgica*. 27 (1979) 47–58. doi:10.1016/0001-6160(79)90055-5.
 - [148] C.A. Schuh, A.C. Lund, Atomistic basis for the plastic yield criterion of metallic glass, *Nat Mater.* 2 (2003) 449–452. doi:10.1038/nmat918.

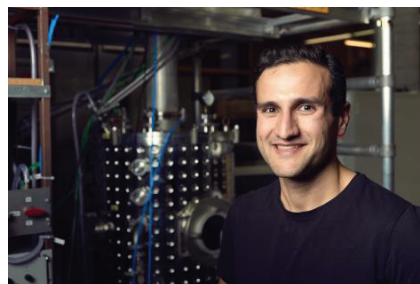
-
- [149] Z. Yan, W. Hao, Y. Hu, K. Song, M. Stoica, S. Scudino, J. Eckert, Evidence for viscous flow nature in Zr60Al15Ni25 metallic glass subjected to cold rolling, *Applied Physics Letters*. 103 (2013) 21907. doi:10.1063/1.4813497.
 - [150] N. Boucharat, R. Hebert, H. Rösner, R. Valiev, G. Wilde, Nanocrystallization of amorphous Al88Y7Fe5 alloy induced by plastic deformation, *Scripta Materialia*. 53 (2005) 823–828. doi:10.1016/j.scriptamat.2005.06.004.
 - [151] P. Rizzi, F. Scaglione, L. Battezzati, Nanoporous gold by dealloying of an amorphous precursor, *Journal of Alloys and Compounds*. 586, Supplement 1 (2014) S117–S120. doi:10.1016/j.jallcom.2012.11.029.
 - [152] L.Y. Watanabe, S.N. Roberts, N. Baca, A. Wiest, S.J. Garrett, R.D. Conner, Fatigue and corrosion of a Pd-based bulk metallic glass in various environments, *Materials Science and Engineering: C*. 33 (2013) 4021–4025. doi:10.1016/j.msec.2013.05.044.
 - [153] M.T. Clavaguera-Mora, N. Clavaguera, D. Crespo, T. Pradell, Crystallisation kinetics and microstructure development in metallic systems, *Progress in Materials Science*. 47 (2002) 559–619. doi:10.1016/S0079-6425(00)00021-9.
 - [154] U. Köster, J. Meinhardt, NATO-Advanced Research Workshop on Undercooled Metallic Melts: Properties, Solidification and Metastable Phases Crystallization of highly undercooled metallic melts and metallic glasses around the glass transition temperature, *Materials Science and Engineering: A*. 178 (1994) 271–278. doi:10.1016/0921-5093(94)90553-3.
 - [155] U. Köster, J. Meinhardt, NATO-Advanced Research Workshop on Undercooled Metallic Melts: Properties, Solidification and Metastable Phases Crystallization of highly undercooled metallic melts and metallic glasses around the glass transition temperature, *Materials Science and Engineering: A*. 178 (1994) 271–278. doi:10.1016/0921-5093(94)90553-3.
 - [156] A. Inoue, Amorphous, nanoquasicrystalline and nanocrystalline alloys in Al-based systems, *Progress in Materials Science*. 43 (1998) 365–520. doi:10.1016/S0079-6425(98)00005-X.
 - [157] D.V. Louzguine, A. Inoue, Crystallization behaviour of Al-based metallic glasses below and above the glass-transition temperature, *Journal of Non-Crystalline Solids*. 311 (2002) 281–293. doi:10.1016/S0022-3093(02)01375-3.
 - [158] A.L. Greer, Partially or fully devitrified alloys for mechanical properties, *Materials Science and Engineering: A*. 304–306 (2001) 68–72. doi:10.1016/S0921-5093(00)01449-0.
 - [159] H.S. Kim, P.J. Warren, B. Cantor, H.R. Lee, Mechanical properties of partially crystallized aluminum based amorphous alloys, *Nanostructured Materials*. 11 (1999) 241–247. doi:10.1016/S0965-9773(99)00037-9.
 - [160] M.R. Scanlon, R.C. Cammarata, Mechanical properties of nanocomposite granular metal thin films, *Journal of Applied Physics*. 76 (1994) 3387–3393. doi:10.1063/1.357465.
 - [161] A.L. Greer, Partially or fully devitrified alloys for mechanical properties, *Materials Science and Engineering: A*. 304–306 (2001) 68–72. doi:10.1016/S0921-5093(00)01449-0.
 - [162] A.A. Csontos, G.J. Shiflet, Formation and chemistry of nanocrystalline phases formed during deformation in aluminum-rich metallic glasses, *Nanostructured Materials*. 9 (1997) 281–289. doi:10.1016/S0965-9773(97)90068-4.
 - [163] M.E. Siegrist, D.P. Steinlin, J.F. Löffler, Processing of diamond-reinforced bulk metallic glass composites, *Materials Science and Engineering: A*. 447 (2007) 298–302. doi:10.1016/j.msea.2006.10.013.
 - [164] Y.-H. Kim, A. Inoue, T. Masumoto, Ultrahigh Tensile Strengths of Al88Y2Ni9M1 (M=Mn or Fe) Amorphous Alloys Containing Finely Dispersed fcc-Al Particles, *Materials Transactions, JIM*. 31 (1990) 747–749. doi:10.2320/matertrans1989.31.747.
 - [165] Z.C. Zhong, X.Y. Jiang, A.L. Greer, Ninth International Conference on Rapidly Quenched and Metastable Materials Micro structure and hardening of Al-based nanophase composites, *Materials Science and Engineering: A*. 226 (1997) 531–535. doi:10.1016/S0921-5093(97)80062-7.
 - [166] P.G. Boswell, The wear resistance of a liquid quenched metallic glass, *J Mater Sci*. 14 (n.d.) 1505–1507. doi:10.1007/BF00549329.
 - [167] R.I. Wu, G. Wilde, J.H. Perepezko, Glass formation and primary nanocrystallization in Al-base metallic glasses, *Materials Science and Engineering: A*. 301 (2001) 12–17. doi:10.1016/S0921-5093(00)01390-3.
 - [168] C. Fan, C. Li, A. Inoue, Nanocrystal composites in Zr–Nb–Cu–Al metallic glasses, *Journal of Non-Crystalline Solids*. 270 (2000) 28–33. doi:10.1016/S0022-3093(00)00078-8.
 - [169] B.A. Legg, J. Schroers, R. Busch, Thermodynamics, kinetics, and crystallization of Pt57.3Cu14.6Ni5.3P22.8 bulk metallic glass, *Acta Materialia*. 55 (2007) 1109–1116. doi:10.1016/j.actamat.2006.09.024.
 - [170] A. Inoue, N. Nishiyama, H. Kimura, Preparation and Thermal Stability of Bulk Amorphous Pd40Cu30Ni10P20 Alloy Cylinder of 72 mm in Diameter, *Materials Transactions, JIM*. 38 (1997) 179–183. doi:10.2320/matertrans1989.38.179.
 - [171] J. Schroers, Y. Wu, W.L. Johnson, Heterogeneous influences on the crystallization of Pd43Ni10Cu27P20, *Philosophical Magazine A*. 82 (2002) 1207–1217. doi:10.1080/01418610208240026.
 - [172] J.J. Wall, C.T. Liu, W.-K. Rhim, J.J.Z. Li, P.K. Liaw, H. Choo, W.L. Johnson, Heterogeneous nucleation in a glass-forming alloy, *Applied Physics Letters*. 92 (2008) 244106. doi:10.1063/1.2948861.
 - [173] J.S. Yu, Y.Q. Zeng, T. Fujita, T. Hashizume, A. Inoue, T. Sakurai, M.W. Chen, On the effect of impurities in metallic glass formation, *Applied Physics Letters*. 96 (2010) 141901. doi:10.1063/1.3373528.
 - [174] J.F. Löffler, J. Schroers, W.L. Johnson, Time–temperature–transformation diagram and microstructures of bulk glass forming Pd40Cu30Ni10P20, *Applied Physics Letters*. 77 (2000) 681–683. doi:10.1063/1.127084.
 - [175] C. Ma, N. Nishiyama, A. Inoue, Phase Equilibria and Thermal Stability of Pd–Cu–Ni–P Alloys, *Materials Transactions*. 43 (2002) 1161–1165. doi:10.2320/matertrans.43.1161.
 - [176] N. Nishiyama, A. Inoue, Stability and thermodynamics of primary precipitation in supercooled Pd–Cu–Ni–P melt, *Journal of Non-Crystalline Solids*. 312–314 (2002) 575–580. doi:10.1016/S0022-3093(02)01784-2.
 - [177] D. Turnbull, R.E. Cech, Microscopic Observation of the Solidification of Small Metal Droplets, *Journal of Applied Physics*. 21 (1950) 804–810. doi:10.1063/1.1699763.

-
- [178] N. Nishiyama, M. Matsushita, A. Inoue, In-situ observation of the early stage of crystallization in undercooled Pd-Cu-Ni-P melt, *Scripta Materialia*. 44 (2001) 1261–1267. doi:10.1016/S1359-6462(01)00694-7.
- [179] S. Cardinal, J. Qiao, J.M. Pelletier, H. Kato, Bulk metallic glasses based on precious metals: Thermal treatments and mechanical properties, *Intermetallics*. 63 (2015) 73–79. doi:10.1016/j.intermet.2015.04.003.
- [180] F. Spaepen, A microscopic mechanism for steady state inhomogeneous flow in metallic glasses, *Acta Metallurgica*. 25 (1977) 407–415. doi:10.1016/0001-6160(77)90232-2.
- [181] W.L. Johnson, Bulk Glass-Forming Metallic Alloys: Science and Technology, *MRS Bulletin*. 24 (1999) 42–56. doi:10.1557/S0883769400053252.
- [182] F. Spaepen, A microscopic mechanism for steady state inhomogeneous flow in metallic glasses, *Acta Metallurgica*. 25 (1977) 407–415. doi:10.1016/0001-6160(77)90232-2.
- [183] F. Spaepen, Homogeneous flow of metallic glasses: A free volume perspective, *Scripta Materialia*. 54 (2006) 363–367. doi:10.1016/j.scriptamat.2005.09.046.
- [184] B. Yang, C.T. Liu, T.G. Nieh, Unified equation for the strength of bulk metallic glasses, *Applied Physics Letters*. 88 (2006) 221911. doi:10.1063/1.2206099.
- [185] J.J. Lewandowski, A.L. Greer, Temperature rise at shear bands in metallic glasses, *Nat Mater*. 5 (2006) 15–18. doi:10.1038/nmat1536.
- [186] J. Schroers, Processing of Bulk Metallic Glass, *Advanced Materials*. 22 (2009) 1566–1597. doi:10.1002/adma.200902776.
- [187] M.F. Ashby, A.L. Greer, Metallic glasses as structural materials, *Scripta Materialia*. 54 (2006) 321–326. doi:10.1016/j.scriptamat.2005.09.051.
- [188] E. Axinte, Metallic glasses from “alchemy” to pure science: Present and future of design, processing and applications of glassy metals, *Materials & Design*. 35 (2012) 518–556. doi:10.1016/j.matdes.2011.09.028.
- [189] W.H. Wang, C. Dong, C.H. Shek, Bulk metallic glasses, *Materials Science and Engineering: R: Reports*. 44 (2004) 45–89. doi:10.1016/j.mser.2004.03.001.
- [190] H.S. Chen, Glassy metals, *Reports on Progress in Physics*. 43 (1980) 353–432. doi:10.1088/0034-4885/43/4/001.
- [191] J. Schroers, W.L. Johnson, Ductile Bulk Metallic Glass, *Phys. Rev. Lett.* 93 (2004) 255506. doi:10.1103/PhysRevLett.93.255506.
- [192] S. Mukherjee, Z. Zhou, J. Schroers, W.L. Johnson, W.K. Rhim, Overheating threshold and its effect on time–temperature–transformation diagrams of zirconium based bulk metallic glasses, *Applied Physics Letters*. 84 (2004) 5010–5012. doi:10.1063/1.1763219.
- [193] Z. Liu, R. Li, G. Liu, K. Song, S. Pauly, T. Zhang, J. Eckert, Pronounced ductility in CuZrAl ternary bulk metallic glass composites with optimized microstructure through melt adjustment, *AIP Advances*. 2 (2012) 32176. doi:10.1063/1.4754853.
- [194] E.R. Arata, High-temperature, ultrahigh-gravity centrifugal processing of metallic melts, *ETH*, 2008.
- [195] D.R. Gaskell, *Introduction to the Thermodynamics of Materials*, Fifth Edition, CRC Press, 2008.
- [196] P. Beiss, R. Ruthardt, H. Warlimont, eds., *Powder Metallurgy Data. Refractory, Hard and Intermetallic Materials*, Springer-Verlag, Berlin/Heidelberg, 2002. <http://materials.springer.com/bp/docs/978-3-540-45660-5> (accessed September 8, 2016).
- [197] H.A. Davies, B.G. Lewis, Metallic glasses and the avoidance of crystallization in metallic melts, *Faraday Discuss. Chem. Soc.* 61 (1976) 100–109. doi:10.1039/DC9766100100.
- [198] N. Ashgriz, *Handbook of Atomization and Sprays: Theory and Applications*, Springer Science & Business Media, 2011.
- [199] J. Schroers, The superplastic forming of bulk metallic glasses, *JOM*. 57 (2005) 35–39. doi:10.1007/s11837-005-0093-2.
- [200] T.A. Waniuk, R. Busch, A. Masuhr, W.L. Johnson, Equilibrium viscosity of the Zr₄₁Ti₁₃Cu_{12.5}Ni₁₀Be_{22.5} bulk metallic glass-forming liquid and viscous flow during relaxation, phase separation, and primary crystallization, *Acta Mater.* 46 (1998) 5229–5236. doi:10.1016/S1359-6454(98)00242-0.
- [201] G. Wu, R. Li, Z. Liu, B. Chen, Y. Li, Y. Cai, T. Zhang, Induced multiple heterogeneities and related plastic improvement by laser surface treatment in CuZr-based bulk metallic glass, *Intermetallics*. 24 (2012) 50–55. doi:10.1016/j.intermet.2012.01.022.
- [202] Y. Terada, K. Ohkubo, T. Mohri, Thermal Conductivities of Platinum Alloys at High Temperatures OBSERVATIONS COMPLIANT WITH THE WIEDEMANN-FRANZ RELATION, *Platin. Met. Rev.* 49 (2005) 21–26. doi:10.1595/147106705X24364.
- [203] H.E. Kissinger, Reaction Kinetics in Differential Thermal Analysis, *Analytical Chemistry*. 29 (1957) 1702–1706. doi:10.1021/ac60131a045.
- [204] M. Lasocka, The effect of scanning rate on glass transition temperature of splat-cooled Te₈₅Ge₁₅, *Materials Science and Engineering*. 23 (1976) 173–177. doi:10.1016/0025-5416(76)90189-0.
- [205] Q. Qin, G.B. McKenna, Correlation between dynamic fragility and glass transition temperature for different classes of glass forming liquids, *Journal of Non-Crystalline Solids*. 352 (2006) 2977–2985. doi:10.1016/j.jnoncrysol.2006.04.014.
- [206] F. Spaepen, Homogeneous flow of metallic glasses: A free volume perspective, *Scripta Materialia*. 54 (2006) 363–367. doi:10.1016/j.scriptamat.2005.09.046.
- [207] W.-W. Zhang, Y. Du, H. Xu, W. Xiong, Y. Kong, W. Sun, F. Pan, A. Tang, Thermodynamic Assessment of the Cu-B System Supported by Key Experiment and First-Principles Calculations, *J. Phase Equilib. Diffus.* 30 (2009) 480. doi:10.1007/s11669-009-9561-7.
- [208] NanoSIMS | LGB, (n.d.). <http://lgb.epfl.ch/NanoSIMS> (accessed September 27, 2016).
- [209] E.P. Ferlito, G. Pizzo, R. De Gregorio, G. Anastasi, R. Ricciari, D. Mello, TOF-SIMS Characterization of Boron and Phosphorus Distribution in sub-atmospheric Chemical Vapour Deposition Borophosphosilicate Glass (SA-CVD BPSG) films, 2013 IEEE International Reliability Physics Symposium (Irps). (2013).

-
- [210] W. Yang, S. Hu, J. Zhang, J. Hao, Y. Lin, NanoSIMS analytical technique and its applications in earth sciences, *Sci. China Earth Sci.* 58 (2015) 1758–1767. doi:10.1007/s11430-015-5106-6.
- [211] B. Kasel, T. Wirtz, Reduction of the SIMS Matrix Effect Using the Storing Matter Technique: A Case Study on Ti in Different Matrices, *Anal. Chem.* 86 (2014) 3750–3755. doi:10.1021/ac4030472.
- [212] T.L. Aselage, The coexistence of silicon borides with boron-saturated silicon: Metastability of SiB₃, *J. Mater. Res.* 13 (1998) 1786–1794. doi:10.1557/JMR.1998.0252.

Curriculum Vitae

Hamed KAZEMI



E-mail: kazemihamed87@gmail.com

Address: Ave. des Oiseaux 9, 1018 Lausanne, Switzerland

Personal cell: +41 78 879 6625

Profile

- **PhD, EPFL** – Design, process and forming of a high performance Pt-alloy.
- Master in Science and Engineering of Materials, EPFL.
- **Structural Materials for Transport, Energy and Infrastructure.**
- Minor in **Management of Technology and Entrepreneurship**, EPFL.

Education

École Polytechnique Fédérale de Lausanne (EPFL), Switzerland

Doctorate in Materials Science and Engineering, (Defense on 10/1/2017)

École Polytechnique Fédérale de Lausanne (EPFL), Switzerland, 2012

Master in Materials Science and Engineering,

École Polytechnique Fédérale de Lausanne (EPFL), Switzerland, 2012

Minor in Management of Technology and Entrepreneurship.

Sharif University of Technology, Tehran, Iran, 2010

Bachelor in Materials Science and Engineering,

Experience

2012-2016 Researcher (Doctoral-Assistant), Laboratory of Mechanical Metallurgy (LMM), EPFL

- Development of a new hard amorphous Pt850 alloy (Patent EP2705170B1).
- Designing of the fabrication process and forming of the Pt-based amorphous alloy in the supercooled liquid region for producing net-shape watch components.
- Fabrication of an atomizer capable of producing up to 1kg of amorphous powder of precious metals.

Management training

International contracts - Managing risks, innovation and dissonance – Market creation – Logistics and demand analysis - Project management and risk analysis - Negotiation techniques - Principles of finance - Principles of microeconomics - Strategic marketing and technology commercialization - Technology and innovation management - Technology strategy and corporate entrepreneurship

Technical skills

Materials characterization

Experiment design, Electron Microscopy, Scanning electron microscopy (SEM), elemental analysis with EDX, mass spectroscopy, X-ray diffraction, Transmission electron microscopy, Differential scanning calorimetry (DSC), Thermo Mechanical Analysis (TMA), Metallography, Micro-hardness, Diverse mechanical tests.

Fabrication and forming of materials

Atomization, Casting, arc-melting, Thermoplastic forming, net-shape production, laser surface treatment, powder technology, Alloy design and production

Languages

Georgian, French, English, Persian, Spanish

Prizes

Best master project in Materials Science and Engineering, EPFL, 2012.

Special prize given by the dean of the faculty of Science and Techniques of Engineering (STI), EPFL

Publications

Articles:

- 1.H. Kazemi, L. Weber, Solid solubility of germanium in silver, *Thermochimica Acta*. 544 (2012) 57–62.
- 2.H. Kazemi, C. Cattin, M. Blank, L. Weber, Development of a new family of phosphorous-free Pt-based bulk metallic glasses, *Journal of Alloys and Compounds*. 695 (2017) 3419–3428.
- 3.H. Kazemi, C. Cattin, G. Hodel, T. Pachova, L. Weber, Effects of partial crystallization in Pt-Si-B-based bulk metallic glasses on glass transition and crystallization of the remaining amorphous matrix, *Journal of Non-Crystalline Solids*.
- 4.H. Kazemi, C. Cattin, A. Arakcheeva, L. Weber, Synchrotron X-ray diffraction of crystallization in Pt-Si-B-Ge-Cu bulk metallic glass, (Submitted to *Journal of alloys and compounds*)
- 5.H. Kazemi, C. Cattin, M. Taconnet de Perrot, A. Schreier, L. Weber, Influence of minor addition of rare-earth metal on thermophysical properties of Pt-Si-B-Ge-Cu bulk metallic glass, (Submitted to *Materials Designs*)

Personal details

29 old, of Georgian and Iranian nationalities.

